Modelling Excited States and Two-Photon Absorption Properties with Frozen Density Embedding Theory

Fu, Mingxue

Université de Genève — Faculté des sciences

Section de chimie et biochimie
Département de chimie physique — Professeur T. A. Wesołowski

Modelling Excited States and Two-Photon Absorption Properties with Frozen Density Embedding Theory

THÈSE

présentée à la Faculté des sciences de l'Université de Genève
pour obtenir le grade de Docteur ès sciences, mention interdisciplinaire

par

Mingxue Fu

de

Maoshan, Chine

Thèse N° 5786

GENÈVE

Ateliers d'impression de l'Université de Genève

2023

For my parents

"The divine law may be spoken of, but it is not the common law. Things may be named, but names are not the things."
-Lao Tzu

Abstract

Modelling excited states properties of molecular systems usually requires a compromise between the accuracy and computational efficiency. This is especially true when modelling the non linear optics, such as two-photon absorption (TPA) cross sections, which requires an accurate description of all excited states. To address these complexities, multiscale methods are employed, designed for complex systems in which a specific "core" part significantly influences the system's behaviour. This approach allows for extensive calculations on large molecular systems where a full quantum mechanical treatment would be not feasible.

Frozen Density Embedding Theory (FDET) is one category of multiscale methods, developed by the Wesołowski group. One important aspect about FDET is that the FDET energy functional is in an exact relation with the Hohenberg-Kohn energy. Nonetheless, in practice, approximations have to be made due to the lack of the necessary exact density functionals. In FDET, the system of interest A is handled using a higher-level theory with the wavefunction variable Ψ_A, while the environment B is treated with a lower-level theory, relying on electron density ρ_B as a descriptor.

This thesis comprises three topics. The first one concerns the confidence level in modelling the two-photon absorption cross section in the condensed phase. The reliability of the used approximations for FDET is assessed comparing the TPA results with advanced excited state methods. The computational challenge in modelling this property has been highlighted. Furthermore, the significance of different environment induced effects has been addressed. This provides insight on the importance of geometry, the polarisation and the role of the Pauli repulsion effect in modelling TPA properties.

The second topic focus on the FDET embedding potential on its ρ_B-dependency when the differential polarisation is focused. Additionally, the asymptotic behaviour of the non-additive kinetic potential in order to improve the accuracy of FDET embedding potential has also been investigated. The third topic delves into the modelling of two-photon absorption cross section with the time-frequency-entangled pairs, rather than classical pairs. This leads to a further exploration on an intriguing phenomenon associated with the entangled pairs, known as entangled TPA (ETPA) transparency, in which the chromophore displays no entangled two-photon absorption cross section signals despite strong classical TPA signals.

Résumé

La modélisation des propriétés des états excités de systèmes moléculaires implique généralement de trouver un compromis entre la précision et l'efficacité computationnelle. C'est particulièrement vrai pour la modélisation de l'optique non linéaire, telle que les *two-photon absorption* (TPA), qui nécessite le calcul de plusieurs états excités. Pour relever ces défis, une méthode multiscalaire est employée, conçue pour les systèmes complexes où une " partie centrale" spécifique influe de manière significative sur le comportement du système. Cette approche permet d'effectuer des calculs détaillés sur des systèmes moléculaires de grande taille pour lesquels un traitement quantique complet serait irréalisable.

Frozen Density Embedding Theory (FDET) fait partie des méthodes multiscalaires et a été développée par le groupe de Wesołowski. Un aspect essentiel de FDET est que sa fonction énergétique est en relation exacte avec l'énergie de Hohenberg-Kohn. Néanmoins, dans la pratique, l'utilisation d'approximations est requise car les fonctionnelles de densité exactes ne sont pas connues. Dans FDET, le système d'intérêt A est traité avec une théorie de niveau supérieur utilisant la variable de la fonction d'onde Ψ_A, tandis que l'environnement B est traité avec une théorie de niveau inférieur, en se basant sur la densité électronique ρ_B comme descripteur.

Cette thèse aborde trois sujets principaux. Le premier concerne le niveau de confiance dans la modélisation de la TPA dans la phase condensée. La fiabilité des approximations utilisées dans FDET est évaluée en comparant des résultats de TPA à des méthodes de modélisation d'états excités plus avancées. Les défis computationnels de la modélisation de cette propriété sont mis en évidence. De plus, l'importance des effets induits par l'environnement est examinée, fournissant des indications sur l'importance de la géométrie, de la polarisation et du rôle de l'effet de répulsion de Pauli dans la modélisation des propriétés de TPA.

Le deuxième sujet se concentre sur le *FDET embedding potential* $\hat{v}_{emb}^{FDET}$ et sa dépendance par rapport à ρ_B lorsqu'une polarisation différentielle est appliquée. De plus, le comportement asymptotique du potentiel cinétique non additif est étudié pour améliorer la précision du $\hat{v}_{emb}^{FDET}$.

Le troisième sujet porte sur la modélisation de TPA cross-section, non pas avec des paires classiques de photons, mais avec des paires de photons intriqués dans le domaine temps-fréquence. Cela conduit à une exploration d'un phénomène intrigant associé aux paires de photons intriqués, appelé *entangled two-photon absorption* (ETPA) transparency, dans lequel le chromophore ne présente aucun signal ETPA, malgré de forts signaux classiques de TPA.

List of publications

1. Fu M, D. Tabakaev, R. T. Thew, and T. A. Wesolowski, "Fine-tuning of entangled two-photon absorption by controlling the one-photon absorption properties of the chromophore", *J. Phys. Chem. Lett.* 14, 2613-2619 (2023)
2. Fu M, Wesolowski TA, "Explicit treatment of the state-specific response of electron density of the environment within Frozen-Density Embedding Theory", *J. Phys. Chem. A.* 127, 535-545 (2023)
3. Fu M, Wesolowski TA, "The Challenge of Accurate Computation of Two-Photon Absorption Properties of Organic Chromophores in the Condensed Phase", *J. Chem. Theory Comput.* 17, 3652-3665 (2021)

Structure of the thesis

This thesis is structured in the following way.

Chapter 1 introduces the fundamental quantum mechanical methods for modelling molecular systems. In **Chapter 2** we introduce multiscale methods with a focus on the Frozen Density Embedding Theory. Specific issues related to the state-dependency and state-specific polarization are discussed within FDET and within other multiscale methods. **Chapter 3** outlines the frameworks of two excited state methods - one based on the polarization propagator and the other on the coupled cluster method. It also includes the derivation of the TPA cross section from the microscopic to macroscopic expression. A detailed derivation of obtaining different orders of time-dependent phase isolated wavefunctions is provided in **Appendix A**.

In **Chapter 4** the approximation used in FDET is examined for evaluating TPA cross section. The analysis is conducted on a small complex for which reference results are available. The TPA cross section, along with absolute and shift values, is presented with different embedding methods alongside the supermolecular reference. **Chapter 5** focuses on the generation of ρ_B, on weather it is state-independent or state-specific in FDET, and its impact on the vertical excitation energy. The benchmarking includes 47 excitations, showing the average error and standard deviation from the use of different ρ_B. The error on the FDET energy can also be attributed to the use of approximation for the non-additive kinetic potential. The asymptotic behaviour of the non-additive kinetic potential approximated by the non-decomposable approach is verified in **Appendix B**.

Chapter 6 explores the utilization of the entangled photon pairs, as opposed to classical pairs, in the TPA cross section. The entangled induced TPA transparency phenomenon is introduced and how the electronic structure of the chromophore influences the entangled induced TPA transparency is investigated with a truncated sum-over-state expression.

Chapter 7 comprises unpublished results addressing the important physical effects in the modelling TPA cross section. In **Chapter 8**, we draw a general conclusion of this thesis. Finally, **Appendix C-F** provides the supporting information for publications from Chapter 4-5.

Contents

Abbreviations

HK	Hohenberg-Kohn
HF	Hartree-Fock
KS-DFT	Kohn-Sham DFT
MP	Møller-Plesset perturbation theory
MP1	Møller-Plesset perturbation theory first order
MP2	Møller-Plesset perturbation theory second order
ADC	algebraic diagrammatic construction
AO	atomic orbital
CC	coupled cluster
EOM-CCSD	equation-of-motion CC singles and doubles
CCSD	CC singles and doubles
CI	configuration interaction
CIS	CI singles
CISD	CI singles and doubles
DFT	density functional theory
FCI	full CI
FDET	Frozen-Density Embedding Theory
LDA	local density approximation
GGA	generalized gradient approximation
ME	monomer expansion
SE	supermolecular expansion
MO	molecular orbital
QM/MM	quantum mechanics / molecular mechanics
SCF	self-consistent field
OPA	one-photon absorption
TPA	two-photon absorption
ETPA	entangled two-photon absorption

Notes on units

The most convenient units used in a quantum mechanical calculations are the atomic unites. The atomic unites are defined by the energy, the radius of the electron orbital (in the classical picture), etc., of the electron of the hydrogen atom in the ground state. The reduced Planck constant, elementary charge, and the mass of electron are set to 1 in atomic unites. There are other unit systems, such as the common international system of units (SI), or the centimetre–gram–second (cgs) system of unites which is widely applied in the spectroscopic measurement.

One interesting fact on the atomic unit is that 1 $a.u.$ of the magnetic field equals $2.5 \cdot 10^5$ Tesla. The magnetic field of the Earth is in the order of $1 \cdot 10^{-2}$ Tesla. This means the same scale of 1 $a.u.$ of the magnetic field can be found on a neutron star.

A table includes the conversion factor between the atomic unit and SI or cgs is given below.

Physical quantity	Atomic units	cgs unit	SI
electron charge	1	$4.8{\cdot}10^{-10}$ esu	$1.6 \cdot 10^{-19}$ C
electron mass	1	$9.1{\cdot}10^{-28}$ g	$9 .1{\cdot}10^{-31}$ kg
$\hbar$	1	$1.05{\cdot}10^{-27}$ erg·s	$1.05{\cdot}10^{-34}$ J·s
fine structure constant	$\frac{1}{137}$	$\frac{1}{137}$	$\frac{1}{137}$
speed of light	137	$3{\cdot}10^{10}$ cm/s	$3{\cdot}10^{8}$ m/s
Bohr radius	1 Bohr	$5.3{\cdot}10^{-9}$ cm	$5.3{\cdot}10^{-11}$ m
Hartree energy E_h	1 Hartree	$4.4{\cdot}10^{-11}$ erg	$4.4{\cdot}10^{-18}$ J
atomic unit of time	1	$2.4{\cdot}10^{-17}$ s	$2.4{\cdot}10^{-17}$ s

Chapter 1

Quantum mechanical methods for molecular systems

1.1 Introduction

In this chapter, we briefly introduce some of the fundamental quantum mechanical methods applied in simulations of molecular systems. The non-relativistic time-independent wavefunction is considered here and the time-dependent case will be covered in Chapter 3.

The non-relativistic time-independent Schrödinger equation [1] is:

$$\hat{H}\Psi = E\Psi \tag{1.1}$$

where the hermitian operator $\hat{H}$ is the Hamiltonian of the system and the corresponding energy E. The Schrödinger equation is a non-linear partial derivative equation , and its eigenvectors Ψ are vectors in a certain Hibert space named the Sobolev space H^1. The wavefunction Ψ is in the Hibert space because it satisfies three properties of the Hibert space, namely:i) the inner products are computable eg. the normalization condition $\langle\Psi|\Psi\rangle = 1$; ii) Ψ forms infinite dimensional vector space; and iii) any linear combination of the solutions also lies in the same space.

The Hamiltonian of a molecular system, which contains the nuclei ($\mathbf{R}_A$) and electron coordinates ($\mathbf{r}_i$), can be written in the following form with atomic units:

$$\hat{H} = -\sum_{i}^{N}\frac{1}{2}\nabla_i^2 - \sum_{A}^{M}\frac{1}{2m_A}\nabla_A^2 - \sum_{i}^{N}\sum_{A}^{M}\frac{Z_A}{\mathbf{r}_{iA}} + \sum_{i}^{N}\sum_{j>i}^{N}\frac{1}{\mathbf{r}_{ij}} + \sum_{A}^{M}\sum_{B>A}^{M}\frac{Z_A Z_B}{\mathbf{R}_{AB}} \tag{1.2}$$

The first two terms are the kinetic operator for the electron and nuclei; the third describes the electronic interaction between the nuclei and electrons; the fourth and fifth, respectively, are the electronic repulsion between electrons and between nuclei.

One immediately realizes that the wavefunction Ψ depends on both electrons and nuclei with the Hamiltonian given in Eq. 1.2. This brings extra complexity or dimensions when solving Eq. 1.2. However, because electrons move much faster than nuclei, we can assume the electrons are moving with the fixed nuclei coordinates. Therefore we can factorize the wavefunction $\Psi(\{\mathbf{r_i}\};\{\mathbf{R_A}\}) =$

$\Psi(\mathbf{r_i})\Psi(\mathbf{R_A})$. This is a fundamental approximation in computational chemistry, known as the Born-Oppenheimer approximation[2]. The approximation might not be sufficient in calculating non-linear optical properties , or for molecules where the vibration of nuclei has to be taken into account. One possible solution is to apply perturbation theory, which will be introduced in Section 1.3.

Within the Born-Oppenheimer approximation, we can safely remove the kinetic operator of nuclei which is the second term in Eq. 1.2. It is worth noting that the final term in Eq. 1.2 can also be disregarded, as it is a constant that only contributes to the eigenvalue without affecting the wavefunction. Moving forward, our focus will be only on the electronic Hamiltonian.

The wavefunction obtained by solving the electronic Hamiltonian must obey certain rules. Electrons, being fermions, have to obey the Pauli exclusion principle. The wavefunction of fermions is antisymetric, meaning that exchanging the electron 1 and electron 2 is not equivalent to the other way round. See following a simple two electrons example:

$$\begin{aligned}\Psi(1,2) &= \Psi_1(1)\Psi_2(2) \\ \Psi(2,1) &= \Psi_1(2)\Psi_2(1) = \Psi_1(1)\Psi_2(2) = \Psi(1,2) \neq -\Psi(1,2)\end{aligned} \tag{1.3}$$

This property can be mathematically represented by a determinant where each row has a different Ψ_i and each column has a different electron, known as a Slater determinant[3]. Exchanging rows in the determinant introduces a negative sign to the new matrix. Further discussion on this topic will be presented in Section 1.2.

Now let us return to the electronic Hamiltonian and address another significant challenge. The kinetic $-\frac{1}{2}\nabla_i^2$ and nuclear attraction operator $\frac{Z_A}{\mathbf{r}_{iA}}$ are both one-electron operators. However, the electron-electron repulsion operator $\frac{1}{\mathbf{r}_{ij}}$ obviously depends on other electronic coordinates. How to deal with this two-electron operator is a central topic in the computational chemistry. In the first section, we begin by a fundamental approximation that forms the basis for various more advanced wavefunction methods.

1.2 The Hartree-Fock approximation

The electron can be fully described by its position vector $\mathbf{r}$ and the spin. Two electron can occupy the same spatial orbital $\psi(\mathbf{r})$ but with the opposite spin. The spin can be either spin up ($\alpha(\omega)$) and spin down ($\beta(\omega)$). A spin orbital $\chi(\mathbf{x})$ describes both the spatial and spin part of an electron, $\chi(\mathbf{x}) = \psi(\mathbf{r})\alpha(\omega)$ or $\chi(\mathbf{x}) = \psi(\mathbf{r})\beta(\omega)$, for example.

The solution of an energy functional can be obtained, according to the variational principle, also known as the minimum energy principle, in the following,

$$E[\Psi] = \frac{\langle\Psi|\hat{H}|\Psi\rangle}{\langle\Psi|\Psi\rangle} \geqslant E_0 \tag{1.4}$$

where E_0 is the exact ground state energy.

The idea of Hartree-Fock(HF) approximation is rather practical. Firstly, since it is challenging to treat $\frac{1}{\mathbf{r}_{ij}}$ as two-electron operator, we assume that other electrons are "frozen" and consider the ith calculating electron in a "mean field" generated by these fixed electronic coordinates. By doing so, the coordinate $\mathbf{r_j}$ can be separated from $\mathbf{r_{ij}}$, simplifying the two-electron operator into a

one-electron operator. This simplification greatly enhances the computational efficiency. Secondly, the Hartree-Fock approximation takes into account the antisymmetry nature of the many-electron wavefunction.

1.2.1 Hartree-Fock equations

With all the approximations made above, the one-electron Schrödinger equation within the Hartree-Fock method [4,5], known as Hartree-Fock equations, can be written as:

$$\left[-\frac{1}{2}\nabla_i^2 - \sum_A^M \frac{Z_A}{\mathbf{r}_{iA}} + \hat{J} - \hat{K}\right]\chi_i(\mathbf{x_i}) = \varepsilon_i\chi_i(\mathbf{x_i}) \tag{1.5}$$

Let us now compare Eq. 1.5 with the original many-electron case Eq. 1.2. The first three terms have obvious anslogues in the two equations, where the last term do not. $\chi_i(\mathbf{x_i})$ is the spin orbital with the space and spin coordinate $\mathbf{x_i}$. The third term is the averaged coulomb potential and it is a summation of electron 2 occupying χ_j with the probability $d\mathbf{x_j}|\chi_j|^2$. The last term is the exchange potential operator arising from the antisymmetric character of fermion wavefunction. The exchange operator is defined as:

$$\hat{J}\chi_i(\mathbf{x_i}) = \sum_{j\neq i}^N \int d\mathbf{x_j}\frac{|\chi_j(\mathbf{x_j})|^2}{\mathbf{r}_{ij}}\chi_i(\mathbf{x_i}) \tag{1.6}$$

$$\hat{K}\chi_i(\mathbf{x_i}) = \sum_{j\neq i}^N \int d\mathbf{x_j}\chi_j^*(\mathbf{x_j})\frac{1}{\mathbf{r}_{ij}}\chi_i(\mathbf{x_j})\chi_j(\mathbf{x_i}) \tag{1.7}$$

It can be seen in Eq. 1.7 that this is a nonlocal operator. On the left of the equation, the operator acts on the electron with the coordinate $\mathbf{x_i}$ occupying the spin orbital χ_i, while on the right the $\chi_i(\mathbf{x_i})$ has been replaced by $\chi_i(\mathbf{x_j})$. There has been an exchange of the electron with the coordinate $\mathbf{x_i}$ and $\mathbf{x_j}$ hence the name "exchange operator". This operator is nonlocal because it acts on $\chi_i(\mathbf{x_i})$ which also relies on the term $\chi_i(\mathbf{x_j})$ lying on the right hand side of Eq. 1.7. To sum up, the Hamiltonian of the Hartree-Fock equation in Eq. 1.5 can be written as the summation of the one-electron Fock operator $f(1)$,

$$\hat{f}(1) = \hat{h}(1) + \hat{v}^{HF}(1) \tag{1.8}$$

where $\hat{h}(1)$ is the core-Hamiltonian operator and is always the same for all quantum mechanical methods. $\hat{v}^{HF}(1)$ is the one-electron effective Hartree-Fock potential.

The solution from Eq. 1.5 corresponds to a single electron case. For a many-electron system, one may be tempted to describe the eigenstate of the molecular Hamiltonian as a product of the eigenfunctions of non-interacting electrons. This is a Hartree product, which, however, does not satisfy the antisymmetry property of the many-fermion wavefunction. Instead, the idea of determinant in linear algebra perfectly satisfies this property by changing sign upon exchange rows. John Slater [3]

first showed that the generation of N-electron wavefunction Φ can be written as:

$$\Phi(\mathbf{x_1}, \mathbf{x_2}, \cdots, \mathbf{x_N}) = \frac{1}{\sqrt{N!}} \begin{vmatrix} \chi_1(\mathbf{x_1}) & \chi_2(\mathbf{x_1}) & \cdots & \chi_N(\mathbf{x_1}) \\ \chi_1(\mathbf{x_2}) & \chi_2(\mathbf{x_2}) & \cdots & \chi_N(\mathbf{x_2}) \\ \vdots & \vdots & \ddots & \vdots \\ \chi_1(\mathbf{x_N}) & \chi_2(\mathbf{x_N}) & \cdots & \chi_N(\mathbf{x_N}) \end{vmatrix} \tag{1.9}$$

$\chi_1(\mathbf{x_1})$ in Eq. 1.9 denotes that electron one occupies the spin orbital $\chi_1(\mathbf{x})$. Spin orbitals in the Slater determinants satisfy the orthonormal condition,

$$\langle \chi_i | \chi_j \rangle = \delta_{ij}, \tag{1.10}$$

where δ_{ij} is the Kronecker delta function. It is clear that the Slater determinant is zero if there exists two rows or columns being identical. Multiplying Eq. 1.5 by $\langle \chi_i |$ on the left, we obtain the orbital energy,

$$\epsilon_i = \langle i | \hat{h}_i | i \rangle + \sum_j^N \langle ij | ij \rangle - \sum_j^N \langle ij | ji \rangle \tag{1.11}$$

where we have adopted here the Dirac notation,

$$\langle i | \hat{h}_i | i \rangle = \int \psi_i^*(\mathbf{r_i}) \hat{h}_i \psi_i(\mathbf{r_i}) d\mathbf{r_i} \tag{1.12}$$

$$\langle ij | ij \rangle = \int\int \psi_i^*(\mathbf{r}_1) \psi_j^*(\mathbf{r}_2) r_{12}^{-1} \psi_i(\mathbf{r}_1) \psi_j^*(\mathbf{r}_2) d\mathbf{r}_1 d\mathbf{r}_2 \tag{1.13}$$

The total electronic energy. The total electronic energy of a molecular system in the Hartree-Fock approximation is

$$\begin{aligned} E_{HF} &= \sum_i^N \langle i | \hat{h}_i | i \rangle + \sum_i^N \sum_{j>i}^N \langle ij | ij \rangle - \sum_i^N \sum_{j>i}^N \langle ij | ji \rangle \\ &= \sum_i^N \langle i | \hat{h}_i | i \rangle + \frac{1}{2} \sum_{ij}^N [\langle ij | ij \rangle - \langle ij | ji \rangle] \\ &= \sum_i \epsilon_i - \frac{1}{2} \sum_{ij}^N [\langle ij | ij \rangle - \langle ij | ji \rangle] \end{aligned} \tag{1.14}$$

It is worth noting that the total energy is not the sum of the orbital energy. The sum of the orbital energy is larger than the total energy by a factor of one half of the electron-electron interaction energy due to double counting.

The electron density. The probability of finding an electron within a volume element $d\mathbf{r}_1$ at a point $\mathbf{r}$ in a closed-shell system, where the spin part of spin orbitals can be neglected ($\rho(\mathbf{r}) = 2\rho(\mathbf{r})^\alpha = 2\rho(\mathbf{r})^\beta$), is given as,

$$\begin{aligned} \rho(\mathbf{r}) &= \langle \Psi | \hat{\rho}(\mathbf{r}) | \Psi \rangle \\ &= N \int \cdots \int |\Psi(\mathbf{r}_1, \mathbf{r}_2, \cdots, \mathbf{r}_N)|^2 d\mathbf{r}_2 d\mathbf{r}_3 \cdots d\mathbf{r}_N \end{aligned} \tag{1.15}$$

where the density operator is defined as $\hat{\rho}(\mathbf{r}) = \sum_i^N \delta(\mathbf{r}_i - \mathbf{r})$. If the wavefunction is in the form of the Slater determinant, the electron density in Eq. 1.15 can be written with spatial orbitals,

$$\rho(\mathbf{r}) = 2\sum_i^{N/2} |\psi_i(\mathbf{r})|^2 \tag{1.16}$$

1.2.2 Hartree-Fock equations in atomic orbital basis

The construction of spatial part of spin orbitals are required, in practice, in order to solve HF equations numerically as given in Eq. 1.5. The most widely used approach starts from the one-electron basis functions known as atomic orbitals. These atomic orbitals are often constructed as linear combinations of Gaussian functions for computational efficiency. Additionally, one- and two-electron integrals can be solved analytically when using these Gaussian-based atomic orbitals.

Molecular orbitals (MOs) are obtained as a linear combination of atomic orbitals (AOs) [6],

$$\psi_i(\mathbf{r}) = \sum_\mu C_{\mu i}\phi_\mu(\mathbf{r}) \tag{1.17}$$

$C_{\mu i}$ is the expansion coefficient of the atomic orbital basis $\phi_\mu(\mathbf{r})$. The advantage of this approach is that the nonlinear differential HF equations can be easily programmed with efficient linear algebra operations. The HF equation in the AOs basis expressed in the matrix form, known as the Roothaan-Hall equation [6], is given as,

$$\mathbf{FC} = \mathbf{SC}\varepsilon \tag{1.18}$$

where $\mathbf{F}$ is the Fock matrix with its element $F_{\mu\nu} = \langle\phi_\mu|\hat{f}|\phi_\nu\rangle$. $\mathbf{S}$ is the overlap matrix $S_{\mu\nu} = \langle\phi_\mu|\phi_\nu\rangle$ between the non-orthogonal atomic basis functions. The non-orthogonal atomic basis can be transformed into the orthogonal basis by a non-unitary transformation thus satisfying the orthonormal condition given in Eq. 1.10.

The Roothaan-Hall equation in the transformed orthonormal basis $\tilde{\mathbf{C}}$ is now converted to solving the eigenvalue problem,

$$\mathbf{F}\tilde{\mathbf{C}} = \tilde{\mathbf{C}}\varepsilon \tag{1.19}$$

The diagonalization of the Fock matrix yields the eigenvalue ε.

Electron density in the AO basis. The electronic charge density given in Eq. 1.16 in AO basis reads,

$$\begin{aligned}\rho(\mathbf{r}) &= 2\sum_i^{N/2} |\psi_i(\mathbf{r})|^2 = 2\sum_i^{N/2}\sum_{\mu\nu} C_{\mu i}C^*_{\nu i}\phi_\mu(\mathbf{r})\phi_\nu(\mathbf{r}) \\ &= 2\sum_{\mu\nu} P_{\mu\nu}\phi_\mu(\mathbf{r})\phi_\nu(\mathbf{r})\end{aligned} \tag{1.20}$$

where we have defined the *density matrix* $P_{\mu\nu} = \sum_i^{N/2} C_{\mu i}C^*_{\nu i}$. Since $\phi_\mu(\mathbf{r})\phi_\nu(\mathbf{r})$ is already given known function, obtaining the density matrix in practical calculations thus becomes the

main target. Many properties can be calculated directly from the density matrix. The dipole moment is given as a example in the following.

Dipole moment in the AO basis. The classical definition of the dipole moment, which is origin independent for a neutral system, is as follows:

$$\vec{\mu} = \sum_i q_i \mathbf{r}_i \tag{1.21}$$

where q is a point charge at the position $\mathbf{r}_i$. Similarly, the dipole moment evaluated quantum mechanically is,

$$\vec{\mu} = \langle \Phi_0 | - \sum_i^N \mathbf{r}_i | \Phi_0 \rangle + \sum_A Z_A \mathbf{R}_A \tag{1.22}$$

where Z_A is a classical nuclei charge at the position $\mathbf{R}_A$. The dipole moment can be directly evaluated from the density matrix:

$$\vec{\mu} = -\sum_{\mu\nu} P_{\mu\nu} \langle \phi_\mu(\mathbf{r}) | \mathbf{r} | \phi_\nu(\mathbf{r}) \rangle + \sum_A Z_A \mathbf{R}_A \tag{1.23}$$

The total energy obtained from HF approximation is expected to have an overestimated energy due to a underestimated description on the fact that electrons are interacting with each other. The correlation energy, characterizing such an effect, is defined as the difference between the exact energy and the HF energy with the complete basis set,

$$E_c = E_0 - E_{HF} \tag{1.24}$$

In fact, the single determinant form of the wavefunction is often not enough for describing most of molecular systems. The error can be reduced by employing a correlated method such as the use of the multi-determinant wavefunction, or by applying the perturbation theory which will be introduced in the next section.

1.3 Møller-Plesset perturbation theory

If the exact Hamiltonian $\hat{H}$ can be expressed as the sum of a reference Hamiltonian $\hat{H}_0$, whose modelling is known, plus a small perturbation $\mathscr{V}$, perturbation theory can be applied. With a carefully chosen zeroth-order Hamiltonian $\hat{H}_0$, the perturbation expansions are expected to converge quickly. Rayleigh-Schrödinger perturbation theory (RSPT)[7] is applied to derive a perturbation series for the wavefunction and the energy. This technique will resurface later in the context of response theory in the time-dependent domain. RSPT can be conveniently demonstrated to be size-consistent by employing a diagrammatic representation[7,8] of the algebraic expression for each order of the energy correction.

The eigenvalue problem can be solved in a perturbative manner by utilizing the eigenfunctions and eigenvalues of the unperturbed Hamiltonian:

$$(\hat{H}_0 + \lambda \mathscr{V}) | \Psi_i \rangle = \mathscr{E}_i | \Psi_i \rangle, \tag{1.25}$$

$$\hat{H}_0 | \psi_i^{(0)} \rangle = E_i^{(0)} | \psi_i^{(0)} \rangle, \tag{1.26}$$

where $\mathscr{E}_i$ and $|\Psi_i\rangle$ are exact eigenvalues and eigenfunctions. The zeroth-order wavefunction obtained from the unperturbed Hamiltonian $\hat{H}_0$ satisfies the normalization condition,

$$\langle\psi_i^{(0)}|\psi_i^{(0)}\rangle = 1. \tag{1.27}$$

The advantage of the perturbation theory is that the exact eigenvalues and eigenfunctions can be written with the already known sets of $\{E_i^0\}$ and $\{\psi_i^0\}$. An ordering parameter λ is introduced in Eq. 1.25 to systematically obtain improved unperturbed eigenfunctions and eigenvalues. This parameter is later used to equate coefficients. The exact eigenfunctions and eigenvalues can be expanded in Taylor series with the λ parameter:

$$\mathscr{E}_i = E_i^{(0)} + \lambda E_i^{(1)} + \lambda^2 E_i^{(2)} + \cdots \tag{1.28}$$

$$|\Psi_i\rangle = \psi_i^{(0)} + \lambda\psi_i^{(1)} + \lambda^2\psi_i^{(2)} + \cdots \tag{1.29}$$

The intermediate normalization $\langle\psi_i^{(0)}|\Psi_i\rangle = 1$ is applied to ensure the preservation of the orthogonality between unperturbed $\psi_i^{(0)}$ and n-th order wavefunction. This can be shown by multiplying $\langle\psi_i^{(0)}|$ on the left of Eq. 1.29.

By substituting Eq. 1.29 and Eq. 1.28 back into Eq. 1.25, sorting the equation based on the order of λ, and utilizing the orthogonality relation, we arrive at the expression for the nth-order energies:

$$E_i^{(0)} = \langle\psi_i^{(0)}|\hat{H}_0|\psi_i^{(0)}\rangle \tag{1.30}$$

$$E_i^{(1)} = \langle\psi_i^{(0)}|\mathscr{V}|\psi_i^{(0)}\rangle \tag{1.31}$$

$$E_i^{(2)} = \langle\psi_i^{(0)}|\mathscr{V}|\psi_i^{(1)}\rangle \tag{1.32}$$

The first-order wavefunction $\psi_i^{(1)}$ appears first in the second-order energy $E_i^{(2)}$ as can be seen in Eq. 1.32. The expression for $\psi_i^{(1)}$ can be derived by expanding $\psi_i^{(1)}$ in a linear combination of $\{\psi_n^0\}$. As a result, the second-order energy reads[7],

$$E_i^{(2)} = \sum_{n\neq i} \frac{\langle\psi_i^{(0)}|\mathscr{V}|\psi_n^{(0)}\rangle^2}{E_i^{(0)} - E_n^{(0)}} \tag{1.33}$$

We pause at the second-order energy for now and return to our objective, which is to evaluate the correlation energy using the perturbation technique introduced thus far.

The second-order correlation energy from the perturbation theory.

Møller and Plesset[9] first propose to use the Hartree-Fock Hamiltonian as $\hat{H}_0$ to calculate the correlation energy of N-electron systems. The perturbation $\mathscr{V}$ in this case is the difference of the two-particle electron repulsion and the effective Hartree-Fock potential,

$$\mathscr{V} = \sum_{j>i} \mathbf{r}_{ij}^{-1} - \sum_i \hat{v}^{HF}(i) \tag{1.34}$$

Substitution of the perturbation potential to Eq. 1.33 gives the second order correction for the correlation energy. From Eq. 1.30 to Eq. 1.32, it can be seen that the zero-order energy

in Hartree-Fock Hamiltonian is simply the sum of the orbital energies. The sum of the zeroth-order and the first-order perturbation gives the Hartree-Fock energy.
The final second-order perturbation energy for the ground state reads,

$$E_0^{(2)} = \sum_{n\neq 0} \frac{\langle \psi_0^{(0)} | \mathscr{V} | \psi_n^{(0)} \rangle^2}{E_0^{(0)} - E_n^{(0)}} \tag{1.35}$$

$$= \sum_{\substack{b>a \\ s>r}} \frac{|\langle ab|rs\rangle - \langle ab|sr\rangle|^2}{\varepsilon_a + \varepsilon_b - \varepsilon_r - \varepsilon_s} \tag{1.36}$$

In Eq. 1.36, the symbol "ab" denotes the occupied molecular orbitals and "rs" for the unoccupied orbitals. The contribution to the second order correlation energy comes from the pair of electrons in the occupied orbitals. Importantly, the single excitation character does not contribute to the summation in Eq. 1.36. In order to see this, one can rewrite $\mathscr{V} = \hat{H} - \hat{H}_0$ and use the Brillouin's theorem [7] [a] , as well as the fact that the spin orbitals are the eigenfunctions of $\hat{H}_0$.

1.4 Density Functional Theory

1.4.1 Hohenberg-Kohn theorems

In Hartree-Fock theory, the total energy $E[\Phi]$ is minimized by means of the determinant wavefunction. Hohenberg-Kohn theorems, on the other hand, use the electron density as the basic variable. For an N-electron system, the number of electrons and the external potential $v_{ext}(\mathbf{r})$ determine all properties of the system. The external potential takes the following form,

$$v_{ext}(\mathbf{r}) = -\sum_A^M \frac{Z_A}{\mathbf{r}_{iA}} \tag{1.37}$$

The question is whether there is a one-to-one relation between the external potential and the electron density. If such a relation exists, how do we determine the density corresponding to the ground state?

Hohenberg-Kohn theorem 1 *"The external potential $v_{ext}(\mathbf{r})$ is determined, within a trivial additive constant, by the electron density $\rho(\mathbf{r})$."*

The first Hohenberg-Kohn theorem [10] can be proved by using the minimum energy principle for the ground state. The first Hohenberg-Kohn theorem answers our first question by stating that there cannot exist two different $v_(\mathbf{r})$ which give the same density for the ground state [10].

As a result, the total energy is a functional of the electron density and has an explicit dependence on $v_{ext}(\mathbf{r})$ in the following,

$$\begin{aligned} E_v[\rho] =& T[\rho] + V_{ne}[\rho] + V_{ee}[\rho] \\ =& \int \rho(\mathbf{r}) v_{ext}(\mathbf{r}) d\mathbf{r} + F_{HK}[\rho]. \end{aligned} \tag{1.38}$$

[a]. **Brillouin's Theorem** Singly excited determinants $|\Phi_a^r\rangle$ will not interact directly with a reference Hartree-Fock determinant $|\Phi_0\rangle$, that is $\langle \Phi_0 | \hat{H} | \Phi_a^r \rangle = 0$.

$F_{HK}[\rho]$ is the universal Hohenberg-Kohn functional includes the kinetic energy functional $T[\rho]$ and the electron repulsion energy $V_{ee}[\rho]$. Their exact forms are unknown. Many attempts have been made on a better approximation of the kinetic energy functional [11].

Hohenberg-Kohn theorem 2 *"For a trial density $\tilde{\rho}(\mathbf{r})$, such that $\tilde{\rho}(\mathbf{r}) \geqslant 0$ and $\int \tilde{\rho}(\mathbf{r})d\mathbf{r} = N$",*

$$E_0 \leqslant E_v[\tilde{\rho}] \tag{1.39}$$

The second Hohenberg-Kohn theorem [10] addresses our second question by introducing the energy variational principle based on the density. The ground-state density must satisfy the stationary principle, and subject to the constrain on the total number of electrons N. This constrain can be imposed using the Euler-Lagrange equation [12],

$$\delta[E_v[\rho] - \mu(\int \rho(\mathbf{r})d\mathbf{r} - N)] = 0, \tag{1.40}$$

where μ is the chemical potential. The working equation Eq. 1.40 is applied to obtain the ground state density.

The density is *v-representable* if it is the density associated with the ground state wavefunction obtained by some external potential. This is especially important for the definition of $F_{HK}[\rho]$ functional because ρ entering in $F_{HF}[\rho]$ has to be v-representable. However, the exact conditions for v-representable densities are unknown. Instead the electron density is the *N-representable* [13] density if it satisfies,

$$\rho(\mathbf{r}) \geqslant 0, \int \rho(\mathbf{r})d\mathbf{r} = N, \text{and} \int |\nabla \rho(\mathbf{r})^{1/2}|^2 d\mathbf{r} < \infty \tag{1.41}$$

Eq. 1.41indicates that, in addition to the constraint on the number of electrons, the N-representable density requires a continuous wavefunction. This condition is less restrictive than that of v-representability. In practice, the N-representable density minimizing the total energy is obtained by the Levy constrained-search approach [14].

Levy constrained-search [14]. There exists a one-to-one mapping between the ground state electron density ρ_0 and the ground state wavefunction. However, the reverse mapping does not exist. An infinite number of antisymmetric wavefunctions can yield the same density. Of course, according to the minimum energy principle, among all the wavefunctions yielding ρ_0, the one that minimizes the expectation value of $\langle \hat{T} + \hat{V}_{ee} \rangle$ gives the ground state wavefunctions Ψ_0. However, how to obtain ρ_0, the v-representable ground state density, is still not clear.

Since the v-representable ground state density is from the antisymmetric wavefunctions, we can extend the domain of v-representable to N-representable densities and define,

$$F[\rho] = \min_{\Psi \to \rho} \langle \Psi | \hat{T} + \hat{V}_{ee} | \Psi \rangle \tag{1.42}$$

where $F[\rho]$ takes all N-representable densities. Hence, the constrained-search formula above eliminates the v-representable requirement for the functional $F_{HK}[\rho]$ with a replacement of $F[\rho]$. In practice, the constrain-search is split into two steps; i) the inner minimization minimizing within the space of all the wavefunctions yields ρ; ii) the outer minimization searching among all admissible ρ that integrate to the total number of electrons.

1.4.2 Kohn-Sham formalism

The Hohenberg-Kohn theorems provide the theoretic foundation for density functional theory. However, the explicit form of the universal functional $F_{HK}[\rho]$ is unknown, especially the kinetic functional $T[\rho]$ which is in the same order of magnitude as the total energy.

Kohn and Sham (KS) in 1965 [15] introduced a formalism to calculate practically the total energy, without relying on the approximation for $T[\rho]$. In the KS approach, an artificial reference system of non-interacting electrons is introduced, and it is assumed that the density associated with the non-interacting reference system is identical to the one obtained from the interacting system. In such a case, $T[\rho]$ can be evaluated explicitly, whereas the interacting/non-classical part in the total energy is collected by the exchange-correlation functional $E_{xc}[\rho]$.

The Hamiltonian of the KS non-interacting electrons moving in an effective potential is,

$$\hat{H}_{KS} = -\sum_{i}^{N} \frac{1}{2}\nabla_i^2 + \sum_{i}^{N} v_{eff}(\mathbf{r}_i) \tag{1.43}$$

The kinetic energy functional $T_s[\rho]$ is defined by the constrained search formalism,

$$T_s[\rho] = \min_{\Phi\to\rho} \langle \Phi|\hat{T}|\Phi\rangle \tag{1.44}$$

The density must be derived from antisymmetric wavefunctions.The exchange-correlation functional $E_{xc}[\rho]$ is defined as the difference between the exact kinetic energy and the Kohn-Sham kinetic potential plus the non-classical part of the electron-electron interaction $V_{ee}[\rho]$,

$$E_{xc}[\rho] = T[\rho] - T_s[\rho] + V_{ee}[\rho] - J[\rho] \tag{1.45}$$

where the classical coulomb repulsion energy is,

$$J[\rho] = \frac{1}{2}\int\int \frac{\rho(\mathbf{r})\rho(\mathbf{r}')}{|\mathbf{r}-\mathbf{r}'|} d\mathbf{r}' d\mathbf{r} \tag{1.46}$$

The effective potential now can be defined,

$$v_{eff}(\mathbf{r}) = v_{ext}(\mathbf{r}) + \frac{\delta J[\rho]}{\delta\rho(\mathbf{r})} + \frac{\delta E_{xc}[\rho]}{\delta\rho(\mathbf{r})} \tag{1.47}$$

Total KS energy. The total KS energy can be written with the optimal orbitals Φ_i determined from the Euler-Lagrange equations,

$$E_{KS}[\rho] = \sum_{i}^{N} \langle \Phi_i[\rho]| - \frac{1}{2}\nabla_i^2 |\Phi_i[\rho]\rangle + J[\rho] + V_{ne}[\rho] + E_{xc}[\rho] \tag{1.48}$$

$$V_{ne}[\rho] = \int v_{ext}(\mathbf{r})\rho(\mathbf{r}) d\mathbf{r} \tag{1.49}$$

Density functional approximation. In the practical KS-DFT calculations, various levels of approximation have been made to the exchange-correlation functional $E_{xc}[\rho]$. Following the

so called "Jacob's ladder", the simplest approximation to $E_{xc}[\rho]$ starts from the local density approximation[15] where $E_{xc}[\rho]$ depends on the local value of $\rho(\mathbf{r})$ especially aimed for slow varying electron densities. In molecular systems, however, where the electron density varies rapidly, a generalized gradient approximation has been introduced for which $\rho(\mathbf{r})$ depends on the density gradient $\nabla\rho(\mathbf{r})$. Advancing up the "Jacob's ladder," the exact exchange energy from HF theory is partially included using Kohn-Sham orbitals Φ_i, leading to what is known as hybrid functionals[16]. The computational time increases as one ascends the "Jacob's ladder."

The comparison to the HF approximation. Let us compare now the Hartree-Fock and Kohn-Sham Density Functional Theory (KS-DFT). Both approximations use the single determinant wavefunctions. In HF theory the wavefunction of the interacting system is approximated by a single determinant, whereas KS-DFT employs a single determinant that corresponds to the exact wavefunction of a fictitious non-interacting system. The HF total energy does not include the correlation effect, by definition. KS-DFT, however, does account for the correlation effect through the exchange-correlation functional $E_{xc}[\rho]$. The accuracy of KS-DFT thus relies on the approximation for the exchange-correlation functional $E_{xc}[\rho]$.

The computational scaling is different for two approximations. In HF theory, the evaluation of the two-electron integral $\langle ij|kl\rangle$, which are four-index integrals with each index ranging from 1 to N (where N is the number of atomic orbitals), approximately scales as N^4. In KS-DFT, the formal scaling can be reduced to N^3 due to the introduction of an auxiliary basis. This auxiliary basis replaces the product of two atomic orbitals $\phi_\mu(\mathbf{r})\phi_\nu(\mathbf{r})$ with a single orbital $\phi'(\mathbf{r})$. This auxiliary basis can be introduced because there are no exchange integrals in KS-DFT. Moreover, if the density is represented numerically on a grid, the scaling can be reduced furthermore.

Chapter 2

Multiscale Methods

We have seen in the previous chapter that the computational time scales as N^3 [17] in Kohn-Sham Density Functional Theory, where N is the number of basis function which in turn is proportional to the number of electrons/atoms. The formal scaling factor is N^4 [17] in Hartree-Fock method and for more advanced methods such as MP2 is N^5 [7]. This unfavourable scaling is, however, not practical for most of complex molecular systems. One breakthrough in addressing this problem is the utilization of the multiscale method which was recognized with the Nobel Prize in 2013. In the multiscale method, a complex system is divided into subsystems, with the system of interest, the part of the system which is considered to be mainly responsible for the physical behaviour treated using high-level computational methods. Other subsystems, everything but the system of interest are treated with low-level methods. This approach allows for efficient simulations of complex systems that would be otherwise computationally infeasible using conventional methods.

Multiscale methods involve solving the problem of the quantum mechanic (QM) region with the isolated Hamiltonian of the chromophore $\hat{H}_{N_A}$ and an embedding operator $\hat{v}_{emb}$ including the interaction between the chromophore and the environment, in the following form:

$$\left[\hat{H}_{N_A} + \hat{v}_{emb}\right] \Psi_A = \lambda_A \Psi_A \tag{2.1}$$

Multiscale methods reduce quantum N_{A+B} body to N_A electrons problem and is efficient if $N_A \ll N_{A+B}$. The embedding operator can be generated from either a classical representation of the environment; such as i) the polarisable dielectric continuum (PCM) and ii) the parameterized force field which is commonly referred by QM/molecular mechanics (MM) [18], or in the quantum mechanical way in which the environment is represented by the electron density such as subsystem DFT methods [19]. These diverse methods addressing various physical effects, can be efficiently applied to a wide range of molecular systems where a full quantum mechanical treatment is not feasible.

In this chapter, we first describe the PCM embedding in more details since it is highly relevant for later applications concerning two-photon absorption calculations. We then introduce the Frozen Density Embedding Theory (FDET) with a focus on the FDET embedding potential.

2.1 Polarisable dielectric continuum model

Embedding approaches that model each atom in the environment individually are referred to as "discrete." The advantage of a discrete representation lies in its ability to efficiently model various physical interactions between the solute and the solvent. However, when modeling solvation effects, the statistical nature of the solvent must also be considered. This becomes particularly crucial in a fluctuating environment. The typical approach to address this in a discrete model is by capturing multiple snapshots of the solvent and then calculating a statistical average of the property based on the geometry of each snapshot. A recent study has shown that the electronic embedding, as opposed to the simple electrostatic embedding, is required to correctly describe the solvent structure for charge-transfer-to-solvent states [20].

The continuum solvation models use the macroscopic dielectric constant ε to approximate the statistical averaging of the configurations of the solvent. The simplest solvation model that combines the quantum description of the solute was proposed by Kirkwood and Onsager [21,22]. The solute in this approach is placed in a spherical cavity. The charge density of the solute is described by a multipolar expansion. The radius of the cavity needs to be carefully chosen in this model because the solvation energy is very sensitive to the radius.

A more sophisticated model treats the charge density exactly. The cavity is constructed using a set of atom-centered spheres, typically determined by their van der Waals radii. The solute is then placed within this cavity. The polarizable continuum responds to the electrostatic potential of the solute, and the induced polarization from the solvent is quantified by the apparent surface charges distributed on the surface of the cavity. A collection of models commonly referred to as the polarizable dielectric continuum model (PCM) includes variations such as the conductor-like PCM (CPCM), the conductor-like screening model (COSMO), and the integral equation formalism PCM (IEFPCM) [23], among others. These different formulations of PCM models vary in how the apparent surface charge is determined. COSMO can be regarded as a special case of IEFPCM. In IEFPCM, the influence of the solute charges located outside the cavity (referred to as "outlying" charges) is implicitly considered. This effect stems from the surface charge not satisfying Gauss's law at the boundary surface. A comprehensive review can be found in Ref. 24. It is important to note that PCM can describe the long-range electrostatic interaction but not the short-range interaction, the interaction on the surface, for instance. In this case, the embedding operator is the reaction field, which depends on the charge density of the solute. Therefore, the reaction field must be updated in every iteration.

Here, we will first review the equilibrium solvation case, in which the solute and the solvent are in an equilibrium state. This involves the ground state or the long-lived excited state that has a lifetime much longer than the timescale of the molecular vibration.We will then proceed to discuss the formulation for the nonequilibrium case, in which the response from the solvent is separated, typically applies for short-lived excited states or the vertical excitation.

2.1.1 Equilibrium formulation of PCM

The embedding operator in PCM is the reaction field potential operator $\hat{R}$ [25],

$$\hat{R}_i = \int_S \frac{\sigma_i(s)}{|r-s|} ds = \int_S \hat{V}(r,s)\sigma_i(s) ds \tag{2.2}$$

where S is the cavity surface and s is the surface element. The apparent surface charge $\sigma_i(s)$ is given,

$$\sigma_i(s) = \int_S V(s')A_\varepsilon^{-1}(s,s')ds' \tag{2.3}$$

The electrostatic potential $V(s)$ arising from the polarisation of the continuum, for the given wavefuctions Ψ_i at the point s can be obtained by integrating $V(r,s)$ over r. A_ε^{-1} is the PCM kernel which varies for various PCM models. This kernel depends on the geometry of the cavity and the dielectric constant of the continuum. The fact that the kernel takes two arguments (s,s') indicates that it takes into account the mutual polarisation between the surface charges. To better understand the generation of the surface charges, a schematic illustration is shown in Fig. 2.1 outlining the general procedure of PCM calculations.

The reaction field can also be written in the form of a surface charge operator $\hat{Q}$ and the solute potential $\hat{V}$,

$$(\hat{H}_{\text{vac}} + \langle\Psi_i|\hat{Q}|\Psi_i\rangle \cdot \hat{V})|\Psi_i\rangle = \lambda_i|\Psi_i\rangle \tag{2.4}$$

where $\hat{Q} = \int_S \hat{V}(r,s')A_\varepsilon^{-1}(s,s')ds'$ and $\hat{V}\sigma_i(s) = \int_S V(s)\sigma_i(s)ds$. The free energy of the solute is,

$$G_i = \langle\Psi_i|\hat{H}_{\text{vac}} + \frac{1}{2}\langle\Psi_i|\hat{Q}|\Psi_i\rangle \cdot \hat{V}|\Psi_i\rangle \tag{2.5}$$

The factor $\frac{1}{2}$ appearing in Eq. 2.5 is due to the work required to create surface charges on the cavity surface.

2.1.2 Nonequilibrium formulation - vertical excitations in PCM

The response time for microscopic particles reacting to the external electric field to reach again the equilibrium varies for different microscopic particles. The response from the solvent, in reality, consists of the orientational, atomic, electronic polarisation, respectively due to the motion of molecule, atoms, and electrons.

When the vertical excitation from the electronic transition is considered, only the electrons are relaxed during the excitation while the nuclei degree of freedom is frozen according to the Frank-Condon's rule. The response of the solvent is split into two parts.

There are two schemes to treat this nonequilibrium response from the solvent. The first scheme partitions the total polarisation from the solvent into fast and slow contributions from the electron and nuclei response. The second scheme divides the polarisation into inertial and dynamic response. Depending on which scheme is applied, the final expression for the free energy is different, for more discussion, see Ref.[25]. In the following we will review the first scheme.

The apparent surface charge operator $\hat{Q}$ and the reaction field $\hat{R}_i$ can be split into the slow $\hat{Q}^s$ and fast $\hat{Q}^f$ contribution,

$$\hat{Q} = \hat{Q}^s + \hat{Q}^f. \tag{2.6}$$

The Hamiltonian for the nonequilibrium excited state Ψ_j is expressed as,

$$\begin{aligned} \hat{H}_j &= \hat{H}_{\text{vac}} + [\langle\Psi_i^{equ}|\hat{Q}^s|\Psi_i^{equ}\rangle + \langle\Psi_j|\hat{Q}^f|\Psi_j\rangle] \cdot \hat{V} \\ &= \hat{H}_{\text{vac}} + \hat{R}_i^s + \hat{R}_j^f \end{aligned} \tag{2.7}$$

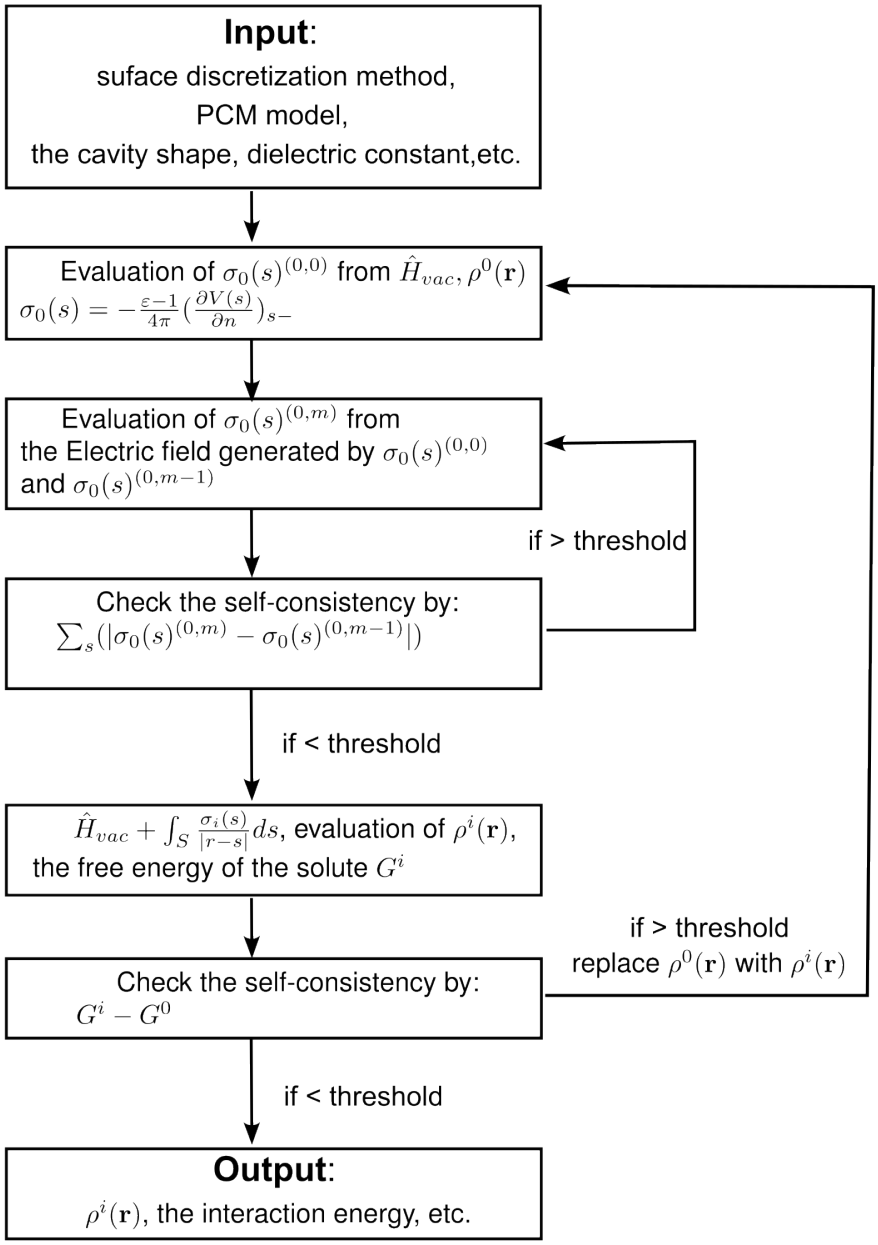

Figure 2.1 – A flow chat modified based on Ref.[25] for the PCM calculation procedure. Note that the procedure experiences two times self-consistence calculations. One concerns the surface charge iteration and the other concerns the solute charge density.

where Ψ_i^{equ} is obtained from the equilibrium Hamiltonian case described in the previous section.

It is evident that the Hamiltonian $\hat{H}_j$ in Eq. 2.7 depends on Ψ_j. This introduces a break in orthogonality between excited states, posing challenges when evaluating the properties of excited states.

A commonly employed method to tackle this state-dependent problem is the use of perturbation theory. If the electronic response from Ψ_j is only a small perturbation to the total electrostatic potential, one can write the perturbative Hamiltonian as,

$$\hat{H}_j = \hat{H}_{\text{vac}} + \hat{R}_i^{s+f} + \lambda(\hat{R}_j^f - \hat{R}_i^f) \tag{2.8}$$

Thus we obtain the zeroth-order expectation value of the Hamiltonian,

$$E_j^{(0)} = \langle \Psi_j^{(0)} | \hat{H}_{\text{vac}} + \hat{R}_i^{s+f} | \Psi_j^{(0)} \rangle \tag{2.9}$$

and the first-order correction,

$$E_j^{(1)} = \langle \Psi_j^{(0)} | \hat{R}_j^f - \hat{R}_i^f | \Psi_j^{(0)} \rangle \tag{2.10}$$

where $\Psi_j^{(0)}$ is obtained from the unperturbed Hamiltonian $\hat{H}_{\text{vac}} + \hat{R}_i^{s+f}$ which does not depend on Ψ_j.

2.2 Frozen Density Embedding Theory

Frozen Density Embedding Theory, features on the short-range nonelectrostaic Pauli repulsion effect in density embedding theory. The total electron density of the whole system is constructed by the electron density of the embedded species ρ_A and the environment ρ_B,

$$\rho_{AB}(\mathbf{r}) = \rho_A(\mathbf{r}) + \rho_B(\mathbf{r}) \tag{2.11}$$

FDET was originally introduced using the embedded single determinant for the non-interacting reference system[26] optimised in the constrained minimisation of the Hohenberg-Kohn energy functional $E_v^{HK}[\rho]$. It was later extended to the variational embedded wavefunction Ψ_A in an interacting Hamiltonian[27], and one-particle reduced density matrix[28], based on the same principle.

Most recent addition to the formal framework of FDET is the exact relation between the Hohenberg-Kohn energy functional $E_v^{HK}[\rho]$, and the correlation energy obtained from non-variational methods[29]. With this last addition, the formal framework of FDET covers practically all methods of molecular quantum mechanics which might be used to solve Eq. 2.1.

In the following, we introduce the FDET framework in which the variational embedded wavefunction Ψ_A in a interacting Hamiltonian[27] is considered.

2.2.1 Embedded interacting wavefunctions

Starting from the Hohenberg-Kohn energy of two subsystems, the total external potential v_{AB} is partitioned into two components:v_A corresponding to the embedded system A, and v_B which is associated to the environment B. If density of $\rho_B(\mathbf{r})$ is frozen, the optimisation of the total density

is equivalent to the optimisation of the density of the embedded system A. The Hohenberg-Kohn energy in such case can be written[27],

$$\begin{aligned} E_{HK}[\rho_A+\rho_B] &= \min_{\Psi_A\to\rho_A}\langle\Psi_A|\hat{T}+\hat{V}_{ee}|\Psi_A\rangle + V_A[\rho_A] \\ &+ \underbrace{T_s[\rho_B]+J[\rho_B]+V_B[\rho_B]+E_{xc}[\rho_B]}_{E_{HK}[\rho_B]} \\ &+ +V_B[\rho_A]+V_A[\rho_B]+J_{AB}[\rho_A,\rho_B]+E^{nad}_{xcT}[\rho_A,\rho_B] \\ &+ F_{HK}[\rho_A]-\min_{\Psi_A\to\rho_A}\langle\Psi_A|\hat{T}+\hat{V}_{ee}|\Psi_A\rangle \end{aligned} \tag{2.12}$$

where $E^{\mathrm{nad}}_{xcT}[\rho_A,\rho_B]$ is the non-additive exchange-correlation and kinetic functional,

$$\begin{aligned} \rho_A(\mathbf{r}) &= \langle\Psi_A|\hat{\rho}|\Psi_A\rangle \\ V_B[\rho_A] &= \int v_B(\mathbf{r})\rho_A(\mathbf{r})d\mathbf{r} \\ V_A[\rho_B] &= \int v_A(\mathbf{r})\rho_B(\mathbf{r})d\mathbf{r} \\ J_{AB}[\rho_A,\rho_B] &= \int\int \rho_A(\mathbf{r})\rho_B(\mathbf{r}')d\mathbf{r}d\mathbf{r}' \end{aligned}$$

The nuclear-nuclear repulsion energy has been neglected.

Let us dwell on Eq. 2.12, $E_{HK}[\rho_A+\rho_B]$ is rewritten in such a way that,

- $\min_{\Psi_A\to\rho_A}\langle\Psi_A|\hat{T}+\hat{V}_{ee}|\Psi_A\rangle$ is added and subtracted. This allows us to define a new functional, in analogy to $F[\rho]$ in Levy's constrained search, in which the trial wavefunctions are instead the interacting wavefunctions.
- The resulting new FDET energy functional $E^{\mathrm{FDET}}_{v_{AB}}[\Psi_A,\rho_B]$ can be derived which relates to the exact Hohenberg-Kohn energy.

The FDET total energy functional $E^{\mathrm{FDET}}_{v_{AB}}[\Psi_A,\rho_B]$ depends on two independent variables: i) the embedded N_A-body wavefunction Ψ_A, and ii) the electron density ρ_B of the environment B. Because these two variables are independent, it gives FDET a large flexibility from choosing a suitable quantum mechanical method to solve i) and generate ii). Especially for the charge density ρ_B can be generated from any theoretical models that provides the electron density, even with a macroscopic experimental one[30].

Apart from the constraint on the total number of electrons, the optimisation of the electron density in FDET depends on an additional constrain $\forall\mathbf{r}\rho(\mathbf{r})\geqslant\rho_B(\mathbf{r})$ imposed on the total electron density,

$$\begin{aligned} \min_{\Psi_A\to N_A} E^{FDET}_{v_{AB}}[\Psi_A,\rho_B] &= E^{FDET}_{v_{AB}}[\Psi^o_A,\rho_B] = E^{HK}_{v_{AB}}[\rho^o_A+\rho_B] \\ &= \min_{\substack{\forall_{\mathbf{r}}\rho(\mathbf{r})\geq\rho_B(\mathbf{r}) \\ \rho(\mathbf{r})\to N_{AB}}} E^{HK}_{v_{AB}}[\rho] \end{aligned} \tag{2.13}$$

However, the exact ground state density is unknown before the additional constrain is imposed. As a result, the optimal energy obtained from FDET can lie above the exact ground state energy of the

total system,

$$E_{v_{AB}}^{FDET}[\Psi_A^o, \rho_B] \geqslant E_{v_{AB}}^{HK}[\rho_{v_{AB}}^o] \tag{2.14}$$

The total FDET energy functional reads [27],

$$\begin{aligned} E_{v_{AB}}^{\mathrm{FDET}}[\Psi_A, \rho_B] &= \langle \Psi_A | \hat{H}_A + \hat{v}_{emb}^{FDET}[\rho_A, \rho_B; v_B] | \Psi_A \rangle + E_{xcT}^{\mathrm{nad}}[\rho_A, \rho_B] + \Delta F[\rho_A] \\ &- \int \left(v_{xcT}^{\mathrm{nad}}[\rho_A, \rho_B](\mathbf{r}) \right) \rho_A(\mathbf{r}) d\mathbf{r} + E_{v_B}^{HK}[\rho_B] + V_A[\rho_B] \end{aligned} \tag{2.15}$$

where,

- $\hat{H}_A$ is the Hamiltonian for the isolated subsystem A with an external potential $v_A(\mathbf{r})$. Ψ_A is the embedded interacting wavefunction that has a multi-determinant form.
- $E_{xcT}^{\mathrm{nad}}[\rho_A, \rho_B]$ is the non-additive exchange-correlation and kinetic functional depends on pairs of electron densities $\rho_A(\mathbf{r})$ and $\rho_B(\mathbf{r})$,

$$E_{xc}^{\mathrm{nad}}[\rho_A, \rho_B] = E_{xc}[\rho_A + \rho_B] - E_{xc}[\rho_A] - E_{xc}[\rho_B] \tag{2.16}$$
$$E_{T}^{\mathrm{nad}}[\rho_A, \rho_B] = T_s[\rho_A + \rho_B] - T_s[\rho_A] - T_s[\rho_B] \tag{2.17}$$
$$E_{xcT}^{\mathrm{nad}}[\rho_A, \rho_B] = E_{xc}^{\mathrm{nad}}[\rho_A, \rho_B] + E_{T}^{\mathrm{nad}}[\rho_A, \rho_B] \tag{2.18}$$

- $\Delta F[\rho_A]$ in Eq. 2.15 is a term arising from the third line of Eq. 2.12, which results from the extension of the admissible wavefunctions in the constrain search, and is defined as:

$$\begin{aligned} \Delta F[\rho_A] &= \min_{\Psi_A \to \rho_A} \langle \Psi_A | \hat{T} + \hat{V}_{ee} | \Psi_A \rangle \\ &- \min_{\Psi_A^{WF} \to \rho_A} \langle \Psi_A^{WF} | \hat{T} + \hat{V}_{ee} | \Psi_A^{WF} \rangle \end{aligned} \tag{2.19}$$

  In Eq. 2.19, Ψ_A represents the trial wavefunction which admits all *v-representable* densities. On the other hand, Ψ_A^{WF} , depending on the specific wavefunction-based method being used and can range from a single determinant to the full configuration interaction form. $\Delta F[\rho_A]$ has shown contributing negligibly in the total energy [31] and is usually neglected or approximated by the correlation energy [29,32] in the practical applications of FDET formalism.
- The subtraction of $\int v_{xcT}^{\mathrm{nad}}[\rho_A, \rho_B](\mathbf{r}) \rho_A(\mathbf{r}) d\mathbf{r}$ from the expectation value is due to the inhomogeneity property of the FDET embedding operator $\hat{v}_{emb}^{FDET}[\rho_A, \rho_B; v_B]$ [33], where the functional derivative of $E_{xcT}^{\mathrm{nad}}[\rho_A, \rho_B]$ with respect to ρ_A is not linear in ρ_A, in other words, $\int \rho_A(\mathbf{r}) \frac{\delta E_{xcT}^{\mathrm{nad}}[\rho_A, \rho_B]}{\delta \rho_A(\mathbf{r})} d\mathbf{r} \neq E_{xcT}^{\mathrm{nad}}[\rho_A, \rho_B]$.
- $E_{v_B}^{HK}$ is the Hohenberg-Kohn energy of subsystem B. In practice, it can be approximated by any desired quantum methods. It is worthwhile noting that if the energy difference between two states in $E_{v_{AB}}^{\mathrm{FDET}}[\Psi_A, \rho_B]$ is concerned, and the same ρ_B used in both states, then $E_{v_B}^{HK}$ cancels out.

The lowest energy stationary embedded wavefunction is determined by solving the Euler-Lagrange equation:

$$\frac{\delta E_{v_{AB}}^{FDET}[\Psi_A, \rho_B]}{\delta \Psi_A} - \lambda \Psi_A = 0 \tag{2.20}$$

Here, λ is the Lagrange multiplier, imposing the constraint of normalized embedded wavefunctions.

2.2.2 FDET embedding potential

The multiplicative embedding operator can be seen as the embedding potential [27],

$$\begin{aligned}\hat{v}_{emb}^{FDET} &= v_{emb}^{FDET}[\rho_A, \rho_B; v_B](\mathbf{r}) \\ &= v_B(\mathbf{r}) + \int \frac{\rho_B(\mathbf{r}')}{|\mathbf{r}' - \mathbf{r}|} d\mathbf{r}' + \left.\frac{\delta E_{xcT}^{nad}[\rho, \rho_B]}{\delta \rho(\mathbf{r})}\right|_{\rho(\mathbf{r})=\rho_A(\mathbf{r})}\end{aligned} \tag{2.21}$$

The first two terms represent the electrostatic part from the environment, and the last term, which is a nonelectrostatic part depending on two densities. Below, we look at the embedding potential from different perspectives.

2.2.3 Nonadditive kinetic functional

As we have pointed out previously, the kinetic energy is at the same order of the total energy. The approximation in the kinetic energy functional is thus important and can lead to large errors in the total energy due to its magnitude.

We begin by introducing two exact kinetic functionals for two limit cases. The first one is the Thomas-Fermi (TF) kinetic functional [34,35] for the homogeneous electron gas which is given as:

$$T_s^{\mathrm{TF}} = C_F \int \rho^{5/3}(\mathbf{r}) d^3r \tag{2.22}$$

$C_F = \frac{3}{10}(3\pi^2)^{2/3}$ is the Thomas-Fermi constant. It is referred as the local density approximation (LDA) when TF functional is applied in the inhomogeneous case.

The second exact kinetic functional, applied in the spin-compensated two-electron systems, was introduced by von Weizsäcker [36] as:

$$T_s^{\mathrm{VW}} = \frac{1}{8} \int \frac{|\nabla \rho(\mathbf{r})|^2}{\rho(\mathbf{r})} d^3r \tag{2.23}$$

These two exact kinetic functionals are significant for later developments, as they serve as a basis for the nonadditive kinetic potential.

The approximation for nonadditive kinetic potential entering in the FDET embedding potential represents a challenge in both FDET and subsystem DFT theory. Moreover, it is important to note that the accuracy of the kinetic functional is not correlated with the nonadditive kinetic functional. Some example cases have been demonstrated in Appendix B.

There are in general two strategies to evaluate $v_t^{nad}[\rho_A, \rho_B]$.

The top-down approach. The top-down approach can be evaluated directly from the kinetic energy functional in, e.g. the orbital-free DFT, and taking the functional derivative of the nonadditive part with respect to ρ_A as expressed in Eq. 2.21. The top-down approach of evaluating $v_t^{nad}[\rho_A, \rho_B]$ is decomposable because its approximation denoted as $\tilde{v}_t^{nad}[\rho_A, \rho_B]$ can be simply expressed as:

$$\tilde{v}_t^{nad}[\rho_A, \rho_B] = \frac{\delta T_s[\rho_A + \rho_B]}{\delta \rho_A} - \frac{\delta T_s[\rho_A]}{\delta \rho_A} \tag{2.24}$$

The bottom-up approach. The alternative approach does not aim at approximating $T_s^{nad}[\rho_A, \rho_B]$ but directly constructing $v_t^{nad}[\rho_A, \rho_B]$ based on its exact properties, such as the nondecomposable approximation using first and second derivative of the density (NDSD) in which the embedding potential is improved near the nuclei of the environment [37]. It is non-decomposable because $\frac{\delta T_s[\rho_A+\rho_B]}{\delta \rho_A}$ and $\frac{\delta T_s[\rho_A]}{\delta \rho_A}$ cannot be reconstructed from $v_t^{nad}[\rho_A, \rho_B]$. In NDSD, $v_t^{nad}[\rho_A, \rho_B]$ is approximated in the following form :

$$\tilde{v}_t^{nad}[\rho_A, \rho_B] = \tilde{v}_t^{\text{decomposable}} + f[\rho_A, \rho_B] v_t^{\text{limit}}[\rho_B] \tag{2.25}$$

where $\tilde{v}_t^{\text{decomposable}}$ can be approximated from any known kinetic functional. $f[\rho_A, \rho_B]$ is the switching function which is switched on when in the vicinity of the nuclei of the environment. $v_t^{\text{limit}}[\rho_B]$ is the limit potential. This potential built from a limit case where $\rho_A \to 0$ and $\int \rho_B d\mathbf{r} = 2$, is derived from the von Weizsäcker functional introduced in Eq. 2.23.

In Appendix B, verification of the $\tilde{v}_t^{nad}[\rho_A, \rho_B]$ based on the bottom-up approach introduced in Ref 38 was made. The use of different decomposable kinetic energy functionals have been investigated, based on the new nondecomposable complete space (NDCS) functional [38] developed in our group. This investigation aims to assess the performance of the NDCS functional in the long-range.

2.2.4 ρ_A dependency of the FDET embedding potential

Equation Eq. 2.21 reveals a fundamental characteristic of FDET: its embedding potential is inherently reliant on the electron density ρ_A of the embedded system A. This sensitivity to the specific characters of system A can limit the transferability of FDET, distinguishing it notably from, e.g. pseudopotential theories [39], which can influence the range of systems for which accurate results can be achieved.

The undesired feature of ρ_A dependence of the FDET embedding potential can be removed by the linearisation of the bi-functional $E_{xcT}^{nad}[\rho_A, \rho_B]$ [40]. When the target density does not differ significantly from a reference density, the $E_{xcT}^{nad}[\rho_A, \rho_B]$ can be expanded around a chosen reference density ρ_A^{ref}, approximately as,

$$\tilde{E}_{xct}^{nad(lin)}[\rho_A, \rho_B] \approx \tilde{E}_{xct}^{nad}[\rho_A^{ref}, \rho_B] + \int \left(\rho_A(\mathbf{r}) - \rho_A^{ref}(\mathbf{r})\right) \tilde{v}_{xct}^{nad}[\rho_A^{ref}, \rho_B](\mathbf{r}) d\mathbf{r}. \tag{2.26}$$

The functional derivative of such a linearised functional,

$$\tilde{v}_{xct}^{nad(lin)}[\rho_A, \rho_B] = \frac{\delta \tilde{E}_{xct}^{nad(lin)}[\rho_A, \rho_B]}{\delta \rho_A}\Big|_{\rho_A = \rho_A^{ref}} = \tilde{v}_{xct}^{nad}[\rho_A^{ref}, \rho_B] \tag{2.27}$$

As is clear from Eq. 2.27 that taking the functional derivative to $\tilde{E}_{xct}^{nad}[\rho_A, \rho_B]$ with respect to ρ_A has become $\tilde{v}_{xct}^{nad}[\rho_A^{ref}, \rho_B]$ which no longer depends on ρ_A.

The advantage of the linearisation of $E_{xcT}^{nad}[\rho_A, \rho_B]$ is its computational efficiency. The calculation for the desired number of excited states can be made in one shot, without optimizing each excited state, and this brings another benefit that the orthogonality between excited states is thus preserved. This approximation has shown contributing negligibly to the excitation energy errors (less than 10^{-3} eV) [41] from sets of various chromophores in non-covalently bound environments.

2.2.5 ρ_B dependency - the polarisation effect

The mutual polarisation effect between the embedded system and the environment can be included by using polarised densities in density embedding methods.

For the ground state calculations, the polarisation effect can be explicitly considered by optimising densities self-consistently through the *Freeze and Thaw* technique[42,43]. In this technique, the embedded system A is first optimized with the frozen density of environment ρ_B, and then ρ_B is optimized with the embedded subsystem A, vice versa, until the change of the total energy of embedded subsystem A reaches a certain threshold.

In FDET, however, the polarisation of the separated subsystems is not well defined due to two reasons: i) different choice of ρ_B can yield the same total density (Eq. 2.13) and ii) non-linear dependence of the FDET embedding potential on ρ_B. Specifically, it is practically not possible to determine whether the error arises from violating the non-negativity condition ($\forall \mathbf{r}\, \rho(\mathbf{r}) \geqslant \rho_B(\mathbf{r})$) or from the approximation used for the nonadditive functional.

Basis set expansions: In practice, an implicit polarisation[44] is taken into account if a nonlocalised set of basis set functions (*supermolecular expansion*) is used. For instance, if the set of basis functions $\{\chi_\mu\}$ used for $\rho_A(\mathbf{r})$ is centred on both atoms defining $v_A(\mathbf{r})$ and $v_B(\mathbf{r})$ and is referred here as *supermolecular expansion* (SE).

$$\rho_A^{SE}(\mathbf{r}) = \sum_{\mu v} P_{\mu v}^A \chi_\mu^{AB}(\mathbf{r}) \chi_v^{AB}(\mathbf{r}) \tag{2.28}$$

$$\rho_B^{SE}(\mathbf{r}) = \sum_{\mu v} P_{\mu v}^B \chi_\mu^{AB}(\mathbf{r}) \chi_v^{AB}(\mathbf{r}) \tag{2.29}$$

$P_{\mu v}$ is the density matrix. As a comparison, the *monomer expansion* (ME) is given as:

$$\rho_A^{ME}(\mathbf{r}) = \sum_{\mu v} P_{\mu v}^A \chi_\mu^{A}(\mathbf{r}) \chi_v^{A}(\mathbf{r}) \tag{2.30}$$

$$\rho_B^{ME}(\mathbf{r}) = \sum_{\mu v} P_{\mu v}^B \chi_\mu^{B}(\mathbf{r}) \chi_v^{B}(\mathbf{r}) \tag{2.31}$$

The monomer expansion is obviously an approximation and can lead to significant computational savings in FDET.

2.2.6 ρ_B dependency - excitation energies

According to Perdew-Levy theorem[45] on extrema of $E_{v_{AB}}^{HK}[\rho]$ as pointed out by Khait and Hoffman[46], the other than the lowest energy solutions of $E_{v_{AB}}^{HK}[\rho]$ can be interpreted as excited states. The excitation energy is the difference between two total energies,

$$\epsilon_j \equiv E^j - E^o = E_{v_{AB}}^{HK}[\rho_A^j + \rho_B] - E_{v_{AB}}^{HK}[\rho_A^o + \rho_B] = E_{v_{AB}}^{FDET}[\Psi_A^j, \rho_B] - E_{v_{AB}}^{FDET}[\Psi_A^o, \rho_B] \tag{2.32}$$

where Ψ_A^j and Ψ_A^o are the stationary solutions of FDET eigenvalue problem. The first equality in the above equation originates in the Perdew-Levy theorem[45] on extrema of $E_{v_{AB}}^{HK}[\rho]$. It is exact if the density ρ_B does not violate the non-negativity conditions ($\forall_{\vec{r}} \rho_B \leqslant \rho_{v_{AB}}^j$ and $\forall_{\vec{r}} \rho_B \leqslant \rho_{v_{AB}}^o$)[27,47].

The stationary embedded wavefunctions are obtained by solving the FDET eigenvalue problem:

$$\begin{aligned}\left(\hat{H}_A + \hat{v}_{emb}^{FDET}[\rho_A^j, \rho_B; v_B]\right)\Psi_A^j &= \lambda\Psi_A^j \qquad (2.33)\\ &\downarrow \\ \rho_A^j(\mathbf{r}) &= \langle\Psi_A^j|\hat{\rho}|\Psi_A^j\rangle \\ &\downarrow \\ v_{emb}^{FDET}[\rho_A^j, \rho_B; v_B](\mathbf{r}) = v_B(\mathbf{r}) &+ \int\frac{\rho_B(\mathbf{r}')}{|\mathbf{r}-\mathbf{r}'|}d\mathbf{r}' + v_{xct}^{nad}[\rho_A^j, \rho_B](\mathbf{r}). \qquad (2.34)\end{aligned}$$

We address here several issues concerning solving FDET eigenvalue problem in practice.

- The FDET energy functional in Eq. 2.15, Ψ_A has a multi-determinant form. If the embedded wavefunction is approximated by the single determinant, other than the full CI form, the corresponding FDET energy functional comprises the correlation functional $E_c[\rho_A]$, consequently, its derivative - correlation potential in the FDET embedding potential given in Eq. 2.34. However, this is impractical due to lack of good approximation of $E_c[\rho_A]$.
  The use of the correlation potential can be eliminated owing to the recently developed exact equality, which relates the energy obtained variationally with the embedded wavefunction of the single-determinant form, and the correlation energy obtained by means of some non-variational method, to the Hohenberg-Kohn functional.
  This relation reads (Eq. 38 in Ref. 29):

$$\begin{aligned}E_{v_{AB}}^{HK}[\rho_A+\rho_B] &= E_{v_{AB}}^{FDET}[\Phi_A^{'}, \rho_B] + E_{v'}^c \qquad (2.35)\\ &- \int\rho_A^{'}(\mathbf{r})\left(\int\Delta\rho_{v'}^c(\mathbf{r}')f_{xct}^{nad}[\rho_A^{'}, \rho_B](\mathbf{r}, \mathbf{r}')d\mathbf{r}'\right)d\mathbf{r} + O(\Delta^2\rho),\end{aligned}$$

  The superscript $'$ emphasizes neglecting of the correlation functional in the total potential.

$$v' = v_A(\mathbf{r}) + v_B(\mathbf{r}) + \int\frac{\rho_B(\mathbf{r}')}{|\mathbf{r}'-\mathbf{r}|}d\mathbf{r}' + \left.\frac{\delta E_{xcT}^{nad}[\rho, \rho_B]}{\delta\rho(\mathbf{r})}\right|_{\rho(\mathbf{r})=\rho_A^{'}(\mathbf{r})} \qquad (2.36)$$

  $\Phi_A^{'}$ is the stationary single determinant obtained with the potential v', $E_{v'}^c$ is the correlation energy in the N_A-electron system defined by the potential v', $f_{xct}^{nad}[\rho_A^{'}, \rho_B](\mathbf{r}, \mathbf{r}') = \frac{\delta^2 E_{xct}^{nad}[\rho_A, \rho_B]}{\delta\rho_A(\mathbf{r})\delta\rho_A(\mathbf{r}')}$ and is zero when the linearised FDET is applied. $\Delta\rho_{v'}^c$ is the correlation-induced change of the electron density, and $O(\Delta^2\rho)$ collects all contributions to energy due to the effect of correlation on density that are of higher order.
- How to deal with the self-consistency of the embedding potential and the embedded wavefunctions Ψ_A. For each excited state Ψ_A^j, the self consistent calculation must be performed independently. If the linearised FDET is used, the state dependency on ρ_A is eliminated. Moreover, if the same ρ_B is used for the ground and excited state, one plugs in ρ_B in the FDET energy functional and finds that the excitation energy is simply the difference between two eigenvalues,

$$\begin{aligned}\epsilon_j \equiv E^j - E^o &\equiv E_{v_{AB}}^{FDET(lin)}[\Psi_A^j, \rho_B] - E_{v_{AB}}^{FDET(lin)}[\Psi_A^o, \rho_B] \\ &= \lambda_j[\rho_A^{ref}, \rho_B] - \lambda_o[\rho_A^{ref}, \rho_B], \qquad (2.37)\end{aligned}$$

- If different ρ_B is used for two considered states. ρ_B is polarised by the corresponding excited state of the embedded system A, for instance, and the excitation energy in this case is,

$$\begin{aligned} \epsilon_j \equiv E^j - E^o &= E^{HK}_{v_{AB}}[\rho^j_A + \rho^j_B] - E^{HK}_{v_{AB}}[\rho^o_A + \rho^o_B] \\ &= E^{FDET}_{v_{AB}}[\Psi^j_A, \rho^j_B] - E^{FDET}_{v_{AB}}[\Psi^o_A, \rho^o_B]. \end{aligned} \tag{2.38}$$

  The excitation energy is not the difference of two corresponding eigenvalues. It cannot be extracted straightforwardly from an output of the excited state calculation. The result obtained from an FDET excited state calculation with an imported polarised ρ^j_B density corresponds to $E^{FDET}_{v_{AB}}[\Psi^j_A, \rho^j_B] - E^{FDET}_{v_{AB}}[\Psi^o_A, \rho^j_B]$, and is not equal to Eq. 2.38. In Chapter 5, we will address this issue in full details and give the derivation of the final expression for the excitation energy with a state-specific ρ_B for the considered excited state.

2.3 The excitation-induced polarisation effect described by other than FDET methods.

When the chromophore is excited, the surrounding environment induces electronic polarisation. In the Section 2.2.5 and 2.2.6 we have introduce how FDET deals with the excitation-induced polarisation effect. In this section we will look at other multiscale methods in dealing with this effect with some specific examples.

The polarisation response of the environment to the excitation of the chromophore can be crucial in certain applications[48–52]. An illustrative example is the case of the green fluorescent protein(GFP). GFP is characterized by a significant environment-induced red-shift. Filippi et al.[53] initially reported a blue-shifted solvatochromic shift in the anionic form and an insufficient red shift in the neutral form of GFP using various quantum mechanical methods in combination with nonpolarisable force fields. The authors suspected that this discrepancy was likely due to the use of a nonpolarisable force field. It was later established, by Beerepoot et al., that applying a polarisable force field produced the correct red shift for both forms of the protein.[48]

In relation to the impact of a polarisable force field on excitation energies, Slipchenko et al.[54] conducted studies by combining Equation-of-Motion Coupled Cluster with Single and Double (EOM-CCSD) methods and the *ab inito* based polarisable force filed effective fragment potential approach[54]. They showed that a small discrepancy in solvatochromic shifts using this combined method, approximately in the range of 0.01-0.05 eV, compared to full supermolecular EOM-CCSD calculations. In a formaldehyde-water complex, they have shown that the electrostatic component primarily contributes the shift, with the induction effect contributing to approximately 20% of the total shift. Importantly, the polarisation between the chromophore and the environment was not treated self-consistently, meaning that induced dipoles were computed based on the ground-state wavefunction. The excitation energy is stabilized with a correction term based on a self-consistent treatment. However, the magnitude of the correction term is three times smaller than the induction energy itself[55].

In another study by Cappelli et al.[56], a three-layer model was introduced, combining all together quantum mechanical methods, the fluctuating charge method, and the polarisable continuum embedding. This model aimed to account for both the solvent polarisation and bulk solvation effects.

They have demonstrated using this model the importance of the mutual polarisation between the solute and solvent in a formaldehyde-water cluster. The difference in excitation energy was equal to or smaller than 0.1 eV, regardless of whether the third layer of PCM calculations were included or not. However, the error can exceed 0.1 eV when the mutual polarisation of the solute and solvent was not considered.

Concerning density embedding methods, two common approaches were applied to include the polarisation response of the environment: 1) an energy correction term in addition to the excitation energy obtained by only the isolated environment.[51,57]; 2) the use of the state-specific embedding potential[58], similar to FDET where the state-specific ρ_B is used for this purpose.

Additionally, there exist other strategies, such as the inclusion of environment orbitals into the high-level computational method of the chromophore,[57,59] or the approach which involves corrections based on the many-body expansion (MBE), where the excitation of the embedded chromophore alone is considered as the first-order expansion in MBE.[52]

The nonadditive kinetic potential is crucial in research related to subsystem DFT[60], because the nonadditive kinetic energy covers the short-range quantum effect and neglecting it can lead to the charge leak problem[61]. One alternative approach without relying on the nonadditive kinetic potentials is the projection-based embedding approach,[51,57,62] in which the projection operator is applied forcing the orthogonality of molecular orbitals between subsystems. With the projection-based embedding, Wen et al.[51] have shown in the case of an acrolein in two water molecules, that the ground state polarisation already accounts for about 90% of the total polarisation effect. In order to include some averaged behaviour from the polarisation response of the environment, they further introduced a state-averaged approach, in which the environment is polarised by the averaged density of the ground state and the first excited state of the chromophore, and found this state-averaged approach does not always improve the excitation energy. This "state-averaged" approach is also explored in FDET on excitation energies in Chapter 5.

Chapter 3

Modelling the excited states and properties

Performing an accurate calculation of excited states is more challenging than a ground state calculation. There are a number of reasons for it:

- The calculation of excited states involves the electronic transition from the ground state to the excited state. The transition coefficients for multiple possible excited states are calculated and this increases the overall complexity.
- Time-dependent considerations: the time-dependent Schrödinger equation is employed to treat the dynamic behaviour of electrons.
- Correlation effects: the uncorrelated methods, such as the single excitation configuration interaction (CIS) and random phase approximation, often gives qualitative results depending the excited state character, while the highly correlated methods are computational demanding, especially when multiple excited states are required for calculations.
- The excitation character: determining the excitation character of the selected excited state often concerns the visualization of pair of transition of orbitals from all output excited states.

Particular when multiscale methods are used, there are two more complexities:

- The excitation-induced polarisation effect often is needed to be taken into account. The polarisation and diffuse basis sets are required in this case. As the number of basis set functions grows larger, the computational time increases significantly.
- How to deal with the orthogonality between excited states.

The correlated methods investigating excited states include, but not limited to, the most popular density-based time-dependent DFT (TDDFT) which describes the linear response of the ground state density to the time-dependent electric filed, TDDFT depends on the exchange-correlation functional and the excitation energy and transition moment can be calculated without the access to the excited state wavefunction; the wavefunction-based methods, such as EOM-CC; the polarisation propagator based methods, such as the algebraic diagrammatic construction method.

In this chapter, we aim not to review all the excited state methods but only limited to some representative ones, which are the equation-of-motion coupled cluster method and the algebraic diagrammatic construction (ADC) approach. Those two methods are closely related to this work.

3.1 Algebraic diagrammatic construction

The algebraic diagrammatic construction [63] was first derived within the framework of the many-body Green's function due to its well-established perturbation expansions using Feynman diagrams. The Feynman diagram is a graphical representation of the multi-dimensional integrals of the high order correction terms. In ADC, the diagrammatic perturbation expansion is reformulated using an algebraic scheme. The ADC scheme offers a natural approach to construct n-th order ADC infinite partial summations for the modified interaction matrix exact up to n-th order of perturbation theory.

3.1.1 The polarisation propagator derived from Green's functions

The concept of propagators was first introduced in the statistic physics to describe the response of a system to an external perturbation. Hence, it is also closely related to the response theory. One can also derive the equivalent expression for the polarisation propagator from the response theory. The advantage of working with propagators is its physical meaning associated with poles and residues of the propagator. The poles of one-particle electron propagator are the electron affinities and ionization potential, for instance.

In many cases of a quantum system, the question of how the expectation value of an arbitrary operator $\hat{O}$ evolves with time in response to an external perturbation is more appealing and insightful than focusing on wavefunctions. Following this question, it is convenient to introduce Green's functions [b] since the expectation value of the one-particle operator can be directly expressed in terms of the Green's function [65]. The physical interpretation of one-particle Green's function is the probability amplitude of finding a particle at the point $\mathbf{r}'_\mathbf{1}$ at time t'_1 when a particle at $(\mathbf{r}'_\mathbf{1}, t_1)$ is added to a interacting many-body system.

We follow the same symbols as the ones in the derivation presented in Ref. 63 The one and two-particle Green's function are defined as [66]

$$G_{11'} = -i\langle\Psi_0|\hat{T}a_1(t_1)a^\dagger_{1'}(t_{1'})|\Psi_0\rangle \tag{3.1}$$

$$G_{12,1'2'} = (-i)^2\langle\Psi_0|\hat{T}a_1(t_1)a_2(t_2)a^\dagger_{1'}(t_{2'})a^\dagger_{2'}(t_{2'})|\Psi_0\rangle \tag{3.2}$$

where $a^\dagger_i, a_i$ are the *creation* and *annihilation* operator, receptively. $\hat{T}$ is the time-ordering operator, which is a step function of time difference τ defined as,

$$\Theta(\tau) = \begin{cases} 0, & \text{if } \tau < 0. \\ e^{-\eta\tau}, & \text{if } \tau \geqslant 0. \end{cases} \tag{3.3}$$

Here, a positive infinitesimal η guarantees the convergence of the Fourier transform when $t \to \infty$.

The particle-hole $(p-h)$ response function as a particle-hole pair $R_{12,1'2'}$ can be expressed in the form of one and two-particle Green's function [67]:

$$R_{12,1'2'} = G_{12,1'2'} - G_{11'}G_{22'} \tag{3.4}$$

[b]. The Green's function can be determined from an auxiliary noninteracting system with an effective potential, similar to the exchange-correlation potential in Kohn-Sham DFT, namely the *self-energy* which is nonlocal and energy dependent. The interacting and noninteracting Green's function is connected by the Dyson equation [64].

The particle-hole propagator or the polarisation propagator is defined as[63,65]

$$\Pi_{pq,p'q'}(t,t') = \lim_{\substack{t_p,t_q\to t \\ t_{p'},t_{q'}\to t'}} iR_{pq',qp'}(t_p,t_{q'},t_q,t_{p'}) \tag{3.5}$$

The polarisation propagator depends only on the time difference $(t-t')$ if the Hamiltonian is time-independent. Its Fourier transform in the energy domain yields the spectral representation of the polarisation propagator as follows,

$$\begin{aligned}\Pi_{pq,p'q'}(\omega) &= \sum_{k\neq 0}\frac{\langle\Psi_0|a_p^\dagger a_q|\Psi_k\rangle\langle\Psi_k|a_{p'}^\dagger a_{q'}|\Psi_0\rangle}{\omega+E_0-E_k+i\eta}+\sum_{k\neq 0}\frac{\langle\Psi_0|a_{p'}^\dagger a_{q'}|\Psi_k\rangle\langle\Psi_k|a_p^\dagger a_q|\Psi_0\rangle}{-\omega+E_0-E_k+i\eta} \\ &= \Pi_+(\omega)+\Pi_-(\omega)\end{aligned} \tag{3.6}$$

Note that the summation over stats in Eq. 3.6 excludes the ground state due to the subtraction of the multiplication of one-particle Green's function $G_{11'}G_{22'}$ in Eq. 3.4.

3.1.2 Intermediate state representation

The ADC scheme can be viewed as a non-diagonal representation of the polarization propagator compared to the spectral representation provided above. A compact matrix form of the polarisation propagator in the ADC formalism is[63]:

$$\Pi_+(\omega) = \mathbf{f}^\dagger(w\mathbf{1}-\mathbf{M})^{-1}\mathbf{f} \tag{3.7}$$

$\mathbf{f}$ is the effective transition amplitude, and $\mathbf{M}$ is the effective Hamiltonian which is non-diagonal. $\mathbf{f}$ and $\mathbf{M}$ is expanded into Møller-Plesset perturbation series. The n-th order expression for $\mathbf{f}$ and $\mathbf{M}$ is identified from the n-th order diagrammatic perturbation expansion of $\Pi_+(\omega)$.

The excitation energy can be obtained by solving the eigenvalue problem from the n-th order matrix of $\mathbf{M}$,

$$\mathbf{MY} = \mathbf{Y\Omega} \tag{3.8}$$

$\mathbf{\Omega}$ is the matrix contains the excitation energy. $\mathbf{Y}$ contains the eigenvectors of $\mathbf{M}$. The transition dipole moment of exact excited states,

$$T_n(\hat{\mu}) = \langle\Psi_0|\hat{\mu}|\Psi_n\rangle = \mathbf{f}^\dagger\mathbf{Y}_n \tag{3.9}$$

So far, the expressions for the excitation energy and transition dipoles of the excited states are known. In order to access the excited state wavefunctions, the intermediate states representation is used to derive the exact expression for the excited state wavefunctions. The intermediate states are denoted as Ψ_I and Ψ_J. The intermediate states[68] are generated by the pair of the creation and annihilation operator $a_r^\dagger a_b$, $a_r^\dagger a_s^\dagger a_b a_c$ acting on the Hartree-Fock orbitals, corresponding to $p-h$, $2p-2h$ excitation, respectively. The orthogonality between the intermediate states is assured by the Gram-Schmidt orthogonalization procedure.

The exact excited state is written in the basis of the intermediate states[68],

$$|\Psi_n\rangle = \sum_I Y_{nI}|\Psi_I\rangle \tag{3.10}$$

Therefore not only the transition dipole of the excite states can be expressed, but also the transition dipole moment between $|\Psi_m\rangle$ and $|\Psi_n\rangle$ can be given below:

$$T_{mn}(\hat{\mu}) = \langle\Psi_m|\hat{\mu}|\Psi_n\rangle = \mathbf{Y}_m^\dagger \mathbf{B}\mathbf{Y}_n \tag{3.11}$$

and the transition dipole moment in the intermediate representation,

$$B_{IJ}(\hat{\mu}) = \langle\Psi_I|\hat{\mu}|\Psi_J\rangle \tag{3.12}$$

There are several advantages to work with ADC(n) scheme compared with other excite state methods: 1) the Block-Lanczos diagonalization (Davidson) procedure [69,70] accelerates the convergence of the matrix $\mathbf{M}$ with a small number of iterations [71]; 2) a more compact and explicit configuration space is used and this is important for states with significant doubly excited configurations; 3) it is size-consistent.

3.2 Coupled cluster methods

3.2.1 The exponential ansatz

The coupled cluster theory is often compared with another correlated method which is the configuration interaction (CI) approach [7] in terms of the *size-consistency* [c] problem. Not satisfying the *Size-consistency* condition can lead to an overestimation of the correlation energy. The coupled cluster theory is size-consistent while the truncated CI, is not. The important difference between these two methods lie in the way how the exact many-electron wavefunction $|\Psi_0\rangle$ is expanded.

The coupled cluster approach employs the "exponential ansatz" [72] through the use of the exponential cluster operator $\hat{T}$ which is expressed as:

$$|\Psi_0^{CC}\rangle \equiv e^{\hat{T}}|\Phi_0^{HF}\rangle = e^{\hat{T}_1+\hat{T}_2}|\Phi_0^{HF}\rangle \tag{3.13}$$

$\hat{T}_1$ and $\hat{T}_2$ are the one and two-orbital cluster operators defined as:

$$\hat{T}_1 = \sum_{bs} t_b^s a_s^\dagger a_b \tag{3.14}$$

$$\hat{T}_2 = \frac{1}{4}\sum_{bcrs} t_{bc}^{rs} a_r^\dagger a_s^\dagger a_b a_c \tag{3.15}$$

where t_b^s, t_{bc}^{rs} are the cluster amplitudes. $a_i^\dagger, a_i$ are the *creation* and *annihilation* operator, receptively. Truncation of the cluster operator $\hat{T} \to \hat{T}_1 + \hat{T}_2$ leads to the Couple Cluster Singles and Doubles (CCSD) excitation approximation. The cluster operators $\hat{T}$ are also called the excitation operators since they involve excitation of orbitals in the Slater determinant.

[c]. **Size-consistency**: For two infinitely separated systems A and B, the sum of the energy computed for each system is the same as the the energy computed from the supermolecular way, that is $E_{AB} = E_A + E_B$ for the infinite distance.

It is possible to factorize the CC wavefunction in the form of $e^{\hat{T}_A}e^{\hat{T}_B}\Phi_0^{HF}$, therefore the energy can be separated in the infinite distance. This is not possible, however, in the CI wavefunction:

$$|\Psi_0^{CI}\rangle = (1 + \hat{C}_A + \hat{C}_B)|\Phi_0^{HF}\rangle, \tag{3.16}$$

This is due to the action of a linear excitation operator on the Slater determinant, where $\hat{C}$ is the excitation operator defined in analogy to $\hat{T}$.

Eq. 3.13 can be expanded:

$$e^{\hat{T}}|\Phi_0^{HF}\rangle = (1 + \hat{T} + \frac{1}{2!}\hat{T}^2 + \frac{1}{3!}\hat{T}^3 + \cdots)|\Phi_0^{HF}\rangle. \tag{3.17}$$

The cluster operators is non-linear. As a result, if only single and double excitations are considered, one substitutes $\hat{T}_1 + \hat{T}_2$ into Eq. 3.17 and finds the term $\hat{T}_2\hat{T}_2$ containing a quadruple excitation. These terms also contribute to a rapid convergence compared to the CI approach, as CC implicitly includes higher excitations for the same level of truncation of the excitation operator.

The ground state CC energy can be obtained by substituting the Ψ_0^{CC} into the Schrödinger equation leading to:

$$\hat{H}|\Psi_0^{CC}\rangle = E^{CC}|\Psi_0^{CC}\rangle. \tag{3.18}$$

It is convenient to introduce the similarity transformed Hamiltonian $\bar{H} = e^{-\hat{T}}\hat{H}e^{\hat{T}}$ such that [d]

$$\bar{H}|\Phi_0^{HF}\rangle = E^{CC}|\Phi_0^{HF}\rangle. \tag{3.19}$$

The advantage of transforming Hamiltonian is that the one and two-electron integrals related to the Salter determinant can be easily derived. Hence, projection on the left of Eq. 3.19 of the reference determinant $\langle\Psi_0^{HF}|$ leads to the CC energy,

$$E^{CC} = \langle\Phi_0^{HF}|\bar{H}|\Phi_0^{HF}\rangle. \tag{3.20}$$

However, it's important to note that the transformed Hamiltonian $\bar{H}$ is no longer Hermitian. If the cluster operator $\hat{T}$ is not truncated, $\bar{H}$ has the same eigenvalue as the original Hamiltonian. The matrix elements of $\bar{H}$ are non-symmetric. The off-diagonal matrix elements $\langle\Phi_a^r|\bar{H}|\Phi_0\rangle$ and $\langle\Phi_{ab}^{rs}|\bar{H}|\Phi_0\rangle$ are zero, while their corresponding complex conjugates are not zero. As a result, the differentiation between the ket and bra eigenvalue problems is necessary.

3.2.2 Equation-of-motion coupled cluster theory

The application of CC theory on the calculations of excited states is commonly achieved by the linear response theory [73] or the equation of motion formulation [74,75]. In linear response approach, the poles are recognized as the excitation energies and the residues are the transition amplitudes. More details on this approach will be discussed in the response function part. Here, we outline the basic idea of the equation-of-motion approach [75]. A comprehensive review can be found in Ref. 76.

[d]. Multiplying on the left of the Eq. 3.18 the inverse of the exponential operator $e^{\hat{T}}$ and substituting the CC wavefunction leads to Eq. 3.19.

The formulation of the equation-of-motion method is derived from two general Schrödinger equations,

$$\hat{H}|\Psi_k\rangle = E_k|\Psi_k\rangle \tag{3.21}$$
$$\hat{H}|\Psi_0\rangle = E_0|\Psi_0\rangle \tag{3.22}$$

Ψ_k denotes the excited state and can be generated from an excitation operator $\hat{\Omega}$. Subtracting the two Schrödinger equations and left multiplying $\hat{\Omega}$ arrives to the equation of motion:

$$[\hat{H}, \hat{\Omega}_k]|\Psi_0\rangle = \omega_k \hat{\Omega}_k|\Psi_0\rangle \tag{3.23}$$

where $\omega_k = E_k - E_0$.

In the case of CC, the left and right eigenvector can be written by the operator $\hat{\mathscr{L}}$ and $\hat{\mathscr{R}}$ in the same form as the cluster operator $\hat{T}$ acting on Φ_0, respectively. Same eigenvalues can be obtained from either the left-hand or right-hand side eigenvalue problem, that is,

$$\langle\Phi_0|\hat{\mathscr{L}}_k\bar{H} = \langle\Phi_0|\hat{\mathscr{L}}_k E_k \tag{3.24}$$
$$\bar{H}\hat{\mathscr{R}}_k|\Phi_0\rangle = E_k\hat{\mathscr{R}}_k|\Phi_0\rangle \tag{3.25}$$

The orthogonality between the left and right eigenvectors is imposed.

$$\langle\Phi_0|\hat{\mathscr{L}}_m\hat{\mathscr{R}}_n|\Phi_0\rangle = \delta_{mn} \tag{3.26}$$

A more general CC energy expression than Eq. 3.20 is given by:

$$E_k = \langle\Phi_0|\hat{\mathscr{L}}_m\bar{H}\hat{\mathscr{R}}_n|\Phi_0\rangle \tag{3.27}$$

Substituting $|\Psi_0^{CC}\rangle$ and the excitation operator $\hat{\mathscr{R}}$ into Eq. 3.23 gives EOM-CC,

$$[\bar{H}, \hat{\mathscr{R}}_k] = \omega_k\hat{\mathscr{R}}_k|\Phi_0\rangle \tag{3.28}$$

Truncation of $\hat{\mathscr{R}}$ to the singles and doubles leads to EOM-CCSD. The density matrix, the oscillator strength can also be readily obtained using the left and right eigenvectors.

3.3 Linear response properties

In the presence of a static electric field, molecular properties such as electric dipole moments μ, and polarizabilities $\alpha_{\alpha\beta}$, can be viewed as the first-order and second-order changes in energy with respect to the electric field. However, the energy is not well-defined with a time-oscillating electric field due to the rapid exchange of energy between the field and molecules. One way to address this issue is to define the time-dependent *quasi energy* as the expectation value of the difference between the Hamiltonian and the energy operator ($i\hbar\frac{\partial}{\partial t}$).

In this section, we will review another alternative, which involves no differentiation on the field, based on time-dependent perturbation theory, to obtain the molecular properties. The response theory is essentially a reformulation of the time-dependent Schrödinger equation but treated in a perturbative way. A question the reader might ask is, "why not calculate directly the time propagation of the time-dependent Schrödinger equation itself?" The reasons are in the following:

1. The time evolution of the wavefunction ($\Psi(t)$) is not our direct interest. It is the time evolution of the expectation value of the operator namely the observable we look more on it.
2. Nonlinear effects, such as nonlinear optics, are challenging to separate from the direct approach, where it is comparatively easier within the response theory involving high-order expansions.
3. Error can propagates and difficult to control in the direct approach.
4. Calculations regard on vibrational contributions are not practically feasible in the non-perturbational approach.

3.3.1 Time evolution of the observable

The time-dependent Schrödinger equation is,

$$i\hbar\frac{\partial}{\partial t}\Psi(t) = \hat{H}\Psi(t) \tag{3.29}$$

In the Schrödinger picture, the wavefunction carries the time dependence, and the time-dependent wavefunction $\Psi(t)$ reads,

$$\Psi(t) = \Psi_n e^{-iE_n t/\hbar} \tag{3.30}$$

where Ψ_n, E_n are the true (exact) eigenfunctions and eigenvalues of the time-independent Hamiltonian $\hat{H}_0$. Time-dependent wavefunctions $\Psi(t)$ can be written as the product of two time-dependent functions,

$$\Psi(t) = e^{-i\phi(t)}\bar{\Psi}(t) \tag{3.31}$$

where $\phi(t)$ represents a phase [e] which is a real function and $\bar{\Psi}(t)$ is the phase isolated wavefunction, corresponding to $E_n t/\hbar$ and Ψ_n in the absence of the external field, respectively.

Parametrization of $\Psi(t)$. The parametrization of $\Psi(t)$ in practice is required to solve the time-dependent Schrödinger equation in Eq. 3.29. A common parametrization scheme is to expand $\Psi(t)$ as a linear combination of time-independent eigenfunctions as following,

$$\Psi(t) = \sum_n c_n(t)\Psi_n \tag{3.32}$$

where the time-dependent coefficient $c_n(t)$ carries the time evolution. The disadvantage of this parametrization is that the condition on the normalization of the time-dependent wavefunctions has always to be fulfilled. It is, therefore worthwhile to consider another parametrization scheme which is achieved not by projections but rotations.

The alternative parametrization for $\bar{\Psi}(t)$ is written as,

$$|\bar{\Psi}(t)\rangle = e^{-i\hat{P}(t)}|\Psi_0\rangle \tag{3.33}$$

[e]. The phase does not play a role in determining molecular properties. To see this, one plugging in Eq. 3.31 into Eq. 3.29 will find the *quasi energy* is the expectation value on the phase isolated wavefunctions,

$$Q(t) = \langle\bar{\Psi}(t)|(\hat{H} - i\hbar\frac{\partial}{\partial t})|\bar{\Psi}(t)\rangle$$

where the operator $\hat{P}(t)$ is defined,

$$\hat{P}(t) = \sum_{n>0} [P_n(t)|\Psi_n\rangle\langle\Psi_0| + P_n^*(t)|\Psi_0\rangle\langle\Psi_n|] \tag{3.34}$$

Here, the unitary operator $e^{-i\hat{P}(t)}$ assures that the condition on the normalization of the time-dependent wavefunctions is automatically satisfied. Note that when dealing with approximate states, such as single determinant wavefunctions, $\hat{P}$ takes different forms, resulting in a different expression for the response functions.

Choice of the equation of motion. Rather than examining the time evolution of the wavefunctions by the equation of motion derived from the Schrödinger equation, we focus on the time evolution of the expectation value using the Ehrenfest theorem.

The Ehrenfest theorem[77] states that the time evolution of an observable, specifically the expectation value of a time-independent operator $\hat{\Omega}$, is given by:

$$\frac{\partial}{\partial t}\langle\hat{\Omega}\rangle = \left\langle \frac{\partial\Psi(t)}{\partial t}|\hat{\Omega}|\Psi(t)\right\rangle + \left\langle \Psi(t)|\hat{\Omega}|\frac{\partial\Psi(t)}{\partial t}\right\rangle \tag{3.35}$$

$$= \frac{1}{i\hbar}\langle\left[\hat{\Omega},\hat{H}\right]\rangle \tag{3.36}$$

By replacing $\frac{\partial}{\partial t}\Psi(t)$ by $\frac{1}{i\hbar}\hat{H}\Psi(t)$ according to Eq. 3.29, we arrive from Eq. 3.35 to Eq. 3.36. Therefore we observe that the Ehrenfest theorem is equivalent to the time-dependent Schrödinger equation.

Time evolution of the expectation value. The next step is to use the parametrized phase isolated wavefunctions introduced above to obtain the time-dependent coefficient $P_n(t)$ from the operator $\hat{P}(t)$. To make the best use of Eq. 3.36, we first need to determine the forms of the two operators $\hat{\Omega}$ and $\hat{H}$.

$\hat{H}$ is relatively straightforward and can be expressed as the sum of the unperturbed Hamiltonian $\hat{H}_0$ and the interaction $\hat{V}(t)$ between the radiation field and the molecule. $\hat{V}(t)$ can be written in the following form:

$$\hat{V}(t) = \sum_{\omega} \hat{V}_\alpha^\omega F_\alpha^\omega e^{-i\omega t} e^{\xi t} \tag{3.37}$$

where $\hat{V}_\alpha^\omega$ represents the coupling term between the field and molecules. α denotes the Cartesian axis, following an oscillating electric field that is turned on at $t \to -\infty$, and ξ is a positive infinitesimal.

The equation of motion can be rewritten after substituting $\Psi(t)$ with the phase isolated wavefunction from Eq. 3.33,

$$\frac{\partial}{\partial t}\langle\Psi_0|e^{-i\hat{P}(t)}\hat{\Omega}e^{-i\hat{P}(t)}|\Psi_0\rangle = \frac{1}{i\hbar}\Psi_0|e^{-i\hat{P}(t)}\left[\hat{\Omega},\hat{H}_0+\hat{V}(t)\right]e^{-i\hat{P}(t)}|\Psi_0\rangle \tag{3.38}$$

The key equation of Eq. 3.38 can be solved by a particular choice of the operator $\hat{\Omega}$ and a perturbation expansion on the coefficient $P_n(t)$. A more detailed derivation can be found in the Appendix A or in the Ref. 78.

In the end, the zeroth-order expansion of the phase isolated wavefunction $\bar{\Psi}(t)$ is simply,

$$\bar{\Psi}(t)^{(0)} = |\Psi_0\rangle. \tag{3.39}$$

The first-order correction reads,

$$\bar{\Psi}(t)^{(1)} = -\frac{1}{\hbar}\sum_{n>0}\sum_{\omega}\frac{\langle\Psi_n|\hat{V}_\alpha^\omega|\Psi_0\rangle F_\alpha^\omega e^{-i\omega t}e^{\xi t}}{\omega_{n0}-\omega-i\xi}|\Psi_n\rangle \tag{3.40}$$

Now, if we denote $\hat{\Omega}$ as the operator corresponding to the observable of the interest, the expectation value of $\hat{\Omega}$ can be expressed in expansions of phase isolated wavefunctions as follows,

$$\begin{aligned}\langle\hat{\Omega}\rangle &= \langle\bar{\Psi}(t)^{(0)}|\hat{\Omega}|\bar{\Psi}(t)^{(0)}\rangle \\ &+ \langle\bar{\Psi}(t)^{(1)}|\hat{\Omega}|\bar{\Psi}(t)^{(0)}\rangle + \langle\bar{\Psi}(t)^{(0)}|\hat{\Omega}|\bar{\Psi}(t)^{(1)}\rangle \\ &+ \langle\bar{\Psi}(t)^{(2)}|\hat{\Omega}|\bar{\Psi}(t)^{(0)}\rangle + \langle\bar{\Psi}(t)^{(1)}|\hat{\Omega}|\bar{\Psi}(t)^{(1)}\rangle + \langle\bar{\Psi}(t)^{(0)}|\hat{\Omega}|\bar{\Psi}(t)^{(2)}\rangle \\ &+ \cdots\end{aligned} \tag{3.41}$$

Eq. 3.41 can be reformulated based on the Kubo relation [79] derived in 1957, providing a more general expression for molecular properties following the response to an external field:

$$\begin{aligned}\langle\hat{\Omega}\rangle &= \langle\bar{\Psi}(t)^{(0)}|\hat{\Omega}|\bar{\Psi}(t)^{(0)}\rangle \\ &+ \sum_{\omega_1} \ll\hat{\Omega};\hat{V}_\alpha^{\omega_1}\gg F_\alpha^{\omega_1}e^{-i\omega_1 t}e^{\xi t} \\ &+ \frac{1}{2}\sum_{\omega_1,\omega_2} \ll\hat{\Omega};\hat{V}_\alpha^{\omega_1},\hat{V}_\beta^{\omega_2}\gg F_\alpha^{\omega_1}F_\beta^{\omega_2}e^{-i(\omega_1+\omega_2)t}e^{2\xi t} \\ &+ \frac{1}{6}\sum_{\omega_1,\omega_2,\omega_3} \ll\hat{\Omega};\hat{V}_\alpha^{\omega_1},\hat{V}_\beta^{\omega_2},\hat{V}_\gamma^{\omega_3}\gg F_\alpha^{\omega_1}F_\beta^{\omega_2}F_\gamma^{\omega_3}e^{-i(\omega_1+\omega_2+\omega_3)t}e^{3\xi t} \\ &+ \cdots\end{aligned} \tag{3.42}$$

where $\ll\hat{\Omega};\hat{V}_\alpha^{\omega_1}\gg$ represents the linear response function. $\ll\hat{\Omega};\hat{V}_\alpha^{\omega_1},\hat{V}_\beta^{\omega_2}\gg$ corresponds to the quadratic response function, and $\ll\hat{\Omega};\hat{V}_\alpha^{\omega_1},\hat{V}_\beta^{\omega_2},\hat{V}_\gamma^{\omega_3}\gg$ denotes the cubic response function. In the following, we aim to identify the explicit forms of these functions.

3.3.2 Linear response function for exact states

The first order correction to the expectation value of the operator $\hat{\Omega}$ can be recognised by substituting the first-order correction of phase isolated wavefunction $\bar{\Psi}(t)^{(1)}$ into Eq. 3.41 and use

the fact $[F^{\omega}]^* = F^{-\omega}$,

$$\begin{aligned}
\langle\hat{\Omega}\rangle^{(1)} &= \langle\bar{\Psi}(t)^{(1)}|\hat{\Omega}|\bar{\Psi}(t)^{(0)}\rangle + \langle\bar{\Psi}(t)^{(0)}|\hat{\Omega}|\bar{\Psi}(t)^{(1)}\rangle \\
&= -\frac{1}{\hbar}\sum_{n>0}\sum_{\omega}\frac{\langle\Psi_n|\hat{V}_{\alpha}^{\omega}|\Psi_0\rangle\langle\Psi_0|\hat{\Omega}|\Psi_n\rangle[F_{\alpha}^{\omega}e^{-i\omega t}]^* e^{\xi t}}{\omega_{n0}-\omega+i\xi} \\
&- \frac{1}{\hbar}\sum_{n>0}\sum_{\omega}\frac{\langle\Psi_0|\hat{\Omega}|\Psi_n\rangle\langle\Psi_n|\hat{V}_{\alpha}^{\omega}|\Psi_0\rangle F_{\alpha}^{\omega}e^{-i\omega t}e^{\xi t}}{\omega_{n0}-\omega-i\xi} \\
&= -\frac{1}{\hbar}\sum_{n>0}\sum_{\omega}\left[\frac{\langle\Psi_n|\hat{V}_{\alpha}^{\omega}|\Psi_0\rangle\langle\Psi_0|\hat{\Omega}|\Psi_n\rangle}{\omega_{n0}+\omega+i\xi} + \frac{\langle\Psi_0|\hat{\Omega}|\Psi_n\rangle\langle\Psi_n|\hat{V}_{\alpha}^{\omega}|\Psi_0\rangle}{\omega_{n0}-\omega-i\xi}\right] F_{\alpha}^{\omega}e^{-i\omega t}e^{\xi t} \quad (3.43)
\end{aligned}$$

The linear response function can be readily obtained by a direct comparison of Eq. 3.43 and Eq. 3.42, and reads,

$$\ll\hat{\Omega};\hat{V}_{\alpha}^{\omega}\gg = -\frac{1}{\hbar}\sum_{n>0}\left[\frac{\langle\Psi_n|\hat{V}_{\alpha}^{\omega}|\Psi_0\rangle\langle\Psi_0|\hat{\Omega}|\Psi_n\rangle}{\omega_{n0}+\omega+i\xi} + \frac{\langle\Psi_0|\hat{\Omega}|\Psi_n\rangle\langle\Psi_n|\hat{V}_{\alpha}^{\omega}|\Psi_0\rangle}{\omega_{n0}-\omega-i\xi}\right] \quad (3.44)$$

It is worth noting that the linear response function is equivalent to the one derived in the quasi-energy approach, recognized as the second-order derivative with respect to the field.

The polarisability tensor. The physical interpretation of the linear response function depends on the choice of the operator $\hat{\Omega}$ corresponding to the observable, and the coupling operator $\hat{V}_{\alpha}^{\omega}$ between the field and molecules. In the electric dipole approximation, $\hat{V}_{\alpha}^{\omega} = -\hat{\mu}$. If we choose $\hat{\Omega} = \hat{\mu}$, and neglect ξ (provided the divergence issue is avoided), the polarisability tensor can be calculated according to Eq. 3.44 as:

$$\begin{aligned}
\alpha_{\alpha\beta}(-\omega;\omega) &= \ll\hat{\mu}_{\alpha};-\hat{\mu}_{\beta}\gg \\
&= \frac{1}{\hbar}\sum_{n>0}\left[\frac{\langle\Psi_0|\hat{\mu}_{\alpha}|\Psi_n\rangle\langle\Psi_n|\hat{\mu}_{\beta}|\Psi_0\rangle}{\omega_{n0}-\omega} + \frac{\langle\Psi_n|\hat{\mu}_{\beta}|\Psi_0\rangle\langle\Psi_0|\hat{\mu}_{\alpha}|\Psi_n\rangle}{\omega_{n0}+\omega}\right] \quad (3.45)
\end{aligned}$$

Poles and residues. From Eq. 3.45, for the pole ω_{n0} with order one, the residue is,

$$\lim_{\omega\to\omega_{n0}}(\omega_{n0}-\omega)\alpha_{\alpha\beta}(-\omega;\omega) = \langle\Psi_0|\hat{\mu}_{\alpha}|\Psi_n\rangle\langle\Psi_n|\hat{\mu}_{\beta}|\Psi_0\rangle \quad (3.46)$$

One immediately realizes the pole of the polarisability tensor corresponds to the excitation energies, and its residue is the transition dipoles.

3.3.3 One-photon absorption

The first-order transition amplitude from the ground state to the final state $|\Psi_f\rangle$ can be obtained from the first-order coefficient $P_n(t)^{(1)}$ derived in Eq. A.15. It is expressed with a monochromatic field as:

$$p_f(t)^{(1)} = \frac{1}{i\hbar}\left[\frac{\langle\Psi_f|\hat{V}_{\alpha}^{\omega}|\Psi_0\rangle F_{\alpha}^{\omega}e^{-i\omega t}e^{\xi t}}{\omega_{f0}-\omega-i\xi} + \frac{\langle\Psi_0|\hat{V}_{\alpha}^{\omega}|\Psi_f\rangle F_{\alpha}^{\omega}e^{i\omega t}e^{\xi t}}{\omega_{f0}+\omega-i\xi}\right] \quad (3.47)$$

The two singularities at $\omega = \omega_{f0}$ correspond to absorption, and $\omega = -\omega_{f0}$ for the emission. When the absorption is considered, in the electric dipole approximation, the probability to find the system in the final state $|\Psi_f\rangle$ is,

$$P_{f\leftarrow 0}(t) = |p_f(t)^{(1)}|^2 = \frac{1}{\hbar^2}\frac{|\langle\Psi_f|\hat{\mu}_\alpha|\Psi_0\rangle|^2 (F_\alpha^\omega)^2 e^{2\xi t}}{(\omega_{f0}-\omega)^2+\xi^2} \tag{3.48}$$

The transition rate is thus,

$$\begin{aligned} w_{f\leftarrow 0} = \frac{dP_{f\leftarrow 0}(t)}{dt} &= \frac{1}{\hbar^2}|\langle\Psi_f|\hat{\mu}_\alpha|\Psi_0\rangle|^2 \underbrace{\frac{2\xi}{(\omega_{f0}-\omega)^2+\xi^2}}_{\text{Cauchy distribution } f(\omega;\omega_{f0},\xi)} (F_\alpha^\omega)^2 e^{2\xi t} \\ &= \frac{2\pi}{\hbar^2}|\langle\Psi_f|\hat{\mu}_\alpha|\Psi_0\rangle|^2 f(\omega;\omega_{f0},\xi)(F_\alpha^\omega)^2 e^{2\xi t} \end{aligned} \tag{3.49}$$

The Cauchy distribution $f(\omega;\omega_{f0},\xi)$, in Eq. 3.49 gives a Lorentzian shape. We can simplify the transition rate by considering the limit $\xi \to 0$, and the Cauchy distribution becomes the Dirac delta function,

$$\begin{aligned} w_{f\leftarrow 0} &= \frac{2\pi}{\hbar^2}|\langle\Psi_f|\hat{\mu}_\alpha|\Psi_0\rangle|^2 \delta(\omega_{f0}-\omega)(F_\alpha^\omega)^2 \\ &= \frac{2\pi}{\hbar}|\langle\Psi_f|\hat{\mu}_\alpha|\Psi_0\rangle|^2 \delta(E_f - E_0 - \hbar\omega)(F_\alpha^\omega)^2 \end{aligned} \tag{3.50}$$

Integrating Eq. 3.50 to a continuum of states with the density of states $\rho(E_f)$ leads to the *Fermi golden rule*.

One-photon absorption cross section. In Eq. 3.49, the isotropic transition rate written in terms of the field intensity $I = \frac{1}{2}\varepsilon_0 c F^2$ is,

$$w_{f\leftarrow 0} = \frac{dP_{f\leftarrow 0}(t)}{dt} = \frac{\pi}{3\varepsilon_0 c\hbar^2}\sum_{\alpha=x,y,z}|\langle\Psi_f|\hat{\mu}_\alpha|\Psi_0\rangle|^2 f(\omega;\omega_{f0},\xi) I(\omega) \tag{3.51}$$

where ε_0 is the static dielectric constant and c is the speed of light. The factor $\frac{1}{3}$ arises from the rotational average of orientations of molecules. The energy transfer rate from the field to the molecule is,

$$\hbar\omega w_{f\leftarrow 0} = I(\omega)\sigma(\omega) \tag{3.52}$$

Hence, the one-photon absorption cross section $\sigma(\omega)$ can be expressed as,

$$\sigma(\omega) = \frac{\pi\omega}{3\varepsilon_0 c\hbar}\sum_{\alpha=x,y,z}|\langle\Psi_f|\hat{\mu}_\alpha|\Psi_0\rangle|^2 f(\omega;\omega_{f0},\xi) \tag{3.53}$$

3.4 Nonlinear response properties

3.4.1 Quadratic response function for exact states

In order to identify the quadratic response function, similar to the way obtaining the linear response function from the second line in Eq. 3.41, we need to write the explicit form of the second-order property as following,

$$\langle\hat{\Omega}\rangle^{(2)} = \langle\bar{\Psi}(t)^{(2)}|\hat{\Omega}|\bar{\Psi}(t)^{(0)}\rangle + \langle\bar{\Psi}(t)^{(1)}|\hat{\Omega}|\bar{\Psi}(t)^{(1)}\rangle + \langle\bar{\Psi}(t)^{(0)}|\hat{\Omega}|\bar{\Psi}(t)^{(2)}\rangle \tag{3.54}$$

where the $\bar{\Psi}(t)^{(1)}$ is known and $\bar{\Psi}(t)^{(2)}$ is not. Following the same logic of the procedure of obtaining $P_n(t)^{(1)}$, a more complexed equation of motion than Eq. A.12 containing a nested commutator of $(\hat{P}^{(1)}, \hat{P}^{(2)}, \hat{H}_0, \hat{\Omega})$ has to be solved to obtain $P_n(t)^{(2)}$ thus $\bar{\Psi}(t)^{(2)}$.

Here, we parachute the expression for $P_n(t)^{(2)}$,

$$P_n(t)^{(2)} = -\frac{1}{i\hbar^2}\sum_{\omega_1,\omega_2}\sum_{k>0}\frac{\langle\Psi_n|\bar{\hat{V}}_\alpha^{\omega_1}|\Psi_k\rangle\langle\Psi_k|\hat{V}_\beta^{\omega_2}|\Psi_0\rangle F_\alpha^{\omega_1}F_\beta^{\omega_2}}{(\omega_{n0}-\omega_1-\omega_2-2i\xi)(\omega_{k0}-\omega_2-i\xi)}e^{-i(\omega_1+\omega_2)t}e^{2\xi t} \tag{3.55}$$

where the fluctuation operator $\bar{\hat{\Omega}}$ is defined as $\bar{\hat{\Omega}} = \hat{\Omega} - \langle\Psi_0|\hat{\Omega}|\Psi_0\rangle$. The second-order correction $\bar{\Psi}(t)^{(2)}$ identified from Eq. A.7 can be obtained using the expression of $P_n(t)^{(1)}$ and $P_n(t)^{(2)}$,

$$\bar{\Psi}(t)^{(2)} = -i\sum_{n>0}P_n(t)^{(2)}|\Psi_n\rangle - \frac{1}{2}\sum_{n>0}|P_n(t)^{(1)}|^2|\Psi_0\rangle \tag{3.56}$$

The expression after inserting $\bar{\Psi}(t)^{(2)}$ and $\bar{\Psi}(t)^{(1)}$ into Eq. 3.54, is not symmetric with the exchange of α and β. However, the resulting response function is intrinsic symmetric. This can be resolved by using the permutator $\frac{1}{2}\sum\mathscr{P}_{1,2}$ which sums over the permutation on the pair of (α,ω_1) and (β,ω_2). The quadratic response function identified after comparing Eq. 3.42 and the symmetrized form of Eq. 3.54 is given by:

$$\begin{aligned}
\ll\hat{\Omega};\hat{V}_\alpha^{\omega_1},\hat{V}_\beta^{\omega_2}\gg \;=\; & \frac{1}{\hbar^2}\sum\mathscr{P}_{1,2}\sum_{n,k>0}\Bigg[\frac{\langle\Psi_0|\hat{\Omega}|\Psi_n\rangle\langle\Psi_n|\bar{\hat{V}}_\alpha^{\omega_1}|\Psi_k\rangle\langle\Psi_k|\hat{V}_\beta^{\omega_2}|\Psi_0\rangle}{(\omega_{n0}-\omega_1-\omega_2-2i\xi)(\omega_{k0}-\omega_2-i\xi)} \\
& + \frac{\langle\Psi_0|\hat{V}_\beta^{\omega_2}|\Psi_n\rangle\langle\Psi_n|\bar{\hat{V}}_\alpha^{\omega_1}|\Psi_k\rangle\langle\Psi_k|\hat{\Omega}|\Psi_0\rangle}{(\omega_{n0}+\omega_2+i\xi)(\omega_{k0}+\omega_1+\omega_2+2i\xi)} \\
& + \frac{\langle\Psi_0|\hat{V}_\alpha^{\omega_1}|\Psi_n\rangle\langle\Psi_n|\bar{\hat{\Omega}}|\Psi_k\rangle\langle\Psi_k|\hat{V}_\beta^{\omega_2}|\Psi_0\rangle}{(\omega_{n0}+\omega_1+i\xi)(\omega_{k0}-\omega_2-i\xi)}\Bigg]
\end{aligned} \tag{3.57}$$

The first-order hyperpolarisability tensor. The substitution of $\hat{\Omega} = \hat{\mu_\gamma}$, $\hat{V}_\alpha^{\omega_1} = -\hat{\mu_\alpha}$ and $\hat{V}_\beta^{\omega_2} = -\hat{\mu\beta}$ into the quadratic response function yields the first-order hyperpolarisability tensor, and let $\xi = 0$,

$$\beta_{\gamma\alpha\beta}(\omega_{-\sigma};\omega_1,\omega_2) = \frac{1}{\hbar^2}\sum\mathscr{P}_{-\sigma,1,2}\sum_{n,k>0}\frac{\langle\Psi_0|\hat{\mu_\gamma}|\Psi_n\rangle\langle\Psi_n|\bar{\hat{\mu_\alpha}}|\Psi_k\rangle\langle\Psi_k|\hat{\mu\beta}|\Psi_0\rangle}{(\omega_{n0}-\omega_\sigma)(\omega_{k0}-\omega_2)} \tag{3.58}$$

The excited state properties that can be extracted from the above expression include: the excitation energies, the ground to excited state and excited state to excited state transition dipole moments, and the permanent dipole of the excited states.

3.4.2 Two-photon absorption cross sections

Two-photon absorption is not a quadratic response property, but rather depends on the cubic response. However, if the two-photon absorption (TPA) transition strength is of interest—namely, the TPA cross-section—it can already be derived from the residues of the quadratic response function [80].

To see its nonlinear dependence on the external radiation field, we derive the TPA cross section following the similar logic as in the one-photon absorption case. One-photon absorption cross section was derived with the first-order coefficient amplitude $P_n(t)^{(1)}$ before. TPA cross section can be derived with the second-order coefficient $P_n(t)^{(2)}$ given in Eq. 3.55 which we will rewrite slightly different. The factor $-\frac{1}{i\hbar^2}$ is replaced by $\frac{1}{\hbar^2}$, because we will later take the square modules of the amplitude anyway. The transition amplitude from the initial ground state to a final state $|\Psi_f\rangle$ is thus,

$$p_f(t)^{(2)} = \frac{1}{\hbar^2} \sum_{\omega_1,\omega_2} \sum_k \frac{\langle \Psi_f | \bar{\hat{V}}_\alpha^{\omega_1} | \Psi_k \rangle \langle \Psi_k | \hat{V}_\beta^{\omega_2} | \Psi_0 \rangle F_\alpha^{\omega_1} F_\beta^{\omega_2}}{(\omega_{f0} - \omega_1 - \omega_2 - 2i\xi)(\omega_{k0} - \omega_2 - i\xi)} e^{2\xi t} \tag{3.59}$$

The transition probability for molecules from the initial to the final state at time t in the electric dipole approximation reads,

$$\begin{aligned} P_{f\leftarrow 0(t)} &= |p_f(t)^{(2)}|^2 \\ &= \frac{1}{\hbar^4} \sum_{\omega_1,\omega_2} \sum_k \left| \frac{\langle \Psi_f | \hat{\mu}_\alpha | \Psi_k \rangle \langle \Psi_k | \hat{\mu}_\beta | \Psi_0 \rangle F_\alpha^{\omega_1} F_\beta^{\omega_2}}{(\omega_{k0} - \omega_2 - i\xi)} \right|^2 \frac{e^{4\xi t}}{(\omega_{f0} - (\omega_1 + \omega_2))^2 + (2\xi)^2} \end{aligned} \tag{3.60}$$

The transition rate,

$$\begin{aligned} w_{f\leftarrow 0(t)} &= \frac{dP_{f\leftarrow 0}(t)}{dt} \\ &= \frac{2\pi}{\hbar^4} \sum_{\omega_1,\omega_2} \sum_k \left| \frac{\langle \Psi_f | \hat{\mu}_\alpha | \Psi_k \rangle \langle \Psi_k | \hat{\mu}_\beta | \Psi_0 \rangle F_\alpha^{\omega_1} F_\beta^{\omega_2}}{(\omega_{k0} - \omega_2 - i\xi)} \right|^2 f(\omega_1, \omega_2; \omega_{f0}, 2\xi) \end{aligned} \tag{3.61}$$

From Eq. 3.61, it can be seen that the most probable transition happens when $\omega_{f0} = \omega_1 + \omega_2$ where the function $f(\omega_1, \omega_2; \omega_{f0}, 2\xi)$ is peaked. The matrix element M_{f0} corresponding to the transition strength can be identified with a symmetrized form invariant with exchange of the indices ω_1 and ω_2,

$$M_{f0}^{\alpha\beta} = \sum_k \frac{\langle \Psi_f | \hat{\mu}_\alpha | \Psi_k \rangle \langle \Psi_k | \hat{\mu}_\beta | \Psi_0 \rangle}{(\omega_{k0} - \omega_1)} + \frac{\langle \Psi_f | \hat{\mu}_\beta | \Psi_k \rangle \langle \Psi_k | \hat{\mu}_\alpha | \Psi_0 \rangle}{(\omega_{k0} - \omega_2)} \tag{3.62}$$

The sum-over-state expression given in Eq. 3.62 for the exact state is usually not applied in the practical calculations. Instead, the response function based on the approximate state, depending on the excited state method, is solved. The working equations for obtaining M_{f0} for ADC(n) method can be found in Ref. 71 and for the EOM-CCSD method see in Ref. 81.

Above, we have discussed the transition probability between the discrete level of states. In order to derive the TPA cross section corresponds to a macroscopic case, we need to consider the

ground state transition to a continuum with the density of state. In such a case, the transition probability for the TPA absorption from the initial to the final state, with the incident laser photon flux $\mathscr{F}$ (photons $cm^{-2}s^{-1}$), the energy flux of photon 2 $I(\omega_2)$ per unit frequency, and the normalized lineshape function $g(\omega)$, can be written in the following form [82],

$$w_{f\leftarrow 0} = \frac{8\pi^3 e^4}{\hbar^4 c^2}\mathscr{F}_1 \hbar\omega_1 I(\omega_2)|M_{f0}^{\alpha\beta}|^2 g(\omega_{f0}) \tag{3.63}$$

The captured cross section for the second photon light is,

$$\sigma_2 I(\omega_2) = w_{f\leftarrow 0}(\omega_1, \omega_2)\hbar\omega_2 \tag{3.64}$$

The derived cross section,

$$\sigma_2 = \frac{8\pi^3 e^4}{\hbar^2 c^2}\mathscr{F}_1 \omega_1\omega_2|M_{f0}^{\alpha\beta}|^2 g(\omega_{f0}), \tag{3.65}$$

is apparently dependent on the incident laser intensity $\mathscr{F}$. A convenient measurable parameter used to characterize the TPA absorption strength is obtained by taking $\sigma_2/\mathscr{F}$, so the final TPA cross section is,

$$\delta = \frac{8\pi^3 e^4}{\hbar^2 c^2}\omega_1\omega_2|M_{f0}^{\alpha\beta}|^2 g(\omega_{f0}) \tag{3.66}$$

Orientation averages. When one attempts to connect the microscopic calculated quantity to the macroscopic measurable one, Eq. 3.66 cannot be applied in a straightforward way because the matrix element $M_{f0}^{\alpha\beta}$ in Eq. 3.62 is evaluated under the molecular frame. However, the TPA cross section obviously depends on the orientation of the radiation field. In the spectroscopy, the measured TPA cross section is proportional to the rotational average of all the orientations of $M_{f0}^{\alpha\beta}$. In the following, we aim to find the factor that accounts for this effect.

The matrix element can be rewritten by considering the coupling of the polarisation vector λ of the field in the lab reference of frame, and the transition moment $\mathbf{V_{0k}}$ in the molecule frame as follows:

$$M_{f0}(\lambda_\mathbf{1}, \lambda_\mathbf{2}) = \sum_k \frac{\lambda_\mathbf{1}\cdot\mathbf{V}_{fk}\mathbf{V}_{k0}\cdot\lambda_\mathbf{2}}{(\omega_{k0}-\omega_1)} + \frac{\lambda_\mathbf{2}\cdot\mathbf{V}_{fk}\mathbf{V}_{k0}\cdot\lambda_\mathbf{1}}{(\omega_{k0}-\omega_2)} \tag{3.67}$$

The polarisation of photon one $\lambda_\mathbf{1}$ and photon two $\lambda_\mathbf{2}$ can be manipulated in the experiment. The basic idea is to transform the transition moment in the molecular frame into the lab frame by a *directional cosine* transformation. [f] In the end, our target is to obtain the rotational

[f]. Assuming the origin of the lab and molecular frame is the same and located somewhere inside the molecule, the vector component R_i with $\mathbf{R} = R_x\mathbf{e}_x + R_y\mathbf{e}_y + R_z\mathbf{e}_z$ where $\mathbf{e}^i$ is the unit vector, can be transform into another frame with $R_{i'}$ by the cosine function, that is

$$R_{i'} = \sum_j cos\theta_{i'j}R_j.$$

The transformed vector component in lab frame is span with the molecular frame component with the coefficient of cosine of the angle between i' and j.

average of a fourth-rank tensor $\langle M_{ijkl}\rangle$. There are several ways to achieve this goal, see Ref.[83] for example. One systematic way to solve it is the use of the isotropic tensor, which is rotationally invariant and serves as a basis expansion for any general high-rank tensors. For more details about this approach see Ref. 78.

As a result, the rotational averaged TPA transition strength is given as[83],

$$\langle |M_{0f}|^2\rangle = \frac{1}{30}\sum_{\alpha,\beta}\Big[F\cdot M_{\alpha\alpha}M^*_{\beta\beta} + G\cdot M_{\alpha\beta}M^*_{\alpha\beta} + H\cdot M_{\alpha\beta}M^*_{\beta\alpha}\Big]. \tag{3.68}$$

Depending on the polarisation of two incident photon light, the constants (F, G, H) take different values. Specifically, $F = G = H = 2$ for parallel polarisation and $F = H = -1, G = 4$ for the perpendicular polarisation between two incident photons. The polarisation dependence of the incident light, on the other hand, can be used in the experiment to recognize the symmetry of excite states[84].

Atomic to macroscopic units. The formula for TPA cross section in Eq. 3.66 is expressed in atomic unites. Often, a comparison with the experiment is needed, and thus the conversion to macroscopic unites is necessary.

The conventional unites for TPA cross section is GM named after Göppert-Mayer[85], where 1 GM is 10^{-50} cm^4s photon$^-1$. By writing the corresponding unit of each term in the cross section and collecting the factor in front of Eq. 3.66, we have, in centimetre–gram–second (cgs) system of units where $4\pi\varepsilon_0 = 1$,

$$\begin{aligned}\delta_{[cgs]} &= 8\pi^3\alpha^2\left[\frac{a_0^4}{E_h^2}\right][E_h\hbar] \\ &= \frac{8\pi^3\alpha a_0^5}{c}\delta_{[a.u.]}\end{aligned} \tag{3.69}$$

where α is the fine structure constant, a_0 is the Bohr radius, E_h is the Hartree energy, and c is the speed of light.

Chapter 4

The challenge of accurate computation of Two-photon absorption properties of organic chromophores in the condensed phase

4.1 Motivation and outcome

Nonlinear phenomena, such as two-photon absorption (TPA), present a significant computational challenge due to the need for high accuracy which requires extensive computational time. The sum-over-state expression for calculating nonlinear properties, requires an accurate description of not only one excited state but of many other excited states, in terms of energies and wavefunctions. The widely applied time-dependent Density Functional Theory depends on the choice of the exchange-correlation functional and can lead to unpredictable errors concerning simulations of the TPA cross-section.

The question of *"what accuracy level of modelling the TPA cross-section can we expect?"* still remains in the literature. We first examined the absolute TPA cross-section using advanced correlated methods and compared it with the 'golden standard' method of equation-of-motion coupled cluster methods. Then we shift the focus on the complexation induced shift of TPA cross-section due to the presence of the environment. We found achieving the accuracy of the absolute TPA cross-section below 100 atomic units and their shifts below 10 atomic units remains a challenge. On the other hand, FDET with the linearized version has demonstrated greater reliability compared with other embedding methods which only include the electrostatic interaction between fragments. The equivalent shift value can be obtained compared with the reference supermolecular results with the largest basis set.

Reprint of the paper is provided in the following pages. [Fu M, Wesolowski TA, *J. Chem. Theory Comput.* 17, 3652-3665 (2021)]

Supporting information for this paper can be found in Appendix C. Additional analysis made after the publication is provided in Appendix D.

JCTC Journal of Chemical Theory and Computation

pubs.acs.org/JCTC Article

The Challenge of Accurate Computation of Two-Photon Absorption Properties of Organic Chromophores in the Condensed Phase

Mingxue Fu* and Tomasz A. Wesolowski

Cite This: J. Chem. Theory Comput. 2021, 17, 3652−3665 Read Online

ACCESS | Metrics & More | Article Recommendations | Supporting Information

ABSTRACT: Two strategies are applied to evaluate the effect of the environment on the two-photon absorption (TPA) cross sections for two characteristic excited states of C_2H_4 upon complexation with H_2O. The supermolecular strategy provides the reference complexation-induced shifts and uses either the EOM-CCSD or ADC(2) method. The embedding strategy is based on frozen-density-embedding theory (FDET) and uses only fundamental constants. The TPA cross sections from high-level supermolecular calculations are extremely basis-set-sensitive. Literature data and the present study indicate that accuracy of the absolute TPA cross sections below 100 atomic units and their shifts below 10 atomic units remains a challenge. The obtained FDET results show a similar basis-set behavior. For the largest basis set (d-aug-cc-pVQZ), TPA cross sections obtained from these two strategies are in excellent agreement. The complexation-induced shifts have the correct sign of the effect and a small (12−33%) relative error in magnitude. The deviations of the FDET-derived shifts from the reference are of similar magnitude as the reliability threshold of the reference shifts.

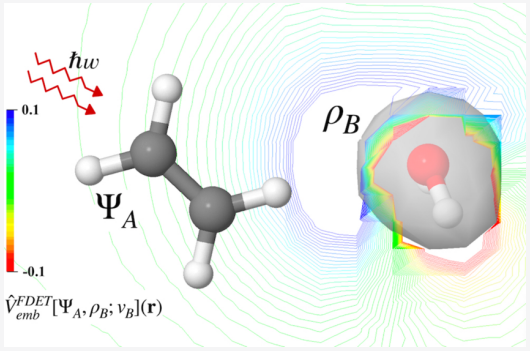

1. INTRODUCTION

Two-photon absorption (TPA) spectroscopy offers a broad area for applications. It makes it possible to observe dark states, for which the dipole transitions are not permitted. Unlike in the case of one-photon absorption (OPA), the TPA absorption intensity depends nonlinearly on the incident radiation intensity, thus providing a variety of promising applications such as microfabrication, three-dimensional data storage, optical power limiting, and so forth.[1] The longer wavelength of photons also makes it possible to study chromophores embedded in biological tissues. Increasing interest has been focused on the design and synthesis of more efficient TPA dyes, such as well-adopted D−π−A systems, where D and A are donor and acceptor groups, respectively, and π represents the π-conjugated bridge. The absorption intensity can reach a magnitude of 10^3 GM subject to the choice of D/A groups and the length of the π-conjugated bridge.[1−4] The applications of TPA spectroscopy concern mainly the condensed phase.

Several factors contribute to the TPA cross sections measured in the condensed phase. Based on the available experimental and simulation data, establishing their relative importance is, unfortunately, not always straightforward. For example, the surrounding solvent can affect the intensity and direction of intramolecular charge-transfer states in the chromophore, and the solvent effect is especially important for a bioprobe due to the requirement of a large Stokes shift.[5] In ref 6, Woo et al. have shown that the TPA cross section of the distyrylbenzene-based chromophores has a nonmonotonic relation with the solvent polarity. The maximum TPA cross section was measured with the intermediate polarity, and the lowest was observed in the water. Using the TDDFT/polarized continuum model, Wang et al. predicted the nonmonotonic relation with the solvent polarity and demonstrated the importance of the electron correlation.[7] Using the same method, Frediani et al. showed that the refractive index of the solvent—instead of the polarity—plays a key role in the enhancement of TPA cross sections.[8]

In principle, quantum chemistry simulation methods can provide insights and an understanding of the TPA activity of a chromophore in a given environment. Although the precondition for a reliable prediction of the TPA properties measured in the condensed phase is the use of adequate electronic structure methods to determine them at a given conformation of the chromophore, other factors must also be properly simulated such as the vibronic coupling[9] or the environment effect on the geometry of the chromophore, for instance. The present work focusses on the first factor—the electronic structure method to evaluate the TPA cross section

Received: February 26, 2021
Published: May 4, 2021

of an embedded chromophore. The methods based on responses in time-dependent density functional theory (DFT) (LR-TDDFT[10] or QR-TDDFT[11,12]) are attractive strategies applicable for modeling OPA and TPA properties of chromophores in the condensed phase. Favorable scaling makes them applicable for clusters representing the chromophore and the nearest molecules in its environment. The range-separated functionals seem to be most appropriate for TPA because they describe both the valence and charge-transfer excitations in a balanced way. The latter are known to be incorrectly described by semilocal and even hybrid functionals.[13] The range-separated functionals are not free, however, from qualitative failures in calculating TPA properties. For instance, CAM-B3LYP[14] predicts spurious features in the calculated TPA spectra of oligophenylvinylene molecules[15] never observed experimentally. According to Beerepoot et al.,[16] the unstable numerical results obtained using this functional are due to the systematic underestimation of the excited-state dipole moment. In a more recent publication, the same authors showed also that both the semilocal and hybrid functionals exhibit an unpredictable error. The smaller error calculated using some approximations for the exchange−correlation energy was explained by the cancellation of errors in excitation energies and in transition dipole moments leading them to the conclusion that development of new approximations capable of describing both quantities properly is needed.[17]

The so-called few-state model[18,19] also provides an inexpensive tool for obtaining the TPA cross sections. In some cases, it explains very well the experimentally observed trends failing, however, to describe TPA corresponding to some high-lying states. The semiempirical method—intermediate neglect of differential overlap INDO/S-CIS(CISD)—with specially optimized parameters for electronic excitations was also applied for the TPA cross section.[20] The method reproduces well the excitation energy for $\pi\pi^*$ and $n\pi^*$ excitations but fails for charge-transfer states, Rydberg states, and states with prominent double excitation character.

Concerning the ab initio correlated methods, they can be expected to lead to more reliable TPA properties. They are capable of describing excited states of various characters (valence excitations, charge-transfer excitations, double excitations, in particular) in a balanced way. Methods to evaluate TPA cross sections combining the response theory and the configuration interaction series,[21−23] random phase approximation,[23−26] algebraic-diagrammatic construction (ADC),[27] and equation-of-motion coupled cluster (EOM-CC),[28] for instance, were developed. For example, the CIS model successfully explained that an enhancement of TPA cross sections of diacetylene molecules in the shorter wavelength is due to a double resonance from one-photon to two-photon states.[23] Due to the unfavorable scaling with the number of basis functions (N^5, N^6, and N^7 for CC2, CCSD, and CC3, respectively), the high-quality ab initio correlated methods have a limited range of applicability as far as chromophores in the condensed phase are concerned. The study by Nielsen et al.[25] on small organic chromophores showed that reaching the confidence threshold in the calculated absolute values of the TPA cross section beyond 100 atomic units is not possible in practice. The TPA cross sections obtained from EOM-CCSD calculations reported recently by Nanda and Krylov concerned complexes comprising an organic chromophore of biological interest and a few solvent molecules consisting of no more than 34 atoms mark the current practical size limit for the ab initio-correlated methods.[28] For the chromophores of this size, the authors used the 6-31+G* basis set,[30] which most likely is not large enough to obtain converged absolute TPA cross sections. The success of the advanced ab initio methods in modeling TPA properties of relatively small chromophores in the gas phase and frequently erratic results obtained by means of response theory-based TD-DFT methods prompt a legitimate question: Is accurate modeling of TPA activity for chromophores in the condensed phase possible? What accuracy can be expected? The comprehensive study by Nielsen et al.[25] concludes with the suggestion that accurate predictions of the absolute two-photon cross sections is rather out of reach for high-level ab initio methods and that such methods should rather aim at predicting the relative cross sections in different species. For the above reasons, we analyze the applicability of different methods to evaluate the differences of OPA and TPA properties—complexation-induced shifts in the excitation energy and TPA cross section in particular.

For the evaluation of the environment-induced shifts, the multilevel simulations make it possible to escape the dilemma between the unfavorable scaling of accurate ab initio methods and lowering the accuracy expectations if the DFT-based methods are used. Such methods have been successfully applied to model the potential energy surface and are frequently referred by a collective acronym (QM/MM). The key feature of such methods is that the embedded wave function associated with the embedded species is obtained from the Schrödinger equation in which the isolated species Hamiltonian is modified by addition of the "embedding operator". In the simplest case, the operator is just electrostatic potential generated by the molecules of the environment of the embedded species. Methods designed for modeling electronic excitations have been developed. Their field of applicability includes also the simulating TPA activity.[31−36] These studies show invariably that the embedding potential must go beyond the electrostatic potential generated by a fixed distribution of charges in the environment.

The interest in accurate modeling of TPA activities in host−guest complexes is systematically growing (see the recent work by Alam and Ruud[37] for instance) and multilevel methods seem to offer the only viable alternative as far as accurate predictions and/or interpretation of experimental data are concerned. In the present work, the method based on frozen-density-embedding theory (FDET) is used. In FDET, the embedded wave function is obtained from constrained minimization of the energy of the total system, in which the constraints are imposed on the density. The FDET embedding operator is multiplicative (embedding potential) and is constructed in such a way that the minimal energy equals to that given by the energy functional defined in the second Hohenberg−Kohn theorem.[38] The non-Coulombic effects on the embedded wave function (intermolecular Pauli repulsion or quantum confinement) are represented in FDET by the potential ($v_{\mathrm{xct}}^{\mathrm{nad}}[\rho_A, \rho_B](\mathbf{r})$ see below) determined uniquely by the electron density of the environment and that of the embedded species. Because this operator is multiplicative, it can be interpreted as a confining potential. On the other hand, its kinetic part represents the effects due to Fermi statistics on the embedded electron density, it can also be attributed to the intermolecular Pauli repulsion. These descriptive terms can be misleading. The confining potential does not have to be repulsive as shown for exactly solvable systems in FDET[39] and

https://doi.org/10.1021/acs.jctc.1c00204
J. Chem. Theory Comput. 2021, 17, 3652−3665

the Pauli repulsion relates rather to the effect on the wave function, whereas $v_{xct}^{nad}[\rho_A, \rho_B](\mathbf{r})$ originates from the condition satisfied by the exact density.[40] The differential electronic polarization of the environment is treated in FDET implicitly. In practice, $v_{xct}^{nad}[\rho_A, \rho_B](\mathbf{r})$ is approximated.

The approximations in this work were already tested on OPA energies in a comprehensive benchmarking study on the lowest few excitations in ref 52 in representative complexed chromophores showing that the used approximations in FDET provide a practical alternative to the conventional calculations, that is, where the chromophore and the environment molecule constitute one quantum mechanical system. In the benchmarking set, the average magnitude of the deviations of the "embedded ADC(2)" excitation energies from their supermolecular ADC(2) reference equals 0.036 eV—a small value compared to the complexation-induced shifts.[41] The benchmarking set included neither the chromophores covalently bound to the environment nor excitations involving the charge transfer between the chromophore and the environment. Such cases lie outside the range of applicability of the benchmarked approximations in FDET. Turning back to the TPA cross sections derived from response theory-based approaches, their quality depends critically on the accuracy of the energy of not just one state but that of several nearby lying excited states. The fact that the quality of the FDET-derived excitation energies did not show any sign of deterioration for higher lying states suggests that the approximations used in FDET, which were tested in ref 41, can be applied also for the TPA properties.

The notorious basis set sensitivity of the TPA cross sections obtained from correlated wave function-based methods represents a critical limitation as far as adequacy of approximations used in FDET is concerned. Numerically stable complexation-induced shifts of the TPA properties, which could be used as a reference for interpretation of the errors in the FDET-derived shifts, require the use of large basis sets.[25] The basis set sensitivity of FDET-derived TPA cross sections has not been investigated so far. For this reason, the present study concerns a small model system comprising a chromophore (C_2H_4) weakly bound to only one molecule (H_2O). The small size makes it possible to explore the accuracy limits of the applied approximations in FDET and apply the gained experience in subsequent simulations of TPA properties for the chromophores weakly bound to the molecules in the environment (solvent, biomolecules, surface, porous solid, etc.). For the references shifts, ADC(2) is treated to treat electron−electron correlation effects in the complex and in the isolated chromophore. The EOM-CCSD results are also reported to confirm the reliability of the ADC(2) reference shifts and to determine the accuracy threshold in the evaluated observables for meaningful interpretation of errors in the FDET-derived shifts. In FDET, the ADC(2) treatment is applied for the embedded wave functions.

The deviations of the shifts obtained from "embedded ADC(2)" calculations from the supermolecular ADC(2) reference are used to determine the range of applicability of the applied approximations in FDET and to estimate the expected accuracy of the FDET-derived shifts. The reported study is proposed as a model for the introductory stage of any multilevel simulation of TPA properties for chromophores in the condensed phase that is based on FDET.

2. THEORETICAL BACKGROUND

2.1. Excited States from FDET. For a system comprising N_{AB} electrons in the external potential $v_{AB}(\mathbf{r})$, the lowest-energy stationary embedded N_A-electron wave function is obtained from the following eigenvalue equation:

$$(\hat{H}_A + \hat{v}_{emb}^{FDET}[\rho_A, \rho_B; v_B])\Psi_A = \lambda\Psi_A \tag{1}$$

in which $\rho_A(\mathbf{r}) = \langle\Psi_A|\sum_{i=1}^{N_A}\delta(\mathbf{r}_i - \mathbf{r})|\Psi_A\rangle$ and $v_{emb}^{FDET}[\rho_A, \rho_B; v_B]$ is given by

$$v_{emb}^{FDET}[\rho_A, \rho_B; v_B](\mathbf{r}) = v_B(\mathbf{r}) + \int\frac{\rho_B(\mathbf{r}')}{|\mathbf{r} - \mathbf{r}'|}\,d\mathbf{r}' + v_{xct}^{nad}[\rho_A, \rho_B](\mathbf{r}) \tag{2}$$

where $\hat{H}_A$ is the Hamiltonian corresponding to N_A electrons of an external potential $v_A(\mathbf{r})$ with $N_A < N_{AB}$; $v_A(\mathbf{r})$ is an arbitrarily chosen component of the total potential $v_{AB}(\mathbf{r})$, which is partitioned as $v_{AB}(\mathbf{r}) = v_A(\mathbf{r}) + v_B(\mathbf{r})$; and $v_{xct}^{nad}[\rho_A, \rho_B](\mathbf{r})$ is given as a functional determined uniquely by the pair of electron densities $\rho_A(\mathbf{r})$ and $\rho_B(\mathbf{r})$.

For the definition of the functional $v_{xct}^{nad}[\rho_A, \rho_B](\mathbf{r})$, the expression for the total energy, and the relation between the eigenvalue λ and the total energy, see the original publications concerning various possible choices for the method to solve eq 1: ref 42 for an embedded reference systems of noninteracting electrons, ref 40 for the exact (interacting) Hamiltonian, and ref 43 for the embedded one-particle spinless reduced density matrix. For the exact relation, involving the total FDET energy and quantities available if nonvariational methods are used to solve eq 1, see ref 44.

The stationary embedded wave function Ψ_A° is obtained from eq 1 with the self-consistent embedding potential, that is, $v_{emb}^{FDET}[\rho_A^\circ, \rho_B; v_B](\mathbf{r})$, where $\rho_A^\circ(\mathbf{r}) = \langle\Psi_A^\circ|\sum_{i=1}^{N_A}\delta(\mathbf{r}_i - \mathbf{r})|\Psi_A^\circ\rangle$.

According to the Levy−Perdew theorem,[45] solutions of eq 1 obtained with the self-consistent potential (i.e., $v_{xct}^{nad}[\rho_A^I, \rho_B](\mathbf{r})$, where $\rho_A^I(\mathbf{r}) = \langle\Psi_A^I|\sum_{i=1}^{N_A}\delta(\mathbf{r}_i - \mathbf{r})|\Psi_A^I\rangle$), Ψ^I, other than the lowest-energy one can be interpreted as excited states.[46,47]

In the present work, the indices A and B refer to the chromophore and the environment, respectively. We point out that such attribution is arbitrary in FDET. Partitioning the external potential into $v_{AB}(\mathbf{r}) = v_A(\mathbf{r}) + v_B(\mathbf{r})$ does not affect the FDET results at all. Partitioning of the total number of electrons into $N_{AB} = N_A + N_B$ on the other hand is not related to the localization of the embedded wave function. The attribution of the indices is only relevant to the choice of $\rho_B(\mathbf{r})$ at which the FDET equations are solved. The attribution of these indices acquires, however, a concrete meaning if localized and incomplete set of basis set functions are used. For instance, if the set of basis functions $\{\chi_\mu\}$ used for $\rho_A(\mathbf{r})$ is centered only on atoms defining $v_A(\mathbf{r})$, whereas the basis functions used for $\rho_B(\mathbf{r})$ are centered only on atoms defining $v_B(\mathbf{r})$ such attribution of indices is meaningful and is referred to here as monomer expansion (ME).

$$\rho_A^{ME}(\mathbf{r}) = \sum_{\mu\nu} P_{\mu\nu}^A\chi_\mu^A(\mathbf{r})\chi_\nu^A(\mathbf{r}) \tag{3}$$

$$\rho_B^{ME}(\mathbf{r}) = \sum_{\mu\nu} P_{\mu\nu}^B\chi_\mu^B(\mathbf{r})\chi_\nu^B(\mathbf{r}) \tag{4}$$

The ME is obviously an approximation. If applicable, it can lead to huge computational savings potentially. Most of the

https://doi.org/10.1021/acs.jctc.1c00204
J. Chem. Theory Comput. 2021, 17, 3652−3665

numerical results discussed in the present work use the ME. The supermolecular expansion refers to calculations where this approximation is lifted, that is, where the densities have the form given below

$$\rho_{\mathrm{A}}^{\mathrm{SE}}(\mathbf{r}) = \sum_{\mu\nu} P_{\mu\nu}^{\mathrm{A}} \chi_{\mu}^{\mathrm{AB}}(\mathbf{r}) \chi_{\nu}^{\mathrm{AB}}(\mathbf{r}) \tag{5}$$

$$\rho_{\mathrm{B}}^{\mathrm{SE}}(\mathbf{r}) = \sum_{\mu\nu} P_{\mu\nu}^{\mathrm{B}} \chi_{\mu}^{\mathrm{AB}}(\mathbf{r}) \chi_{\nu}^{\mathrm{AB}}(\mathbf{r}) \tag{6}$$

2.2. TPA Cross Sections from Linearized FDET Embedded Wave Functions. The general framework of the linear and quadratic responses will be used to obtain the TPA properties.[48,49] In the particular case of two resonant photons ω_1 and ω_2 such that $\omega_1 = \omega_2 = {}^1/_2\Omega_n$, where Ω_n is the resonance frequency for OPA, the TPA transition magnitude is given by[27]

$$M_{\mathrm{a,b}} = \sum_{k\neq 0} \left[\frac{\langle 0|\hat{\mu}^{\mathrm{a}}|k\rangle\langle k|\bar{\hat{\mu}}^{\mathrm{b}}|n\rangle}{\omega_k - \omega_1} + \frac{\langle 0|\hat{\mu}^{\mathrm{b}}|k\rangle\langle k|\bar{\hat{\mu}}^{\mathrm{a}}|n\rangle}{\omega_k - \omega_2} \right] \tag{7}$$

where $\hat{\mu}^i$ and $\bar{\hat{\mu}}^i$ are the Cartesian components ($i = x, y, z$) of the dipole moment operator and the fluctuation operator ($\bar{\hat{\mu}}^i = \hat{\mu}^i - \langle 0|\hat{\mu}^i|0\rangle$), respectively, whereas $|k\rangle$ denotes the intermediate states.

The above sum-over-state expression for the transition magnitude indicates that the quality of not just one state but all nearby lying states determines the overall quality of the calculated transition magnitude. This rather tough accuracy requirement is the principal reason why the simulation of TPA activities remains a challenge for molecular quantum mechanics methods and results in erratic results obtained using TDDFT-based strategies.

Figure 1 illustrates eq 7 for a system of the D_{2h} symmetry, such as the isolated C_2H_4 molecule, for which the ground state

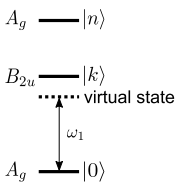

Figure 1. Sketch for the symmetry-allowed TPA process ($A_g \rightarrow A_g$) for a molecule with the D_{2h} symmetry.

has the A_g symmetry, whereas the two excited states considered in the present work have the B_{2u} and A_g symmetries, respectively. The final A_g state in the TPA process is symmetry-allowed but the corresponding TPA magnitude depends on all intermediate states. The B_{2u} states are symmetry-forbidden in TPA processes but they contribute to the TPA magnitude. Obviously, they are symmetry-allowed in OPA processes. The error of $|k\rangle$ and ω_k obtained from a given quantum mechanical methods of all states of the B_{2u} symmetry near the final A_g affects, thus, the overall quality of the TPA magnitude for the final A_g state.

Equation 7 applies for isolated systems. The states are obtained at some external potentials usually corresponding to the potential due to nuclear charges. For such external potentials as well as for the more general class of external potentials that are state-independent, the states are orthogonal. The FDET embedding potential is, however, state-dependent. The last term in eq 2 ($v_{\mathrm{xct}}^{\mathrm{nad}}[\rho_{\mathrm{A}}^{\mathrm{I}}, \rho_{\mathrm{B}}](\mathbf{r})$) is different for different states. In linearized FDET,[47] which is an approximation within FDET,

$$E_{\mathrm{xct}}^{\mathrm{nad}}[\rho_{\mathrm{A}}, \rho_{\mathrm{B}}] \approx E_{\mathrm{xct}}^{\mathrm{nad}}[\rho_{\mathrm{A}}^{\mathrm{ref}}, \rho_{\mathrm{B}}] + \int (\rho_{\mathrm{A}}(\mathbf{r}) - \rho_{\mathrm{A}}^{\mathrm{ref}}(\mathbf{r})) v_{\mathrm{xct}}^{\mathrm{nad}}[\rho_{\mathrm{A}}^{\mathrm{ref}}, \rho_{\mathrm{B}}](\mathbf{r})\, \mathrm{d}\mathbf{r} \tag{8}$$

the orthogonality of the embedded wave function is preserved. The errors in energy due to linearization depend on the expansion point $\rho_{\mathrm{A}}^{\mathrm{ref}}(\mathbf{r})$. Using the ground-state density of the embedded species as $\rho_{\mathrm{A}}^{\mathrm{ref}}(\mathbf{r})$ was shown to be a very good approximation. It introduces negligible errors (1 meV or less) in the OPA energies.[50] Using the linearized FDET embedding potential leads to additional benefits if the self-consistent embedded density is used as $\rho_{\mathrm{A}}^{\mathrm{ref}}(\mathbf{r})$. With such a choice for $\rho_{\mathrm{A}}^{\mathrm{ref}}(\mathbf{r})$, recently derived exact relation between the Hohenberg–Kohn total energy functional and quantities, which can be obtained from nonvariational correlated wave-function-based methods (eq 38 in ref 44), can be applied. As a result, not only energy differences but also absolute energies obtained from linearized FDET become consistent from Hohenberg–Kohn theorems.

The negligible errors due to the linearization of $E_{\mathrm{xct}}^{\mathrm{nad}}[\rho_{\mathrm{A}}, \rho_{\mathrm{B}}]$ on the OPA energies suggest that TPA properties derived from eq 7 and the linearized FDET embedding potential with the same expansion point is also applicable for simulating TPA activities.

For other types of embedding operators, which are state-independent [the case of exact Coulomb embedding or point charge (PC) embedding considered in this work], eq 7 can be applied in a straightforward manner.

3. COMPUTATIONAL DETAILS

Decomposable local-density approximation was used for each component of $v_{\mathrm{xct}}^{\mathrm{nad}}[\rho_{\mathrm{A}}, \rho_{\mathrm{B}}](\mathbf{r})$ defined in ref 40: Slater–Dirac functional[51] for exchange, Vosko–Wilk–Nusair parameterization[52] for correlation, and Thomas–Fermi[53,54] functional for the kinetic component, whereas its $v_{\mathrm{c}}[\rho_{\mathrm{A}}](\mathbf{r})$ part was entirely neglected. The vertical excitation energies (ϵ) and cross sections (δ_{TPA}) were evaluated using FDET-based (or simpler embedding methods) implemented in the Q-Chem[55] program, using the ADC(2) level of description for the electronic excitations in the embedded subsystem. The reference values of ϵ and cross sections δ_{TPA} were obtained using also the program Q-Chem [for ADC(2) and EOM-CCSD].

The calculations were made using several Gaussian atomic basis sets including two series of correlation-consistent basis sets: aug-cc-pVXZ(X = D,T,Q) and d-aug-cc-pVXZ(X = D,T,Q).[29] The results obtained with the 6-31+G* basis set are also reported[30] for comparison purposes. It is frequently applied in simulations of electronic excitations. In particular, it has been used in the EOM-CCSD calculations of two-photon activities of several larger chromophores by Krylov and collaborators (see refs 28 and 31 for instance).

All considerations in the present work concerning the excited state properties use ground-state optimized geometry obtained by means of the second-order Møller–Plesset perturbation theory and the cc-pVTZ basis set. The structure of the complex is shown in Figure 2. For the coordinates, see Supporting Information. For the shifts defined as $\Delta\epsilon$ =

https://doi.org/10.1021/acs.jctc.1c00204
J. Chem. Theory Comput. 2021, 17, 3652−3665

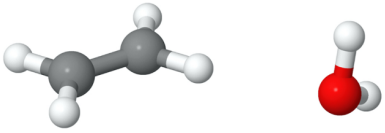

Figure 2. C_2H_4−H_2O complex used throughout calculations.

$\epsilon^{C_2H_4-H_2O} - \epsilon^{C_2H_4}$ and $\Delta\delta_{TPA} = \delta_{TPA}^{C_2H_4-H_2O} - \delta_{TPA}^{C_2H_4}$, the numerical values corresponding to the isolated chromophore were evaluated at the same geometry as that in the complex.

The FDET embedding potential used in the linearized FDET expression for the excitation energies $v_{emb}^{FDET}[\rho_A^{ref}, \rho_B; v_B]$-$(\mathbf{r})$ was evaluated at the density $\rho_A^{ref}(\mathbf{r})$ being the first-order Møller−Plesset density of the isolated chromophore. Various choices for constructing $\rho_B(\mathbf{r})$ are considered including the monomer and supermolecular expansions. In each case, $\rho_B(\mathbf{r})$ is generated from Hartree−Fock wave function corresponding to either the isolated water molecule or optimized through the freeze-and-thaw minimization of the total energy of the complex[56] as described in ref 57 for the embedded Hartree−Fock variant of FDET.

The complexation-induced shifts of the TPA cross sections are analyzed for two excited states well characterized in the isolated C_2H_4: the lower (B_{2u}) and the higher (A_g). TPA is symmetry-allowed and OPA is symmetry-forbidden for A_g. For B_{2u}, TPA is symmetry-forbidden and OPA is symmetry-allowed. Both states have the $\pi\pi^*$ character and will be labeled as the first and second $\pi\pi^*$ state for both isolated and complexed C_2H_4. The symmetry labels do not apply for the complex. Breaking the symmetry upon complexation is expected to result in the TPA activity of the first $\pi\pi^*$ state. The corresponding states are identified based on the oscillator strength and on the visual inspection of the canonical−natural transition orbitals for 10 lowest excitations available in both supermolecular and embedding calculations. Due to the known extreme basis set sensitivity of the TPA cross sections,[25] only basis sets including diffuse functions are considered (data for smaller basis sets are provided in the Supporting Information). Moreover, without augmented functions, the two considered states could not be found among the 10 available states for some of the considered methods.

Atomic units are used for the reported orientation- and polarization-averaged TPA cross sections using the averaging factor for the linearly polarized light (see ref 58). The conversion to macroscopic units depends on the conditions of the experiment (see the detailed discussion in ref 16). For the double-beam experiment, the macroscopic units for the TPA cross section (σ_{TPA} in 1 GM = 10^{-50}cm^{4}s/photon) are related to TPA cross sections expressed in atomic units (δ_{TPA}) as[16]

$$\sigma_{TPA} = \frac{8\pi^2 \alpha a_0^5 \omega^2}{c\Gamma}\delta_{TPA} \tag{9}$$

where α is the fine structure constant, c is the speed of light, a_0 is the Bohr radius, and Γ is a damping parameter, which can be extracted from the experiment assuming Lorentzian broadening of the absorption band.

4. RESULTS AND DISCUSSION

The results are discussed in the following way. In the first part, the vertical excitation energies, two-photon cross sections, and the corresponding complexation-induced shifts of these quantities are evaluated using conventional methods [ADC(2) and EOM-CCSD] and a series of atomic basis sets of increasing quality. The obtained results are used to discuss their numerical stability and they are used as references for discussing the quality of the approximations used in the considered embedding method. The following section concerns the simplest embedding strategy in which the embedding potential includes only the Coulomb component of the FDET embedding potential (either exact or approximated by PCs). The comprehensive analysis of the performance of the FDET methods is given in the last two subsections.

4.1. Supermolecular Strategy. The principal quantity of interest in the present work is the evaluation of the effect of the environment on a given observable (vertical excitation energy or TPA cross section). Table 1 collects the results obtained by

Table 1. Vertical Excitation Energies ϵ^{isol} (in eV) and the Two-Photon Cross Sections δ_{TPA}^{isol} (in Atomic Units) for the Two Lowest $\pi\pi^*$ Transitions from the Conventional ADC(2) Calculations Applied to the Isolated C_2H_4 and the Corresponding Shifts in the C_2H_4−H_2O Complex[a]

basis set	ϵ^{isol}	$\Delta\epsilon$	δ_{TPA}^{isol}	$\Delta\delta_{TPA}$
		First $\pi\pi^*$ State		
6-31 + G*	8.146(8.283)	−0.062 (−0.057)	0(0)	25.2 (4.6)
aug-cc-pVDZ	7.900(8.043)	−0.094 (−0.081)	0(0)	43.2 (20.1)
aug-cc-pVTZ	7.928(8.029)	−0.060 (−0.061)	0(0)	40.4 (22.2)
aug-cc-pVQZ	7.947[b]	−0.076	0	20.8
d-aug-cc-pVDZ	7.866[b]	−0.088	0	22.3
d-aug-cc-pVTZ	7.914(8.018)	−0.069 (−0.066)	0(0)	23.7 (17.2)
d-aug-cc-pVQZ	7.940	−0.083	0	35.9
		Second $\pi\pi^*$ State		
6-31 + G*	9.075 (9.109)	−0.125 (−0.125)	791.0(745.0)	10.1 (15.6)
aug-cc-pVDZ	8.866 (8.982)	−0.353 (−0.309)	829.5(730.7)	−140.9 (−73.7)
aug-cc-pVTZ	8.788 (8.854)	−0.287 (−0.262)	823.5(763.7)	−87.9 (−45.7)
aug-cc-pVQZ	8.721 (8.760)	−0.247 (−0.231)	817.0(775.5)	−51.6 (−46.1)
d-aug-cc-pVDZ	8.121 (8.336)	−0.181 (−0.182)	774.9(732.2)	−32.9 (−35.2)
d-aug-cc-pVTZ	8.335 (8.461)	−0.182 (−0.182)	724.1(693.7)	−21.0 (−19.5)
d-aug-cc-pVQZ	8.422	−0.184	698.9	−20.7

[a]The EOM-CCSD results (if available) are given in parentheses. [b]The first $\pi\pi^*$ state was not found among the available 10 states in EOM-CCSD calculations.

https://doi.org/10.1021/acs.jctc.1c00204
J. Chem. Theory Comput. 2021, 17, 3652−3665

means of high-quality methods [ADC(2) and EOM-CCSD] using various basis sets. Beyond the d-aug-cc-pVTZ basis sets, the EOM-CCSD calculations are not possible due to the limitations of the available computational resources.

For the first $\pi\pi^*$ state, the ADC(2) excitation energies show a remarkable numerical stability if the augmented basis sets are used (7.90 eV < ϵ^{isol} < 7.95 eV). The complexation-induced shifts of the excitation energy are small in this case and vary even less (−0.060 eV < $\Delta\epsilon$ < −0.094 eV). The EOM-CCSD excitation energies evaluated using the same basis sets (if available) are systematically slightly larger but the shifts are practically equivalent to the ADC(2) ones. TPA cross sections show, however, different trends. For the complex, they depend critically on the used basis sets. Even for the largest two basis sets, the TPA cross sections differ significantly (23.7 vs 35.9 atomic units). These difficulties in converging the TPA cross sections are in line with the results reported by Nielsen et al.,[25] where it was found that even for such a small molecule as H_2O, it is difficult to obtain numerically stable TPA cross sections for all considered excited states. One of the possible explanations for a large jump in the TPA shift for this excitation might originate from the fact that there is absence of any error compensation. For the first $\pi\pi^*$ state of the isolated chromophore, the TPA activity is symmetry forbidden. Any method yields the correct exact result ($\delta^{\text{isol}}_{\text{TPA}} = 0$), which is not the case of the complex. Note that for the second $\pi\pi^*$, for which the TPA activity is symmetry-allowed for both the isolated chromophore and the complex, $\delta^{\text{isol}}_{\text{TPA}}$ changes from 724.1 to 698.9 atomic units if the basis set changes from d-aug-cc-pVTZ to d-aug-cc-pVQZ but the shift changes by only 0.3 atomic units.

For the second $\pi\pi^*$ state, the TPA cross section shifts evaluated using the two largest basis sets (d-aug-cc-pVTZ and d-aug-cc-pVQZ) and EOM-CCSD and ADC(2) methods vary within a narrow range (from −19.5 to −21.0 atomic units). Such accuracy involves, however, significant computational costs. The numerical values: $\Delta\epsilon^{\text{second }\pi\pi*} = -0.184$ eV and $\Delta\delta^{\text{second }\pi\pi*}_{\text{TPA}} = -20.7$ atomic units represent ideal targets for embedding methods. The effect of the environment is noticeable and significantly larger than the scatter of the shifts obtained with the largest considered basis sets and the two correlated methods. Using such a big basis set does not assure similar confidence level for the first $\pi\pi^*$ state. At d-aug-cc-pVTZ, EOM-CCSD and ADC(2) shifts agree quite well (17.2 vs 23.7 atomic units). Unfortunately, the further increase of the basis set to d-aug-cc-pVQZ increases the ADC(2)-derived shift from 23.7 to 35.9 atomic units. It is worthwhile to notice that the conventional counterpoise technique to account for the incompleteness of the basis sets[36,59] does not reduce this difference (see Supporting Information). Reaching accuracy of the shifts below 10 atomic units seems, therefore, to be out of reach for routine calculations using high-quality correlated methods applied within the supermolecular strategy. The 10 atomic unit accuracy threshold is probably not needed for interpretation of the experimental data on TPA activities in most cases. In the case of the second $\pi\pi^*$ state, which is symmetry-allowed in the isolated chromophore, the absolute TPA cross section is about 30 times larger than the shift itself. We target such a high accuracy for the identification of the key factors determining the effect of environment on the TPA activities. The shifts are actually equal to the absolute TPA cross sections if the transition is symmetry-forbidden in the isolated chromophore. Moreover, such accuracy is indispensable for the sake of identification of the source of errors in the used FDET-based method. The subsequent sections concern the accuracy and numerical stability of the shifts obtained from embedding methods.

4.2. Vertical Excitation Energies and TPA Cross Sections from Exact Coulomb- and PC-Embedding Potentials. In these cases, the embedding potential comprises only the classical electric potential generated by the continuous or discrete charge distribution. The quantum-mechanical effects on the embedded wave function, which are represented by means of the potential $v^{\text{nad}}_{\text{xct}}[\rho_A, \rho_B](\mathbf{r})$ in FDET, are neglected entirely. Usually, the electrostatic potential is not evaluated from the charge density but using simpler methods: from atomic net charges and from multicenter multipole expansion (including electronic polarizability or not), for instance. In continuum methods, it comprises also contributions from the reaction field. If the exact charge densities are used for this purpose, the electrostatic potential is given as:

$$v^{\text{FDET}}_{\text{emb}}[\rho_A, \rho_B; v_B](\mathbf{r}) \approx v^{\text{exactCoulomb}}_{\text{emb}}(\mathbf{r}) \quad (\rho_A\text{-independent}) \tag{10}$$

where

$$v^{\text{exactCoulomb}}_{\text{emb}}(\mathbf{r}) = v_B(\mathbf{r}) + \int \frac{\rho_B(\mathbf{r}')}{|\mathbf{r} - \mathbf{r}'|}\, d\mathbf{r}' = \sum_B \frac{Z_B}{|\mathbf{r} - R_B|} + \int \frac{\rho_B(\mathbf{r}')}{|\mathbf{r} - \mathbf{r}'|}\, d\mathbf{r}'$$

In PC embedding methods, this potential is simplified further

$$v^{\text{FDET}}_{\text{emb}}[\rho_A, \rho_B; v_B](\mathbf{r}) \approx v^{\text{PC}}_{\text{emb}}(\mathbf{r}) = \sum_B \frac{q^{\text{net}}_B}{|\mathbf{r} - R_B|} \quad (\rho_A\text{-independent}) \tag{11}$$

$v^{\text{PC}}_{\text{emb}}(\mathbf{r})$ is the simplest embedding approximation applied frequently in multilevel simulations. It is an approximation to $v^{\text{exactCoulomb}}_{\text{emb}}(\mathbf{r})$. The net charges ($q_H$ and q_O) used in this work are derived from the electrostatic potential generated by $\rho^{\text{isol}}_B(\mathbf{r})$ by means of the CHELPG method.[60] The net charges are given in the Supporting Information. The potentials $v^{\text{exactCoulomb}}_{\text{emb}}(\mathbf{r})$ and $v^{\text{PC}}_{\text{emb}}(\mathbf{r})$ coincide in the long-range limit but differ qualitatively near the nuclei of the environment. This qualitative difference is responsible for the numerical instability of the results obtained using $v^{\text{exactCoulomb}}_{\text{emb}}(\mathbf{r})$ and such basis sets, which extend to the environment.[61,62] In both eqs 10 and 11 cases, the ME is used. We underline that the ME is invariably linked to the Coulomb embedding (exact or simplified using PC embedding) if used in multilevel simulations. Whereas exact Coulomb embedding is considered in the present work to address directly the effect of $v^{\text{nad}}_{\text{xct}}[\rho_A, \rho_B](\mathbf{r})$ on the embedded wave function, PC embedding is considered for reasons of practical nature. $v^{\text{PC}}_{\text{emb}}(\mathbf{r})$ is much simpler to evaluate than the FDET embedding potential. Numerous studies and applications showed its usefulness for simulating environment effects on OPA properties. It is worthwhile to investigate in detail how $v^{\text{PC}}_{\text{emb}}(\mathbf{r})$ performs for properties, which require using correlated wave function-based methods combined with large basis sets on properties depending on the quality of more than two electronic states. Although indirectly, PC embedding also includes the non-Coulombic effects on the wave function. Reducing the continuous distribution of charge to just one

https://doi.org/10.1021/acs.jctc.1c00204
J. Chem. Theory Comput. 2021, 17, 3652−3665

negative charge on the nucleus leads to almost perfect screening of the attractive potential due to the nuclear charge. As a result, a collapse of the embedded wave function onto the nucleus localized in the environment is hindered to some extent. In FDET, $v_{xct}^{nad}[\rho_A, \rho_B](\mathbf{r})$ assures that not only such collapse is avoided but assures that the corresponding expression for the total energy is consistent with the Hohenberg−Kohn theorem. Unfortunately, in the applied method, $v_{xct}^{nad}[\rho_A, \rho_B](\mathbf{r})$ is approximated. It is not known a priori, how these two ways treating non-Coulombic effects deal with the challenges of predicting the environment effect on TPA properties.

The complexation-induced shifts of the vertical excitation energies are shown in Table 2. The shifts obtained from eq 10 reproduce fairly the reference values for each basis set except the largest one (d-aug-cc-pVQZ for which the embedding calculation applying $v_{emb}^{exactCoulomb}(\mathbf{r})$ leads to a large number of excited states but none of the $\pi\pi^*$ character, see Supporting Information for some example states). The deviations from the reference are small compared to the magnitude of the shifts (the relative errors in the 4−32% range). This indicates a spurious feature resulting from the neglect of nonclassical effects in $v_{emb}^{exactCoulomb}(\mathbf{r})$ (see the subsequent section). In almost all remaining cases, $v_{emb}^{exactCoulomb}(\mathbf{r})$ leads to the shifts approximating better than $v_{emb}^{PC}(\mathbf{r})$ compared to the reference shifts.

Table 2. Complexation-Induced Shifts of the Vertical Excitation Energy ($\Delta\epsilon$, in eV) from Embedded ADC(2) Calculations Using Different Embedding Potentials Evaluated with $\rho_B(\mathbf{r}) = \rho_B^{isolH_2O}(\mathbf{r})$: Exact Coulomb Embedding (eq 10), PC Embedding (eq 11), and Linearized FDET Embedding (eq 2)

basis set	$\Delta\epsilon^{emb}$ (eq 11)	$\Delta\epsilon^{emb}$ (eq 10)	$\Delta\epsilon^{emb}$ (eq 2)
	First $\pi\pi^*$ State		
6-31 + G*	−0.052	−0.077	−0.084
aug-cc-pVDZ	−0.050	−0.063	−0.065
aug-cc-pVTZ	−0.065	−0.056	−0.065
aug-cc-pVQZ	−0.055	−0.070	−0.063
d-aug-cc-pVDZ	−0.047	−0.084	−0.117
d-aug-cc-pVTZ	−0.039	−0.055	−0.096
d-aug-cc-pVQZ	−0.072	−[a]	−0.087
ADC(2)/d-aug-cc-pVQZ reference		$\Delta\epsilon^{ADC} = -0.083$	
EOM-CCSD/d-aug-cc-pVTZ reference		$\Delta\epsilon^{CCSD} = -0.066$	
	Second $\pi\pi^*$ State		
6-31 + G*	−0.077	−0.109	−0.121
aug-cc-pVDZ	−0.080	−0.095	−0.132
aug-cc-pVTZ	−0.091	−0.108	−0.150
aug-cc-pVQZ	−0.099	−0.120	−0.165
d-aug-cc-pVDZ	−0.114	−0.151	−0.183
d-aug-cc-pVTZ	−0.117	−0.160	−0.199
d-aug-cc-pVQZ	−0.119	−[a]	−0.207
ADC(2)/d-aug-cc-pVQZ reference		$\Delta\epsilon^{ADC} = -0.184$	
EOM-CCSD/d-aug-cc-pVTZ reference		$\Delta\epsilon^{CCSD} = -0.182$	

[a]No $\pi\pi^*$ states were found among the available 10 states obtained with this potential.

The shifts in the TPA cross sections obtained using the exact Coulomb- and PC-embedding methods and different basis sets are collected in Table 3 showing a failure of the exact Coulomb embedding for simulating this property. In contrast to what happened for excitation energies, where exact Coulomb embedding led to the improvement compared to the PC embedding in almost all cases, the calculated TPA cross sections are erratic. The need including non-Coulombic effects on the embedded wave function in order to reach numerically stable TPA cross sections has long been recognized in the literature (see the recent overview in ref 32, for instance). In FDET, it is made through the $v_{xct}^{nad}[\rho_A, \rho_B](\mathbf{r})$ component of the embedding potential. The shifts obtained from the PC embedding are less erratic and agree well with the reference $\Delta\delta_{TPA}$ for the first $\pi\pi^*$ state. The shift is, however, significantly underestimated for the second $\pi\pi^*$ state. Before moving to the next section reporting the FDET results, it is useful to analyze the origin of reported erratic TPA cross sections obtained by the exact Coulomb embedding in more detail. To this end, the natural transition orbitals[63] for the two simplified embedding approximations are shown in Figure 3 together with the reference natural transition orbital. The reference hole natural transition orbital and its embedding counterparts obtained using the embedding potential given in either eqs 10 or 11 are very similar. The particle natural transition orbitals obtained with the two embedding potential feature, however, qualitative differences. Equation 10 leads to a spurious lobe on the top of the chromophore present in neither the supermolecular reference nor in the eq 11 embedding cases. Near the C−C bond, the reference particle natural transition orbital and both orbitals obtained by means of electrostatic embedding differ by being principally localized on only one carbon atom (see Figure 3).

Table 3. Complexation-Induced Shifts of the TPA Cross Section ($\Delta\delta_{TPA}$, in Atomic Units) from Embedded ADC(2) Calculations Using Different Embedding Potentials Evaluated with $\rho_B(\mathbf{r}) = \rho_B^{isolH_2O}(\mathbf{r})$: Exact Coulomb Embedding (eq 10), PC Embedding (eq 11), and Linearized FDET Embedding (eq 2)

basis set	$\Delta\delta_{TPA}^{emb}$ (eq 11)	$\Delta\delta_{TPA}^{emb}$ (eq 10)	$\Delta\delta_{TPA}^{emb}$ (eq 2)
	First $\pi\pi^*$ State		
6-31+G*	26.2	3.9	12.7
aug-cc-pVDZ	9.1	3.1	19.2
aug-cc-pVTZ	48.4	6.9	10.1
aug-cc-pVQZ	17.1	5.3	13.7
d-aug-cc-pVDZ	35.7	45.4	81.5
d-aug-cc-pVTZ	32.1	62.1	36.7
d-aug-cc-pVQZ	43.9	−[a]	24.1
ADC(2)/d-aug-cc-pVQZ reference		$\Delta\delta_{TPA}^{ADC} = 35.9$	
EOM-CCSD/d-aug-cc-pVTZ reference		$\Delta\delta_{TPA}^{CCSD} = 17.2$	
	Second $\pi\pi^*$ State		
6-31 + G*	8.8	11.5	22.5
aug-cc-pVDZ	−0.6	109.3	−62.0
aug-cc-pVTZ	17.0	85493.2	35.0
aug-cc-pVQZ	8.9	−42.0	−121.8
d-aug-cc-pVDZ	−21.5	32.6	−82.9
d-aug-cc-pVTZ	−8.0	−140.8	−25.6
d-aug-cc-pVQZ	−6.0	−[a]	−23.2
ADC(2)/d-aug-cc-pVQZ reference		$\Delta\delta_{TPA}^{ADC} = -20.7$	
EOM-CCSD/d-aug-cc-pVTZ reference		$\Delta\delta_{TPA}^{CCSD} = -19.5$	

[a]No $\pi\pi^*$ states were found among the available 10 states obtained with this potential.

https://doi.org/10.1021/acs.jctc.1c00204
J. Chem. Theory Comput. 2021, 17, 3652−3665

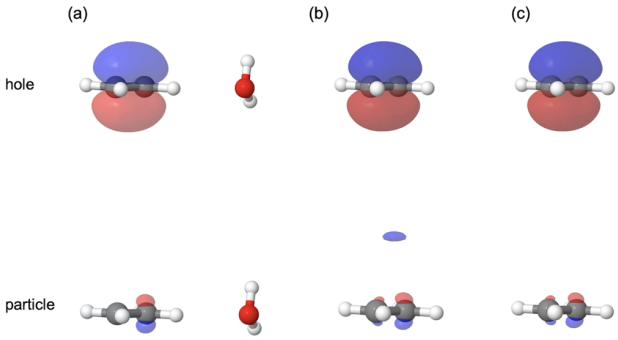

Figure 3. Natural transition orbitals of the second $\pi\pi^*$ state calculated using the aug-cc-pVDZ basis set in different methods—the reference ADC(2) supermolecular calculations (a) and embedding calculations with the embedding potential given in either eq 10 (b) or eq 11 (c). The cutoff was chosen to be 0.05 (in atomic units) in all cases.

4.3. Vertical Excitation Energies and TPA Cross Sections from Linearized FDET. The results collected in the previous section show clearly that the neglecting non-Coulombic effects in the embedding potential, although commonly used in multiscale simulations of OPA properties of embedded chromophores cannot be used for reliable prediction of TPA properties. In terms of intermolecular interaction theory such as SAPT,[64] in which the wave function of the environment is available, the antisymmetrization operator is missing. In terms of FDET, the numerical instability of the TPA cross sections originates from neglecting the nonelectrostatic component of the FDET embedding potential $v_{\mathrm{xct}}^{\mathrm{nad}}[\rho_A,\rho_B](\mathbf{r})$. In the FDET-based method used here, $v_{\mathrm{xct}}^{\mathrm{nad}}[\rho_A,\rho_B](\mathbf{r})$ is not treated exactly but it is approximated by means of a simple analytic formula. This approximation can lead to errors in the obtained properties as compared to reference supermolecular calculations. The deviations from the reference can arise also from the used $\rho_B(\mathbf{r})$. From the practical perspective, it is useful to explore also the applicability of the ME, which (if applied) is the third factor contributing to the deviations from the reference results. The subsequent parts address these three sources of errors in detail.

4.3.1. Simplest FDET Protocol: ME and $\rho_B(\mathbf{r})$ from the Isolated H_2O Molecule. In this protocol, the embedding potential is given by the bifunctional depending on $\rho_A(\mathbf{r})$ and $\rho_B(\mathbf{r})$ given in eq 2, but evaluated at $\rho_B(\mathbf{r}) = \rho_B^{\mathrm{isol}}(\mathbf{r})$

$$v_{\mathrm{emb}}^{\mathrm{FDET}}[\rho_A^{\mathrm{ref}}, \rho_B^{\mathrm{isol}}; v_B](\mathbf{r}) \approx v_B(\mathbf{r}) + \int \frac{\rho_B^{\mathrm{isol}}(\mathbf{r}')}{|\mathbf{r}-\mathbf{r}'|}\,\mathrm{d}\mathbf{r}' + \tilde{v}_{\mathrm{xct}}^{\mathrm{nad(LDA)}}[\rho_A, \rho_B^{\mathrm{isol}}](\mathbf{r}) \quad (12)$$

This choice of $\rho_B(\mathbf{r})$ was made previously used for a large class of embedded chromophores, where it was shown to yield very small deviations from the reference shifts obtained from the corresponding supermolecular calculations.[41]

For all considered basis sets, the FDET shifts of the excitation energies agree very well with the corresponding supermolecular counterparts (see Tables 1 and 2 column 3). The deviations do not exceed 0.03 eV.

Neglecting the $v_{\mathrm{xct}}^{\mathrm{nad}}[\rho_A,\rho_B](\mathbf{r})$ component of the FDET embedding potential worsens the shifts. For the largest basis set, neglecting this component leads to several spurious states none of them with the $\pi\pi^*$ character.

The complexation-induced shifts of the TPA cross section obtained from FDET show a stronger dependency on the basis set as their reference counterparts (see Tables 1 and 3 column 3). For the largest basis sets (double augmented), the FDET shifts approach monotonically the d-aug-cc-pVQZ limits. For the second $\pi\pi^*$ state, this limit agrees remarkably with its reference counterpart (−23.2 vs −20.7 atomic units). For this state, the reference ADC(2) shifts obtained using augmented basis sets behave monotonically. The above result convergence of the shifts obtained from FDET and supermolecular strategies is especially significant taking into account that the shifts obtained in EOM-CCSD calculations and the largest used basis set (d-aug-cc-pVTZ) is very similar (−19.5 atomic units).

For the first $\pi\pi^*$ state, however, the reference shifts do not behave monotonically and a jump from 23.7 to 35.9 atomic units occurs if the basis set increases from d-aug-cc-pVTZ to d-aug-cc-pVQZ. The corresponding FDET shifts are 36.7 atomic units and 24.1 atomic units. Using the Coulomb embedding potential given in eq 11, in which $v_{\mathrm{xct}}^{\mathrm{nad}}[\rho_A,\rho_B](\mathbf{r})$ is also neglected, whereas the exact Coulomb component is approximated by the potential due to the net atomic charge, brings the shifts closer to both FDET and reference values. Compared to the reference shifts, the FDET results are slightly (the first $\pi\pi^*$ state) or noticeably (the second $\pi\pi^*$ state) superior to the ones obtained using the PC embedding.

Neglecting $v_{\mathrm{xct}}^{\mathrm{nad}}[\rho_A,\rho_B](\mathbf{r})$ (embedding potential given in eq 10) results in several spurious states leading to meaningless TPA cross sections at the photon frequency corresponding to the second $\pi\pi^*$ state. For this state, the PC embedding also fails but less dramatically.

Figure 4 shows the effect of addition of $v_{\mathrm{xct}}^{\mathrm{nad}}[\rho_A,\rho_B](\mathbf{r})$ on the particle natural transition orbital. For a full embedding potential, in which $v_{\mathrm{xct}}^{\mathrm{nad}}[\rho_A,\rho_B](\mathbf{r})$ is included, the electron density is well localized around the chromophore and resembles closely to the corresponding orbital obtained in the reference calculations (see also Figure 3). If this term is neglected (embedding potential given in eq 10), the electron density is more likely to be attracted by the nuclei of H_2O going through the slit in Figure 4b. The repulsion part (blue) of the embedding potential in Figure 4a is more dark than in Figure 4b.

Concerning the complexation-induced shifts of TPA cross sections, going beyond Coulomb embedding is indispensable. The results obtained with neglected $v_{\mathrm{xct}}^{\mathrm{nad}}[\rho_A,\rho_B](\mathbf{r})$ (exact Coulomb embedding) are erratic if the basis set changes. The shifts obtained using the other two embedding potentials (PC embedding and FDET embedding) are also strongly basis set dependent but agree within 13 atomic units for the two largest basis sets. The magnitude of the effect of going from d-aug-cc-pVTZ to d-aug-cc-pVQZ is about the same in reference ADC(2) and in the two embedding methods (PC embedding and FDET embedding): 12.2, 11.8, and 12.6 atomic units, respectively, for the first $\pi\pi^*$ state. For the second $\pi\pi^*$ state, the corresponding values are 0.3, 2.0, and 2.4 atomic units. For the first $\pi\pi^*$ state and the largest basis sets, both PC- and FDET-embedding deviate from the ADC(2) reference by about the same amount (8 atomic units and 11.8 atomic units). For the second state, the FDET and ADC(2) reference values agree within 2.5 atomic units and the PC embedding significantly underestimates the reference shift (−6.0 vs −20.7 atomic units). Interestingly, the results obtained with

https://doi.org/10.1021/acs.jctc.1c00204
J. Chem. Theory Comput. 2021, 17, 3652−3665

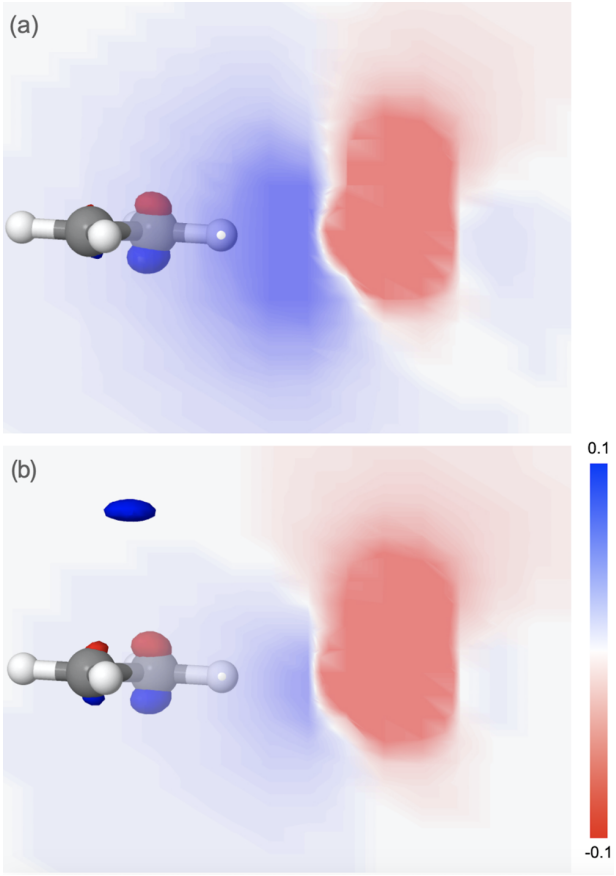

Figure 4. Particle natural transition orbital and the corresponding embedding potential for the second $\pi\pi^*$ state obtained by eq 12 (a) or FDET embedding potential with the neglected $v_{xct}^{nad}[\rho_A, \rho_B](\mathbf{r})$ component (b) using the aug-cc-pVDZ basis set. For the orbital, the same cutoff of 0.05 (in atomic units) was used.

the largest basis sets for vertical excitation energies show a clear advantage of the FDET over PC embedding in both cases.

The residual deviations between the reference ADC(2)- and "embedded ADC(2)" shifts in the OPA and TPA properties evaluated using the d-aug-cc-pVQZ basis sets and the protocol considered in this section can be attributed to following factors: (i) the incompleteness of the basis set used in the reference ADC calculations; (ii) the incompleteness of the basis set used in the FDET calculations; (iii) the choice made for $\rho_B(\mathbf{r})$, i.e., $\rho_B(\mathbf{r}) = \rho_B^{isol}(\mathbf{r})$, which might lead to the inequality

$$E_{v_{AB}}^{HK}[\rho^I] = E_{v_{AB}}^{I} \leq E_{v_{AB}}^{FDET(I)}[\Psi_A^I, \rho_B^{isol}] = E_{v_{AB}}^{HK}[\rho_A^I + \rho_B] \tag{13}$$

where $E_{v_{AB}}^{I}$ is the exact energy of the state I, $E_{v_{AB}}^{FDET}[\Psi_A, \rho_B]$ is the FDET energy functional,[40] and Ψ_A^I is a stationary solution of eq 1; (iv) the used approximation $v_{xct}^{nad}[\rho_A, \rho_B](\mathbf{r}) \approx \tilde{v}_{xct}^{nad}[\rho_A, \rho_B](\mathbf{r})$.

Concerning the third factor (point iii), the quality of both sides of eq 13 is assured only if $\rho_B(\mathbf{r})$ satisfies the condition

$$\forall_r \, \rho_{v_{AB}}^{I}(\mathbf{r}) \geq \rho_B(\mathbf{r}) \tag{14}$$

which cannot be determined a priori. The equality on the left-hand side of eq 13 is assured by the Levy–Perdew theorem on extrema of the Hohenberg–Kohn functional,[45] whereas the equality on the right-hand side by construction of the FDET energy functional.[40] In the case of the linearized FDET, the equality holds only up to the quadratic terms in the density difference between ground and excited states. FDET can, therefore, provide only the upper estimate of the energy of each state. It is worthwhile to notice that the difference of energy in the two states might be exact even if the condition given in eq 14 is violated for two states. Because the effect on the total energy for a given state due to the chosen $\rho_B(\mathbf{r})$ is non-negative by construction, a partial compensation of errors occurs always if energy difference is evaluated. This explains a very small error in the excitation energies obtained using the same approximations as the ones used in the present work in a benchmark set of embedded chromophores[50] even if the effect of interactions with the chromophore is not taken into account explicitly in $\rho_B(\mathbf{r})$.

The third factor (point iii) has some relation to the effect known in embedding methods based on the intermolecular interaction theories or energy decomposition schemes as the effect of electronic polarization of the environment.[31,32] In FDET, it can be modeled explicitly by means of the state-specific optimization of $\rho_B(\mathbf{r})$.[65] Keeping the same $\rho_B(\mathbf{r})$ for different states has this advantage that combined with linearized FDET leads to a set of orthogonal wave functions, which can be used in the response theory in a straightforward manner. The differential polarization of the environment is treated implicitly in FDET even if each embedded wave function for different states is obtained using the same $\rho_B(\mathbf{r})$ for each state.[57] If the ME is used, the total density can be different for different states only in the $\rho_A - \rho_B$ overlap region. If the supermolecular expansion is used, the total density can be different anywhere.

Concerning the fourth factor (point *iv*), it is impossible in practice to disentangle the effect on the calculated shift due to $v_{xct}^{nad}[\rho_A, \rho_B](\mathbf{r}) \approx \tilde{v}_{xct}^{nad}[\rho_A, \rho_B](\mathbf{r})$ and due to the choice of $\rho_B(\mathbf{r})$. In FDET, that is, for the exact $v_{xct}^{nad}[\rho_A, \rho_B](\mathbf{r})$, the infinite number of choices for $\rho_B(\mathbf{r})$ leads to the same exact total energy of a given state. The sufficient condition is the satisfaction of the inequality given in eq 14 by the used $\rho_B(\mathbf{r})$. If $v_{xct}^{nad}[\rho_A, \rho_B](\mathbf{r})$ is approximated, even if this condition is satisfied, the calculated energy is not exact and depends on $\rho_B(\mathbf{r})$. The two effects combine.

In the subsequent section, two refined protocols are used to estimate the combined effect of these two factors and to investigate the dependence of the FDET results on the choice made for $\rho_B(\mathbf{r})$.

4.3.2. Refined Treatments of $\rho_A(\mathbf{r})$ and $\rho_B(\mathbf{r})$ in FDET. In the first refined FDET model, the complexation-induced shifts of OPA or TPA properties are evaluated using the same functional for the ρ_A-dependent embedding potential given in eq 2 but evaluated at the freeze-and-thaw optimized $\rho_B(\mathbf{r})$

$$v_{emb}^{FDET}[\rho_A^{FAT}, \rho_B^{FAT}; v_B](\mathbf{r}) \approx v_B(\mathbf{r}) + \int \frac{\rho_B^{FAT}(\mathbf{r}')}{|\mathbf{r} - \mathbf{r}'|} d\mathbf{r}' + \tilde{v}_{xct}^{nad(LDA)}[\rho_A^{FAT}, \rho_B^{FAT}](\mathbf{r}) \tag{15}$$

The excited states are still evaluated at the same $\rho_B(\mathbf{r})$, which is optimized in the ground-state minimization of the total energy functional for a given approximation to $v_{xct}^{nad}[\rho_A, \rho_B](\mathbf{r})$.

The other refinement consists of using the supermolecular expansion (eqs 5 and 6) for both $\rho_A(\mathbf{r})$ and $\rho_B(\mathbf{r})$. The

https://doi.org/10.1021/acs.jctc.1c00204
J. Chem. Theory Comput. 2021, 17, 3652–3665

supermolecular expansion makes it possible to take into account the differential polarization of the total density not only in the overlap region but in the whole space. Using the basis sets centered on all atoms in the system allows detecting the flaws of the used approximation for $v_{xct}^{nad}[\rho_A, \rho_B](\mathbf{r})$. The optimized density $\rho_B(\mathbf{r})$ minimizes not the exact FDET energy functional but the approximated ones. On the other hand, supermolecular expansion might be used as an ultimate verifications of the numerical stability of the results as far as the completeness of the basis set is concerned for the used approximation to $v_{xct}^{nad}[\rho_A, \rho_B](\mathbf{r})$.

As a consequence of the variational character of FDET, these refinements [optimization of $\rho_B(\mathbf{r})$ or adding more basis set functions] can only lower the total energy at each state for a given approximation to $\rho_B(\mathbf{r})$. For vertical excitations, therefore, the effect of these refinements on excitation energies can be both positive, negative, or cancel completely.

We start with the analysis of the complexation-induced shifts of the excitation energies collected in Table 4 obtained using

Table 4. Complexation-Induced Shifts of the Vertical Excitation Energy ($\Delta\epsilon$, in eV) from Embedded ADC(2) Calculations Using the Linearized FDET Embedding Potential (eq 2) Evaluated at Different $\rho_B(\mathbf{r})$: $\rho_B^{isolH_2O}(\mathbf{r})$—Density of the Isolated Water Molecule; $\rho_B^{FAT}(\mathbf{r})$—Freeze-and-Thaw Optimized Density; and $\rho_B^{isol-gh-H_2O}(\mathbf{r})$)—Density of the isolated Water Molecule Represented Using the Supermolecular Basis Set for Both $\rho_A(\mathbf{r})$ and $\rho_B(\mathbf{r})$

basis set	$\Delta\epsilon^{FDET}[\rho_B^{isol-gh-H_2O}]$	$\Delta\epsilon^{FDET}[\rho_B^{FAT}]$	$\Delta\epsilon^{FDET}[\rho_B^{isolH_2O}]$
First $\pi\pi^*$ State			
6-31 + G*	−0.103	−0.087	−0.084
aug-cc-pVDZ	−0.110	−0.070	−0.065
aug-cc-pVTZ	−0.099	−0.068	−0.065
aug-cc-pVQZ	−0.089	−0.066	−0.063
d-aug-cc-pVDZ	−0.137	−0.123	−0.117
d-aug-cc-pVTZ	−0.104	−0.100	−0.096
d-aug-cc-pVQZ	−0.092	−0.090	−0.087
ADC(2)/d-aug-cc-pVQZ reference		$\Delta\epsilon^{ADC}$ = −0.083	
EOM-CCSD/d-aug-cc-pVTZ reference		$\Delta\epsilon^{CCSD}$ = −0.066	
Second $\pi\pi^*$ State			
6-31 + G*	−0.176	−0.125	−0.121
aug-cc-pVDZ	−0.548	−0.139	−0.132
aug-cc-pVTZ	−0.417	−0.156	−0.150
aug-cc-pVQZ	−0.342	−0.171	−0.165
d-aug-cc-pVDZ	−0.190	−0.191	−0.183
d-aug-cc-pVTZ	−0.207	−0.229	−0.199
d-aug-cc-pVQZ	−0.213	−0.215	−0.207
ADC(2)/d-aug-cc-pVQZ reference		$\Delta\epsilon^{ADC}$ = −0.184	
EOM-CCSD/d-aug-cc-pVTZ reference		$\Delta\epsilon^{CCSD}$ = −0.182	

the FDET embedding potential at different choices for $\rho_B(\mathbf{r})$ and different basis sets. Data collected in Table 4 show that these refinements do not improve the shifts. Optimization of $\rho_B(\mathbf{r})$ affects negligibly the shifts of the excitation energies, whereas the supermolecular expansion worsens them significantly especially if smaller basis sets are used. For the largest basis sets used, the shifts obtained by means of the considered three variants of FDET are very similar. This remarkable convergence of the FDET results has its origin in the variational principle and parallels the trends for the interaction energies.[66]

Turning back to TPA cross sections, data collected in Table 5 show that these refinements do not improve the results. The

Table 5. Complexation-Induced Shifts of the TPA Cross Section ($\Delta\delta_{TPA}$, in Atomic Units) from Embedded ADC(2) Calculations Using the FDET Embedding Potential (eq 2) Evaluated at Different $\rho_B(\mathbf{r})$: $\rho_B^{isolH_2O}(\mathbf{r})$—Density of the Isolated Water Molecule; $\rho_B^{FAT}(\mathbf{r})$—Freeze-and-Thaw Optimized Density; and $\rho_B^{isol-gh-H_2O}(\mathbf{r})$)—Density of the Isolated Water Molecule Represented Using the Supermolecular Basis Set for Both $\rho_A(\mathbf{r})$ and $\rho_B(\mathbf{r})$

basis set	$\Delta\delta_{TPA}^{FDET}[\rho_B^{isol-gh-H_2O}]$	$\Delta\delta_{TPA}^{FDET}[\rho_B^{FAT}]$	$\Delta\delta_{TPA}^{FDET}[\rho_B^{isolH_2O}]$
First $\pi\pi^*$ State			
6-31+G*	13.3	11.4	12.7
aug-cc-pVDZ	44.6	11.6	19.2
aug-cc-pVTZ	27.0	9.1	10.1
aug-cc-pVQZ	20.5	12.0	13.7
d-aug-cc-pVDZ	104.9	89.5	81.5
d-aug-cc-pVTZ	43.6	38.8	36.7
d-aug-cc-pVQZ	26.7	24.4	24.1
ADC(2)/d-aug-cc-pVQZ reference		$\Delta\delta_{TPA}^{ADC}$ = 35.9	
EOM-CCSD/d-aug-cc-pVTZ reference		$\Delta\delta_{TPA}^{CCSD}$ = 17.2	
Second $\pi\pi^*$ State			
6-31+G*	13.2	23.9	22.5
aug-cc-pVDZ	−319.4	−119.5	−62.0
aug-cc-pVTZ	−215.8	37.1	35.0
aug-cc-pVQZ	−153.3	−42.6	−121.8
d-aug-cc-pVDZ	−115.4	−89.1	−82.9
d-aug-cc-pVTZ	−40.6	−26.7	−25.6
d-aug-cc-pVQZ	−32.9	−22.3	−23.2
ADC(2)/d-aug-cc-pVQZ reference		$\Delta\delta_{TPA}^{ADC}$ = −20.7	
EOM-CCSD/d-aug-cc-pVTZ reference		$\Delta\delta_{TPA}^{CCSD}$ = −19.5	

optimization of $\rho_B(\mathbf{r})$ affects the TPA cross sections rather negligibly especially for the largest basis sets. The freeze-and-thaw procedure leads to a slight increase of errors in the TPA cross sections for the first $\pi\pi^*$ state especially for smaller basis sets. Supermolecular expansion, on the other hand, affects the TPA cross sections more noticeably leading to unacceptable errors for some basis sets. This, most likely, is due do the used approximation for $v_{xct}^{nad}[\rho_A, \rho_B](\mathbf{r})$. The approximation used for this component of the embedding potential might lead to a change in the order of states of different symmetry. This actually takes place if the d-aug-cc-pVDZ basis set is used. The large discrepancy (82.6 au) between TPA cross sections obtained using the supermolecular expansion and the reference in the first $\pi\pi^*$ state is due to the additional intermediate state located just below the first $\pi\pi^*$ state. As a result, δ_{TPA} increases almost 5 times. The emergence of this additional state affects also the δ_{TPA} for the second $\pi\pi^*$ resulting in also a large discrepancy (82.5 au).

Similar to the trend observed for excitation energy shifts, the differences between the shifts obtained using the three considered FDET protocols decrease with the increasing basis set size. For the largest basis set used, shifts obtained by means of the considered three variants of FDET approach each other closely for both states, thus showing great numerical robustness of FDET.

From the practical perspective, the comparison of the results (complexation-induced shifts in the excitation energies and in the TPA cross sections in the C_2H_4−H_2O complex) obtained by means of the three considered variants of FDET

https://doi.org/10.1021/acs.jctc.1c00204
J. Chem. Theory Comput. 2021, 17, 3652−3665

calculations provides useful guidelines for setting up a FDET based multiscale simulation. The convergence can be reached by either expanding the size of the basis sets in the ME to include diffuse functions or by including basis functions centered in the environment via the supermolecular expansion. The observed convergence indicates that the first strategy should be rather used if the evaluated property (such as the TPA cross sections) requires a large basis set including diffuse functions. The supermolecular expansion should rather be avoided for evaluating the two-photon activities despite the fact that it provides the implicit way to represent in FDET the effects on the electronic state due to the polarization of the environment by the embedded species.[57] In summary, among the considered three variants of FDET, in which $\rho_B(\mathbf{r})$ is taken from the isolated water evaluated within the ME used also for $\rho_A(\mathbf{r})$ appears as the most robust one. Ground-state optimization of $\rho_B(\mathbf{r})$ negligibly affects the TPA cross section. The supermolecular expansion takes into the full account the effect of state-specific polarization of the electron-density everywhere in space but also makes the different stationary states prone to different errors due to the used approximation for $v_{xct}^{nad}[\rho_A,\rho_B](\mathbf{r})$ and is not systematically reducing the deviations from the reference.

Finally, we turn back to the relation between the FDET and conventional embedding methods. Table 6 collects the OPA and TPA properties obtained using the simplest variants of two embedding strategies: FDET and PC embedding. Excitation energies are quite well described using the two embedding methods. The relative errors of the PC-embedding-derived excitation energy shifts are almost 3 times larger than the corresponding errors of the FDET shifts. Because ME was used in both cases, the quantum confinement effects are taken into account implicitly. The smaller errors of the FDET shifts are probably due to the implicit treatment of differential polarization of the environment. For TPA cross section shifts, the PC embedding fails for the second $\pi\pi^*$ state. For the first $\pi\pi^*$ state, FDET shifts underestimate the reference value, whereas PC embedding overestimates it. The magnitude of the error in the FDET shift (11.8 atomic units) is actually larger than that obtained using the PC embedding (8.0 atomic units). We recall that for this excitation the reference ADC(2) value might still not be completely converged.

Table 6. Complexation-Induced Shifts of the Vertical Excitation Energy ($\Delta\epsilon$, in eV) and TPA Cross Sections ($\Delta\delta_{TPA}$, in Atomic Units) Obtained Using Different Embedding Methods, the ADC(2) Treatment of Electron−Electron Correlation, and the d-aug-cc-pVQZ Atomic Basis Sets[a]

method	$\Delta\epsilon^{first\pi\pi*}$	$\Delta\epsilon^{second\pi\pi*}$	$\Delta\delta_{TPA}^{first\pi\pi*}$	$\Delta\delta_{TPA}^{second\pi\pi*}$
FDET	−0.087 (+5%)	−0.207 (+12%)	24.1 (−33%)	−23.2 (12%)
PC embedding	−0.072 (−13%)	−0.119 (−35%)	43.9 (+22%)	−6.0 (−71%)
ADC(2) reference	−0.083	−0.184	35.9	−20.7

[a]FDET results are obtained at $\rho_B \equiv \rho^{isolH_2O}$. In PC embedding, the CHELPG charges[60] generated for ρ^{isolH_2O} are used. In embedding calculations, ME (eqs 3 and 4) is used. Relative errors are given in the parentheses.

5. CONCLUSIONS

The present studies demonstrate the limitations of the conventional (supermolecular) strategy for simulating the effect of environment on TPA properties of an embedded chromophore. Unlike in the case of OPA, the high-end ab initio-correlated methods lead to numerically unstable absolute TPA cross sections and their shifts unless large basis sets comprising diffuse functions are used. Even using high-quality correlated methods in the supermolecular strategy and a rather large basis set does guarantee obtaining numerically stable results. For instance, the reference shifts of the TPA cross sections obtained from EOM-CCSD and ADC(2) using d-aug-cc-pVTZ differ from each other by as much as 6.5 atomic units, whereas the change of the basis set from d-aug-cc-pVTZ to d-aug-cc-pVQZ affects the TPA cross section by as much as 12.2 atomic units. The effects of the environment on the TPA cross section of an embedded chromophore of a magnitude smaller than the above values can rather not be expected to be a good target for high-level simulations based on the supermolecular strategy. For systems comprising a typical organic chromophore together with several molecules representing its condensed phase environment, the supermolecular strategy applying such methods is not practical (if not possible at all).

The exploratory study performed for the C_2H_4−H_2O complex shows that the multilevel methods, based on FDET, provide an alternative that is applicable for larger systems. For the largest basis sets, the basic FDET protocol applying only fundamental constants without system-specific parametrization of the embedding potential and the simplest way to generate $\rho_B(\mathbf{r})$ leads to environment-induced shifts in the TPA properties of a good or excellent accuracy: $\Delta\delta_{TPA}^{FDET/ADC}$ = 24.1 versus $\Delta\delta_{TPA}^{ADC}$ = 35.9 atomic units for the first $\pi\pi^*$ state and $\Delta\delta_{TPA}^{FDET/ADC}$ = -23.2 versus $\Delta\delta_{TPA}^{ADC}$ = −20.7 atomic units for the second $\pi\pi^*$ state. The remaining deviations from the reference could be attributed to several factors: (i) the local density approximation for $v_{xct}^{nad}[\rho_A,\rho_B](\mathbf{r})$, (ii) the choice of $\rho_B(\mathbf{r})$ corresponding to the isolated molecule representing the environment, and (iii) the linearization of $E_{xct}^{nad}[\rho_A,\rho_B]$ with the chosen expansion point $\rho_A^{ref}(\mathbf{r})$. Whereas the last factor can be expected to affect the quality of the FDET results negligibly based on its small role in OPA properties, the first two combine and cannot be separated. Improvements of $v_{xct}^{nad}[\rho_A,\rho_B](\mathbf{r})$ will reduce the relative significance of the first factor. The second one, on the other hand, depends very much on a particular system (type of excitation and the character of the chromophore−environment interaction). In view of practical impossibility of disentangling the two factors and surprisingly good results obtained using the applied first-principle-based computational protocol, it can be recommended as the basic protocol providing the proper description of the dominant effects in pair with the conventional supermolecular strategy. The numerical values lie within the range determined by the largest two basis sets applied in the reference supermolecular ADC(2) calculations.

The computational effort in FDET-based calculations is determined by the size of the chromophore rather than that of the environment. The FDET results depend on the choice made for $\rho_B(\mathbf{r})$ but this dependency is rather weak in the studied system. Owing to the $v_{xct}^{nad}[\rho_A,\rho_B](\mathbf{r})$ term, great numerical stability of the FDET shift is achieved especially if the largest basis sets are used. Without this term, the TPA spectrum of excited states becomes meaningless if large basis

https://doi.org/10.1021/acs.jctc.1c00204
J. Chem. Theory Comput. 2021, 17, 3652−3665

sets are used. Worsening the results if the supermolecular basis set is used in FDET indicates, however, that improvement over the used local density approximation for $v_{xct}^{nad}[\rho_A, \rho_B](\mathbf{r})$ is needed to assure a complete numerical stability of the FDET results as far as the finite basis sets are concerned. At the present stage of development of approximations to $v_{xct}^{nad}[\rho_A, \rho_B](\mathbf{r})$, the undesired effects of the deficiencies of this functional can be eliminated by including only basis sets centered on atoms in the chromophore as it is made usually in multilevel simulations.

Good performance of the used approximations in describing the complexation-induced shifts in the TPA cross sections could be expected. Prior to the present studies, it was already established that the magnitude of the errors in the individual excitation energies due to these approximations rarely exceeds 0.05 eV for valence excitations in chromophores weakly bound to the molecules in the environment.[41,67,68]

The used approximation for $v_{xct}^{nad}[\rho_A, \rho_B](\mathbf{r})$ and recommended choice for $\rho_B(\mathbf{r})$ have clearly defined the limits of applicability as far as the amenable systems are concerned. Local or semilocal approximations feature an artificial enhancement of the repulsion between $\rho_A(\mathbf{r})$ and $\rho_B(\mathbf{r})$.[39] As a result, neither choosing the isolated molecule density as $\rho_B(\mathbf{r})$ nor optimizing it could lead to the proper description of the electronic structure of a species covalently bound to the molecules in the environment. For the same reasons, if the excitation involves transfer of the charge between subsystems, these approximations are doomed to fail leaving many interesting systems (see ref 37) out of reach.

Concerning the approximations in FDET applied in this work, we notice that neither electronic polarization of the environment nor intermolecular correlation giving rise to London dispersion forces are taken into account explicitly. Mutual polarization of the interacting molecules is taken into account in FDET implicitly provided that the used basis sets comprise the functions allowing for some overlap between $\rho_A(\mathbf{r})$ and $\rho_B(\mathbf{r})$ even if the used $\rho_B(\mathbf{r})$ is the electron density of the isolated water molecule. The $v_{xct}^{nad}[\rho_A, \rho_B](\mathbf{r})$ component of the FDET embedding potential represents all non-Coulombic effects on the embedded density (and the embedded wave function), including the ones due to the fermion statistics (via its kinetic component) and due to the electron−electron correlation. These two effects behave differently at large separations. Taking into account the former is needed only if the densities $\rho_A(\mathbf{r})$ and $\rho_B(\mathbf{r})$ overlap. Neglecting the kinetic component may lead to spilling the charge density to the environment (and vice versa) and to the enhanced mutual polarization. No such effect has been observed in the largest basis sets used indicating the adequacy of the local-density approximation to $v_{xct}^{nad}[\rho_A, \rho_B](\mathbf{r})$. Concerning the intermolecular correlation effects, semilocal approximations to $v_{xct}^{nad}[\rho_A, \rho_B](\mathbf{r})$ neglect it completely in the absence of the $\rho_A(\mathbf{r})$ and $\rho_B(\mathbf{r})$ overlap.

■ ASSOCIATED CONTENT

Supporting Information

The Supporting Information is available free of charge at https://pubs.acs.org/doi/10.1021/acs.jctc.1c00204.

Cartesian coordinates of the investigated complex; net atomic charges of isolated water molecule derived from the electrostatic potential and different basis sets; vertical excitation energies and TPA cross sections obtained using basis sets not comprising diffuse functions; counterpose-corrected shifts of the vertical excitation energies and TPA cross sections obtained using different basis sets; and examples of natural transition orbitals obtained using exact Coulomb embedding (PDF)

■ AUTHOR INFORMATION

Corresponding Author

Mingxue Fu − *Department of Physical Chemistry, University of Geneva, CH-1211 Genève 4, Switzerland;* Email: Mingxue.Fu@unige.ch

Author

Tomasz A. Wesolowski − *Department of Physical Chemistry, University of Geneva, CH-1211 Genève 4, Switzerland;* orcid.org/0000-0001-5792-4616

Complete contact information is available at: https://pubs.acs.org/10.1021/acs.jctc.1c00204

Notes

The authors declare no competing financial interest.

■ ACKNOWLEDGMENTS

This research was supported by a grant from the Swiss National Science Foundation (grant no. 200020-172532). M.F. thanks Dr. Cristina E.González-Espinoza for all the explanations concerning the TPA code implementations in Q-Chem.

■ REFERENCES

(1) Albota, M.; Beljonne, D.; Brédas, J.-L.; Ehrlich, J. E.; Fu, J.-Y.; Heikal, A. A.; Hess, S. E.; Kogej, T.; Levin, M. D.; Marder, S. R. Design of organic molecules with large two-photon absorption cross sections. *Science* **1998**, *281*, 1653−1656.

(2) Pawlicki, M.; Collins, H. A.; Denning, R. G.; Anderson, H. L. Two-photon absorption and the design of two-photon dyes. *Angew. Chem., Int. Ed.* **2009**, *48*, 3244−3266.

(3) Rumi, M.; Ehrlich, J. E.; Heikal, A. A.; Perry, J. W.; Barlow, S.; Hu, Z.; McCord-Maughon, D.; Parker, T. C.; Röckel, H.; Thayumanavan, S.; Marder, S. R.; Beljonne, D.; Brédas, J.-L. Structure- property relationships for two-photon absorbing chromophores: bis-donor diphenylpolyene and bis (styryl) benzene derivatives. *J. Am. Chem. Soc.* **2000**, *122*, 9500−9510.

(4) Kuzyk, M. G. Fundamental limits on two-photon absorption cross sections. *J. Chem. Phys.* **2003**, *119*, 8327−8334.

(5) Jiang, M.; Gu, X.; Lam, J. W. Y.; Zhang, Y.; Kwok, R. T. K.; Wong, K. S.; Tang, B. Z. Two-photon AIE bio-probe with large Stokes shift for specific imaging of lipid droplets. *Chem. Sci.* **2017**, *8*, 5440−5446.

(6) Woo, H. Y.; Liu, B.; Kohler, B.; Korystov, D.; Mikhailovsky, A.; Bazan, G. C. Solvent effects on the two-photon absorption of distyrylbenzene chromophores. *J. Am. Chem. Soc.* **2005**, *127*, 14721−14729.

(7) Wang, C.-K.; Zhao, K.; Su, Y.; Ren, Y.; Zhao, X.; Luo, Y. Solvent effects on the electronic structure of a newly synthesized two-photon polymerization initiator. *J. Chem. Phys.* **2003**, *119*, 1208−1213.

(8) Frediani, L.; Rinkevicius, Z.; Ågren, H. Two-photon absorption in solution by means of time-dependent density-functional theory and the polarizable continuum model. *J. Chem. Phys.* **2005**, *122*, 244104.

(9) Milojevich, C. B.; Silverstein, D. W.; Jensen, L.; Camden, J. P. Probing two-photon properties of molecules: Large non-Condon effects dominate the resonance hyper-Raman scattering of rhodamine 6g. *J. Am. Chem. Soc.* **2011**, *133*, 14590−14592.

(10) Casida, M. E. In *Recent Advances in Computational Chemistry, Part 1*; Chong, D. P., Ed.; World Scientific: Singapore, 1995; Vol. I, pp 155−192.
(11) Sałek, P.; Vahtras, O.; Helgaker, T.; Ågren, H. Density-functional theory of linear and nonlinear time-dependent molecular properties. *J. Chem. Phys.* **2002**, *117*, 9630−9645.
(12) Sałek, P.; Vahtras, O.; Guo, J.; Luo, Y.; Helgaker, T.; Ågren, H. Calculations of two-photon absorption cross sections by means of density-functional theory. *Chem. Phys. Lett.* **2003**, *374*, 446−452.
(13) Peach, M. J. G.; Benfield, P.; Helgaker, T.; Tozer, D. J. Excitation energies in density functional theory: An evaluation and a diagnostic test. *J. Chem. Phys.* **2008**, *128*, 044118.
(14) Yanai, T.; Tew, D. P.; Handy, N. C. A new hybrid exchange−correlation functional using the Coulomb-attenuating method (CAM-B3LYP). *Chem. Phys. Lett.* **2004**, *393*, 51−57.
(15) Nayyar, I. H.; Masunov, A. E.; Tretiak, S. Comparison of TD-DFT methods for the calculation of two-photon absorption spectra of oligophenylvinylenes. *J. Phys. Chem. C* **2013**, *117*, 18170−18189.
(16) Beerepoot, M. T. P.; Friese, D. H.; List, N. H.; Kongsted, J.; Ruud, K. Benchmarking two-photon absorption cross sections: performance of CC2 and CAM-B3LYP. *Phys. Chem. Chem. Phys.* **2015**, *17*, 19306−19314.
(17) Beerepoot, M. T. P.; Alam, M. M.; Bednarska, J.; Bartkowiak, W.; Ruud, K.; Zaleśny, R. Benchmarking the performance of exchange-correlation functionals for predicting two-photon absorption strengths. *J. Chem. Theory Comput.* **2018**, *14*, 3677−3685.
(18) Cronstrand, P.; Luo, Y.; Ågren, H. Generalized few-state models for two-photon absorption of conjugated molecules. *Chem. Phys. Lett.* **2002**, *352*, 262−269.
(19) Wang, C.-K.; Macak, P.; Luo, Y.; Ågren, H. Effects of π centers and symmetry on two-photon absorption cross sections of organic chromophores. *J. Chem. Phys.* **2001**, *114*, 9813−9820.
(20) Kishi, R.; Nakano, M.; Yamada, S.; Kamada, K.; Ohta, K.; Nitta, T.; Yamaguchi, K. Structure−property relation in two-photon absorption for symmetric molecules involving diacetylene π-conjugated bridge. *Chem. Phys. Lett.* **2004**, *393*, 437−441.
(21) Hohlneicher, G.; Dick, B. Two-photon spectroscopy of dipole-forbidden transitions. II. Calculation of two-photon cross sections by the CNDO−CI method. *J. Chem. Phys.* **1979**, *70*, 5427−5437.
(22) Shuai, Z.; Beljonne, D.; Brédas, J. L. Nonlinear optical processes in short polyenes: Configuration interaction description of two-photon absorption and third-harmonic generation. *J. Chem. Phys.* **1992**, *97*, 1132−1137.
(23) Ohta, K.; Kamada, K. Theoretical investigation of two-photon absorption allowed excited states in symmetrically substituted diacetylenes by ab initio molecular-orbital method. *J. Chem. Phys.* **2006**, *124*, 124303.
(24) Moccia, R.; Rizzo, A. Two-photon transition probability calculations: electronic transitions in the water molecule. *J. Phys. B: At. Mol. Phys.* **1985**, *18*, 3319.
(25) Nielsen, C. B.; Rettrup, S.; Sauer, S. P. A. Two-photon absorption cross sections: An investigation of the accuracy of calculated absolute and relative values. *J. Chem. Phys.* **2006**, *124*, 114108.
(26) Paterson, M. J.; Christiansen, O.; Pawłowski, F.; Jørgensen, P.; Hättig, C.; Helgaker, T.; Sałek, P. Benchmarking two-photon absorption with CC3 quadratic response theory, and comparison with density-functional response theory. *J. Chem. Phys.* **2006**, *124*, 054322.
(27) Knippenberg, S.; Rehn, D. R.; Wormit, M.; Starcke, J. H.; Rusakova, I. L.; Trofimov, A. B.; Dreuw, A. Calculations of nonlinear response properties using the intermediate state representation and the algebraic-diagrammatic construction polarization propagator approach: Two-photon absorption spectra. *J. Chem. Phys.* **2012**, *136*, 064107.
(28) Nanda, K. D.; Krylov, A. I. Two-photon absorption cross sections within equation-of-motion coupled-cluster formalism using resolution-of-the-identity and Cholesky decomposition representations: Theory, implementation, and benchmarks. *J. Chem. Phys.* **2015**, *142*, 064118.
(29) Woon, D. E.; Dunning, T. H., Jr Gaussian basis sets for use in correlated molecular calculations. V. Core-valence basis sets for boron through neon. *J. Chem. Phys.* **1995**, *103*, 4572−4585.
(30) Rassolov, V. A.; Ratner, M. A.; Pople, J. A.; Redfern, P. C.; Curtiss, L. A. 6-31G* basis set for third-row atoms. *J. Comput. Chem.* **2001**, *22*, 976−984.
(31) Nanda, K. D.; Krylov, A. I. The effect of polarizable environment on two-photon absorption cross sections characterized by the equation-of-motion coupled-cluster singles and doubles method combined with the effective fragment potential approach. *J. Chem. Phys.* **2018**, *149*, 164109.
(32) Reinholdt, P.; Jørgensen, F. K.; Kongsted, J.; Olsen, J. M. H. Polarizable Density Embedding for Large Biomolecular Systems. *J. Chem. Theory Comput.* **2020**, *16*, 5999−6006.
(33) Steindal, A. H.; Beerepoot, M. T. P.; Ringholm, M.; List, N. H.; Ruud, K.; Kongsted, J.; Olsen, J. M. H. Open-ended response theory with polarizable embedding: multiphoton absorption in biomolecular systems. *Phys. Chem. Chem. Phys.* **2016**, *18*, 28339−28352.
(34) Curutchet, C.; Muñoz-Losa, A.; Monti, S.; Kongsted, J.; Scholes, G. D.; Mennucci, B. Electronic energy transfer in condensed phase studied by a polarizable QM/MM model. *J. Chem. Theory Comput.* **2009**, *5*, 1838−1848.
(35) Di Remigio, R.; Giovannini, T.; Ambrosetti, M.; Cappelli, C.; Frediani, L. Fully polarizable QM/fluctuating charge approach to two-photon absorption of aqueous solutions. *J. Chem. Theory Comput.* **2019**, *15*, 4056−4068.
(36) Kongsted, J.; Osted, A.; Pedersen, T. B.; Mikkelsen, K. V.; Christiansen, O. The $n \rightarrow \pi^*$ electronic transition in microsolvated formaldehyde. A coupled cluster and combined coupled cluster/molecular mechanics study. *J. Phys. Chem. A* **2004**, *108*, 8624−8632.
(37) Alam, M.; Ruud, K. Two-photon absorption in host-guest complexes. *Mol. Phys.* **2020**, *118*, No. e1777335.
(38) Hohenberg, P.; Kohn, W. Inhomogeneous Electron Gas. *Phys. Rev.* **1964**, *136*, B864−B871.
(39) Wesolowski, T. A.; Savin, A. In *Recent Progress in Orbital-free Density Functional Theory*; Wesolowski, T. A., Wang, Y. A., Eds.; Recent Advances in Computational Chemistry; World Scientific: Singapore, 2013; Vol. *6*, pp 275−295.
(40) Wesołowski, T. A. Embedding a multideterminantal wave function in an orbital-free environment. *Phys. Rev. A* **2008**, *77*, 012504.
(41) Zech, A.; Ricardi, N.; Prager, S.; Dreuw, A.; Wesolowski, T. A. Benchmark of Excitation Energy Shifts from Frozen-Density Embedding Theory: Introduction of a Density-Overlap-Based Applicability Threshold. *J. Chem. Theory Comput.* **2018**, *14*, 4028−4040.
(42) Wesolowski, T. A.; Warshel, A. Frozen density functional approach for ab initio calculations of solvated molecules. *J. Phys. Chem.* **1993**, *97*, 8050−8053.
(43) Pernal, K.; Wesolowski, T. A. Orbital-free effective embedding potential: Density-matrix functional theory case. *Int. J. Quantum Chem.* **2009**, *109*, 2520−2525.
(44) Wesolowski, T. A. On the Correlation Potential in Frozen-Density Embedding Theory. *J. Chem. Theory Comput.* **2020**, *16*, 6880−6885.
(45) Perdew, J. P.; Levy, M. Extrema of the density functional for the energy: Excited states from the ground-state theory. *Phys. Rev. B* **1985**, *31*, 6264−6272.
(46) Khait, Y. G.; Hoffmann, M. R. Embedding theory for excited states. *J. Chem. Phys.* **2010**, *133*, 044107.
(47) Wesolowski, T. A. Embedding potentials for excited states of embedded species. *J. Chem. Phys.* **2014**, *140*, 18A530.
(48) Olsen, J.; Jorgensen, P. Linear and nonlinear response functions for an exact state and for an MCSCF state. *J. Chem. Phys.* **1985**, *82*, 3235−3264.

https://doi.org/10.1021/acs.jctc.1c00204
J. Chem. Theory Comput. 2021, 17, 3652−3665

(49) Oddershede, J.; Jørgensen, P.; Yeager, D. L. Polarization propagator methods in atomic and molecular calculations. *Comput. Phys. Rep.* **1984**, *2*, 33−92.
(50) Zech, A.; Aquilante, F.; Wesolowski, T. A. Orthogonality of embedded wave functions for different states in frozen-density embedding theory. *J. Chem. Phys.* **2015**, *143*, 164106.
(51) Dirac, P. A. M. Note on Exchange Phenomena in the Thomas Atom. *Math. Proc. Cambridge Philos. Soc.* **1930**, *26*, 376−385.
(52) Vosko, S. H.; Wilk, L.; Nusair, M. Accurate spin-dependent electron liquid correlation energies for local spin density calculations: a critical analysis. *Can. J. Phys.* **1980**, *58*, 1200−1211.
(53) Thomas, L. H. The calculation of atomic fields. *Math. Proc. Cambridge Philos. Soc.* **1927**, *23*, 542−548.
(54) Fermi, E. Eine statistische Methode zur Bestimmung einiger Eigenschaften des Atoms und ihre Anwendung auf die Theorie des periodischen Systems der Elemente. *Z. Phys.* **1928**, *48*, 73−79.
(55) Shao, Y.; Gan, Z.; Epifanovsky, E.; Gilbert, A. T.; Wormit, M.; Kussmann, J.; Lange, A. W.; Behn, A.; Deng, J.; Feng, X. Advances in molecular quantum chemistry contained in the Q-Chem 4 program package. *Mol. Phys.* **2015**, *113*, 184−215.
(56) Wesolowski, T. A.; Weber, J. Kohn-Sham equations with constrained electron density: an iterative evaluation of the ground-state electron density of interacting molecules. *Chem. Phys. Lett.* **1996**, *248*, 71−76.
(57) Ricardi, N.; Zech, A.; Gimbal-Zofka, Y.; Wesolowski, T. A. Explicit vs. implicit electronic polarisation of environment of an embedded chromophore in frozen-density embedding theory. *Phys. Chem. Chem. Phys.* **2018**, *20*, 26053−26062.
(58) Monson, P. R.; McClain, W. M. Polarization dependence of the two-photon absorption of tumbling molecules with application to liquid 1-chloronaphthalene and benzene. *J. Chem. Phys.* **1970**, *53*, 29−37.
(59) Boys, S. F.; Bernardi, F. The calculation of small molecular interactions by the differences of separate total energies. Some procedures with reduced errors. *Mol. Phys.* **1970**, *19*, 553−566.
(60) Breneman, C. M.; Wiberg, K. B. Determining atom-centered monopoles from molecular electrostatic potentials. The need for high sampling density in formamide conformational analysis. *J. Comput. Chem.* **1990**, *11*, 361−373.
(61) Fradelos, G.; Wesołowski, T. A. Importance of the Intermolecular Pauli Repulsion in Embedding Calculations for Molecular Properties: The Case of Excitation Energies for a Chromophore in Hydrogen-Bonded Environments. *J. Phys. Chem. A* **2011**, *115*, 10018−10026.
(62) Fradelos, G.; Wesolowski, T. A. The Importance of Going beyond Coulombic Potential in Embedding Calculations for Molecular Properties: The Case of Iso-G for Biliverdin in Protein-Like Environment. *J. Chem. Theory Comput.* **2011**, *7*, 213−222.
(63) Mayer, I. Using singular value decomposition for a compact presentation and improved interpretation of the CIS wave functions. *Chem. Phys. Lett.* **2007**, *437*, 284−286.
(64) Jeziorski, B.; Moszynski, R.; Szalewicz, K. Perturbation Theory Approach to Intermolecular Potential Energy Surfaces of van der Waals Complexes. *Chem. Rev.* **1994**, *94*, 1887−1930.
(65) Daday, C.; König, C.; Valsson, O.; Neugebauer, J.; Filippi, C. State-specific embedding potentials for excitation-energy calculations. *J. Chem. Theory Comput.* **2013**, *9*, 2355−2367.
(66) Wesolowski, T. A. In *Computational Chemistry: Reviews of Current Trends*; Leszczynski, J., Ed.; World Scientific, 2006; Vol. *10*, pp 1−82
(67) Fradelos, G.; Lutz, J. J.; Wesołowski, T. A.; Piecuch, P.; Włoch, M. Embedding vs Supermolecular Strategies in Evaluating the Hydrogen-Bonding-Induced Shifts of Excitation Energies. *J. Chem. Theory Comput.* **2011**, *7*, 1647−1666.
(68) Fradelos, G.; Lutz, J. J.; Wesołowski, T. A.; Piecuch, P.; Włoch, M. In *Advances in the Theory of Quantum Systems in Chemistry and Physics*; Hoggan, P. E. E., Brandas, E. J. J., Maruani, J., Piecuch, P., Delgado-Barrio, G., Eds.; Progress in Theoretical Chemistry and Physics; Springer Netherlands, 2012; Vol. *22*, pp 219−248

https://doi.org/10.1021/acs.jctc.1c00204
J. Chem. Theory Comput. 2021, 17, 3652−3665

Chapter 5

Excitation energies of embedded chromophores from Frozen-Density Embedding Theory using state-specific electron densities of the environment

5.1 Motivation and outcome

In multi scale methods, the importance of considering the excitation induced polarization response from the environment has been widely recognized. In the density embedding methods this can be achieved by the use of the state-specific embedding potential. However, the use of the state-specific density from the environment to the expression of the excitation energy lacks a clear and established relation.

In the framework of FDET, starting from the Perdew-Levy theorem, and the recent formulation concerning the exact relation between i) the FDET energy functional for the use of variationally obtained single determinant form of the embedded wavefunction and the correlation energy obtained by non-variational methods, and ii) the Hohenberg-Kohn energy functional, a general formula was derived to achieve the exact relation for the excitation energy in case of state-specific density from the environment. Each term in this formula has its physical meaning and can be obtained by a suitable quantum mechanical method in any computational software. This formula was used to demonstrated the effect of the explicit consideration of the state-specific polarization response from the environment. We showed that the effect of explicit treatment of the polarization is usually at meV level. Depending on the targeting property, such as the need for multiple excited states, the user might choose the optimal strategy in evaluation of the excitation energy within the FDET formal framework.

Reprint of the paper is provided in the following pages. [Fu M, Wesolowski TA, *J. Phys. Chem. A.* 127, 535-545 (2023)]

Supporting information for this paper can be found in Appendix E.

THE JOURNAL OF PHYSICAL CHEMISTRY A
A JOURNAL OF THE AMERICAN CHEMICAL SOCIETY

pubs.acs.org/JPCA Article

Excitation Energies of Embedded Chromophores from Frozen-Density Embedding Theory Using State-Specific Electron Densities of the Environment

Mingxue Fu* and Tomasz A. Wesolowski*

Cite This: J. Phys. Chem. A 2023, 127, 535−545 Read Online

ACCESS | Metrics & More | Article Recommendations | Supporting Information

ABSTRACT: Starting from the Perdew−Levy theorem on extrema of the Hohenberg−Kohn functional, the expression for the vertical excitation energy is derived within the formal framework of Frozen-Density Embedding Theory (FDET) that makes it possible to use state-specific electron densities of the environment (ρ_B) of an embedded species. The derived general expression involves the embedded wave functions for ground and excited states that are orthogonal and is exact up to quadratic terms in the appropriate density expansion. It can be applied in practice using various methods differing in the treatment of the electron−electron correlation for embedded electrons, the method to evaluate different contributions to the excitation energy, the method to generate state-specific ρ_B, and the approximation used for the non-electrostatic component of the FDET embedding potential. The derived expression is applied for 47 local excitations in 10 embedded organic chromophores. The explicit treatment of the differential polarization of ρ_B improves indeed the accuracy of the excitation energy as compared to the implicit treatment in which the same ρ_B is used for all states of embedded chromophore. For 47 local excitations in 10 embedded organic chromophores, the average absolute errors in excitation energies drop from 0.04 to 0.03 eV and their standard deviations from 0.032 to 0.025 eV, respectively. The maximal errors show similar trends.

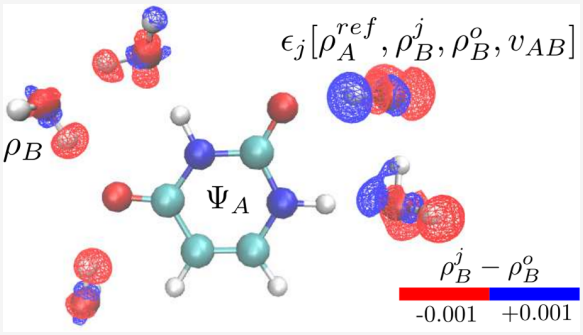

INTRODUCTION

Multiscale numerical simulations are frequently used for modeling localized excitations in condensed phase. A common element in such simulations is the use of some embedding operator ($\hat{v}_{emb}$) as an addition to the isolated-chromophore Hamiltoninan ($\hat{H}_A$). The embedded N_A electron wave function is evaluated from the eigenvalue equation of the general form

$$[\hat{H}_{N_A} + \hat{v}_{emb}]\Psi = \lambda\Psi \quad (1)$$

Multiscale/multilevel in this context means that eq 1 not only reduces a quantum N-body problem to N_A electrons (with $N_A \ll N$) but also that the generation of $\hat{v}_{emb}$ involves either less expensive methods of molecular quantum mechanics or methods beyond quantum mechanics. The embedding operator $\hat{v}_{emb}$ comprises usually atom-specific terms representing classical electrostatic interactions. The non-electrostatic contributions to the total energy originating in the Fermi statistic of electrons are taken into account either a posteriori as a correction to energy or directly as a component of the $\hat{v}_{emb}$. Concerning the electrostatic contributions, they might be represented by means of net effective atomic charges, atomic/molecular dipoles, and atomic/molecular polarizabilities, for instance. The constantly growing body of numerical data available in the literature indicate that taking into account the electronic polarization in the electrostatic component of the embedding potential is frequently indispensable if methods based on eq 1 are used for evaluation of the electronic excitation energies (see refs 1−14 for representative examples). In methods featuring, besides the electrostatic component of $\hat{v}_{emb}$, also a part representing the non-electrostatic effects on the embedded wave function, this additional component of $\hat{v}_{emb}$ is constructed starting from various basic principles: partitioning the wave function following the pseudopotential strategy,[15] partitioning the one-particle density matrix,[16] or partitioning the electron density.[17] In the last case, the embedding operator is multiplicative. Moreover, it is uniquely determined by the charge densities—that of the embedded species (ρ_A) and that of its environment (ρ_B); i.e., it is a functional of these quantities. Such unique dependency makes it ideally suited for multilevel simulations.[18] Not only the generation of ρ_B can be decoupled from the optimization of ρ_A

Received: November 3, 2022
Revised: December 14, 2022
Published: January 4, 2023

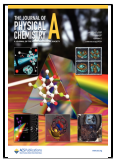

but also the embedding potential can be generated by means of an universal functional applicable for both atomistic and continuum levels of description for the environment[19,20] and include even experimentally derived ρ_B.[21] In our original work, a non-interacting reference system was used as the quantum descriptor for embedded N_A electrons optimized in the constrained minimization of the Hohenberg−Kohn energy functional $E_v^{HK}[\rho]$.[18,22] Frozen-Density Embedding Theory (FDET) is based on the same principle, but the constrained minimization is performed by means of optimization of other descriptors: interacting wave function[22] or one-particle spinless reduced density matrix.[23] Most recent addition to the formal framework of FDET is the exact relation between $E_v^{HK}[\rho]$ and the correlation energy obtained form nonvariational methods.[24] With this last addition, the formal framework of FDET covers practically all methods of molecular quantum mechanics which might be used to solve eq 1 and provides the exact relations between $E_v^{HK}[\rho]$, the stationary embedded wave function, embedding potential, and—in the case of nonvariational methods—the correlation energy and correlation density in a specific auxiliary system of N_A electrons. Concerning accessing the excited-state properties, FDET provides two possibilities: either via other-than-the-lowest-energy stationary solutions of the FDET eigenvalue equation (see the next section) or via the Linear-Response Time-Dependent Density Functional Theory.[25]

The present work builds upon the numerical experience concerning such FDET-based methods, in which the density ρ_B is generated without taking into account the effect of the embedded chromophore on ρ_B. It was shown that such treatment of ρ_B results in a rather accurate description of the effect of the environment on the vertical excitation energies.[26] If a state-independent ρ_B is used for all electronic states, the electronic polarization of the environment is taken into account implicitly. The implicit treatment might, however, result in the error in the energy of each state. Following the second Hohenberg−Kohn theorem, the FDET expression for the energy yields the upper bound for the energy of each state if an arbitrary ρ_B is used.[22] For the vertical excitation energy, the errors in the FDET energy of each state compensate at least partially even if common ρ_B is used. Numerical results show indeed that the errors in the FDET energies of each state are larger than the errors in the excitation energies.[26,27] The compensation of errors is more complete in the case of FDET than in the case of methods using electrostatic embedding only because of the variational character of FDET and the consistency of the FDET energy functional with the Hohenberg−Kohn theorems. For the electrostatic-only embedding potential, the limit on either the sign or the magnitude of the error does not exist. Ricardi et al. showed recently that the errors in the total energy of a given state can be greatly reduced if the common for all states density ρ_B is not that of the isolated molecules of the environment but the density of these molecules polarized by the field generated by the chromophore.[27] From the practical application perspective, the question arises, therefore, whether the reduction of the errors in the total energy of each state leads to a systematic reduction of errors for all states, improving thus the vertical excitation energies. This question cannot be answered in a straightforward and general manner. First of all, the electronic polarization of ρ_B is an ill-defined concept. (Exact) FDET equations yield the same total energy for different ρ_B.[28] The generation of state-specific densities ρ_B relies thus on some arbitrary choices. Moreover, if approximations are used for the non-electrostatic components of the embedding potential, they contribute also to the error of the energy in each state. This error does not have to be the same in all states. Finally, the numerical results obtained with a common ρ_B yield already rather good vertical excitation energies. Our previous work indicates that using a state-independent environment density ρ_B for all electronic states is an adequate choice for excitations localized in the embedded chromophore.[26,29] For 351 excitations in 52 clusters, the average absolute error of the excitation energy due to all approximations used in the FDET-based method (including the use of state-independent ρ_B) is as low as 0.039 eV.[26] Neugebauer and collaborators explored the potential benefits of using state-dependent ρ_B a method sharing with FDET several elements.[30−32] The used method involved several approximations/choices concerning the generation of state-dependent and state-independent ρ_B. The obtained excitation energies were compared to their state-independent counterparts for several embedded/solvated chromophores. Generally a good performance of the state-independent variant of the method was reported with the errors below 0.1 eV with a few exceptions. For the $\pi-\pi$ excitation in PNA complexed in water, the error of state-independent excitation energy was the largest (0.24 eV) and was reduced to 0.002 or 0.09 eV in two types of state-dependent methods to generate ρ_B. On the other hand, calculations with state-dependent ρ_B worsened the results in some cases.

In this work, we take a closer look at the potential benefits from using state-dependent ρ_B in FDET-based methods in an attempt to disentangle various factors contributing to the errors in the final excitation energies. The results obtained with a common ρ_B depend on the choice made for this density. On the other hand, using a state-dependent ρ_B relies on the choice of the method to generate ρ_B for each state. In any case, the excitation energies are affected by the approximations used for the functionals $E_{xct}^{nad}[\rho_A, \rho_B]$ and $v_{xct}^{nad}[\rho_A,\rho_B](\mathbf{r})$ in FDET (see next section). In calculations using state-independent ρ_B, the method used is based on the linearized variant of FDET equations formulated[33] and applied[26] previously.

The present work is organized as follows, we start with overviewing the key elements of FDET and deriving the expression for the excitation energy in the case where different ρ_B are used for different states. The derivation is presented here for the first time. In the numerical results part, the errors in the vertical excitation energies are analyzed for 47 local excitations in 10 embedded organic chromophores evaluated using either state-independent or state-dependent ρ_B. The state-dependent densities ρ_B are generated using the electric field generated by the embedded chromophore in the corresponding state.

THEORY

We start with the notations and key elements of FDET concerning electronic ground states. The formal framework of FDET concerns different quantum mechanical descriptors used for the embedded species. In each case, it is based on constrained optimization of the energy of the whole system (embedded species and the environment) expressed using the Hohenberg−Kohn density functional $E_v^{HK}[\rho]$. If the quantum descriptor for the embedded N_A electron system is a Kohn−Sham-like reference determinant ($\Phi^{(KS)}{}_A$), the exact relation between the FDET energy functional and the Hohenberg−

https://doi.org/10.1021/acs.jpca.2c07747
J. Phys. Chem. A 2023, 127, 535−545

Kohn energy functional, involving (a) the optimal embedded wave function $\Phi^{o(KS)}{}_A$, (b) the not-optimized component of the total density ρ_B, and (c) the embedding potential $v_{emb}^{FDET}[\rho_A,\rho_B;v_B](\mathbf{r})$ expressed as a functional of charge densities, is given in refs 18 and 22. Similar relations for embedded interacting wave function Ψ_A^o and one-particle reduced density matrix (Γ_A^o) are derived in refs 22 and 23, respectively. In all of the above cases, the FDET energy functional $E_{v_{AB}}^{FDET}[\Psi_A,\rho_B]$ satisfies the basic equality. For the embedded interacting wave function, it reads as

$$\min_{\Psi_A\to N_A} E_{v_{AB}}^{FDET}[\Psi_A,\rho_B] = E_{v_{AB}}^{FDET}[\Psi_A^o,\rho_B] = E_{v_{AB}}^{HK}[\rho_A^o+\rho_B] = \min_{\substack{\forall_{\mathbf{r}}\rho(\mathbf{r})\geq\rho_B(\mathbf{r})\\ \rho(\mathbf{r})\to N_{AB}}} E_{v_{AB}}^{HK}[\rho] \tag{2}$$

The optimization of the embedded wave function proceeds through solving the FDET eigenvalue problem:

$$(\hat{H}_A + \hat{v}_{emb}^{FDET}[\rho_A^j,\rho_B;v_B])\Psi_A^j = \lambda\Psi_A^j \tag{3}$$

$$\downarrow$$

$$\rho_A^j(\mathbf{r}) = \langle\Psi_A^j|\sum_{i=1}^{N_A}\delta(\mathbf{r}_i-\mathbf{r})|\Psi_A^j\rangle$$

$$\downarrow$$

$$v_{emb}^{FDET}[\rho_A^j,\rho_B;v_B](\mathbf{r}) = v_B(\mathbf{r}) + \int\frac{\rho_B(\mathbf{r}')}{|\mathbf{r}-\mathbf{r}'|}\,d\mathbf{r}' + v_{xct}^{nad}[\rho_A^j,\rho_B](\mathbf{r}) \tag{4}$$

where $\hat{H}_A$ is the Hamiltonian corresponding to N_A electrons at an external potential $v_A(\mathbf{r})$ with $N_A < N_{AB}$; $v_A(\mathbf{r})$ is an arbitrarily chosen component of the total potential partitioned as $v_{AB}(\mathbf{r}) = v_A(\mathbf{r}) + v_B(\mathbf{r})$; and $v_{xct}^{nad}[\rho_A,\rho_B](\mathbf{r}) = \frac{\delta E_{xct}^{nad}[\rho_A,\rho_B]}{\delta\rho(\mathbf{r})}|_{\rho=\rho_A}$, where $E_{xct}^{nad}[\rho_A,\rho_B]$ is a functional determined uniquely by the pair of electron densities $\rho_A(\mathbf{r})$ and $\rho_B(\mathbf{r})$ defined in ref 22.

The FDET energy functional $E_{v_{AB}}^{FDET}[\Psi_A,\rho_B]$ reads as

$$E_{v_{AB}}^{FDET}[\Psi_A,\rho_B] = \langle\Psi_A|\hat{H}_A + v_{emb}^{FDET}[\rho_A,\rho_B;v_B]|\Psi_A\rangle + E_{xct}^{nad}[\rho_A,\rho_B] - \int v_{xct}^{nad}[\rho_A,\rho_B](\mathbf{r})\rho_A(\mathbf{r})\,d\mathbf{r} + E_{v_B}^{HK}[\rho_B] + V_A[\rho_B] \tag{5}$$

where

$$\rho_A(\mathbf{r}) = \langle\Psi_A|\sum_{i=1}^{N_A}\delta(\mathbf{r}_i-\mathbf{r})|\Psi_A\rangle$$

$$V_A[\rho_B] = \int v_A(\mathbf{r})\rho_B(\mathbf{r})\,d\mathbf{r}$$

Due to the dependency of $v_{emb}^{FDET}[\rho_A,\rho_B;v_B]$ on the embedded wave function, the expectation value of $v_{emb}^{FDET}[\rho_A,\rho_B;v_B]$ cannot be interpreted as the energy of interaction between the embedded species and its environment. As a consequence, the eigenvalue λ^j in eq 3 is not simply related to the energy. For nonvariational methods used to obtain λ^j from eq 3, the expression relating the solution of this equation to $E_{v_{AB}}^{HK}[\rho]$ was derived recently.[24] It is used in the present work to derive the exact relation for excitation energy in the case of state-specific ρ_B.

FDET was originally formulated for ground states. The solution of eq 3, for which $E_{v_{AB}}^{FDET}[\Psi_A^j,\rho_B]$ has the lowest value, corresponds to the ground state. If eq 3 yields more than one solution, the other-than-the-lowest-energy solutions can be interpreted as excited states on the virtue of the Perdew–Levy theorem[34] on extrema of $E_{v_{AB}}^{HK}[\rho]$ as pointed out by Khait and Hoffmann.[35] According to this interpretation, the excitation energy equals the difference between the total energies given in eq 5 evaluated for the embedded wave functions (Ψ_A^j and Ψ_A^o) being the stationary solutions of eq 3:

$$\epsilon_j \equiv E^j - E^o = E_{v_{AB}}^{HK}[\rho_A^j+\rho_B] - E_{v_{AB}}^{HK}[\rho_A^o+\rho_B] = E_{v_{AB}}^{FDET}[\Psi_A^j,\rho_B] - E_{v_{AB}}^{FDET}[\Psi_A^o,\rho_B] \tag{6}$$

where $\rho_A^j(\mathbf{r}) = \langle\Psi_A^j|\sum_{i=1}^{N_A}\delta(\mathbf{r}_i-\mathbf{r})|\Psi_A^j\rangle$ and $\rho_A^o(\mathbf{r}) = \langle\Psi_A^o|\sum_{i=1}^{N_A}\delta(\mathbf{r}_i-\mathbf{r})|\Psi_A^o\rangle$.

The first equality in the above equation originates in the Perdew–Levy theorem[34] on extrema of $E_{v_{AB}}^{HK}[\rho]$. It is exact if the density ρ_B does not violate the non-negativity conditions of the target density:[27]

$$\forall_{\vec{r}}\ \rho_B \leq \rho_{v_{AB}}^j \tag{7}$$

and

$$\forall_{\vec{r}}\ \rho_B \leq \rho_{v_{AB}}^o \tag{8}$$

where $\rho_{v_{AB}}^j$ and $\rho_{v_{AB}}^o$ are the exact densities for the whole system for the two considered states. If the above conditions are not satisfied, the energy given by eq 5 evaluated for each state using the corresponding embedded wave function lies above the exact one (it follows from the the second Hohenberg–Kohn theorem and the basic equality of FDET given in eq 2). The second equality in eq 6 follows directly from eq 2.

Excitation Energies from FDET with a State-Independent ρ_B. The straightforward use of eq 6 is impractical for two principal reasons. One is of a computational nature. The self-consistency of the embedding potential and the embedded wave function requires repetitive solution of quantum N_A-electron problem with different embedding potentials. Each time a multideterminant form of the embedded wave function must be used to take into account electron–electron correlation. Moreover, such an iterative procedure must be performed independently for each electronic state. The second practical drawback of eq 6 is due to the fact that the stationary solutions of the FDET eigenvalue problems Ψ_A^o and Ψ_A^j are not expected to be orthogonal. They are solutions of a N_A-electron problem for two different external potentials. Using them to evaluate the transition moments and/or in combination with response theory must involve additional approximations.

The non-orthogonality problem can be circumvented by means of linearization of $E_{xct}^{nad}[\rho_A,\rho_B]$:[33]

$$E_{xct}^{nad}[\rho_A,\rho_B] = E_{xct}^{nad}[\rho_A^{ref},\rho_B] + \int(\rho_A-\rho_A^{ref})v_{xct}^{nad}[\rho_A^{ref},\rho_B]\,d\mathbf{r} + O^{eq9}(\Delta^2\rho) \approx E_{xct}^{nad}[\rho_A^{ref},\rho_B] + \int(\rho_A-\rho_A^{ref})v_{xct}^{nad}[\rho_A^{ref},\rho_B]\,d\mathbf{r} \tag{9}$$

which is not only numerically robust but also eliminates the need to perform independent calculations for each electronic state. The contributions from beyond-the-linear terms remain negligible for ρ_A^{ref}, being either the ground-state density of a free chromophore or the ground-state density of the embedded chromophore, for instance.[36] Linearization of $E_{xct}^{nad}[\rho_A,\rho_B]$ combined with the Perdew–Levy interpretation of extrema of the Hohenberg–Kohn density functional leads to a very simple relation between the eigenvalues obtained from eq 3, in

https://doi.org/10.1021/acs.jpca.2c07747
J. Phys. Chem. A 2023, 127, 535–545

which embedded wave-function-independent potential $v_{\mathrm{xct}}^{\mathrm{nad}}[\rho_A^{\mathrm{ref}},\rho_B]$ is used in eq 3 instead of $v_{\mathrm{xct}}^{\mathrm{nad}}[\rho_A^{x},\rho_B]$ with $x = 0$ or j:[33]

$$\epsilon_j \equiv E^j - E^o \equiv E_{v_{AB}}^{\mathrm{FDET(lin)}}[\Psi_A^j, \rho_B] - E_{v_{AB}}^{\mathrm{FDET(lin)}}[\Psi_A^o, \rho_B] = \lambda_j[\rho_A^{\mathrm{ref}}, \rho_B] - \lambda_o[\rho_A^{\mathrm{ref}}, \rho_B] \quad (10)$$

where $E_{v_{AB}}^{\mathrm{FDET(lin)}}[\Psi_A,\rho_B]$ differs from $E_{v_{AB}}^{\mathrm{FDET}}[\Psi_A,\rho_B]$ by replacing $E_{\mathrm{xct}}^{\mathrm{nad}}[\rho_A,\rho_B]$ by $E_{\mathrm{xct}}^{\mathrm{nad}}[\rho_A^{\mathrm{ref}},\rho_B] + \int(\rho_A - \rho_A^{\mathrm{ref}})\, v_{\mathrm{xct}}^{\mathrm{nad}}[\rho_A^{\mathrm{ref}},\rho_B]\, \mathbf{dr}$.

The eigenvalues $\lambda_j[\rho_A^{\mathrm{ref}},\rho_B]$ and $\lambda_o[\rho_A^{\mathrm{ref}},\rho_B]$ correspond to different stationary solutions of eq 3 for *for the same* effective potential (v) which does not depend on Ψ_A and is given as

$$v(\mathbf{r}) = v_{AB}(\mathbf{r}) + \int \frac{\rho_A^{\mathrm{ref}}(\mathbf{r}') + \rho_B(\mathbf{r}')}{|\mathbf{r} - \mathbf{r}'|}\, \mathbf{dr}' + v_{xct}^{\mathrm{nad}}[\rho_A^{\mathrm{ref}}, \rho_B](\mathbf{r}) \quad (11)$$

Any correlated method (variational and nonvariational), which yields excitation energies for N_A electrons in a fixed external potential, can be used to obtain the difference $\lambda_j[\rho_A^{\mathrm{ref}},\rho_B] - \lambda_o[\rho_A^{\mathrm{ref}},\rho_B]$. For the absolute energy ($E_{v_{AB}}^{\mathrm{FDET(lin)}}[\Psi_A^x,\rho_B]$, $x = 0$ or j), the availability of the eigenvalue $\lambda_x]\rho_A^{\mathrm{ref}},\rho_B]$ is not sufficient.

Excitation Energies from FDET with State-Specific ρ_B. As in the previously considered case, we start with eq 6 relating the excitation energy to the extrema of the Hohenberg−Kohn energy functional and to the corresponding energies given by $E_{v_{AB}}^{\mathrm{FDET}}[\Psi_A,\rho_B]$). If different ρ_B are used for different states,

$$\epsilon_j \equiv E^j - E^o = E_{v_{AB}}^{\mathrm{HK}}[\rho_A^j + \rho_B^j] - E_{v_{AB}}^{\mathrm{HK}}[\rho_A^o + \rho_B^o] = E_{v_{AB}}^{\mathrm{FDET}}[\Psi_A^j, \rho_B^j] - E_{v_{AB}}^{\mathrm{FDET}}[\Psi_A^o, \rho_B^o] \quad (12)$$

The straightforward application of the above formula is not practical for the same reasons as in the case of a state-independent ρ_B discussed in the previous section. The requirement that the embedded wave function has an adequate multideterminant form (full CI form in the exact limit) can in principle be avoided in both cases. For embedded wave function of a truncated CI form, the corresponding FDET energy functional differs from the one given in eq 5 (see ref 22). In the case of an embedded single determinant, the corresponding FDET energy functional comprises the correlation functional $E_c[\rho_A]$. As a consequence, the embedding potential comprises also its derivative—correlation potential. Both possibilities—the use of full CI form of the embedded wave function or the use of the correlation potential in the embedded single-determinant case—are impractical: the former due to the involved computational costs, whereas the latter due to the absence of good approximations for the functional $E_c[\rho]$ and its functional derivative in particular.

The linearization of $E_{\mathrm{xct}}^{\mathrm{nad}}[\rho_A,\rho_B]$ can be made as in the case of a state-independent ρ_B discussed in the previous section, but it will not result in the cancellation of the corresponding terms in the FDET energy if ρ_B differs for different states. A formula similar to that given in eq 10, which would involve only eigenvalues, does not exist, as the result.

The use of the correlation potential can be eliminated owing to the recently developed exact equality, which relates the quantities obtained in computationally efficient methods to treat electron−electron correlations with the Hohenberg−Kohn functional. In the case of the embedded wave function of the single-determinant form (Φ_A') and the correlation energy obtained by means of some nonvariational method, this relation reads as (eq 38 in ref 24):

$$E_{v_{AB}}^{\mathrm{HK}}[\rho_A + \rho_B] = E_{v_{AB}}^{\mathrm{FDET}}[\Phi_A', \rho_B] + E_{v'}^{\mathrm{c}} - \int \rho_A'(\mathbf{r}) \left(\int \Delta\rho_{v'}^{\mathrm{c}}(\mathbf{r}') f_{\mathrm{xct}}^{\mathrm{nad}}[\rho_A', \rho_B](\mathbf{r}, \mathbf{r}')\, \mathbf{dr}' \right) \mathbf{dr} + O^{\mathrm{eq}\,13}(\Delta^2\rho) \quad (13)$$

where $\rho_A(\mathbf{r})$ is the density obtained from the exact solution of eq 3, $\rho_A'(\mathbf{r}) = \langle \Phi_A' | \sum_{i=1}^{N_A} \delta(\mathbf{r}_i - \mathbf{r}) | \Phi_A' \rangle$, $v'(\mathbf{r}) = v_A(\mathbf{r}) + v_{\mathrm{emb}}^{\mathrm{FDET}}[\rho_A',\rho_B;v_B](\mathbf{r})$, Φ_A' is the stationary single determinant obtained with the potential v', $E_{v'}^{\mathrm{c}}$ is the correlation energy in the N_A-electron system defined by the potential v', $f_{\mathrm{xct}}^{\mathrm{nad}}[\rho_A', \rho_B](\mathbf{r}, \mathbf{r}') = \frac{\delta^2 E_{\mathrm{xct}}^{\mathrm{nad}}[\rho_A,\rho_B]}{\delta\rho_A(\mathbf{r})\delta\rho_A(\mathbf{r}')}$, and $\Delta\rho_{v'}^{\mathrm{c}}$ is the correlation-induced change of the electron density, and $O^{\mathrm{eq}\,13}(\Delta^2\rho)$ collects all contributions to energy due to the effect of correlation on density that are of higher order.

Note that, for a given v_{AB} and ρ_B, eq 13 derived in ref 24 holds only for specific ρ_A, Ψ'_A, v', and $E_{v'}^{\mathrm{c}}$. It is this relation for numbers, not a relation for functionals such as the basic FDET equation given in eq 2. All quantities in the right-hand side are available in practical calculations in which $E_{\mathrm{xct}}^{\mathrm{nad}}[\rho_A,\rho_B]$ is approximated by some analytical expression ($E_{\mathrm{xct}}^{\mathrm{nad}}[\rho_A,\rho_B] \approx \tilde{E}_{\mathrm{xct}}^{\mathrm{nad}}[\rho_A,\rho_B]$). The energy given in the left-hand side corresponds to the total energy $\rho_{AB}(\mathbf{r}) = \rho_A(\mathbf{r}) + \rho_B(\mathbf{r})$. The density $\rho_A(\mathbf{r})$ differs from $\rho_A'(\mathbf{r})$. The former is the stationary density obtained self-consistently using N_A-electron functions of the full CI form, whereas $\rho_A'(\mathbf{r})$ is the stationary density obtained self-consistently using N_A-electron functions of the single-determinant form AND with the neglected $v_c[\rho_A]$ component of the FDET embedding potential.

Neglecting the higher-order contributions to energy $O(\Delta^2\rho)$ in eq 13 makes it possible to reduce significantly the computational effort needed to evaluate the absolute energy. The iterative evaluation of the embedded single determinant is, however, still needed in order to satisfy the condition of self-consistency of the embedded wave function and embedding potential. For excitation energy, such self-consistent solution of the FDET eigenvalue problem is made independently for the ground and the excited states. Once the self-consistent optimal determinants corresponding to the two electronic states are obtained, the excitation energy is given by inserting eq 13 into the second line of eq 12.

In the following considerations, a further approximation is made. $E_{\mathrm{xct}}^{\mathrm{nad}}[\rho_A,\rho_B]$ is linearized near some ρ_A^{ref}. This leads to a significant further simplification of eq 12. The term in the right-hand side of eq 13 depending on the kernel $f_{\mathrm{xct}}^{\mathrm{nad}}$ disappears upon linearization of $E_{\mathrm{xct}}^{\mathrm{nad}}[\rho_A,\rho_B]$. The final expression for the excitation energy is obtained from the second line of eq 12 upon addition and subtraction of $E_{v_{AB}}^{\mathrm{FDET}}[\Psi_A^o,\rho_B^j]$ (see the full derivation in the Supporting Information) and by use of eq 13 for the total energy of each state reads as

https://doi.org/10.1021/acs.jpca.2c07747
J. Phys. Chem. A 2023, 127, 535−545

$$\epsilon_j[\rho_A^{\mathrm{ref}}, \rho_B^j, \rho_B^o, v_{AB}] \equiv \overbrace{\lambda_j[\rho_A^{\mathrm{ref}}, \rho_B^j] - \lambda_o[\rho_A^{\mathrm{ref}}, \rho_B^j]}^{\epsilon_j^A} + \overbrace{\langle \Phi_A'^{o(j)}|\widehat{H}_A + \hat{v}_{\mathrm{emb}}^{\mathrm{FDET}}[\rho_A^{\mathrm{ref}}, \rho_B^j]|\Phi_A'^{o(j)}\rangle - \langle \Phi_A'^{o(o)}|\widehat{H}_A + \hat{v}_{\mathrm{emb}}^{\mathrm{FDET}}[\rho_A^{\mathrm{ref}}, \rho_B^o]|\Phi_A'^{o(o)}\rangle + E_{v'^j}^{\mathrm{c}} - E_{v'^o}^{\mathrm{c}}}^{\epsilon_j^B}$$
$$- \overbrace{\left(\int \rho_A^{\mathrm{ref}}(\mathbf{r}) v_{\mathrm{xct}}^{\mathrm{nad}}[\rho_A^{\mathrm{ref}}, \rho_B^j](\mathbf{r})\, \mathrm{d}\mathbf{r} - \int \rho_A^{\mathrm{ref}}(\mathbf{r}) v_{\mathrm{xct}}^{\mathrm{nad}}[\rho_A^{\mathrm{ref}}, \rho_B^o](\mathbf{r})\, \mathrm{d}\mathbf{r}\right) + E_{\mathrm{xct}}^{\mathrm{nad}}[\rho_A^{\mathrm{ref}}, \rho_B^j] - E_{\mathrm{xct}}^{\mathrm{nad}}[\rho_A^{\mathrm{ref}}, \rho_B^o]}^{\epsilon_j^C} + \overbrace{E_{v_B}^{\mathrm{HK}}[\rho_B^j] - E_{v_B}^{\mathrm{HK}}[\rho_B^o]}^{\epsilon_j^D}$$
$$+ \overbrace{V_A[\rho_B^j] - V_A[\rho_B^o]}^{\epsilon_j^E} \tag{14}$$

where $\Phi'^{o(j)}$ is the ground-state Slater determinant for the N_A-electron system in the external potential equal to $v'^j = v_A + v_{\mathrm{emb}}^{\mathrm{FDET}}[\rho_A^{\mathrm{ref}}, \rho_B^j; v_B]$, $\Phi'^{o(o)}$ is the ground-state Slater determinant for the N_A-electron system in the external potential equal to $v'^o = v_A + v_{\mathrm{emb}}^{\mathrm{FDET}}[\rho_A^{\mathrm{ref}}, \rho_B^o; v_B]$, and ρ_A^{ref} is the density used for linearization of $E_{\mathrm{xct}}^{\mathrm{nad}}[\rho_A, \rho_B]$.

For self-consistent ρ_A^{ref} and $\Phi'^{o(j)}$, i.e., if $\rho_A^{\mathrm{ref}}(\mathbf{r}) = \langle \Phi_A'^{o(j)}|\sum_{i=1A}^{N} \delta(\mathbf{r}_i - \mathbf{r})|\Phi_A'^{o(j)}\rangle$, the excitation energy given by eq 14 ($\epsilon_j[\rho_A^{\mathrm{ref}}, \rho_B^j, \rho_B^o, v_{AB}]$) satisfies the following equality:

$$E_{v_{AB}}^{\mathrm{HK}}[\rho_A^j + \rho_B^j] - E_{v_{AB}}^{\mathrm{HK}}[\rho_A^o + \rho_B^o] = \epsilon_j[\rho_A^{\mathrm{ref}}, \rho_B^j, \rho_B^o, v_{AB}] + O^{\mathrm{eq}\,13}(\Delta^2\rho) + O^{\mathrm{eq}\,9}(\Delta^2\rho) \tag{15}$$

The equality given in eq 15 assures that the energy evaluated according to it is free from over- or undercounting any contributions to the energy (up to small terms of the $O(\Delta^2\rho)$ order). Since the equality given in eq 14 holds only if $\rho_A^{\mathrm{ref}}(\mathbf{r}) = \langle \Phi_A'^{o(j)}|\sum_{i=1}^{N_A} \delta(\mathbf{r}_i - \mathbf{r})|\Phi_A'^{o(j)}\rangle$, i.e., if the embedding potential and the embedded wave functions are self-consistent. The procedure such as the one used in ref 36 can be used for this purpose. Note that owing to the relation given in eq 13, the condition of self-consistency between $v_{\mathrm{emb}}[\rho_A, \rho_B; v_B]$ and ρ_A is required only at the Hartree−Fock level and results only in small deviation from the energy given by the Hohenberg−Kohn functional in the order of $O^{\mathrm{eq}\,13}(\Delta^2\rho)$.[24] Our previous work shows also even the computational effort due to this condition can be avoided owing to the linearization of $E_{\mathrm{xct}}^{\mathrm{nad}}[\rho_A, \rho_B]$ in the considered type of systems and the used approximations for $E_{\mathrm{xct}}^{\mathrm{nad}}[\rho_A, \rho_B]$. If the ρ_A^{ref} used in eq 9 is the density of the Hartree−Fock density of the isolated chromophore, neglecting the higher-than-linear terms in the expansion results in errors in the total energy rarely exceeding 0.001 eV.[36] They are thus more than 1 order of magnitude smaller than the magnitude of errors, which are the subject of the analysis of the present work. In the numerical examples given in this work, the discussed energies are obtained from the first iteration. The subsequent iteration starting from ρ_A^{ref} being the Hartree−Fock density of the isolated chromophore affects the excitation energies by less 0.002 eV at the most.

Equation 14 is particularly suitable for multilevel simulations. All terms in the right-hand side of eq 14 can be evaluated at the desired accuracy by means of an appropriate method for each of them.

- $\epsilon_j^A = E_{v'^j}^j - E_{v'^j}^o$ is the excitation energy for the system of the N_A-electron system in the external potential equal to $v'^j = v_A + v_{\mathrm{emb}}^{\mathrm{FDET}}[\rho_A^{\mathrm{ref}}, \rho_B^j; v_B]$. The potential v'^j does not depend on the embedded wave function. The ϵ_j^A component of the excitation energy can be, thus, obtained from any conventional method of molecular quantum chemistry describing adequately the excited state of the system of interest.
- $\epsilon_j^B = E_{v'^j}^o - E_{v'^o}^o$ is the difference between ground-state energies for two N_A-electron systems defined by two different external (embedded wave function independent) potentials: $v_A + v_{\mathrm{emb}}^{\mathrm{FDET}}[\rho_A^{\mathrm{ref}}, \rho_B^j; v_B]$ and $v_A + v_{\mathrm{emb}}^{\mathrm{FDET}}[\rho_A^{\mathrm{ref}}, \rho_B^o; v_B]$. For each potential, the ground-state energy is represented as the sum of the Hartree−Fock and correlation energy. ϵ_j^B can be obtained from any conventional method of molecular quantum chemistry adequate for obtaining ground-state energies for the system of interest.
- ϵ_j^C is a residual component due to nonlinear dependence of $E_{\mathrm{xct}}^{\mathrm{nad}}[\rho_A, \rho_B]$ on ρ_B. This term could be in principle also subject to the linearization approximation by expanding $E_{\mathrm{xct}}^{\mathrm{nad}}[\rho_A, \rho_B]$ around some ρ_B^{ref}. Such an expansion is not made here as it does not lead to any computational advantages. Moreover, although $E_{\mathrm{xct}}^{\mathrm{nad}}[\rho_A, \rho_B]$ is symmetric with respect of exchanging ρ_A with ρ_B, the corresponding functional derivatives are not. The adequacy of linearization of $E_{\mathrm{xct}}^{\mathrm{nad}}[\rho_A, \rho_B]$ with respect to ρ_A does not imply, therefore, that the same can be made for ρ_B. Its magnitude might be also affected by the approximation used for $E_{\mathrm{xct}}^{\mathrm{nad}}[\rho_A, \rho_B]$.
- ϵ_j^D represents a "strain"—the energy needed to change the density of the environment from ρ_B^o to ρ_B^j without changing the external potential (position of nuclei for instance). In multilevel simulations, the change from ρ_B^o to ρ_B^j might reflect the differential electronic polarization of the environment due to the change of the electronic state of the embedded species. In such a case, ϵ_j^D has a simple interpretation and the evaluation of ϵ_j^D does not involve the quantum mechanical level of description. It is the energy expense needed to polarize an atom or molecule (case of atomic or molecular polarizabilities in QM/MM type of simulations) or to polarize a volume element (case of continuum models). ϵ_j^D can be also evaluated using a quantum mechanical method (see Miscellaneous Computational Details) as it is made in the present work.
- ϵ_j^E is the contribution to the excitation energy due to the effect of changing ρ_B on its interaction with the nuclei of the embedded species. The evaluation of this term is straightforward regardless of whether ρ_B is obtained from quantum or classical levels of description.

Protocols to Generate ρ_B in FDET Calculations of Vertical Excitation Energies. We start with the observation that in FDET the embedding potential is state-dependent even if the same density ρ_B is used for each state of the chromophore. Its $v_{\mathrm{xct}}^{\mathrm{nad}}[\rho_A, \rho_B]$ component depends on the ρ_A

https://doi.org/10.1021/acs.jpca.2c07747
J. Phys. Chem. A 2023, 127, 535−545

which corresponds to the embedded wave function. This kind of state-dependency results in non-orthogonality of the embedded wave functions for different states. The amount of the overlap between the functions for different states depends on the system and the used approximation for $v_{xct}^{nad}[\rho_A,\rho_B]$. Dresselhaus and Neugebauer showed that the violation of orthogonality is not numerically significant in the considered model systems. For the sake of evaluation of the transition moments, the violation of the orthogonality could be thus ignored.[32] In the present work, we deal with this source of non-orthogonality in a more general and system-independent way. In all methods considered in this work, state-dependency of the FDET embedding potential arising due to its dependency on the embedded wave function (see eq 3) was eliminated owing to the linearization of $E_{xct}^{nad}[\rho_A,\rho_B]$ proposed in ref 33, which was shown to lead to negligible errors[36] that are due to higher-than-linear contributions in the expansion of $E_{xct}^{nad}[\rho_A,\rho_B]$. The used protocols differ, however, in the treatment of state-dependency of ρ_B and are described below. In all of them, ρ_B was obtained form Hartree−Fock calculations but with different polarizing potentials added to v_B.

- Protocol A: It is a basic protocol in which ρ_B corresponds to the density of the molecules in the environment that is not affected by the interactions with the embedded species at all. It was used in ref 26 to evaluate 351 excitations in 32 representative clusters, each comprising a chromophore and a few non-covalently bound molecules considered as the environment in FDET. In this set, the complexation-induced shifts in the vertical excitation energy ($\Delta\epsilon$) vary from −0.7 to 1.5 eV, whereas the mean absolute error ($\delta\epsilon$) of the excitation energy is equal to 0.039 eV.
- Protocol B: This protocol represents a refinement of Protocol A.[37] A common ρ_B is still used, but the interactions with the embedded species are taken into account explicitly in a pragmatic way. The external electric field generated by the isolated chromophore in its ground state is used to polarize the environment.
- Protocol C: This protocol is similar to Protocol B, but the prepolarizing field is not generated by the isolated chromophore in its ground state but rather the average of the fields corresponding to the 11 lowest electronic states of the isolated chromophore.
- Protocol D: FDET equations are solved independently for each state. In each case, ρ_B is prepolarized by the field generated by the isolated chromophore in the corresponding electric state as introduced in ref 37.
- Protocol E: This protocol requires a prior calculation following Protocol B. The prepolarization stage is repeated but with the prepolarizing field corresponding to the embedded (not isolated as in the case of Protocol D) chromophore. The difference between the prepolarizing charges in Protocols D and E is used as a measure of self-consistency of the final solution. In principle, Protocol E can be used iteratively until full self-consistency between the field polarizing ρ_B and that obtained from the embedded wave function is reached.

Protocols A−C are computationally attractive. The FDET eigenvalue problem is solved only once with a common embedding potential for each and every state. As a result, the eigenfunctions are orthogonal and can be used in a straightforward manner to obtain transition moments or to be used in response-based formalisms.[29] The polarization of the environment (either state-specific or not) is taken into account implicitly if the densities ρ_A and ρ_B do overlap. The implicit treatment is not complete if the exact total density corresponding to any of the involved states is locally smaller than ρ_B used in the evaluation of the embedding potential.[37] If the basis sets centered on separate subsets of atoms are used for the embedded species and for the environment, the contribution to the excitation energy due to the differential polarization of ρ_B is completely neglected. Protocol C takes into account the effect of interaction between the chromophore and the environment in an average way. It is a protocol not explored previously. It could be expected to combine the attractiveness of a method in which a common embedding potential with the average treatment of the environment response. Protocols D and E are computationally more demanding because the quantum N_A-electron problem has to be solved independently for each excited state. Although the embedded wave functions for different excited states might be non-orthogonal, each excited state is orthogonal to that of the ground state (see eq 14).

MISCELLANEOUS COMPUTATIONAL DETAILS

The FDET vertical excitation energies and their supermolecular counterparts were obtained using the Q-Chem[38] program. In all calculations the cc-pVDZ basis sets were used.[39] For checking the soundness of the reported numerical results, some calculations were repeated using augmented basis sets. The second-order Algebraic Diagrammatic Construction (ADC(2)) method was used to evaluate vertical excitation energies for reference supermolecular calculations.

The individual components of the excitation energy defined in eq 14 are evaluated using the different methods. ϵ_j^A was obtained from the ADC(2) calculations. For ϵ_j^B, the second-order Møller−Plesset theory was used. For ϵ_j^D the Hartree−Fock energies were used. Since the polarized density was always obtained from the Hartree−Fock calculations, this choice assures that the reference supermolecular ADC(2) and embedding calculations yield the same excitation energies at the dissociation limit.

In FDET, the basis sets used for ρ_A and ρ_B were restricted to the ones centered on atoms defining v_A and v_B, respectively (monomer expansion[40]).

Decomposable local-density approximation was used for each component of $v_{xct}^{nad}[\rho_A,\rho_B](\mathbf{r})$ defined in ref 22, the Slater−Dirac functional[41] for exchange, Vosko−Wilk−Nusair parametrization[42] for correlation, and Thomas−Fermi[43,44] functional for the kinetic component, whereas its $v_c[\rho_A](\mathbf{r})$ part was neglected to satisfy the condition at which eq 13 is applicable. The reference density made for ρ_A^{ref} is the ground-state density of the isolated chromophore obtained from the wave function given in the first-order Møller−Plesset perturbation theory.

Atomic charges were generated from the electron density obtained from the first-order Møller−Plesset perturbation theory using the CHELPG method[45] based on fitting them to the electrostatic potential.

Embedded Chromophores. The clusters chosen for the present analysis form a representative sample differing in the hydrogen-binding strength and arrangement. Each one consists of a heterocyclic organic chromophore and up to five molecules in its environment (see Figure 1).

The clusters were selected from a larger set of 52 clusters used previously to estimate the overall errors in the vertical

https://doi.org/10.1021/acs.jpca.2c07747
J. Phys. Chem. A 2023, 127, 535−545

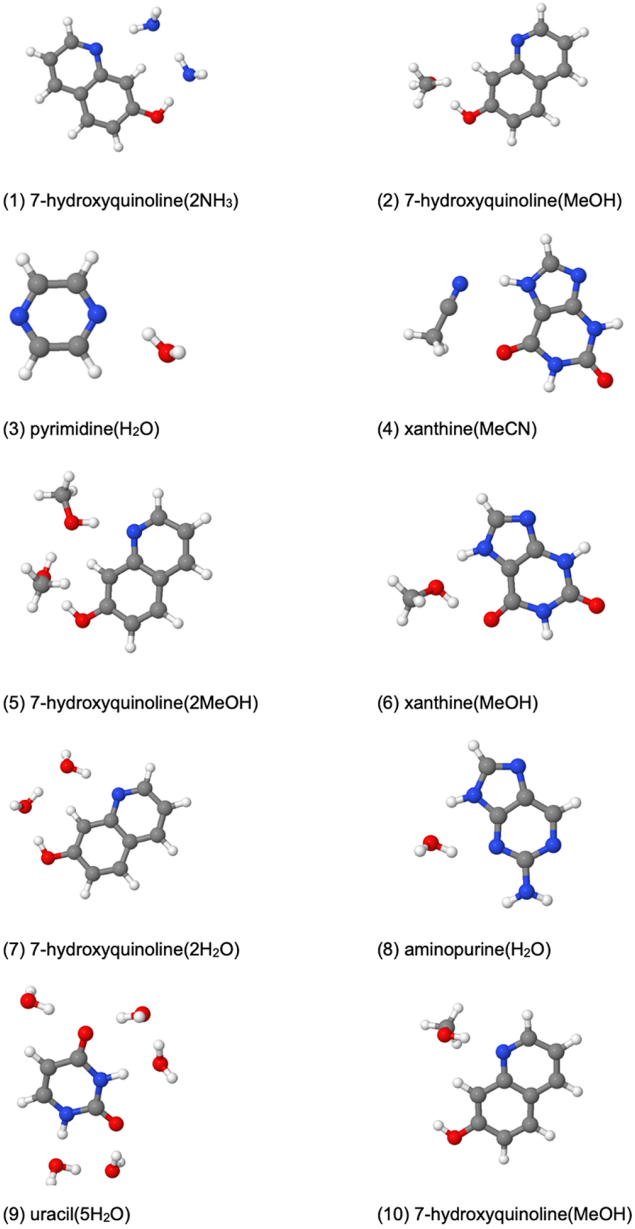

Figure 1. Complexed organic chromophores. The molecules in the environment described by means of ρ_B in FDET are specified in the parentheses.

excitation energies localized in the chromophore due to the approximations applied in the simplest FDET protocol considered in the present work (Protocol A).[26] The mean absolute error in the vertical excitation energies ($\langle|\delta\epsilon|\rangle$) for 351 assigned excitation in these clusters is equal to 0.039 eV. Note that the error in shift of a given excitation energy due to complexation $\delta\Delta\epsilon^j$ is numerically equivalent to the error in the excitation energy $\delta\epsilon^j$. The quantities $\Delta\epsilon^j$ and ϵ^j differ by the constant—excitation energy of the isolated chromophore. In the selected subset of the data consisting of 47 excitations in 10 clusters, the complexation-induced shifts in the excitation energies span the 0.5 eV wide range (-0.35 eV $< \Delta\epsilon <$ 0.15 eV; see Results and Discussion), which is more than on order of magnitude larger than the mean absolute error of the excitation energy in the full set.

The geometries of the clusters are also taken from ref 26.

RESULTS AND DISCUSSION

Table 1 collects the average errors ($\langle|\delta\epsilon|\rangle$) in the vertical excitation energies due to the approximations used in FDET (the approximation for the bifunctionals $E_{xct}^{nad}[\rho_A,\rho_B]$ and $v_{xct}^{nad}[\rho_A,\rho_B](\mathbf{r})$ and the monomer expansion in the basis set) and ρ_B generated using several protocols. For Protocol A, $\langle|\delta\epsilon|\rangle$ = 0.047 eV, the value which is slightly larger than the one reported in ref 26 (0.039 eV) but which is still 1 order of magnitude smaller than the range of the effect of the environment on the vertical excitations in this set of reference data. This also indicates that the chosen set of clusters does not favor cases where the errors are small. The individual errors are shown in Figures 2 and 3. The maximal error (0.159 eV) occurs for the sixth excitation in the uracil$-5H_2O$ cluster for which the complexation results in a red shift (-0.337 eV). For red-shifted cases, Protocol A underestimates systematically the magnitude of the shifts. Polarization of the environment density ρ_B (Protocol B) by means of the electric field generated by the isolated chromophore in its ground state leads to smaller errors. $\langle|\delta\epsilon|\rangle$ drops from 0.0468 to 0.0395 eV. More importantly, the standard deviations are reduced even more (from 0.0414 to 0.0322 eV), which indicates that Protocol B systematically improves the model. In some cases, the magnitude of the errors increases compared to Protocol A but the increase is rather small. Using the polarizing field averaged over the 11 lowest states of the isolated chromophore (Protocol C) leads, however, to the increase of errors $\langle|\delta\epsilon|\rangle$ from 0.0468 to 0.0527 eV. Similar deterioration of the result was observed for a lower number of states used for averaging. For this reason, such treatment of polarization of ρ_B was not considered further. Protocol B emerges thus as the most efficient among the ones which use the same embedding potential for different states.

The simplest state-dependent embedding potential (Protocol D) leads to a small further reduction of the average absolute error. Compared to Protocol B, $\langle|\delta\epsilon|\rangle$ drops from

Table 1. Average Absolute Errors in the Vertical Excitation Energies ($\langle|\delta\epsilon|\rangle$) due to the Approximations Used in FDET and Different Choices of ρ_B[a]

	$\langle|\delta\epsilon|\rangle$ (eV) for different choices of ρ_B				
	state-independent embedding potential			state-dependent embedding potential	
excitation type	Protocol A	Protocol B	Protocol C	Protocol D	Protocol E
$\pi-\pi^*$	0.0529 (0.0381)	0.0445 (0.0308)	0.0603 (0.0406)	0.0431 (0.0333)	0.0329 (0.0229)
$n-\pi^*$	0.0208 (0.0261)	0.0185 (0.0222)	0.0208 (0.0220)	0.0104 (0.0200)	0.0177 (0.0276)
all	0.0468 (0.0414)	0.0395 (0.0322)	0.0527 (0.0418)	0.0384 (0.0337)	0.0300 (0.0258)

[a]Standard deviations are given in parentheses.

https://doi.org/10.1021/acs.jpca.2c07747
J. Phys. Chem. A 2023, 127, 535−545

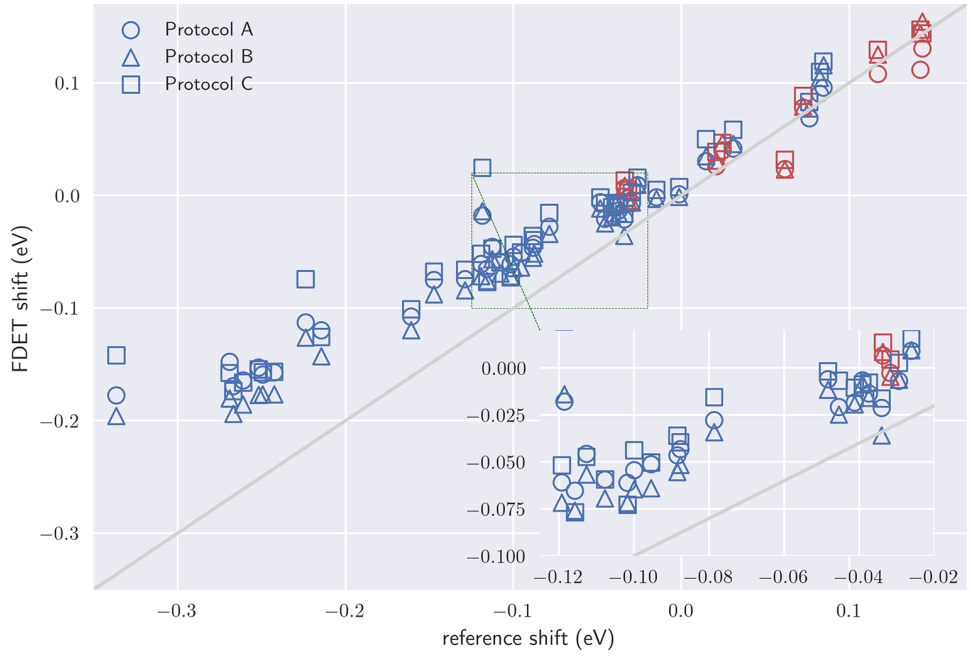

Figure 2. Complexation-induced shifts of vertical excitation energies ($\Delta\epsilon$in [eV]) obtained using Protocols A, B, and C, to generate ρ_B used in "embedded ADC(2)" calculations. $n-\pi^*$excitations are shown in red. The reference shifts are obtained from conventional ADC(2) calculations.

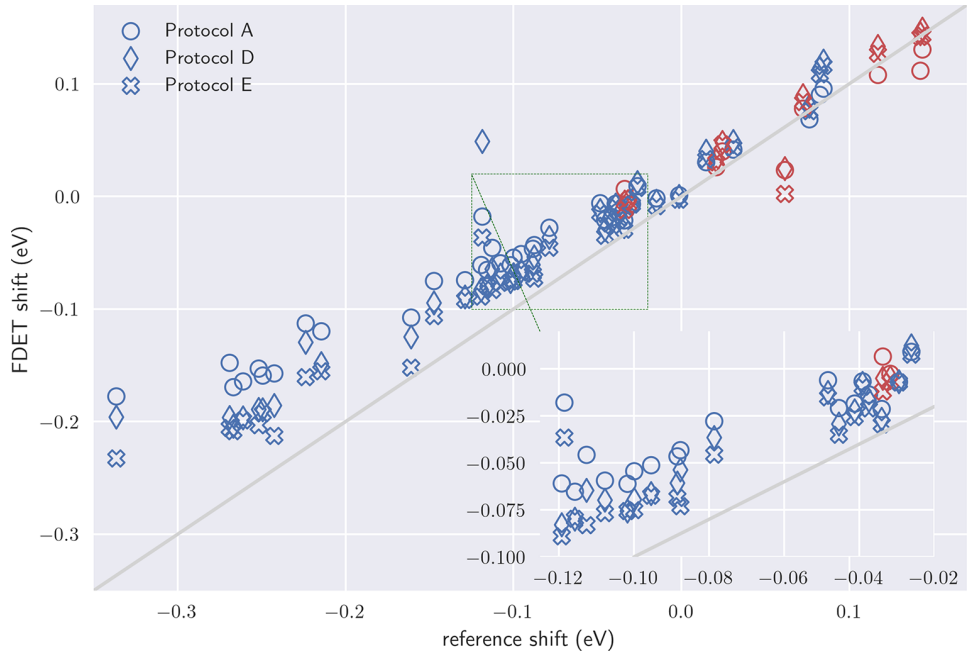

Figure 3. Complexation-induced shifts of vertical excitation energies ($\Delta\epsilon$ [eV]) obtained using Protocols A, D, and E, to generate different densities ρ_B for "embedded ADC(2)" calculations. $n-\pi^*$ excitations are shown in red. The reference shifts are obtained form conventional ADC(2) calculations.

0.0395 to 0.0384 eV. Interestingly, this overall improvement leaves some cases behaving differently than the overall trend. The most striking is the eighth state in the uracil−H_2O cluster for which $\delta\epsilon$ increases from 0.105 to 0.167 eV. This anomalous behavior occurs for the excitation for which the effect of environment on the excitation energy is rather small (0.119 eV). The fact that the magnitude of the error for this excitation is even larger than the complexation-induced shift is disturbing and calls for a more detailed analysis.

We notice that the polarizing field takes into account the effect of the environment on the chromophore in neither Protocol B nor Protocol D. The results obtained using Protocol E provide the interpretation of this anomalous behavior. For the eighth excitation in the uracil−$5H_2O$ complex, errors of the excitation energy ($\delta\epsilon$ are equal to 0.101, 0.105, 0.167, and 0.082 eV for Protocols A, B, D, and E, respectively). The failure of Protocols A, B, and D, in this case, originates from the fact that the difference in the state-specific polarizing electric fields cannot be represented sufficiently well

https://doi.org/10.1021/acs.jpca.2c07747
J. Phys. Chem. A 2023, 127, 535−545

by just the redistribution of electron density occurring in the isolated chromophore upon excitation. This can be illustrated by comparing the net atomic charges used to polarize ρ_B in Protocol D with the charges on the same atoms obtained in Protocol D. The former corresponds to the excitation in the isolated chromophore whereas the latter to the excitation in the embedded chromophore. Actually, these two sets of atomic charges differ the most in cases where Protocol E leads to the largest improvement compared to Protocol D (see Table S3 in the Supporting Information).

The main contribution to ϵ_j is from ϵ_j^A, which is of the same order as the excitation energy itself (see Table S2 in the Supporting Information). The next larger contributions are ϵ_j^B and ϵ_j^D. Their magnitude is significantly smaller than that of ϵ_j^A. Moreover, these two contributions have opposite signs, which leads to an overall small "correction" to ϵ_j^A. ϵ_j^C affects negligibly the excitation energy (it is smaller than 1.3 meV). The last term ϵ_j^E representing the change of energy of the classical electrostatic interaction between the nuclei of the chromophore and ρ_B is small but not negligible (it reaches up to 0.044 eV).

In summary, Protocols A, B, D, and E represent a series of systematically improvable approximations as indicated by the monotonicity of the average absolute errors: 0.0468, 0.0395, 0.0384, and 0.030 eV, along this series.

CONCLUSIONS

The principal result of the present analysis is given in eq 14. Its origin in the Perdew−Levy theorem on extrema of the Hohenberg−Kohn functional together with the derived recently FDET equality given in eq 13 guarantees that no contribution to the total energy is either omitted or counted twice. *Two approximations* are made in eq 14: (i) neglecting $O(\Delta^2\rho)$ and (ii) neglecting the higher-than-linear terms in the expansion of $E_{\mathrm{xct}}^{\mathrm{nad}}[\rho_A,\rho_B]$ in $\rho_A - \rho_A^{\mathrm{ref}}$. Equation 14 is a formal result presented in this work for the first time. A wide spectrum of methods can be used in its practical implementation. The modeler can use it to select the optimal method from the quantum chemistry toolbox to evaluate (a) the electronic excitation for a given external potential (ϵ_j^A) and (b) the ground-state energy of a system with a given external potential (ϵ_j^B). The ϵ_j^D and ϵ_j^E contributions to the excitation energy can be evaluated using either one of the computational chemistry methods as it was made in the present work or without any use of quantum mechanical descriptors of the environment.

Our previous work showed comprehensively that using ρ_B corresponding to the ground-state density of the system comprising only the molecules of the environment (branded Protocol A in the present work), is a good starting point for modeling localized excitations in FDET-based methods.[26,29] The average absolute error due to approximations made in FDET and the above choice of ρ_B is as small as 0.039 eV in the case of 451 representative excitations considered in ref 26. Protocol A rarely leads due to approximations made in FDET exceeding 0.1 eV if used for localized excitations in chromophores in noncovalently bound environments. The accuracy thresholds in the excitation energy of the magnitude of 0.04 eV or even 0.1 eV are acceptable for electronic excitations for interpretation purposes and lie within the range of intrinsic errors of the excitation energy obtained from medium-quality methods of molecular quantum mechanics such as ADC(2), EOM-CCSD.

The computational advantages of Protocol A are evident: (a) combined with the linearization of $E_{\mathrm{xct}}^{\mathrm{nad}}[\rho_A,\rho_B]$ it guarantees that embedded wave functions for different states are orthogonal, (b) its numerical implementation is straightforward because it requires only feeding in the one-electron component of the Hamiltonian to a software solving electronic Schrödinger equation, (c) it is applicable for such multiscale/multilevel simulations that do not use any quantum mechanical descriptor for the environment opening this as a formal possibility to use non-quantum-mechanical methods to generate ρ_B, and (d) evaluation of the excitation energy uses an approximation for the functional $v_{\mathrm{xct}}^{\mathrm{nad}}[\rho_A,\rho_B]$ without relying on the approximation to $E_{\mathrm{xct}}^{\mathrm{nad}}[\rho_A,\rho_B]$.

The disadvantages of Protocol A lie in the fact that its accuracy relies on compensation of errors due to the violation of the non-negativity condition for the two target densities corresponding to two considered states.[27] It is, therefore, not improvable in a systematic way. These errors compensate efficiently because they are non-negative by construction but might still leave room for improvement in order to go beyond the 0.1 eV confidence level. If different densities ρ_B are used for different states, the improvement of accuracy of the excitation energies requires that the errors due to violation of the non-negativity condition are reduced in both considered states. As shown in ref 27, the error due to the violation of the non-negativity condition for a given state can be efficiently reduced by means of polarizing ρ_B with an external electric field generated by the chromophore.

The present work shows that Protocol A can be improved systematically. Concerning other choices for the state-independent ρ_B polarizing it by the field generated by the chromophore in its ground state (Protocol B) represents already an improvement. Our attempt to find an optimal density of the environment for state-independent calculations in the form of the density obtained by polarizing it by a field corresponding to the density of the chromophore averaged over several lowest excited states (Protocol C) failed. Further reduction of errors is possible not by other ad hoc choices of a common density ρ_B but rather by using different ρ_B for different states. Protocols A, B, D, and E represent a series of methods corresponding to choices of ρ_B based on sound physical assumptions. These choices lead usually to a monotonic reduction of the overall errors in the excitation energies. In some cases, the errors do not behave monotonically along the series. We attribute these exceptions to the fact that the errors in the excitation energies are not only due to ρ_B but also due to the approximation used for the functionals ($E_{\mathrm{xct}}^{\mathrm{nad}}[\rho_A, \rho_B]$ and $v_{\mathrm{xct}}^{\mathrm{nad}}[\rho_A,\rho_B]$), which might result in different errors for different pairs ρ_A and ρ_B. We underline that the errors due to the choice of ρ_B and due to approximations for these functionals always combine in practice. Below the certain threshold (0.015 eV in our case), disentangling their individual contribution is not possible therefore. With Protocol A remaining the most efficient computationally and straightforward in practice, Protocol E emerges as its recommended improvement. It is comprehensively shown that the accuracy of excitation energies obtained using Protocol E which reflects differential polarization of ρ_B at different excited states are superior to that obtained from Protocol B in which the common ρ_B is used that takes into account the polarization only for the ground state. The average absolute error drops from 0.0395 ± 0.032 to 0.030 ± 0.026 eV. Especially encouraging is the fact that not only the average absolute

https://doi.org/10.1021/acs.jpca.2c07747
J. Phys. Chem. A 2023, 127, 535−545

errors are reduced along this series but also their standard deviations. The expense for this improvement is a significant increase of the computational costs and the non-orthogonality of the embedded wave functions corresponding to different states. In the case of state-dependent ρ_B, the evaluation of excitation energy for each state requires solving a quantum N_A-electron problem with a different external potential. As a result, the computational effort scales linearly with the number of states for which the excitation energy is evaluated. Given the fact that the gain in accuracy although systematic is not significant in absolute terms, the numerical examples provided in this work indicate that the choice between state-independent and state-dependent evaluation of excitation energy within the FDET formal framework must be made on the case-by-case basis. For most photochemical applications and simulations of the emission spectra, the potential energy surface for just one (the lowest) excited state is usually of principal interest. In the case of Protocol E, the computational effort in state-specific calculations is approximately doubled which is still applicable.The built in orthogonality of the ground and excited state makes it possible to evaluate the transition moments in a straightforward manner. For simulations of absorption spectra, on the other hand, state-specific calculations might be not worthwhile for the effort especially since the embedded wave functions for different excited states will not be mutually orthogonal. The magnitude of the effect of prepolarization on the excitation energy is usually in the range of 0.01−0.03 eV and is a small correction to the shifts evaluated without taking into account the polarization of ρ_B explicitly. The errors drop further if the polarization of ρ_B is state-specific—different field polarizing ρ_B are used for different electronic states of the chromophore. The magnitude of the drop in errors in such calculations is, however, much smaller—a few meV usually. Since state-specific polarization results in non-orthogonality of embedded wave functions corresponding to different electronic state, such calculations do not seem to be worth the additional effort. This conclusion is in line with observations reported by Goodpaster and collaborators.[11]

Finally, eq 14 can be applied for different methods to generate state-specific densities ρ_B. In the present work, the state-specific densities ρ_B were generated by means of polarizing the density of the environment by the electrostatic field generated by net atomic charges localized on the embedded species. For small environments state-specific ρ_B can be generated by inverting the role of the environment and the embedded species in the FDET equations and doing it either once or by means of the *freeze-and-thaw* cycle.[46] The polarizing field comprising not only the electrostatic component but the entire FDET embedding potential is available in such a case. Such approaches have been proposed and explored by Khait and Hoffman[35] and Neugebauer and collaborators.[30,31] Performing the freeze-and-thaw cycle to generate ρ_B is not practical if the size of the environment exceeds significantly that of the embedded species and it is not possible in multiscale methods, which use continuum description of the environment[19,20] or experimental electron densities.[21] Moreover, the freeze-and-thaw optimization of ρ_B cannot be interpreted as the electronic polarization because the change of ρ_B during such an optimization is the result of two effects, none of them directly related to the polarization: the reduction of the violation of the non-negativity condition of the target density[27] and the errors in the used approximation for the non-electrostatic component of the FDET embedding potential.[46] The first effect is not uniquely defined in the subsystem formulation of DFT[17] (see ref 28).

■ ASSOCIATED CONTENT

Supporting Information

The Supporting Information is available free of charge at https://pubs.acs.org/doi/10.1021/acs.jpca.2c07747.

Intermediate steps in the derivation of eq 14, data shown in the figures, and additional results obtained with larger additional basis sets (PDF)

atomic charges (.csv format) used to polarize ρ_B in different protocols (ZIP)

■ AUTHOR INFORMATION

Corresponding Authors

Mingxue Fu − *Department of Physical Chemistry, University of Geneva, CH-1211 4 Genève, Switzerland*; Email: Mingxue.Fu@unige.ch

Tomasz A. Wesolowski − *Department of Physical Chemistry, University of Geneva, CH-1211 4 Genève, Switzerland*; orcid.org/0000-0001-5792-4616; Email: Tomasz.Wesolowski@unige.ch

Complete contact information is available at: https://pubs.acs.org/10.1021/acs.jpca.2c07747

Notes

The authors declare no competing financial interest.

■ ACKNOWLEDGMENTS

The authors dedicate the present work to Prof. Vincenzo Barone, whose work on solvent effects on the electronic structure provided the long-standing inspiration of our interest in solvatchromism.

■ REFERENCES

(1) Nielsen, C. B.; Christiansen, O.; Mikkelsen, K. V.; Kongsted, J. Density functional self-consistent quantum mechanics/molecular mechanics theory for linear and nonlinear molecular properties: Applications to solvated water and formaldehyde. *J. Chem. Phys.* **2007**, *126*, 154112.

(2) Olsen, J. M.; Aidas, K.; Kongsted, J. Excited States in Solution through Polarizable Embedding. *J. Chem. Theory Comput.* **2010**, *6*, 3721−3734.

(3) Marenich, A. V.; Cramer, C. J.; Truhlar, D. G. Sorting Out the Relative Contributions of Electrostatic Polarization, Dispersion, and Hydrogen Bonding to Solvatochromic Shifts on Vertical Electronic Excitation Energies. *J. Chem. Theory Comput.* **2010**, *6*, 2829−2844.

(4) Steindal, A. H.; Ruud, K.; Frediani, L.; Aidas, K.; Kongsted, J. Excitation energies in solution: The fully polarizable QM/MM/PCM method. *J. Phys. Chem. B* **2011**, *115*, 3027−3037.

(5) Gordon, M. S.; Smith, Q. A.; Xu, P.; Slipchenko, L. V. Accurate First Principles Model Potentials for Intermolecular Interactions. *Annu. Rev. Phys. Chem.* **2013**, *64*, 553−578.

(6) Beerepoot, M. T. P.; Steindal, A. H.; Kongsted, J.; Brandsdal, B. O.; Frediani, L.; Ruud, K.; Olsen, J. M. H. A Polarizable Embedding DFT Study of One-Photon Absorption in Fluorescent Proteins. *Phys. Chem. Chem. Phys.* **2013**, *15*, 4735.

(7) Caricato, M.; Lipparini, F.; Scalmani, G.; Cappelli, C.; Barone, V. Vertical Electronic Excitations in Solution with the EOM-CCSD Method Combined with a Polarizable Explicit/Implicit Solvent Model. *J. Chem. Theory Comput.* **2013**, *9*, 3035−3042.

(8) Harczuk, I.; Murugan, N. A.; Vahtras, O.; Ågren, H. Studies of pH-Sensitive Optical Properties of the deGFP1 Green Fluorescent

Protein Using a Unique Polarizable Force Field. *J. Chem. Theory Comput.* **2014**, *10*, 3492−3502.
(9) Guareschi, R.; Valsson, O.; Curutchet, C.; Mennucci, B.; Filippi, C. Electrostatic versus Resonance Interactions in Photoreceptor Proteins: The Case of Rhodopsin. *J. Phys. Chem. Lett.* **2016**, *7*, 4547−4553.
(10) Loco, D.; Polack, É; Caprasecca, S.; Lagardère, L.; Lipparini, F.; Piquemal, J. P.; Mennucci, B. A QM/MM Approach Using the AMOEBA Polarizable Embedding: From Ground State Energies to Electronic Excitations. *J. Chem. Theory Comput.* **2016**, *12*, 3654−3661.
(11) Wen, X.; Graham, D. S.; Chulhai, D. V.; Goodpaster, J. D. Absolutely Localized Projection-Based Embedding for Excited States. *J. Chem. Theory Comput.* **2020**, *16*, 385−398.
(12) Bondanza, M.; Nottoli, M.; Cupellini, L.; Lipparini, F.; Mennucci, B. Polarizable embedding QM/MM: the future gold standard for complex (bio)systems? *Phys. Chem. Chem. Phys.* **2020**, *22*, 14433−14448.
(13) Kim, Y.; Bui, Y.; Tazhigulov, R. N.; Bravaya, K. B.; Slipchenko, L. V. Effective Fragment Potentials for Flexible Molecules: Transferability of Parameters and Amino Acid Database. *J. Chem. Theory Comput.* **2020**, *16*, 7735−7747.
(14) Scholz, L.; Neugebauer, J. Protein Response Effects on Cofactor Excitation Energies from First Principles: Augmenting Subsystem Time-Dependent Density-Functional Theory with Many-Body Expansion Techniques. *J. Chem. Theory Comput.* **2021**, *17*, 6105−6121.
(15) Phillips, J. C.; Kleinman, L. New Method for Calculating Wave Functions in Crystals and Molecules. *Phys. Rev.* **1959**, *116*, 287−294.
(16) Huzinaga, S.; Cantu, A. A. Theory of Separability of Many-Electron Systems. *J. Chem. Phys.* **1971**, *55*, 5543−5549.
(17) Cortona, P. Self-consistently determined properties of solids without band-structure calculations. *Phys. Rev. B* **1991**, *44*, 8454−8458.
(18) Wesolowski, T. A.; Warshel, A. Frozen density functional approach for ab initio calculations of solvated molecules. *J. Phys. Chem.* **1993**, *97*, 8050−8053.
(19) Kaminski, J. W.; Gusarov, S.; Wesolowski, T. A.; Kovalenko, A. Modeling Solvatochromic Shifts Using the Orbital-Free Embedding Potential at Statistically Mechanically Averaged Solvent Density. *J. Phys. Chem. A* **2010**, *114*, 6082−6096.
(20) Laktionov, A. A.; Chemineau-Chalaye, E.; Wesolowski, T. A. Frozen-density embedding theory with average solvent charge densities from explicit atomistic simulations. *Phys. Chem. Chem. Phys.* **2016**, *18*, 21069−21078.
(21) Ricardi, N.; Ernst, M.; Macchi, P.; Wesolowski, T. A. Embedding-theory-based simulations using experimental electron densities for the environment. *Acta Crystallogr., Sect. A* **2020**, *76*, 571−579.
(22) Wesołowski, T. A. Embedding a multideterminantal wave function in an orbital-free environment. *Phys. Rev. A* **2008**, *77*, 012504.
(23) Pernal, K.; Wesolowski, T. A. Orbital-free effective embedding potential: Density-matrix functional theory case. *Int. J. Quantum Chem.* **2009**, *109*, 2520−2525.
(24) Wesolowski, T. A. On the Correlation Potential in Frozen-Density Embedding Theory. *J. Chem. Theory Comput.* **2020**, *16*, 6880−6885.
(25) Wesolowski, T. A. Hydrogen-Bonding-Induced Shifts of the Excitation Energies in Nucleic Acid Bases: An Interplay between Electrostatic and Electron Density Overlap Effects. *J. Am. Chem. Soc.* **2004**, *126*, 11444−11445.
(26) Zech, A.; Ricardi, N.; Prager, S.; Dreuw, A.; Wesolowski, T. A. Benchmark of Excitation Energy Shifts from Frozen-Density Embedding Theory: Introduction of a Density-Overlap-Based Applicability Threshold. *J. Chem. Theory Comput.* **2018**, *14*, 4028−4040.
(27) Ricardi, N.; Gonzalez-Espinoza, C. E.; Wesolowski, T. A. N-representability of the target density in Frozen-Density Embedding Theory based methods: Numerical significance and its relation to electronic polarization. *J. Chem. Phys.* **2022**, *157*, 064108.
(28) Wesolowski, T. A.One-Electron Equations for Embedded Electron Density: Challenge for Theory and Practical Payoffs in Multi-Level Modelling of Complex Polyatomic Systems. In *Computational Chemistry: Reviews of Current Trends*; Leszczynski, J., Ed.; World Scientific, 2006; Vol. *10*; pp 1−82. DOI: 10.1142/9789812773876_0001.
(29) Fu, M.; Wesolowski, T. A. The Challenge of Accurate Computation of Two-Photon Absorption Properties of Organic Chromophores in the Condensed Phase. *J. Chem. Theory Comput.* **2021**, *17*, 3652−3665.
(30) Daday, C.; König, C.; Valsson, O.; Neugebauer, J.; Filippi, C. State-specific embedding potentials for excitation-energy calculations. *J. Chem. Theory Comput.* **2013**, *9*, 2355−2367.
(31) Daday, C.; König, C.; Neugebauer, J.; Filippi, C. Wavefunction in Density Functional Theory Embedding for Excited States: Which Wavefunctions, which Densities? *ChemPhysChem* **2014**, *15*, 3205−3217.
(32) Dresselhaus, T.; Neugebauer, J. Part and whole in wave-function/DFT embedding. *Theor. Chem. Acc.* **2015**, *134*, 97.
(33) Wesolowski, T. A. Embedding potentials for excited states of embedded species. *J. Chem. Phys.* **2014**, *140*, 18A530.
(34) Perdew, J. P.; Levy, M. Extrema of the density functional for the energy: Excited states from the ground-state theory. *Phys. Rev. B* **1985**, *31*, 6264−6272.
(35) Khait, Y. G.; Hoffmann, M. R. Embedding theory for excited states. *J. Chem. Phys.* **2010**, *133*, 044107.
(36) Zech, A.; Aquilante, F.; Wesolowski, T. A. Orthogonality of embedded wave functions for different states in frozen-density embedding theory. *J. Chem. Phys.* **2015**, *143*, 164106.
(37) Ricardi, N.; Zech, A.; Gimbal-Zofka, Y.; Wesolowski, T. A. Explicit vs. implicit electronic polarisation of environment of an embedded chromophore in frozen-density embedding theory. *Phys. Chem. Chem. Phys.* **2018**, *20*, 26053−26062.
(38) Shao, Y.; Gan, Z.; Epifanovsky, E.; Gilbert, A. T.; Wormit, M.; Kussmann, J.; Lange, A. W.; Behn, A.; Deng, J.; Feng, X.; et al. Advances in molecular quantum chemistry contained in the Q-Chem 4 program package. *Mol. Phys.* **2015**, *113*, 184−215.
(39) Dunning, T. H. Gaussian basis sets for use in correlated molecular calculations. I. The atoms boron through neon and hydrogen. *J. Chem. Phys.* **1989**, *90*, 1007−1023.
(40) Wesolowski, T. A. Density functional theory with approximate kinetic energy functionals applied to hydrogen bonds. *J. Chem. Phys.* **1997**, *106*, 8516−8526.
(41) Dirac, P. A. M. Note on Exchange Phenomena in the Thomas Atom. *Mathematical Proceedings of the Cambridge Philosophical Society* **1930**, *26*, 376−385.
(42) Vosko, S. H.; Wilk, L.; Nusair, M. Accurate spin-dependent electron liquid correlation energies for local spin density calculations: a critical analysis. *Can. J. Phys.* **1980**, *58*, 1200−1211.
(43) Thomas, L. H. *calculation of atomic fields. Mathematical Proceedings of the Cambridge Philosophical Society* **1927**, *23*, 542−548.
(44) Fermi, E. Eine statistische Methode zur Bestimmung einiger Eigenschaften des Atoms und ihre Anwendung auf die Theorie des periodischen Systems der Elemente. *Zeitschrift für Physik* **1928**, *48*, 73−79.
(45) Breneman, C. M.; Wiberg, K. B. Determining atom-centered monopoles from molecular electrostatic potentials. The need for high sampling density in formamide conformational analysis. *J. Comput. Chem.* **1990**, *11*, 361−373.
(46) Wesolowski, T. A.; Weber, J. Kohn-Sham equations with constrained electron density: an iterative evaluation of the ground-state electron density of interacting molecules. *Chem. Phys. Lett.* **1996**, *248*, 71−76.

Chapter 6

Fine-tuning of entangled two-photon absorption by controlling the one-photon absorption properties of the chromophore

6.1 Motivation and outcome

The classical photon pairs in two-photon absorption (TPA) can be replaced with the time-frequency- entangled photon pairs (ETPA). However, ETPA phenomenon is not well understood in both experimental and theoretical studies, such as the question of *why some chromophores exhibit large TPA activities in the classical case but no TPA activities in the entangled case.*

The ETPA cross-section obtained quantum mechanically is not an absolute value but exhibits periodic oscillations depending on the entanglement time. In certain cases, its magnitude drops to several orders of magnitude, resulting in ETPA transparency. Our goal is to establish the relationship between ETPA transparency and the electronic structure of the molecule. We found that the electronic structure of the molecular sample, specifically the presence of two dominant intermediate states, determines the oscillation of the ETPA cross-section. A simple relation based on the ETPA transition amplitude was developed, which has the potential to switch on/off ETPA transparency using only one-photon properties.

Reprint of the paper is provided in the following pages. [Fu M, D. Tabakaev, R. T. Thew, and T. A. Wesolowski, *J. Phys. Chem. Lett.* 14, 2613-2619 (2023)]

Supporting information for this paper can be found in Appendix F.

THE JOURNAL OF PHYSICAL CHEMISTRY LETTERS
A JOURNAL OF THE AMERICAN CHEMICAL SOCIETY

pubs.acs.org/JPCL

Letter

Fine-Tuning of Entangled Two-Photon Absorption by Controlling the One-Photon Absorption Properties of the Chromophore

M. Fu,* D. Tabakaev, R. T. Thew, and T. A. Wesolowski*

Cite This: *J. Phys. Chem. Lett.* 2023, 14, 2613−2619

Read Online

ACCESS | Metrics & More | Article Recommendations | Supporting Information

ABSTRACT: The detailed analysis of the sum-over-state formula for the entanglement-induced two-photon absorption (ETPA) transition moment shows that the magnitude of the ETPA cross-section is expected to vary significantly depending on the coherence time T_e and the relative position of just two electronic states. Moreover, the dependency on T_e is periodic. These predictions are confirmed by molecular quantum mechanical calculations for several chromophores.

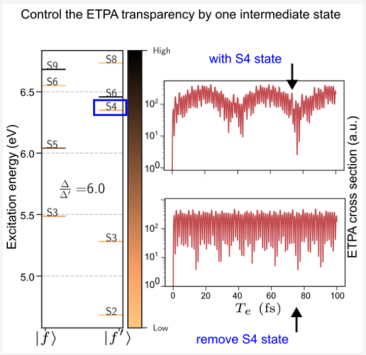

Since the seminal work of M. Göppert-Mayer on the two-photon absorption formalism and its later generalization for the case of entangled pairs,[1−3] there have been multiple attempts to describe the mechanism and properties of entangled two-photon absorption (ETPA) .[4−12] The interest in ETPA was sparked by the potential for a significant increase in efficiency for the absorption process compared to the classical case. These studies have progressively tried to better develop our understanding of this process, but have mostly focused either on possible applications of ETPA, or the optical part of the absorption/excitation process. Beyond this, there has also been some work to find agreement between the calculated ETPA cross-section values and the experimental ones using numerical approaches with the aim of finding a possible mechanism that would allow for the identification of ETPA-sensitive molecules.[13,14]

In other studies, attempts have been made to put some bounds on expected values to gauge why some experiments observe ETPA and others do not.[15,16] This was also motivated by an attempt to understand the large variation−sometimes several orders of magnitude - in the observed values for some ETPA cross-sections,[17] which built on the seminal work of Fei et al.[3] This focused on the connection between the observed and microscopic cross-sections $\varsigma_e = f\frac{\langle\sigma_e\rangle}{AT_e}$, where T_e is the coherence time, A is what is referred to as the entanglement area, which, in practical terms, corresponds to the area of the excitation beam,[18] and f is a correction factor that takes into account possible contributions such as the ratio between the pump and entangled photon bandwidths.

Clearly, the factor AT_e plays a fundamental role in the efficiency of this process and exploiting that will be key for practical schemes.[19] However, another potential explanation for the origin of the variations for the observed ETPA cross-sections has been attributed to the so-called ETPA transparency,[3] which is also related, albeit quite differently, to the photon pair coherence time T_e, giving rise to an harmonic behavior that connects the light−matter interaction. The aim of this work is to relate the observed nonmonotonicity of $\langle\sigma_e(T_e)\rangle$ to the properties of the chromophore, its excited states in particular, in order to identify the origin of such behavior.

The second-order perturbation[11,20] of the light-matter interaction Hamiltonian is given in its general form[7,11]

$$\hat{H}(t) = -\hat{d}\hat{E}(t) + \text{h.c.} \tag{1}$$

where $\hat{d}$ is the dipole-moment operator and E is an electric field operator. In the experimentally relevant case, spontaneous parametric down-conversion is used to generate the signal and idler photons comprising, in general, energy-time entangled pairs.[21] Below, we consider only energy-time entangled pairs as the most general case and do not take into account any other degrees of freedom. A positive-frequency electric field operator of such pairs is the sum of individual operators for signal and idler[22] given as

Received: January 30, 2023
Accepted: February 28, 2023
Published: March 8, 2023

https://doi.org/10.1021/acs.jpclett.3c00272
J. Phys. Chem. Lett. 2023, 14, 2613−2619

$$\hat{E}_{1,2}(t) = \int d\omega_{1,2} \sqrt{\frac{\hbar\omega_{1,2}}{4\pi\epsilon_0 cA}}\, \hat{a}_{1,2}\, \exp^{-i\omega_{1,2}t} \tag{2}$$

where, $\hat{a}_{1,2}$ is the annihilation operator of signal and idler photons with frequencies $\omega_{1,2}$, c is the speed of light, A is the interaction area, and ϵ_0 is a vacuum permittivity. The classical TPA transition moments for two resonant photons are given within the framework for the linear and quadratic responses[23] as

$$M_{a,b}^{\mathrm{TPA}} = \sum_k \left[\frac{\langle 0|\hat{\mu}^a|k\rangle\langle k|\hat{\mu}^b|f\rangle}{\Delta_1^k} + \frac{\langle 0|\hat{\mu}^b|k\rangle\langle k|\hat{\mu}^a|f\rangle}{\Delta_2^k} \right] \tag{3}$$

For the entangled two-photon case, the corresponding matrix elements are given as[3]

$$M_{a,b}^{\mathrm{ETPA}} = \sum_k \left[\frac{D_k^{a,b}(1 - e^{-iT_e\Delta_1^k - T_e\kappa^k/2})}{\Delta_1^k} + \frac{D_k^{b,a}(1 - e^{-iT_e\Delta_2^k - T_e\kappa^k/2})}{\Delta_2^k} \right] \tag{4}$$

where $D_k^{a,b} = \langle 0|\hat{\mu}^a|k\rangle\langle k|\hat{\mu}^b|f\rangle = \vec{\mu}_{0k}^a\vec{\mu}_{kf}^b$, $\hat{\mu}^i$ (i = x, y, or z) are the Cartesian components of the dipole moment operator, $|k\rangle$ denotes the kth intermediate state, κ^k is the lifetime of the kth intermediate state, and $\Delta_{1,2}^k$ denotes the detuning energy $\Delta_{1,2}^k = \omega_k - \omega_{1,2}$.

From now we consider only the degenerate photon case in eq 4, for which $\omega_1 = \omega_2 = \frac{1}{2}\Omega_f$ and $\Delta_k = \Delta_{1,2}^k$, where Ω_f is the resonance frequency for one-photon absorption. The $e^{-T_e\kappa^k/2}$ term in the numerator has a sufficiently minor influence on ETPA cross-section that it can be neglected.[14] Neglecting it leads to an approximate form of eq 4, which, upon explicitly including the ground state $|0\rangle$ and final state $|f\rangle$, leads to the so-called "two-pathway"[24] expression:

$$M'_{a,b} = M_{a,b}^{\mathrm{ETPA}'} = 4i\frac{e^{-\frac{iT_e\Omega_f}{4}}}{\Omega_f}\sin\left(\frac{T_e\Omega_f}{4}\right)[\vec{\mu}_{0f}^a(\vec{\mu}_{ff}^b - \vec{\mu}_{00}^b) + \vec{\mu}_{0f}^b(\vec{\mu}_{ff}^a - \vec{\mu}_{00}^a)] + \sum_{k\neq 0,f} 2i\frac{e^{-\frac{iT_e\Delta_k}{2}}}{\Delta_k}\sin\left(\frac{T_e\Delta_k}{2}\right) \times (D_k^{a,b} + D_k^{b,a}) \tag{5}$$

If only the final state $|f\rangle$ contributes to the sum, the ETPA cross-section is proportional to the permanent dipole difference $\vec{\mu}_{ff} - \vec{\mu}_{00}$ in the ground and final states. This can be considered as a "two-state model". The square module of $M'_{a,b}$, corresponding to the transition probability, oscillates rapidly with a period equal to $4\pi/\Omega_f$. If σ_e shows a periodic dependence on T_e, the period can be interpreted as the oscillation period of the wave packet. These rapid oscillations with a period in the order of a few fs lead to the entanglement-induced TPA transparency. This happens usually for charge-transfer excitations for which excitation energies of other intermediate states are off resonance.

In eq 5, the coupling $|\lambda\cdot M'_{a,b}|^2$ between the polarization λ of the incident light and the orientation of the molecules are not considered and it gives the transition moment in the molecular coordinate system. Taking orientation effects of the laboratory and molecular system of coordinates into account yields the rotationally averaged expression for the ETPA cross-section:[25]

$$\langle\sigma_e\rangle = \frac{1}{30}\sum_{a,b}[F\cdot M'_{a,a}M'^*_{b,b} + G\cdot M'_{a,b}M'^*_{a,b} + H\cdot M'_{a,b}M'^*_{b,a}] \tag{6}$$

with $F = G = H = 2$ for parallel polarization of the light and $F = H = -1$, $G = 4$ for the perpendicular polarization.

In order to identify the key element that determines the oscillation period of the wave packet, we note that the summation over a, b in eq 6 does not affect the detuning energy. The oscillation period of the individual sin functions in eq 5 affects only the weight in front of each periodic function. The oscillation period of the averaged ETPA cross-section $\langle\sigma_e\rangle \propto \|M'_{a,b}\|^2$ can thus be determined as the following compact equation:

$$\|M'_{a,b}\|^2 = 4\left\{\sum_k \sin^2\left(\frac{T_e\Delta_k}{2}\right)\left(\frac{\mathcal{D}_k^{a,b}}{\Delta_k}\right)^2 + \sum_{k_1,k_2,k_1<k_2}\left[\left(\cos^2\left(\frac{T_e(\Delta_{k_1} - \Delta_{k_2})}{2}\right) - \frac{1}{2}\right)(\cos(T_e\Delta_{k_1}) + \cos(T_e\Delta_{k_2}))\right]\frac{\mathcal{D}_{k_1}^{a,b}\mathcal{D}_{k_2}^{a,b}}{\Delta_{k_1}\Delta_{k_2}}\right\} \tag{7}$$

where $\mathcal{D}_k^{a,b} = D_k^{a,b} + D_k^{b,a}$.

Most of the previous analysis of the relation between the molecular properties and the transition moments in the above formula considered only three states, "three-state-model".[3] Below, we make a few observations concerning eq 7. If there is only one intermediate state contributing to the sum-over-state expression, this intermediate state can possibly mitigate the transparency phenomenon. Because if the intermediate state energy is close to the incident photon frequency, supposing $\Delta_k = \omega_k - \frac{1}{2}\Omega_f \approx 1/10\Omega_f$, then $T_1 = 4\pi/\Omega_f$ and $T_2 = 2\pi/\Delta_k$ show that the oscillation period can be 20 times larger than that of permanent dipole pathway (the first term in the right-hand-side in eq 5).

However, a detailed analysis on a more than "three-state model" has not been made so far, and the relation between the electronic structure of chromophores and T_e has not been established yet. Molecular quantum mechanics calculations make it possible to access all relevant states in eq 7. To fill this gap, we take a closer look at eq 7. The effect of multiple intermediate states on the ETPA cross-section is represented by the terms in the second term in the right-hand-side of eq 7. $\|M'_{a,b}\|^2$ is given by a sum of periodic functions of T_e. In such a case, the period of the slowest oscillations is determined by the function with the longest period, which is $\left|\frac{\Delta_{k_1} - \Delta_{k_2}}{2}\right|$. The first line in eq 7 usually does not affect the period of the slowest oscillations.

The second term in the right-hand-side of eq 7 originates from the coupling between different intermediate states. It indicates a possible benefit of molecular quantum mechanical calculations. They can determine the energies and transition

https://doi.org/10.1021/acs.jpclett.3c00272
J. Phys. Chem. Lett. 2023, 14, 2613−2619

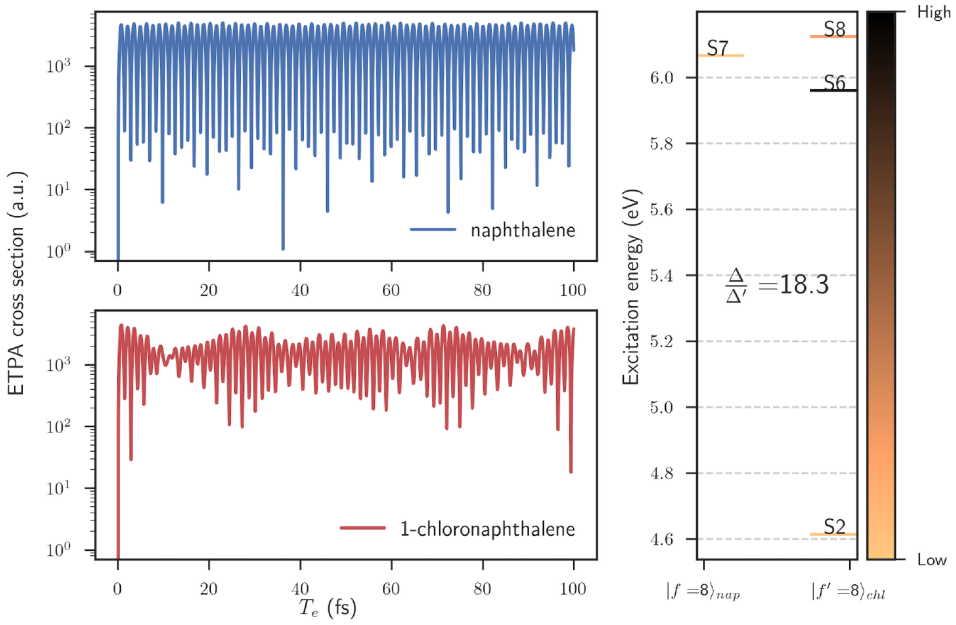

Figure 1. ETPA cross-section of naphthalene and 1-chloronaphthalene molecule as a function of the coherence time T_e, and the electronic structure of the corresponding dominant intermediate states. The same target state in both molecules is considered. Color bar on the right indicates the weight of each intermediate state contribution. The detuning energy $\Delta_{S7} = \epsilon_{S7} - \frac{1}{2}\Omega_{S8}$ for naphthalene and the energy difference $\Delta' = \epsilon_{S8} - \epsilon_{S6}$ for 1-chloronaphthalene were considered.

moments for different intermediate states and, thus, the smallest value of $\left|\frac{\Delta_{k_1} - \Delta_{k_2}}{2}\right|$ for two dominant excited states. Note that $|\Delta_{k_1} - \Delta_{k_2}|$ in the degenerate photon-pair case does not depend on the incident photon frequency and only depends on the excitation energy (ϵ) difference $|\epsilon_{k_1} - \epsilon_{k_2}|$ of these two dominant excited states.

The above considerations suggest that a relatively simple relation between the coherence time and $|\epsilon_{k_1} - \epsilon_{k_2}|$ could be expected. In order to verify this, $\langle\sigma_e(T_e)\rangle$ has been evaluated for several chromophores differing in their spectrum by the number of intermediate states contributing to $\langle\sigma_e(T_e)\rangle$ and/or their relative position on the energy scale of the one-photon absorption levels with respect to the target state. To demonstrate the possibility to control the period of $\langle\sigma_e(T_e)\rangle$ by fine-tuning the one-photon absorption states, pairs of systems were considered in which the position of the intermediates states were perturbed by either intermolecular interactions (free and complexed chromophores) or by the chemical modification of the chromophore. In such a case, we use the following convention Δ*d*enotes the energy differences $\Delta = |\epsilon_{k_1} - \epsilon_{k_2}|$ for nonperturbed chromophore and Δ' for the perturbed case.

The correlated excited state method of the Algebraic Diagrammatic Construction (ADC) family in the second order ADC(2)[26] was employed to calculate the excitation energies and transition dipoles. The correlation-consistent augmented basis set aug-cc-pVDZ developed by Dunning and Woon[27] was used. In all sum-over-state expressions considered in the present work, at least 10 electronic states were used. This number of states was chosen based on the agreement of the transition moments obtained from eq 3 truncated to either 10 or 20 states with the moments obtained from the matrix inversion. For each considered chromophore, the analyses were made for the final target state ($|f\rangle$) chosen in such a way that (*i*) the state shows a substantial TPA cross-section compared with other excited states, for example, with the final state of A_g or B_{2g} symmetry in a D_{2h} group; (*ii*) the same orbitals are involved in the excitation in the corresponding pairs of systems. The optimized structures of the molecules and computational details are listed in the Supporting Information. The pair of systems for which the analysis of the dependence of $\langle\sigma_e\rangle$ on T_e made in this section is naphthalene (D_{2h} symmetry) and 1-chloronaphthalene (C_s symmetry). For naphthalene, the maximum $\langle\sigma_e\rangle$ = 5035 au corresponds to S8 (A_g symmetry) for which Figure 1 shows rapid oscillations of $\langle\sigma_e\rangle$ with the magnitude dropping 1 order of magnitude in one cycle. According to the analysis of eq 7 given in the previous section, we can attribute the very short oscillation period (1.4 fs) to only one intermediate state which is S7 in case of naphthalene (see Figure 1). For 1-chloronaphthalene, the oscillation period is extended to 27.3 fs with the peak ETPA cross-section reduced slightly to 4435 au. In this case, more intermediate states (S2, S6, S8) couple to the final state (S8). As a result, the overall ETPA cross-section fluctuates much less than that in the naphthalene case. The additional intermediate states (S6 and S8) in 1-chloronaphthalene determine the slowest oscillation period of this molecule. The ratio between the detuning energy of naphthalene $\left(\Delta_{S7} = \epsilon_{S7} - \frac{1}{2}\Omega_{S8}\right)$ and $\Delta'(\epsilon_{S8} - \epsilon_{S6})$ of 1-chloronaphthalene determines the ratio between the oscillation periods for the two molecules. In this case, $\frac{\Delta}{\Delta'} = \frac{\Delta_{S7}}{\Delta'(\epsilon_{S8} - \epsilon_{S6})} = 18.3$. The ratio of the oscillation periods between 1-chloronaphthalene and naphthalene (see Figure 1) is 17.3. The small deviation between the two numbers

https://doi.org/10.1021/acs.jpclett.3c00272
J. Phys. Chem. Lett. 2023, 14, 2613−2619

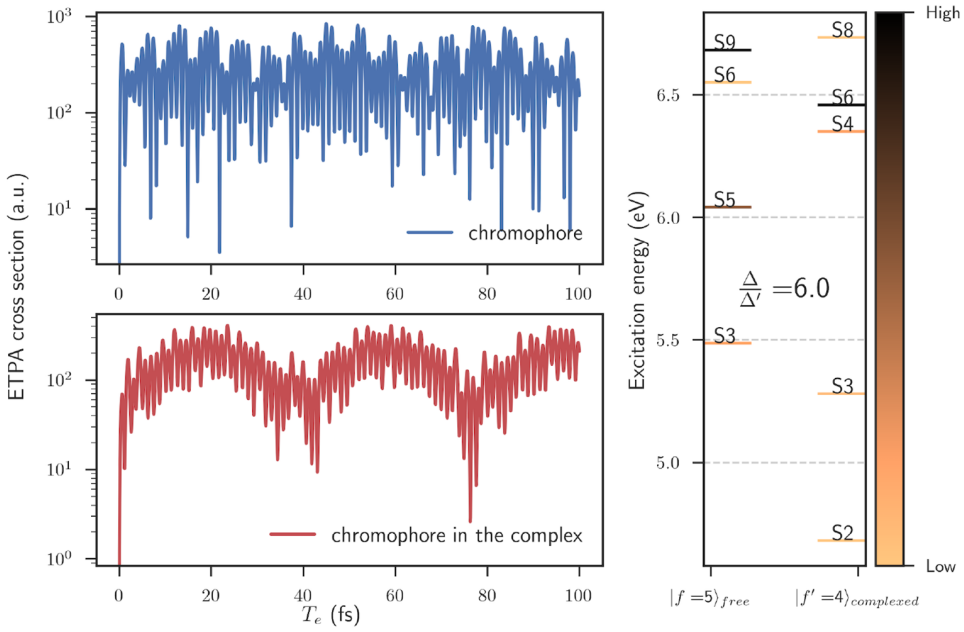

Figure 2. ETPA cross-section of benzaldehyde and the benzaldehyde-2H_2O complex as a function of the coherence time T_e. On the right is the electronic structure of the corresponding dominant intermediate states. The horizontal axis labels the target state $|f\rangle$ for the chromophore in a free and complexed form. Color bar on the right indicates the weight of each intermediate state contribution. $\Delta = \epsilon_{S9} - \epsilon_{S5}$ for the free and $\Delta' = \epsilon_{S6} - \epsilon_{S4}$ for the complexed were considered.

originates from the contributions of other less dominant intermediate states.

In this section, we consider another type of perturbation of the electronic structure of the chromophore which is due to intermolecular interactions. The pairs of systems considered in the discussion of the dependence of $\langle\sigma_e\rangle$ on T_e are the free chromophore and the chromophore in the complex. The same geometry of the chromophore in the complex was used for the calculation of the free chromophore in order to study only the electronic effects. We found the most prominent environment effect in benzaldehyde-2H_2O complex of all systems, as shown in Figure 2. In both free and complexed chromophores, several intermediate states contribute to the final state. The ratio $\frac{\Delta}{\Delta'} = 6$ was calculated with $\Delta(\epsilon_{S9} - \epsilon_{S5})$ for the free and $\Delta'(\epsilon_{S6} - \epsilon_{S4})$ for the complexed chromophore. For the evaluation of the ratio, the excited state S6 of the free benzaldehyde molecule was not considered because its contribution is smaller than that of S5 (see Figure 2).

The maximum microscopic ETPA cross-section for the free benzaldehyde molecule drops from 841 au to 408 au for the benzaldehyde in the complex. The fluctuation of ETPA cross-section is also reduced. The oscillation period for the free (6.9 fs) is 6.3 times shorter than that for the complexed chromophore (43.6 fs). We point out that the sinusoidal shape of the ETPA cross-section of this chromophore in the complex (left corner in Figure 2) makes it most useful for making predictions of cross-sections. It originates from a) the small excitation energy difference between the state S4 and S6; b) a state S4 with a much smaller weight than the state S6. In the case of the small excitation energy difference, the weight depends mostly on the transition dipole moment. The magnitude of the transition dipole of state S4 is 18 times smaller than the state S6.

Table 1 lists the target state $|f\rangle$, the maximum averaged microscopic ETPA cross-sections $\langle\sigma_e\rangle$, the oscillation period P, and the ratio $\frac{\Delta}{\Delta'}$ determined from the difference in excitation energies of the dominant intermediate states k_1, k_2 for all the systems studied here. For all the chromophores, the maximum ETPA cross-section is affected by the surrounding environment. Noticeably, all the chromophores have $\frac{\Delta}{\Delta'} \geq 1$. The period of the complexed chromophore is expected to be either the same or larger than that of the free one. The larger $\frac{\Delta}{\Delta'}$ is, the

Table 1. Oscillation Period P (in fs) and the Ratio of the Energy Differences $\left(\frac{\Delta}{\Delta'}\right)$ between the Free Chromophore and the Chromophore in the Complex for All Systems ($\Delta = |\epsilon_{k_1} - \epsilon_{k_2}|$)[a]

structures	f	k_1, k_2	$\langle\sigma_e\rangle$	period	Δ/Δ'
ethylene	S6	S1,S4	2792	6.1	1.0
ethylene-H_2O	S6	S2,S4	3005	5.9	
pyrazine (D_{2h})	S10	S14,S16	1464	17.4	2.1
pyrazine-H_2O	S11	S16,S17	1349	42.6	
pyrimidine (C_{2v})	S11	S11,S14	580	16.0	2.9
pyrimidine-H_2O	S12	S12,S13	299	53.6	
7-hydroxyquinoline	S8	S7,S8	3964	20.0	1.2
7-hydroxyquinoline-H_2O	S8	S6,S8	4455	23.1	
7-hydroxyquinoline	S8	S7,S8	3876	20.0	1.1
7-hydroxyquinoline-NH_3	S8	S6,S8	5433	21.0	
benzaldehyde	S5	S9,S5	841	6.9	6.0
benzaldehyde-2H_2O	S4	S6,S4	408	43.6	
dimethylaminopyridinium cation	S4	S1,S2	1248	31.1	1.1
dimethylaminopyridinium cation-4H_2O	S5	S1,S2	1286	34.5	

[a] f denotes the target state, k_1, k_2 are two dominant intermediate states, and $\langle\sigma_e\rangle$ (in atomic units) is the averaged ETPA cross-sections in the target state.

https://doi.org/10.1021/acs.jpclett.3c00272
J. Phys. Chem. Lett. 2023, 14, 2613−2619

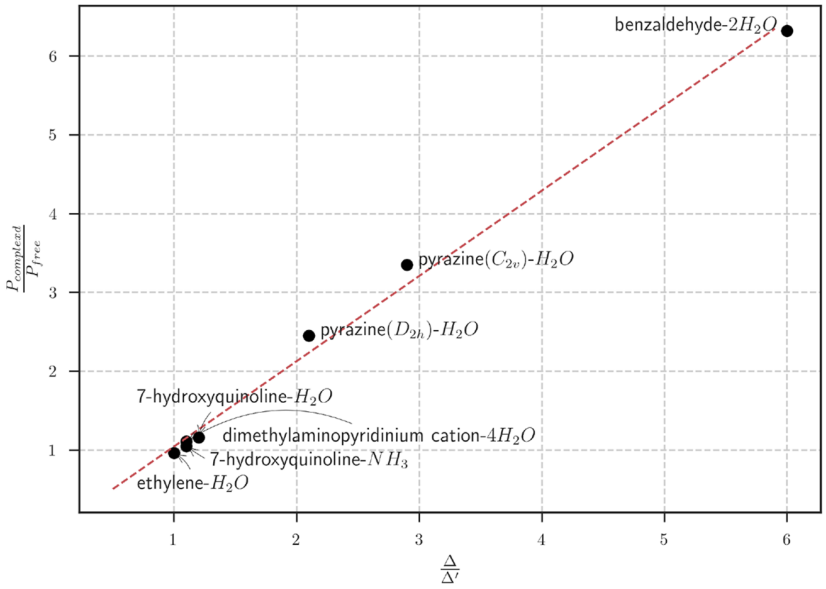

Figure 3. Correlation between the ratio $\frac{\Delta}{\Delta'}$ determined from the electronic structure of the chromophore and the ratio of the period $\frac{P_{\text{complexed}}}{P_{\text{free}}}$ of ETPA cross-sections for all chromophores in free and complexed forms.

smaller the maximum ETPA cross-sections of the complexed chromophore. For instance, in benzaldehyde-$2H_2O$ and pyrimidine-H_2O, $\frac{\Delta}{\Delta'}$ is relatively large (6.0 and 2.9, respectively). The maximum ETPA cross-sections in the complex drop to 48% and 52% of its free chromophore value.

In the remaining complexes, ethylene-H_2O, 7-hydroxyquinoline-H_2O, 7-hydroxyquinoline-NH_3, and dimethylaminopyridinium cation-$4H_2O$, with the ratio $\frac{\Delta}{\Delta'}$ being close to 1, the maximum ETPA cross-section is larger in the complex, especially for 7-hydroxyquinoline-NH_3 (about 40% increase) compared with the free chromophore. Both free 7-hydroxyquinoline in H_2O or NH_3 complexes show the identical period of 20.0 fs, because Δ is almost not affected by the complexation. The difference between excitation energies of the dominant intermediate states for the chromophore in different environments is less than 0.001 eV. We notice, however, an effect of the complexation on the maximum ETPA cross-sections due to the change in the transition dipole moments. The molecules complexed to the chromophore (either H_2O or NH_3) increase the maximum ETPA cross-section of the isolated 7-hydroxyquinoline chromophore while the period P increases only slightly.

For the pyrazine and pyrimidine cases, the ratio $\frac{\Delta}{\Delta'}$ is larger than two. The complexation with the H_2O molecule leads to the increase of the period (P) and the decrease of the peak ETPA cross-section. For some chromophores, however, the ETPA properties, are not affected significantly by the complexation, ethylene-H_2O and dimethylaminopyridinium cation-$4H_2O$, for instance. For ethylene, the peak ETPA cross-section increases by 7.6%, whereas it increases by only 3% for dimethylaminopyridinium cation. For both systems, the ratio $\frac{\Delta}{\Delta'}$ is close to 1 indicating a slight change in the oscillation period.

Figure 3 summarizes the observations concerning the numerical examples. It shows a linear relation between the ratio $\frac{\Delta}{\Delta'}$ and the ratio of the period $\frac{P_{\text{complexed}}}{P_{\text{free}}}$. The former is determined by perturbation of the one-photon absorption properties of the chromophore, whereas the latter is crucially linked to the experimental conditions.

The numerical results show that

(1) The period of the ETPA cross-section oscillations, as a function of photon-pair coherence time, depends on the number of intermediate states involved in the ETPA transition.

(2) Both the amplitude and the period of this oscillation are strongly affected by the intermolecular electronic interactions.

Concerning point 1, breaking the symmetry of a molecule can introduce more intermediate states, that couple with the final state in the sum-over-state expression. As a result, the wave packet behavior of ETPA cross-sections is affected, as clearly shown in the change of the dependency of the ETPA cross-section on T_e. It comes, however, at the price of a reduced amplitude of the cross-sections. One way to resolve this problem is to substitute one atom (hydrogen, e.g.) with a heavier atom.

Concerning point 2, the intermolecular interactions influence the spectrum of excited states. Two nearest dominant intermediate states that has the largest effect on the wavepacket behavior of ETPA cross-section. The oscillation period is inversely proportional to the position of these two states, more specifically Δ and $\Delta = |\epsilon_{k_1} - \epsilon_{k_2}|$.

The intermolecular electronic interactions demonstrated a non-negligible role in the tuning of the microscopic ETPA cross-sections. The ETPA cross-section can be easily predictable, or show the least variation, if there exists at least two dominant intermediate states, and the excitation energy of these two dominant states should be close, while the wave function or the excitation character of these two states differs as much as possible. This could potentially provide an

https://doi.org/10.1021/acs.jpclett.3c00272
J. Phys. Chem. Lett. 2023, 14, 2613−2619

opportunity to tune or switch on/off the complex ETPA process by modifying only one-photon absorption properties.

The simple relation between the properties of just two excites states of the chromophore and its ETPA cross-section properties was demonstrated using a small set of chromophores and a "middle-of-the-road" method from the molecular quantum mechanics toolbox (ADC(2)). This assures us that properties of the considered electronic states (their order and transition moments) used in the sum-over-state expressions are free from qualitative failures for some excitations as it is frequently the case of methods based on the liner-response time-dependent density-functional theory. We believe, therefore, that using better methods to model excited states than ADC(2) would not invalidate the existence of such a simple relation. Another important approximation used in this work is neglecting the vibrionic effects. The analysis was made for the electronic states obtained within the Born−Oppenheimer approximation at the equilibrium geometries. The vibronic effects were comprehensively shown to contribute significantly to the TPA cross-sections in the case of branched chromophores[28] in which large coupling between electronic and vibrational modes is expected (large bond length alternation and similar vibrational modes localized on different branches). It is not the case of the chromophores considered in this work. In principle, the numerical estimation of the effect of vibronic coupling on the relation demonstrated in the present work could be made following the approach proposed in ref 28.

■ ASSOCIATED CONTENT

Supporting Information

The Supporting Information is available free of charge at https://pubs.acs.org/doi/10.1021/acs.jpclett.3c00272.

Geometry of all chromophores; microscopic ETPA cross-sections varied by the coherence time and the corresponding electronic structure for all the complexes (PDF)

Transparent Peer Review report available (PDF)

■ AUTHOR INFORMATION

Corresponding Authors

M. Fu − *Department of Physical Chemistry, University of Geneva, CH-1211 Geneva, Switzerland*; Email: Mingxue.Fu@unige.ch

T. A. Wesolowski − *Department of Physical Chemistry, University of Geneva, CH-1211 Geneva, Switzerland*; orcid.org/0000-0001-5792-4616; Email: Tomasz.Wesolowski@unige.ch

Authors

D. Tabakaev − *Department of Applied Physics, University of Geneva, CH-1211 Geneva, Switzerland*

R. T. Thew − *Department of Applied Physics, University of Geneva, CH-1211 Geneva, Switzerland*

Complete contact information is available at: https://pubs.acs.org/10.1021/acs.jpclett.3c00272

Notes

The authors declare no competing financial interest.

■ ACKNOWLEDGMENTS

We thank Géraldine Haack for fruitful discussions at the beginning of this work. R.T.T. and D.T. acknowledge partial financial support from the Swiss National Science Foundation through the Sinergia grant CRSII5-170981 and the EU Horizon 2020 research and Innovation - QuantERA II - Programme under Grant Agreement No 101017733.

■ REFERENCES

(1) Gea-Banacloche, J. Two-photon absorption of nonclassical light. *Phys. Rev. Lett.* **1989**, *62*, 1603−1606.

(2) Javanainen, J.; Gould, P. L. Linear intensity dependence of a two-photon transition rate. *Phys. Rev. A* **1990**, *41*, 5088−5091.

(3) Fei, H.; Jost, B. M.; Popescu, S.; Saleh, B. E. A.; Teich, M. C. Entanglement-induced two-photon transparency. *Phys. Rev. Lett.* **1997**, *78*, 1679−1682.

(4) Saleh, B. E.; Jost, B. M.; Fei, H.-B.; Teich, M. C. Entangled-photon virtual-state spectroscopy. *Phys. Rev. Lett.* **1998**, *80*, 3483.

(5) Kojima, J.; Nguyen, Q.-V. Entangled biphoton virtual-state spectroscopy of the A2Σ+−X2Π system of OH. *Chem. Phys. Lett.* **2004**, *396*, 323−328.

(6) Roslyak, O.; Mukamel, S. Multidimensional pump-probe spectroscopy with entangled twin-photon states. *Phys. Rev. A* **2009**, *79*, 063409.

(7) Roslyak, O.; Marx, C. A.; Mukamel, S. Nonlinear spectroscopy with entangled photons: Manipulating quantum pathways of matter. *Phys. Rev. A* **2009**, *79*, 033832.

(8) Peřina, J.; Saleh, B. E.; Teich, M. C. Multiphoton absorption cross section and virtual-state spectroscopy for the entangled n-photon state. *Phys. Rev. A* **1998**, *57*, 3972.

(9) Dorfman, K. E.; Schlawin, F.; Mukamel, S. Nonlinear optical signals and spectroscopy with quantum light. *Rev. Mod. Phys.* **2016**, *88*, 045008.

(10) Schlawin, F. Entangled photon spectroscopy. *J. Phys. B* **2017**, *50*, 203001.

(11) Svozilík, J.; Peřina, J.; León-Montiel, R. d. J. Virtual-state spectroscopy with frequency-tailored intense entangled beams. *J. Opt. Soc. Am. B* **2018**, *35*, 460−467.

(12) Varnavski, O.; Pinsky, B.; Goodson, T., III Entangled photon excited fluorescence in organic materials: An ultrafast coincidence detector. *J. Phys. Chem. Lett.* **2017**, *8*, 388−393.

(13) Burdick, R. K.; Varnavski, O.; Molina, A.; Upton, L.; Zimmerman, P.; Goodson, T., III Predicting and controlling entangled two-photon absorption in diatomic molecules. *J. Phys. Chem. A* **2018**, *122*, 8198−8212.

(14) Kang, G.; Nasiri Avanaki, K.; Mosquera, M. A.; Burdick, R. K.; Villabona-Monsalve, J. P.; Goodson, T., III; Schatz, G. C. Efficient modeling of organic chromophores for entangled two-photon absorption. *J. Am. Chem. Soc.* **2020**, *142*, 10446−10458.

(15) Landes, T.; Allgaier, M.; Merkouche, S.; Smith, B. J.; Marcus, A. H.; Raymer, M. G. Experimental feasibility of molecular two-photon absorption with isolated time-frequency-entangled photon pairs. *Phys. Rev. Res.* **2021**, *3*, 033154.

(16) Parzuchowski, K. M.; Mikhaylov, A.; Mazurek, M. D.; Wilson, R. N.; Lum, D. J.; Gerrits, T.; Camp, C. H., Jr; Stevens, M. J.; Jimenez, R. Setting bounds on entangled two-photon absorption cross sections in common fluorophores. *Phys. Rev. Appl.* **2021**, *15*, 044012.

(17) Landes, T.; Raymer, M. G.; Allgaier, M.; Merkouche, S.; Smith, B. J.; Marcus, A. H. Quantifying the enhancement of two-photon absorption due to spectral-temporal entanglement. *Opt. Express* **2021**, *29*, 20022.

(18) Tabakaev, D.; Djorovic, A.; Volpe, L. L.; Gaulier, G.; Ghosh, S.; Bonacina, L.; Wolf, J. P.; Zbinden, H.; Thew, R. T. Spatial properties of entangled two-photon absorption. *Phys. Rev. Lett.* **2022**, *129*, 183601.

(19) Burdick, R. K.; Schatz, G. C.; Goodson, T., III Enhancing entangled two-photon absorption for picosecond quantum spectroscopy. *J. Am. Chem. Soc.* **2021**, *143*, 16930−16934.

(20) Mollow, B. Two-photon absorption and field correlation functions. *Phys. Rev.* **1968**, *175*, 1555.
(21) Franson, J. D. Bell inequality for position and time. *Phys. Rev. Lett.* **1989**, *62*, 2205.
(22) Scully, M.; Zubairy, S. *Quantum optics*; Cambridge University Press: Cambridge, 1997.
(23) Shen, Y.-R. *The principles of nonlinear optics*; Wiley: New York, 1984.
(24) Upton, L.; Harpham, M.; Suzer, O.; Richter, M.; Mukamel, S.; Goodson, T., III Optically excited entangled states in organic molecules illuminate the dark. *J. Phys. Chem. Lett.* **2013**, *4*, 2046−2052.
(25) Monson, P.; McClain, W. Polarization dependence of the two-photon absorption of tumbling molecules with application to liquid 1-chloronaphthalene and benzene. *J. Chem. Phys.* **1970**, *53*, 29−37.
(26) Knippenberg, S.; Rehn, D. R.; Wormit, M.; Starcke, J. H.; Rusakova, I. L.; Trofimov, A. B.; Dreuw, A. Calculations of nonlinear response properties using the intermediate state representation and the algebraic-diagrammatic construction polarization propagator approach: Two-photon absorption spectra. *J. Chem. Phys.* **2012**, *136*, 064107.
(27) Woon, D. E.; Dunning, T. H., Jr Gaussian basis sets for use in correlated molecular calculations. V. Core-valence basis sets for boron through neon. *J. Chem. Phys.* **1995**, *103*, 4572−4585.
(28) Macak, P.; Luo, Y.; Norman, P.; Ågren, H. Electronic and vibronic contributions to two-photon absorption of molecules with multi-branched structures. *J. Chem. Phys.* **2000**, *113*, 7055−7061.

https://doi.org/10.1021/acs.jpclett.3c00272
J. Phys. Chem. Lett. 2023, 14, 2613−2619

Chapter 7

What to take into account in the modelling of two-photon absorption properties in the condensed phase

This chapter serves as a practical guide for setting up the modelling of two-photon absorption (TPA) cross sections in the condensed phase. While the computational methods introduced in previous chapters emphasise various physical effects in modelling solvation effect, we explore the significance of these physical effects on the TPA cross section by analyzing a specific chromophore in a given solvent, represented either by the atomistic cluster or by the polarisable continuum.

The possible physical effects influencing two-photon absorption in the condensed phase can be summarized as follows:

(a) The environment induced change of the chromophore geometry. The geometry of the chromophore changes surrounded by different environments.

(b) The electrostatic interaction with the environment. The electron density of the chromophore is polarised by the electric field generated by the environment.

(c) The long-range non-specific and specific environment polarisation. The state specific excitation calculation is realized in PCM using the perturbation theory introduced in Chapter 2 Section 2.1.2. The state-specific polarisation effect to the TPA cross section is approximated with only the excitation energy corrected by the perturbation technique introduced in Ref. 89, whereas the transition dipole moments are not corrected in the truncated sum-over-state expression given in Eq. 3.62.

(d) The short-range non-electrostatic confinement effect. This effect is introduced by the non-electrostatic part of the embedding potential in FDET, whereas it is neglected in point charge (PC) embedding, see detailed analysis in Chapter 4.

For the purpose of analysis, we decompose the total environment-induced shift of calculated property into two components, arising from: the geometric effects and the electronic effect. For an observable O, with O being the vertical excitation energy ϵ_i, the classical TPA cross section δ_r, this

decomposition reads:

$$\begin{aligned} \Delta O &= O^{chromophore+environment}_{g(chromophore+environment)} - O^{chromophore}_{g(chromophore)} \\ &= \Delta O^{electr} + \Delta O^{geom} \\ \Delta O^{electr} &= O^{chromophore+environment}_{g(chromophore+environment)} - O^{chromophore}_{g(chromophore+environment)} \\ \Delta O^{geom} &= O^{chromophore}_{g(chromophore+environment)} - O^{chromophore}_{g(chromophore+environment)} \end{aligned} \tag{7.1}$$

where:
X in $O^X_{g(Y)}$ specifies the system, for which the property O is evaluated, and Y in $O^X_{g(Y)}$ specifies the system, for which the geometry (either optimised with or without environment). The above decomposition is general and can be applied for observable obtained from conventional treatment of the chromophore and environment as one system or from embedding methods. In the case of electronic excitation ΔO^{electr} is the vertical excitation energy difference evaluated at the complex geometry with and without the environment.

We use the pyrimidine as a mode chromophore and the water solvent to investigate the relative significance of those key factors. The final target state studying in this work was chosen in such a way that: *i*) the state shows a substantial TPA cross-section compared with other excited states; *ii*) the same orbitals are involved in the excitation for the isolated geometry, and the embedded geometry calculated from the reference or from other embedding methods. The excited state S5 chosen for the free chromophore shows a $n - \sigma^*$ transition, while S10 corresponds to a $\pi - \sigma^*$ transition. In addition to the first investigated state S5, S10 shows a more delocalized character as visualized from the particle natural transition orbital.

We first assess the reliability of the FDET method by benchmarking it on a few small clusters containing pyrimidine for which high-level supermolecular reference calculations are feasible. We then proceed to present results obtained by various embedding methods in a much larger cluster.

The discussions regarding the entangled TPA cross section case and the impact of using a different solvent will be addressed in a forthcoming publication.

7.1 Geometric effect

As can be seen in Table 7.1 that the geometric effect is small compared with the absolute value of the isolated chromophore in vacuum. The vertical excitation energy varies in the second decimal place depending on weather the geometry is optimised by the polarisable continuum or by the atomistic representation. The change of TPA cross sections due to a different geometry is also minor, not exceeding 10% of the absolute value observed in a vacuum.

7.2 Environment induced effects on small clusters

For the embedded chromophore, all considered electronic components of the environment-induced shifts (Δ^{electr}_O) presented in this part were obtained using FDET or PC embedding calculations. The shifts obtained from FDET based calculations are not exact due to the approximations used for the

	vacuum	polarisable continuum H_2O	cluster models $1H_2O$	$4H_2O$	$23H_2O$
	O	ΔO^{geom} (Eq. 7.1)			
ϵ_5	6.092	-0.045	0.002	-0.064	-0.062
δ_r	232.19	9.92	-22.69	17.11	5.49
ϵ_{10}	7.082	0.014	0.038		0.043
δ_r	367.78	-2.11	-3.28		-6.56

Table 7.1 – Geometry component of the environment induced shifts of: vertical excitation energy ($\Delta\epsilon^{geom}$ in eV), the classical TPA cross-section ($\Delta{\delta_r}^{geom}$ in a.u.) for the S_5 and S_{10} target states of the isolated pyrimidine. The absolute values of ϵ, δ_r, for the isolated chromophore in vacuum are also given.

		FDET				
	Δ^{geom}	$\Delta^{electr}(\rho_B^{iso})$	$\Delta^{electr}(\rho_B^{pp})$	$\Delta^{electr}(PC^{iso})$	$\Delta^{electr}(PC^{pp})$	Δ_{ref}^{electr}
$\epsilon_5(n-\sigma^*)$	0.002	0.232	0.261	0.238	0.266	0.236
δ_r	-22.69	-40.9	-45.6	-42.7	-47.09	-55.7
$\epsilon_{10}(\pi-\sigma^*)$	0.038	0.093	0.107	0.105	0.12	0.12
δ_r	-3.28	-17.09	-21.6	-26.8	-42.16	-23.5

Table 7.2 – Complexation induced shifts of the vertical excitation (ϵ in eV), the classical TPA cross-section (δ_r in atomic units) for the S_5 and S_{10} states in the pyrimidine-H_2O complex. The geometric and electronic components to the shifts of each observable are defined in Eq. 7.1

bi-functional for the non-electrostatic components of the exact FDET potential and due to the procedure to generate ρ_B.

In all the tables, it can be observed that the electronic effect is much more significant than the geometric effect, typically by one order of magnitude. The magnitude of the excitation energy Δ_O^{electr} increases in all studied cases with the pre-polarised ρ_B for FDET. This can be expected because the ground state of the chromophore is stabilized by the polarised environment density. It is worthwhile to note, however, that the effect of the ground-state pre-polarisation on the environment induced shifts of δ_r does not follow such simple trends observed for ϵ.

In the case of $1 * H_2O$ and $2 * H_2O$:

- Both FDET and PC embedding demonstrate similar electronic polarisation effects in terms of magnitude and direction. However, PC embedding using pre-polarised charges shows an over-polarisation effect on the excitation energy. DFET, on the other hand, gives more stable TPA cross sections, which are invariant of the choice of ρ_B. The difference in Δ_O^{electr} between the choice of ρ^{iso} or ρ_B^{pp} is generally smaller than the corresponding differences in PC embedding.
- The Pauli repulsion effect reduces the excitation energy ϵ in the range of 5 meV to 29 meV and its effect on the TPA cross section δ_r is around 1 to 21 $a.u.$. The inclusion of the Pauli

		FDET				
	Δ^{geom}	$\Delta^{electr}(\rho_B^{iso})$	$\Delta^{electr}(\rho_B^{pp})$	$\Delta^{electr}(PC^{iso})$	$\Delta^{electr}(PC^{pp})$	Δ_{ref}^{electr}
$\epsilon_5(n-\sigma^*)$	-0.038	0.407	0.461	0.438	0.488	0.387
δ_r	2.3	-86.7	-93.72	-89.52	-96.11	-91.25
$\epsilon_{10}(\pi-\sigma^*)$	0.024	0.134	0.156	0.176	0.197	0.164
δ_r	-7.35	-53.8	-36.36	-52.54	-56.79	-30.02

Table 7.3 – Complexation induced shifts of the vertical excitation (ϵ in eV), and the classical TPA cross-section (δ_r in atomic units) for the S_5 and S_{10} states in the pyrimidine-2H_2O complex. The geometric and electronic components to the shifts of each observable are defined in Eq. 7.1

		FDET				
	Δ^{geom}	$\Delta^{electr}(\rho_B^{iso})$	$\Delta^{electr}(\rho_B^{pp})$	$\Delta^{electr}(PC^{iso})$	$\Delta^{electr}(PC^{pp})$	Δ_{ref}^{electr}
$\epsilon_5(n-\sigma^*)$	-0.064	0.446	0.552	0.524	0.446	0.358
δ_r	17.11	-133.03	-147.74	-136.92	-111.19	-74.2

Table 7.4 – Complexation induced shifts of the vertical excitation (ϵ in eV), the classical TPA cross-section (δ_r in atomic units) for the S_5 state in the pyrimidine-4H_2O cluster. The geometric and electronic components to the shifts of each observable are defined in Eq. 7.1

repulsion mitigates the over-polarisation in the PC embedding, particularly in S10 state, from -42 (PC^{pp}) to -22 (ρ_B^{pp}) for a reference value of -23 *a.u.*, and from -57 (PC^{pp}) to -36 (ρ_B^{pp}) for a reference value of -30 *a.u.*. The error of Δ_O^{electr} in the TPA cross section is in general smaller in FDET than in PC embedding.

In the case of $4 * H_2O$, the error increases slightly for both FDET and PC. It's worth noting that the relatively large errors in the TPA cross sections observed in both FDET and PC methods can be attributed to the missing dominant state S7, which is partially localized in the surrounding water environment.

7.3 Environment induced effects on large clusters

7.3.1 Atomic representation by FDET

The benchmarking of the approximations used in FDET made for smaller clusters considered in the previous section provide the justification for using the same approximation to v_{xcT}^{nad} and methods to generate ρ_B.

7.3.2 Continuum representation by PCM

In this section, we analyse the shifts evaluated using the polarisable continuum model of the environment. Two models are considered. Results labelled with $no-ssp$ in Table 7.6 were obtained

		environment induced shifts (ΔO)		
		$23 \cdot H_2O$		
O	O in vacuum	$\Delta^{geom}(O)$	$\Delta^{electr}(O)$ ρ_B^{iso}	$\Delta^{electr}(O)$ ρ_B^{pp}
	S_5 state ($n-\sigma^*$)			
ϵ_5	6.092	-0.062	0.636	0.855
δ_r	232.19	5.49	-90.23	-116.57
	S_{10} state ($\pi-\sigma^*$)			
ϵ_{10}	7.082	0.043	0.435	0.552
δ_r	367.78	-6.56	-194.1	-204.14

Table 7.5 – Complexation induced shifts of the vertical excitation (ϵ in eV), the classical TPA cross-section (δ_r in atomic units) for the S_5 and S_{10} states of pyrimidine embedded in $23 \cdot H_2O$ clusters. The geometric and electronic components to the shifts of each observable are defined in Eq. 7.1. In FDET calculations of the electronic contributions to the shift, either isolated density ρ_B^{isol} of the environment molecules or pre-polarised density (ρ_B^{pp}) was used.

by PCM neglecting the state-specific polarisation of the environment. The reaction field corresponds to the ground state of the chromophore and arises from both electronic and reorientation polarisation of the environment in the ground state. The effect of state-specific response of the environment by the reaction field for the ground and the target excited state is taken into account by means of a method introduced in Ref. 89.

Considering the state-specific polarisation from the solvent lowers all the vertical excitation energy in the range of 0.05-0.07 eV in Table 7.6. However, only a slight modification in the TPA cross sections is observed after implementing this correction. It's crucial to highlight that, in this context, only the denominator, corresponding to the excitation energy in the truncated sum-over-state expression, undergoes correction through the state-specific perturbation technique. Meanwhile, the transition dipoles remain uncorrected. The classical TPA cross section increases about 10 a.u. for the state S5. The alteration in TPA cross sections due to environmental polarisation is only about 8% of that caused by the complexation effect. Regarding S10, the perturbation to Δ_O^{electr} from the environment is minimal, whether it be due to polarisation or electronic complexation.

7.4 Comparison of two representations and summary

We conducted calculations to assess the impact of the environment on the one and two-photon properties of pyrimidine, employing two representations for the environment: atomistic and polarisable continuum. The objective was to investigate the importance of different physical effects in modelling the environment-induced two-photon absorption (TPA) cross section. Our findings indicate a negligible geometric effect (Δ_O^{geom}) on the shifts of ϵ and δ_r, regardless of whether the solvents are modeled as a continuum or a cluster. In contrast, the electronic components (Δ_O^{electr}) dominate the shifts, typically being one order of magnitude larger than the geometric effect.

		environment induced shifts (ΔO)		
O	O in vacuum	$\Delta^{geom}(O)$	$\Delta^{electr}(O)$	
			no-ssp	ssp
	S_5 state ($n-\sigma^*$)			
ϵ_5	6.092	-0.045	0.17	0.098
δ_r	232.19	9.92	-137.44	-128.97
	S_{10} state ($\pi-\sigma^*$)			
ϵ_{10}	7.082	0.014	-0.01	-0.064
δ_r	367.78	-2.11	0.21	-0.01

Table 7.6 – Complexation induced shifts of the vertical excitation (ϵ in eV), the classical TPA cross-section (δ_r in atomic units) for the S_5 and S_{10} states of pyrimidine embedded in water represented as a polarisable continuum. The geometric and electronic components to the shifts of each observable are defined in Eq. 7.1. In the PCM calculations of the electronic contributions to the shift, the differential polarisation of the solvent in the ground and excited states was either neglected (no-ssp) or treated as in Ref. 89 (ssp).

In the results of the larger cluster, Δ_O^{electr} exhibits consistent sign in shift values for both FDET (0.855 eV) and PCM (0.098 eV). However, the magnitude of Δ_O^{electr} is approximately one order of magnitude smaller in the PCM embedding. Notably, this difference in magnitude of the excitation energy does not correspondingly influence the TPA cross section. Δ_O^{electr} values on the TPA cross section for state S5 calculated by FDET closely align with those obtained from PCM. The shift in the TPA cross section is -116.57 *a.u.* in FDET and -137.44 *a.u.* in PCM.

A contrasting result is observed for state S10. The Δ_O^{electr}, as described by FDET, shows an energy shift of 0.552 eV and a corresponding shift in the TPA cross section of -204.14 *a.u.*, whereas in PCM, these values are -0.064 eV and -0.01 *a.u.*, respectively. For this state, PCM embedding fails to capture the environment-induced effect in the modelling of the TPA cross section. This discrepancy may be attributed to the excitation character of the second target state, which exhibits greater delocalization compared to the first state. In such cases, the classical electrostatic effect alone is not sufficient, and the inclusion of the quantum confinement effect becomes necessary to accurately describe these states.

The state-specific polarisation appears to be non-crucial for evaluating TPA properties, as evidenced by the PCM results. It exerts a minor influence on the TPA cross section and does not yield improvements for the S10 state anyway. In the context of FDET, conducting state-specific calculations is not advisable due to the disruption of orthogonality between excited states.

In conclusion, the environment can markedly alter the TPA cross section, leading to a reduction of up to 60% for both target states in the case of pyrimidine in water. The selection of the excited method for obtaining transition dipoles and excitation energy proves to be more critical than the utilization of ground state methods to determine the geometry. An atomistic representation appears to be more reliable than classical PCM representation. The inclusion of Pauli repulsion is essential depending on the character of the target state.

Chapter 8

Conclusions

In previously studies within our group, it has been demonstrated that FDET, employing the simple variant with i) LDA functional to approximate $v_t^{nad}[\rho_A, \rho_B]$ and ii) ρ_B generated by the isolated fragment, already produces reasonable results for vertical excitation energies. A further improvement has been achieved by utilizing pre-polarized ρ_B with the electric field of the isolated chromophore in its ground state. In this thesis, we have explored further into this topic to improve the vertical excitation energy by explicitly including polarization. Calculations made on ten chromophores with 47 excitations show systematic improvement from using pre-polarized ρ_B to the state-specific ρ_B, where ρ_B is polarized by the electric filed of the corresponding excited state of the *embedded* chromophore. However, the improvement was not substantial, typically in the range of 10-20 meV. Consequently, we conclude that users may choose how ρ_B is generated based on the investigated property and the number of excited states. ρ_B generated by the isolated fragment remains a good starting point for excited state calculations due to its computational efficiency and preservation of orthogonality between excited states.

Chapter 4 examined TPA cross-sections evaluated with the simplest variant of FDET. We demonstrated the critical role of including Pauli repulsion in modeling TPA cross-sections, particularly when only the exact Coulomb interaction is present in the embedding potential. Building on this, we further explored the significance of other physical factors in modelling this property in Chapter 7. We found that the environment-induced change in chromophore geometry has an effect approximately one order of magnitude smaller than the electronic complexation effect. Classical PCM embedding completely fails in characterising the solvent effect for one studied state, depending on the excitation character. The atomistic representation of the environment is essential if the state is delocalized. The state-specific polarization effect to TPA properties was shown to be insignificant with PCM embedding.

Finally, we calculated the rotationally averaged entangled TPA cross section using a truncated sum-over-state expression. The oscillation period of the entangled TPA cross section was derived as $T = 2\pi/(\epsilon_{k1} - \epsilon_{k2})$ and validated through QM methods. The inversely proportional relationship between the oscillation period and the excitation energy difference between two close dominant intermediate states can potentially be used to control the entangled TPA transparency.

Appendices

Appendix A

Derivations on expansions of $\bar{\Psi}(t)$

The derivations follow the book by Patrick Norman and others [78].

A.1 Choice of the operator $\hat{\Omega}$

We review the core equation of motion that needs to be solved,

$$\frac{\partial}{\partial t}\langle\Psi_0|e^{-i\hat{P}(t)}\hat{\Omega}e^{-i\hat{P}(t)}|\Psi_0\rangle = \frac{1}{i\hbar}\Psi_0|e^{-i\hat{P}(t)}\left[\hat{\Omega}, \hat{H}_0 + \hat{V}(t)\right]e^{-i\hat{P}(t)}|\Psi_0\rangle \tag{A.1}$$

The goal is to choose a convenient operator which gives back the time-dependent coefficient $P_n(t)$. Applying the Baker-Campbell-Hausdorff (BCH) expansion on the left hand side (l.h.s) of the equation,

$$e^{-i\hat{P}(t)}\hat{\Omega}e^{-i\hat{P}(t)} = \hat{\Omega} + i[\hat{P}, \hat{\Omega}] - \frac{1}{2}[\hat{P}, [\hat{P}, \hat{\Omega}]] - \frac{i}{6}[\hat{P}, [\hat{P}, [\hat{P}, \hat{\Omega}]]] + \cdots \tag{A.2}$$

Plugging Eq. A.2 into l.h.s of Eq. A.1 and using the orthogonality between unperturbed eigenstates, we obtain a series of equations,

$$\begin{aligned}\langle\Psi_0|[\hat{P}, \hat{\Omega}]|\Psi_0\rangle &= \langle\Psi_0|\left[\sum_{n>0}[P_n(t)|\Psi_n\rangle\langle\Psi_0| + P_n^*(t)|\Psi_0\rangle\langle\Psi_n|], \hat{\Omega}\right]|\Psi_0\rangle \\ &= \sum_m\left[P_m^*(t)\langle\Psi_m|\hat{\Omega}|\Psi_0\rangle - P_m(t)\langle\Psi_0|\hat{\Omega}|\Psi_m\rangle\right]\end{aligned} \tag{A.3}$$

The third term in Eq. A.2 reads,

$$\langle\Psi_0|[\hat{P}, [\hat{P}, \hat{\Omega}]]|\Psi_0\rangle = -2\sum_{m,l>0}P_m^*P_l\langle\Psi_m|\bar{\hat{\Omega}}|\Psi_l\rangle \tag{A.4}$$

and $\bar{\hat{\Omega}}$ is the fluctuation operator defined as $\bar{\hat{\Omega}} = \hat{\Omega} - \langle\Psi_0|\hat{\Omega}|\Psi_0\rangle$.

After inspecting Eq. A.3 and Eq. A.4, by choosing the operator $\hat{\Omega}$ as the state transition operator $|\Psi_0\rangle\langle\Psi_n|$, one finds,

$$\begin{aligned}\langle\Psi_0|[\hat{P}, \hat{\Omega}]|\Psi_0\rangle &= -P_n(t) \\ \langle\Psi_0|[\hat{P}, [\hat{P}, \hat{\Omega}]]|\Psi_0\rangle &= 0\end{aligned} \tag{A.5}$$

This immediately reduce the complexity when one tries to solve Eq. A.1.

A.2 Perturbation expansions on $P_n(t)$

Perturbation theory is applied to solve Eq. A.1. $P_n(t)$ is expanded,

$$P_n(t) = P_n(t)^{(0)} + P_n(t)^{(1)} + P_n(t)^{(2)} + \cdots \tag{A.6}$$

The parametrized phase isolated wavefunctions $\bar{\Psi}(t)$,

$$\begin{aligned} \bar{\Psi}(t) &= e^{-i\hat{P}(t)}|\Psi_0\rangle \\ &= (1 + (-i\hat{P}(t)) + \frac{(-i\hat{P}(t))^2}{2!} + \frac{(-i\hat{P}(t))^3}{3!} + \cdots)|\Psi_0\rangle \end{aligned} \tag{A.7}$$

The corresponding phase isolated wavefunctions $\bar{\Psi}(t)$ up to first order after plugging in $\hat{P}(t) = \sum_{n>0}[P_n(t)|\Psi_n\rangle\langle\Psi_0| + P_n^*(t)|\Psi_0\rangle\langle\Psi_n|]$ into Eq. A.7 is expressed as,

$$\bar{\Psi}(t)^{(0)} = |\Psi_0\rangle, \tag{A.8}$$

$$\bar{\Psi}(t)^{(1)} = -i\sum_{n>0} P_n^{(1)}|\Psi_0\rangle. \tag{A.9}$$

The expectation value of the time-independent operator $\hat{\Omega}$ on the unperturbed state does not vary with time,

$$\frac{\partial}{\partial t}\langle\Psi_0|\hat{\Omega}|\Psi_0\rangle = 0, \tag{A.10}$$

The rotational operator $e^{-i\hat{P}(t)}$ up to the first order,

$$\hat{P}(t) = 1 - i\hat{P}(t)^{(1)} \tag{A.11}$$

Now we can rewrite the equation of motion Eq. A.1 up to the first order using Eq. A.10 and Eq. A.11,

$$\frac{\partial}{\partial t}\langle\Psi_0|[\hat{P}^{(1)}(t), \hat{\Omega}]|\Psi_0\rangle = \frac{1}{i\hbar}\langle\Psi_0|[\hat{P}^{(1)}(t), [\hat{\Omega}, \hat{H}_0]]|\Psi_0\rangle - \frac{1}{\hbar}\langle\Psi_0|[\hat{\Omega}, \hat{V}]|\Psi_0\rangle \tag{A.12}$$

The commutator appears in Eq. A.12 can be further simplified,

$$\begin{aligned} [\hat{\Omega}, \hat{H}_0]] &= \Big[|\Psi_0\rangle\langle\Psi_n|, \hat{H}_0\Big] \\ &= E_n|\Psi_0\rangle\langle\Psi_n| - E_0|\Psi_0\rangle\langle\Psi_n| \\ &= \hbar\omega_{n0}\hat{\Omega} \end{aligned} \tag{A.13}$$

Inserting the state transition operator and using Eq. A.13, we arrive to the final equation of motion of the $P_n(t)^{(1)}$ coefficient up to the first order,

$$\frac{\partial}{\partial t}P_n(t)^{(1)} = -i\omega_{n0}P_n(t)^{(1)} + \frac{1}{\hbar}\langle\Psi_n|\hat{V}|\Psi_0\rangle \tag{A.14}$$

Integration over $t \to -\infty$ to t of Eq. A.14 yields the time evolution of $P_n(t)^{(1)}$,

$$P_n(t)^{(1)} = \frac{1}{i\hbar} \sum_{\omega} \frac{\langle \Psi_n | \hat{V}_\alpha^\omega | \Psi_0 \rangle F_\alpha^\omega e^{-i\omega t} e^{\xi t}}{\omega_{n0} - \omega - i\xi} \tag{A.15}$$

One obtains the first order correction to the phase isolated wavefunctions after substituting $P_n(t)^{(1)}$ into Eq. A.9.

Appendix B

The asymptotic behaviour of NDCS functionals

B.1 Definitions of NDCS functionals and its variants

Non-Decomposable Complete Space (NDCS) approximation [90]previous introduced to remove the undesired artificial well in the potential and allowing the complete space of admissible densities, is a Non-decomposable in evaluation of the non-additive kinetic potential as part of the last contribution in Eq. 2.21. The approximation can be written as:

$$\tilde{v}_t^{\mathrm{nad(NDCS)}}[\rho_A, \rho_B] = v_t^{\mathrm{nad(LDA)}}[\rho_A, \rho_B] + f^{\mathrm{NDCS}}(\rho_B) v_t^{\mathrm{limit}}[\rho_B] \tag{B.1}$$

The limit potential $v_t^{\mathrm{limit}}[\rho_B]$ is approximated from the Weizsäcker functional in the limit case where $\rho_A \to 0$ and $\int \rho_B = 2$ and is given as,

$$v_t^{\mathrm{limit}}[\rho_B] = \frac{1}{8} \frac{|\nabla \rho_B|^2 - \rho_B \nabla^2 \rho_B}{\rho_B^2} \tag{B.2}$$

$f^{\mathrm{NDCS}}(\rho_B)$ is the switching function depends only on ρ_B,

$$f^{\mathrm{NDCS}}(\rho_B) = 1 - e^{-\rho_B} \tag{B.3}$$

$v_t^{\mathrm{nad(LDA)}}[\rho_A, \rho_B]$ is non-additive kinetic potential derived from the Thomas-Fermi kinetic energy functional which is the zeroth order expansion to the kinetic energy functional. This approximation has successfully addressed the issue of "charge leak" in charged systems.

GEA2 functional. The Thomas-Fermi kinetic functional can be seen as zeroth-order gradient expansion approximation. The second order gradient expansion (GEA2) [91] reads,

$$T_s^{GEA2} = T_s^{TF} + \frac{1}{9} T_s^{VW} \tag{B.4}$$

where T_s^{GEA2} and T_s^{VW} have been given in Eq. 2.22 and Eq. 2.23 in Chapter 2.

The NDCS functional evaluated with the GEA2 functional as the nondecomposable part in Eq. B.1 is expressed as,

$$\tilde{v}_t^{\mathrm{nad(NDCS-GEA2)}}[\rho_A,\rho_B] = v_t^{\mathrm{nad(LDA)}}[\rho_A,\rho_B] + \frac{1}{9}(1-f^{\mathrm{NDCS}}(\rho_B))v_t^{\mathrm{limit}}[\rho_B] \tag{B.5}$$

LC94 functional. The general gradient approximation (GGA) has general form written as,

$$T_s^{GGA} = C_F \int \rho^{5/3}(\mathbf{r})F(s)d^3r \tag{B.6}$$

where C_F is the Thomas-Fermi constant and $F(s)$ is the enhancement factor.
The generalized gradient approximation LC 94 functional [92] reads,

$$F^{LC94}(s) = \frac{1+0.093907s\cdot arcsinh(76.32s)+(0.26608-0.0809615e^{-100s^2})s^2}{1+0.093907s\cdot arcsinh(76.32s)+0.57767\cdot 10^{-4}s^4} \tag{B.7}$$

where $s=\frac{|\nabla\rho|}{2(3\pi^2)^{1/3}\rho^{4/3}}$ is the dimensionless reduced density gradient.
The NDCS functional evaluated with the LC94 functional as the nondecomposable part in Eq. B.1 is expressed as,

$$\tilde{v}_t^{\mathrm{nad(NDCS-LC94)}}[\rho_A,\rho_B] \;=\; v_t^{\mathrm{nad(LC94)}}[\rho_A,\rho_B] + f^{\mathrm{NDCS}}(\rho_B)v_t^{\mathrm{limit}}[\rho_B] \tag{B.8}$$

B.2 The long-range behavior of non-additive kinetic functionals

The long-range behavior of the non-additive kinetic functionals $\tilde{v}_t^{\mathrm{nad}}$, including the decomposable GEA0, GEA2 and LC94, and the nondecomposable ones defined in the above section. The accuracy of different non-additive kinetic functionals in FDET, was inspected by the analysis of the dipole moment and L^2 distance norm between the embedded density and the reference density.

Systems studied. Three cations Li^+, K^+ and Na^+ are considered, combined with three monomers: CO_2, H_2O and NH_3. The possibility of the charge leak from the environment to the cation differ by the combination of one to another. The combination of $K^+ + NH_3$ leads to the highest possibility of the charge leak issue, for instance. The charge leak happens when the highest molecular orbital (HOMO) energy of one subsystem is close to the lowest molecular orbital (LUMO) energy of another subsystem.

Computational details. The supermolecular basis expansion was used for all calculations. The *Freeze and Thaw* procedure was employed to obtain the subsystem density ρ_A and ρ_B. Kohn-Sham formalism was applied for calculations of the reference supermolecular system and FDET embedding [26]. The exchange correlation functional PBE [93] and the uncontracted $6-311++g^{**}$ basis set [94] were used.

The first line in all tables presented here denotes properties calculated from the equilibrium geometry. The two subsystems are then separated from the equilibrium geometry. The distance of the separation between two subsystems is measured by the coordinate of the center-of-mass of each subsystem.

B.2.1 L^2 distance norm

In this section, the L^2 distance norm is presented evaluated from different nonadditive kinetic potentials in FDET for different combinations of subsystem A and B. The L^2 distance norm is a direct measure of the difference between two densities, and is defined in the following,

$$\begin{aligned} d(\rho_{AB}, \rho_{ref}) &= \|(\rho_{AB} - \rho_{ref})^{1/2}\|^2 \\ &= \int |\rho_{AB} - \rho_{ref}| \end{aligned} \tag{B.9}$$

		Decomposable			**Non-decomposable**		
Separation(Å)	complexation	GEA0	GEA2	LC94	NDCS	NDCS-LC94	NDCS-GEA2
3.038	4.44E-01	3.86E-02	1.03E-01	5.55E-02	2.10E-02	3.61E-02	7.88E-02
3.338	3.73E-01	1.86E-02	7.15E-02	2.82E-02	9.57E-03	1.80E-02	5.65E-02
3.638	3.11E-01	8.56E-03	4.84E-02	1.32E-02	4.15E-03	8.09E-03	3.90E-02
3.938	2.60E-01	3.78E-03	3.15E-02	5.59E-03	1.76E-03	3.18E-03	2.58E-02
4.238	2.20E-01	1.60E-03	1.97E-02	2.18E-03	7.30E-04	1.11E-03	1.62E-02
4.538	1.87E-01	6.60E-04	1.17E-02	7.80E-04	3.00E-04	3.35E-04	9.63E-03
5.038	1.47E-01	1.60E-04		1.10E-04	8.00E-05	7.88E-05	
5.538	1.19E-01	5.00E-05		5.00E-05	4.00E-05	4.83E-05	
6.038	9.80E-02	4.00E-05		3.00E-05	3.00E-05	3.59E-05	
6.538	8.30E-02	3.00E-05		3.00E-05	3.00E-05	2.98E-05	

Table B.1 – The complexation induced density change, labelled as "complexation", of the isolated fragments from the total density of Kohn-Sham treatment of the system is measured by the distance norm $d(\rho_{AB}, \rho_A^{iso}, \rho_B^{iso})$. The errors of the distance norm of two subsystem densities after Freeze and Thaw from the supermolecular reference are shown for the use of different nonadditive kinetic potentials in FDET. The empty entries mean that the Freeze and Thaw procedure is not converged in this separation distance with the corresponding potential. The system is $Li^+ - CO_2$.

		Decomposable			**Non-decomposable**		
Separation(Å)	complexation	GEA0	GEA2	LC94	NDCS	NDCS-LC94	NDCS-GEA2
1.905	3.59E-01	8.09E-02	1.69E-01	1.02E-01	4.69E-02	6.84E-02	1.27E-01
2.205	3.05E-01	5.06E-02	1.37E-01	6.49E-02	2.80E-02	4.28E-02	1.04E-01
2.505	2.53E-01	3.18E-02	1.13E-01	4.07E-02	1.68E-02	2.59E-02	8.54E-02
2.805	2.06E-01	1.97E-02		2.42E-02	9.98E-03	1.49E-02	7.00E-02
3.105	1.67E-01	1.20E-02		1.37E-02	5.81E-03	7.96E-03	
3.405	1.37E-01	6.97E-03		7.39E-03	3.29E-03	4.05E-03	
3.905	1.00E-01	2.56E-03		2.27E-03	1.18E-03	1.10E-03	
4.405	7.70E-02	8.49E-04		6.40E-04	3.91E-04	2.80E-04	
4.905	6.10E-02	2.67E-04		1.70E-04	1.29E-04	7.23E-05	
5.405	5.00E-02	8.76E-05		5.97E-05	5.24E-05	3.68E-05	
5.905	4.20E-02	2.57E-05		1.96E-05	1.81E-05	1.56E-05	

Table B.2 – The complexation induced density change, labelled as "complexation", of the isolated fragments from the total density of Kohn-Sham treatment of the system is measured by the distance norm $d(\rho_{AB}, \rho_A^{iso}, \rho_B^{iso})$. The errors of the distance norm of two subsystem densities after Freeze and Thaw from the supermolecular reference are shown for the use of different nonadditive kinetic potentials in FDET. The empty entries mean that the Freeze and Thaw procedure is not converged in this separation distance with the corresponding potential. The system is $Li^+ - H_2O$.

		Decomposable			**Non-decomposable**		
Separation(Å)	complexation	GEA0	GEA2	LC94	NDCS	NDCS-LC94	NDCS-GEA2
2.05	0.413	1.79E-01	3.15E-01	2.07E-01	1.16E-01	1.46E-01	2.42E-01
2.339	0.385	1.43E-01	2.92E-01	1.66E-01	8.90E-02	1.14E-01	2.24E-01
2.631	0.351	1.19E-01		1.37E-01	7.17E-02	9.12E-02	
2.924	0.312	1.04E-01		1.18E-01	6.00E-02	7.47E-02	
3.218	0.271	9.51E-02		1.05E-01	5.19E-02	6.26E-02	
3.514	0.232	9.00E-02		9.74E-02	4.59E-02	5.33E-02	
4.007	0.175			9.33E-02	3.80E-02	4.10E-02	

Table B.3 – The complexation induced density change, labelled as "complexation", of the isolated fragments from the total density of Kohn-Sham treatment of the system is measured by the distance norm $d(\rho_{AB}, \rho_A^{iso}, \rho_B^{iso})$. The errors of the distance norm of two subsystem densities after Freeze and Thaw from the supermolecular reference are shown for the use of different nonadditive kinetic potentials in FDET. The empty entries mean that the Freeze and Thaw procedure is not converged in this separation distance with the corresponding potential. The system is $Li^+ - NH_3$.

		Decomposable			**Non-decomposable**		
Separation(Å)	complexation	GEA0	GEA2	LC94	NDCS	NDCS-LC94	NDCS-GEA2
3.827	0.283	1.30E-02	5.41E-02	2.77E-02	1.17E-02	1.99E-02	3.37E-02
4.127	0.243	6.22E-03	3.11E-02	1.21E-02	6.32E-03	8.76E-03	2.18E-02
4.427	0.209	2.96E-03		5.21E-03	3.42E-03	3.85E-03	1.47E-02
4.727	0.18	1.41E-03		2.24E-03	1.71E-03	1.70E-03	9.76E-03
5.027	0.156	6.60E-04		9.45E-04	8.00E-04	7.28E-04	6.33E-03
5.327	0.136	3.14E-04		4.09E-04	3.75E-04	3.20E-04	3.96E-03
5.627	0.12	1.70E-04		1.89E-04	1.94E-04	1.54E-04	2.39E-03
5.927	0.106	9.67E-05		1.11E-04	1.02E-04	9.61E-05	1.45E-03
6.427	0.089	5.86E-05		6.32E-05	5.86E-05	6.20E-05	6.17E-04
6.927	0.075	3.53E-05		3.53E-05	3.54E-05	3.54E-05	2.74E-04

Table B.4 – The complexation induced density change, labelled as "complexation", of the isolated fragments from the total density of Kohn-Sham treatment of the system is measured by the distance norm $d(\rho_{AB}, \rho_A^{iso}, \rho_B^{iso})$. The errors of the distance norm of two subsystem densities after Freeze and Thaw from the supermolecular reference are shown for the use of different nonadditive kinetic potentials in FDET. The empty entries mean that the Freeze and Thaw procedure is not converged in this separation distance with the corresponding potential. The system is $K^+ - CO_2$.

		Decomposable			**Non-decomposable**		
Separation(Å)	complexation	GEA0	GEA2	LC94	NDCS	NDCS-LC94	NDCS-GEA2
2.64	0.226	4.78E-02		7.74E-02	2.30E-02	4.02E-02	5.50E-02
2.94	0.192	2.37E-02		4.04E-02	1.18E-02	1.96E-02	3.53E-02
3.24	0.164	1.20E-02		2.13E-02	5.89E-03	9.68E-03	2.42E-02
3.54	0.139	6.03E-03		1.11E-02	2.88E-03	4.77E-03	1.71E-02
3.84	0.118	3.04E-03		5.69E-03	1.50E-03	2.27E-03	1.20E-02
4.14	0.1	1.56E-03		2.89E-03	7.82E-04	1.03E-03	8.26E-03
4.64	0.078	5.44E-04		9.70E-04	2.88E-04	3.10E-04	4.07E-03
5.14	0.063	1.80E-04		2.81E-04	1.04E-04	7.59E-05	1.82E-03
5.64	0.052	6.59E-05		8.22E-05	4.02E-05	3.43E-05	
6.14	0.043				4.58E-05	4.50E-05	3.30E-04
6.64	0.037				4.72E-05	4.76E-05	1.48E-04

Table B.5 – The complexation induced density change, labelled as "complexation", of the isolated fragments from the total density of Kohn-Sham treatment of the system is measured by the distance norm $d(\rho_{AB}, \rho_A^{iso}, \rho_B^{iso})$. The errors of the distance norm of two subsystem densities after Freeze and Thaw from the supermolecular reference are shown for the use of different nonadditive kinetic potentials in FDET. The empty entries mean that the Freeze and Thaw procedure is not converged in this separation distance with the corresponding potential. The system is $K^+ - H_2O$.

		Decomposable			**Non-decomposable**		
Separation(Å)	complexation	GEA0	GEA2	LC94	NDCS	NDCS-LC94	NDCS-GEA2
2.822	0.284				6.12E-02	9.12E-02	
3.111	0.258				3.70E-02	5.82E-02	
3.403	0.232				2.30E-02	3.81E-02	
3.696	0.205				1.46E-02	2.51E-02	6.44E-02
3.99	0.179				9.45E-03	1.66E-02	5.51E-02
4.285	0.155				6.29E-03	1.11E-02	
4.58	0.134				4.31E-03	7.47E-03	
4.876	0.117				2.99E-03	4.77E-03	
5.173	0.101				2.05E-03	2.99E-03	
5.569	0.085				1.19E-03	1.64E-03	
6.064	0.07				5.60E-04	6.94E-04	

Table B.6 – The complexation induced density change, labelled as "complexation", of the isolated fragments from the total density of Kohn-Sham treatment of the system is measured by the distance norm $d(\rho_{AB}, \rho_A^{iso}, \rho_B^{iso})$. The errors of the distance norm of two subsystem densities after Freeze and Thaw from the supermolecular reference are shown for the use of different nonadditive kinetic potentials in FDET. The empty entries mean that the Freeze and Thaw procedure is not converged in this separation distance with the corresponding potential. The system is $K^+ - NH_3$.

		Decomposable			**Non-decomposable**		
Separation(Å)	complexation	GEA0	GEA2	LC94	NDCS	NDCS-LC94	NDCS-GEA2
3.453	0.335	8.00E-03		1.71E-02	1.12E-02	1.24E-02	3.88E-02
3.753	0.285	5.71E-03		6.87E-03	7.73E-03	4.83E-03	2.60E-02
4.053	0.242	3.62E-03	1.88E-02	2.68E-03	4.57E-03	1.87E-03	1.74E-02
4.353	0.206	2.04E-03	1.19E-02	9.20E-04	2.47E-03	8.10E-04	1.12E-02
4.653	0.177	1.07E-03	7.30E-03	4.37E-04	1.26E-03	5.17E-04	6.98E-03
4.953	0.153	5.14E-04	4.35E-03	3.03E-04	5.96E-04	3.64E-04	4.20E-03
5.253	0.134	2.52E-04		1.96E-04	2.83E-04	2.24E-04	2.43E-03
5.553	0.118	1.19E-04	1.39E-03	1.10E-04	1.30E-04	1.19E-04	1.36E-03
6.053	0.098	5.44E-05	5.11E-04	5.65E-05	5.63E-05	5.83E-05	5.04E-04
6.553	0.082	7.18E-05	2.20E-04	7.24E-05	7.19E-05	7.25E-05	2.18E-04

Table B.7 – The complexation induced density change, labelled as "complexation", of the isolated fragments from the total density of Kohn-Sham treatment of the system is measured by the distance norm $d(\rho_{AB}, \rho_A^{iso}, \rho_B^{iso})$. The errors of the distance norm of two subsystem densities after Freeze and Thaw from the supermolecular reference are shown for the use of different nonadditive kinetic potentials in FDET. The empty entries mean that the Freeze and Thaw procedure is not converged in this separation distance with the corresponding potential. The system is $Na^+ - CO_2$.

		Decomposable			**Non-decomposable**		
Separation(Å)	complexation	GEA0	GEA2	LC94	NDCS	NDCS-LC94	NDCS-GEA2
2.298	0.263	1.16E-02	6.58E-02	3.01E-02	1.23E-02	2.14E-02	5.55E-02
2.598	0.224	6.85E-03	4.78E-02	1.37E-02	1.05E-02	8.75E-03	4.12E-02
2.898	0.188	5.30E-03	3.53E-02	5.83E-03	7.80E-03	3.44E-03	3.11E-02
3.198	0.155	3.80E-03	2.58E-02	2.20E-03	5.25E-03	1.38E-03	2.30E-02
3.498	0.129	2.49E-03	1.84E-02	8.85E-04	3.30E-03	1.14E-03	1.66E-02
3.798	0.108	1.48E-03	1.28E-02	6.09E-04	1.92E-03	9.95E-04	1.16E-02
4.298	0.082	5.09E-04	6.30E-03	2.92E-04	6.57E-04	4.33E-04	5.74E-03
4.798	0.065	1.48E-04	2.77E-03	1.35E-04	1.92E-04	1.79E-04	2.53E-03
5.298	0.053	5.09E-05	1.14E-03	5.51E-05	5.93E-05	6.40E-05	1.05E-03
5.798	0.044	3.01E-05		3.29E-05	3.18E-05	3.46E-05	4.22E-04
6.298	0.037	2.53E-05		2.56E-05	2.56E-05	2.58E-05	

Table B.8 – The complexation induced density change, labelled as "complexation", of the isolated fragments from the total density of Kohn-Sham treatment of the system is measured by the distance norm $d(\rho_{AB}, \rho_A^{iso}, \rho_B^{iso})$. The errors of the distance norm of two subsystem densities after Freeze and Thaw from the supermolecular reference are shown for the use of different nonadditive kinetic potentials in FDET. The empty entries mean that the Freeze and Thaw procedure is not converged in this separation distance with the corresponding potential. The system is $Na^+ - H_2O$.

		Decomposable			**Non-decomposable**		
Separation(Å)	complexation	GEA0	GEA2	LC94	NDCS	NDCS-LC94	NDCS-GEA2
2.423	0.335	2.11E-02		5.29E-02	1.36E-02	3.64E-02	
2.713	0.312	9.12E-03		3.14E-02	1.49E-02	1.93E-02	8.16E-02
3.005	0.282	6.45E-03		1.81E-02	1.46E-02	9.50E-03	
3.298	0.249	6.44E-03		9.89E-03	1.30E-02	4.26E-03	
3.593	0.216	5.86E-03		5.01E-03	1.09E-02	2.99E-03	
3.888	0.185	4.95E-03		2.23E-03	8.78E-03	3.77E-03	
4.184	0.158	3.96E-03		1.16E-03	6.83E-03	3.98E-03	
4.481	0.135	3.01E-03		1.44E-03	5.11E-03	3.67E-03	
4.777	0.116	2.17E-03		1.47E-03	3.63E-03	3.01E-03	
5.174	0.095	1.30E-03		1.14E-03	2.15E-03	2.01E-03	
5.67	0.077	6.20E-04		6.77E-04	1.01E-03	1.06E-03	
6.167	0.063	2.86E-04		3.50E-04	4.55E-04	5.08E-04	
6.764	0.052	1.03E-04		1.33E-04	1.59E-04	1.84E-04	

Table B.9 – The complexation induced density change, labelled as "complexation", of the isolated fragments from the total density of Kohn-Sham treatment of the system is measured by the distance norm $d(\rho_{AB}, \rho_A^{iso}, \rho_B^{iso})$. The errors of the distance norm of two subsystem densities after Freeze and Thaw from the supermolecular reference are shown for the use of different nonadditive kinetic potentials in FDET. The empty entries mean that the Freeze and Thaw procedure is not converged in this separation distance with the corresponding potential. The system is $Na^+ - NH_3$.

From all the studies system, we can make the following observations,

- The kinetic energy approximated by the GEA2 functional usually gives more accurate kinetic energies than GEA0. The non-additive kinetic potential generated by GEA2, however, does not yield a more accurate density compared with GEA0. In some cases, GEA2 even fails to converge in the Freeze and Thaw procedure, which means that most likely the electrons from one subsystem are leaked into the other subsystem. One example of such a case in $Li^+ - H_2O$, where GEA2 does not converge will be been shown in the following.

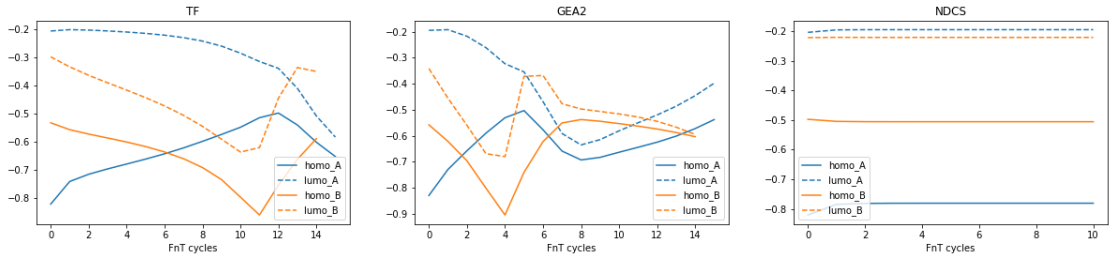

(a) Decomposable: GEA0 (b) Decomposable: GEA2 (c) Non-decomposable: NDCS

Figure B.1 – The HOMO-LUMO energy from each of the freeze and thaw cycles of subsystem A and B obtained by plugging different nonadditive kinetic potentials.

It can be seen in Fig. B.1 that if HOMO of system A is higher in energy than the LUMO of system B, electrons tend to fill the empty orbitals of LUMO of system B. This is the reason why the charge leak happens.

The blue solid line in Fig. B.1 representing HOMO of A, crosses with the orange dash line that represents the LUMO of B, for both GEA0 and GEA2 in later FnT cycles, whereas NDCS impose the LUMO for system A and B in high energy thus avoiding the charge leak problem.

- In case of Li^+ system, both the Non-decomposable: NDCS and NDCS-LC94 are superior than the Decomposable GEA0 in the middle to long-range distance. NDCS-GEA2 sometimes even helps to cure the convergence problem of the nonadditive kinetic functional approximated by the GEA2 function. The results from LC94 is very similar to GEA0.
- In case of K^+ system, with the monomer $K^+ - 1H_2O$ and $K^+ - 1NH_3$ the same conclusion can be made as the one for the Li^+ system. However, in case of $K^+ - CO_2$ the decomposable GEA0 functional is slightly better than NDCS related functional.
- The Na^+ case is more complicated. In the middle range, LC94 functional surpasses other functionals, while in the long-range GEA0 is the best functional. NDCS related functionals, on the other hand, does not show advantages in the middle to long-range distance. This calls a further improvement of NDCS functionals. One possibility is to improve the switching function $f[\rho_B]$.

B.2.2 Dipole moment

In this section, dipole moments [D] is presented evaluated from different nonadditive kinetic potentials in FDET for different combinations of subsystem A and B.

		Decomposable			**Non-decomposable**		
Separation(Å)	complexation	GEA0	GEA2	LC94	NDCS	NDCS-LC94	NDCS-GEA2
3.038	-2.481	-1.22E-01	-3.91E-01	-1.77E-01	-3.58E-02	-9.32E-02	-2.85E-01
3.338	-2.126	-7.23E-02	-3.12E-01	-1.07E-01	-2.25E-02	-5.86E-02	-2.38E-01
3.638	-1.793	-3.92E-02	-2.36E-01	-5.74E-02	-1.15E-02	-3.07E-02	-1.84E-01
3.938	-1.504	-1.99E-02	-1.69E-01	-2.72E-02	-5.40E-03	-1.35E-02	-1.34E-01
4.238	-1.266	-9.51E-03	-1.15E-01	-1.17E-02	-2.32E-03	-5.06E-03	-9.20E-02
4.538	-1.076	-4.30E-03	-7.40E-02	-4.49E-03	-9.42E-04	-1.47E-03	-5.91E-02
5.038	-0.842	-1.07E-03		-6.22E-04	-2.26E-04	9.78E-05	
5.538	-0.68	-2.11E-04		-4.88E-05	-2.31E-05	1.10E-04	
6.038	-0.563	-3.35E-05		2.60E-05	7.05E-06	5.91E-05	
6.538	-0.475	-1.98E-05		-5.54E-06	-1.12E-05	1.55E-06	

Table B.10 – The complexation induced dipole moment change ($\|\mu^{comp}\| = \|\mu_{AB}\| - \|\mu_A^{iso}\| - \|\mu_B^{iso}\|$), labelled as "complexation", of the isolated fragments, from the total dipole of the Kohn-Sham treatment of the system. The errors of the dipole moment of two subsystem after Freeze and Thaw from the supermolecular reference are shown for the use of different nonadditive kinetic potentials in FDET. The empty entries mean that the Freeze and Thaw procedure is not converged in this separation distance with the corresponding potential. The system is $Li^+ - CO_2$.

		Decomposable			**Non-decomposable**		
Separation(Å)	complexation	GEA0	GEA2	LC94	NDCS	NDCS-LC94	NDCS-GEA2
1.905	1.307	2.72E-01	5.98E-01	3.32E-01	1.40E-01	2.05E-01	4.38E-01
2.205	-1.192	2.07E-02	3.77E-01	6.76E-02	-7.61E-02	-2.59E-02	2.34E-01
2.505	-1.031	-1.46E-01	-5.21E-01	-1.78E-01	-7.45E-02	-1.09E-01	-3.87E-01
2.805	-0.858	-1.02E-01		-1.19E-01	-5.07E-02	-7.06E-02	-3.54E-01
3.105	-0.697	-6.80E-02		-7.45E-02	-3.32E-02	-4.22E-02	
3.405	-0.561	-4.32E-02		-4.39E-02	-2.07E-02	-2.36E-02	
3.905	-0.395	-1.78E-02		-1.54E-02	-8.34E-03	-7.43E-03	
4.405	-0.288	-6.46E-03		-4.82E-03	-2.99E-03	-2.10E-03	
4.905	-0.222	-2.16E-03		-1.38E-03	-9.88E-04	-5.11E-04	
5.405	-0.179	-7.04E-04		-4.31E-04	-3.29E-04	-1.63E-04	
5.905	-0.149	-2.17E-04		-1.34E-04	-1.03E-04	-5.39E-05	

Table B.11 – The complexation induced dipole moment change ($\|\mu^{comp}\| = \|\mu_{AB}\| - \|\mu_A^{iso}\| - \|\mu_B^{iso}\|$), labelled as "complexation", of the isolated fragments, from the total dipole of the Kohn-Sham treatment of the system. The errors of the dipole moment of two subsystem after Freeze and Thaw from the supermolecular reference are shown for the use of different nonadditive kinetic potentials in FDET. The empty entries mean that the Freeze and Thaw procedure is not converged in this separation distance with the corresponding potential. The system is $Li^+ - H_2O$.

		Decomposable			**Non-decomposable**		
Separation(Å)	complexation	GEA0	GEA2	LC94	NDCS	NDCS-LC94	NDCS-GEA2
2.05	-1.568	-7.14E-01	-1.25E+00	-7.98E-01	-4.60E-01	-5.57E-01	-9.61E-01
2.339	-1.619	-6.65E-01	-1.35E+00	-7.47E-01	-4.17E-01	-5.09E-01	-1.03E+00
2.631	-1.575	-6.25E-01		-6.99E-01	-3.78E-01	-4.60E-01	
2.924	-1.468	-6.05E-01		-6.67E-01	-3.50E-01	-4.19E-01	
3.218	-1.323	-6.04E-01		-6.55E-01	-3.31E-01	-3.86E-01	
3.514	-1.161	-6.22E-01		-6.63E-01	-3.17E-01	-3.58E-01	
4.007	-0.893			-7.30E-01	-2.95E-01	-3.14E-01	

Table B.12 – The complexation induced dipole moment change ($\|\mu^{comp}\| = \|\mu_{AB}\| - \|\mu_A^{iso}\| - \|\mu_B^{iso}\|$), labelled as "complexation", of the isolated fragments, from the total dipole of the Kohn-Sham treatment of the system. The errors of the dipole moment of two subsystem after Freeze and Thaw from the supermolecular reference are shown for the use of different nonadditive kinetic potentials in FDET. The empty entries mean that the Freeze and Thaw procedure is not converged in this separation distance with the corresponding potential. The system is $Li^+ - NH_3$.

		Decomposable			**Non-decomposable**		
Separation(Å)	complexation	GEA0	GEA2	LC94	NDCS	NDCS-LC94	NDCS-GEA2
3.827	-1.66E+00	-3.60E-02	-2.28E-01	-8.09E-02	9.62E-03	-2.69E-02	-7.81E-02
4.127	-1.40E+00	-1.31E-02	-1.33E-01	-3.78E-02	8.37E-03	-1.26E-02	-5.64E-02
4.427	-1.19E+00	-2.86E-03		-1.50E-02	7.08E-03	-3.60E-03	-3.82E-02
4.727	-1.02E+00	3.79E-04		-5.57E-03	4.93E-03	-4.24E-04	-2.56E-02
5.027	-8.82E-01	6.06E-04		-2.29E-03	2.70E-03	4.16E-05	-1.75E-02
5.327	-7.70E-01	2.71E-04		-1.11E-03	1.24E-03	-3.86E-05	-1.18E-02
5.627	-6.79E-01	1.24E-04		-6.44E-04	5.77E-04	-1.47E-04	-7.72E-03
5.927	-6.03E-01	-2.41E-05		-2.60E-04	1.89E-04	-2.90E-05	-4.92E-03
6.427	-5.04E-01	-7.54E-05		-1.40E-04	-1.57E-05	-7.61E-05	-2.08E-03
6.927	-4.28E-01	-5.54E-05		-3.67E-05	-3.90E-05	-1.95E-05	-7.90E-04

Table B.13 – The complexation induced dipole moment change ($\|\mu^{comp}\| = \|\mu_{AB}\| - \|\mu_A^{iso}\| - \|\mu_B^{iso}\|$), labelled as "complexation", of the isolated fragments, from the total dipole of the Kohn-Sham treatment of the system. The errors of the dipole moment of two subsystem after Freeze and Thaw from the supermolecular reference are shown for the use of different nonadditive kinetic potentials in FDET. The empty entries mean that the Freeze and Thaw procedure is not converged in this separation distance with the corresponding potential. The system is $K^+ - CO_2$.

		Decomposable			**Non-decomposable**		
Separation(Å)	complexation	GEA0	GEA2	LC94	NDCS	NDCS-LC94	NDCS-GEA2
2.64	-9.66E-01	-1.91E-01		-2.92E-01	-2.96E-02	-7.05E-02	-1.30E-01
2.94	-8.05E-01	-1.13E-01		-1.76E-01	-1.60E-02	-4.44E-02	-1.05E-01
3.24	-6.70E-01	-6.42E-02		-1.01E-01	-5.60E-03	-2.34E-02	-7.94E-02
3.54	-5.55E-01	-3.55E-02		-5.68E-02	-2.68E-04	-1.10E-02	-5.92E-02
3.84	-4.62E-01	-2.00E-02		-3.20E-02	1.02E-03	-5.13E-03	-4.44E-02
4.14	-3.86E-01	-1.16E-02		-1.79E-02	7.21E-04	-2.42E-03	-3.29E-02
4.64	-2.93E-01	-4.68E-03		-6.77E-03	7.63E-05	-1.02E-03	-1.81E-02
5.14	-2.29E-01	-1.64E-03		-2.20E-03	-5.55E-06	-2.91E-04	-8.35E-03
5.64	-1.85E-01	-5.19E-04		-6.25E-04	-3.31E-06	-4.12E-05	
6.14	-1.53E-01				-4.61E-05	-3.60E-05	-1.18E-03
6.64	-1.30E-01				8.35E-05	9.18E-05	-3.07E-04

Table B.14 – The complexation induced dipole moment change ($\|\mu^{comp}\| = \|\mu_{AB}\| - \|\mu_A^{iso}\| - \|\mu_B^{iso}\|$), labelled as "complexation", of the isolated fragments, from the total dipole of the Kohn-Sham treatment of the system. The errors of the dipole moment of two subsystem after Freeze and Thaw from the supermolecular reference are shown for the use of different nonadditive kinetic potentials in FDET. The empty entries mean that the Freeze and Thaw procedure is not converged in this separation distance with the corresponding potential.The system is $K^+ - H_2O$.

		Decomposable			**Non-decomposable**		
Separation(Å)	complexation	GEA0	GEA2	LC94	NDCS	NDCS-LC94	NDCS-GEA2
2.822	-1.2696				-2.24E-01	-3.23E-01	
3.111	-1.1779				-1.65E-01	-2.49E-01	
3.403	-1.0732				-1.18E-01	-1.86E-01	
3.696	-0.961				-8.39E-02	-1.37E-01	-3.75E-01
3.99	-0.8473				-6.10E-02	-1.00E-01	-3.53E-01
4.285	-0.7376				-4.56E-02	-7.39E-02	
4.58	-0.6364				-3.46E-02	-5.44E-02	
4.876	-0.5465				-2.59E-02	-3.79E-02	
5.173	-0.4693				-1.88E-02	-2.55E-02	
5.569	-0.3859				-1.16E-02	-1.50E-02	
6.064	-0.3089				-5.85E-03	-6.92E-03	

Table B.15 – The complexation induced dipole moment change ($\|\mu^{comp}\| = \|\mu_{AB}\| - \|\mu_A^{iso}\| - \|\mu_B^{iso}\|$), labelled as "complexation", of the isolated fragments, from the total dipole of the Kohn-Sham treatment of the system. The errors of the dipole moment of two subsystem after Freeze and Thaw from the supermolecular reference are shown for the use of different nonadditive kinetic potentials in FDET. The empty entries mean that the Freeze and Thaw procedure is not converged in this separation distance with the corresponding potential. The system is $K^+ - NH_3$.

		Decomposable			**Non-decomposable**		
Separation(Å)	complexation	GEA0	GEA2	LC94	NDCS	NDCS-LC94	NDCS-GEA2
3.453	-1.865	-4.22E-04		-5.37E-02	2.08E-02	-3.11E-02	-1.54E-01
3.753	-1.62	8.52E-03		-2.32E-02	1.93E-02	-1.16E-02	-1.12E-01
4.053	-1.387	8.55E-03	-8.76E-02	-7.67E-03	1.38E-02	-2.00E-03	-7.97E-02
4.353	-1.185	6.29E-03	-5.87E-02	-9.59E-04	8.83E-03	1.74E-03	-5.44E-02
4.653	-1.017	3.98E-03	-3.78E-02	1.10E-03	5.18E-03	2.36E-03	-3.55E-02
4.953	-0.88	2.17E-03	-2.32E-02	1.22E-03	2.73E-03	1.80E-03	-2.20E-02
5.253	-0.769	1.10E-03		8.16E-04	1.35E-03	1.07E-03	-1.29E-02
5.553	-0.678	5.42E-04	-7.50E-03	4.80E-04	6.51E-04	5.89E-04	-7.21E-03
6.053	-0.561	1.32E-04	-2.74E-03	1.73E-04	1.56E-04	1.96E-04	-2.66E-03
6.553	-0.473	-5.68E-05	-1.08E-03	-4.20E-05	-5.23E-05	-3.77E-05	-1.07E-03

Table B.16 – The complexation induced dipole moment change ($\|\mu^{comp}\| = \|\mu_{AB}\| - \|\mu_A^{iso}\| - \|\mu_B^{iso}\|$), labelled as "complexation", of the isolated fragments, from the total dipole of the Kohn-Sham treatment of the system. The errors of the dipole moment of two subsystem after Freeze and Thaw from the supermolecular reference are shown for the use of different nonadditive kinetic potentials in FDET. The empty entries mean that the Freeze and Thaw procedure is not converged in this separation distance with the corresponding potential. The system is $Na^+ - CO_2$.

		Decomposable			**Non-decomposable**		
Separation(Å)	complexation	GEA0	GEA2	LC94	NDCS	NDCS-LC94	NDCS-GEA2
2.298	-0.963	-1.99E-02	-2.32E-01	-8.26E-02	1.45E-02	-4.63E-02	-1.90E-01
2.598	-0.882	1.70E-03	-1.91E-01	-4.34E-02	2.34E-02	-2.02E-02	-1.61E-01
2.898	-0.76	9.36E-03	-1.55E-01	-1.92E-02	2.27E-02	-4.76E-03	-1.34E-01
3.198	-0.631	1.04E-02	-1.23E-01	-5.66E-03	1.85E-02	3.06E-03	-1.08E-01
3.498	-0.517	8.64E-03	-9.53E-02	6.69E-04	1.35E-02	5.81E-03	-8.42E-02
3.798	-0.423	6.04E-03	-7.10E-02	2.67E-03	8.83E-03	5.60E-03	-6.31E-02
4.298	-0.311	2.54E-03	-3.90E-02	1.74E-03	3.56E-03	2.79E-03	-3.48E-02
4.798	-0.238	8.41E-04	-1.87E-02	9.32E-04	1.17E-03	1.26E-03	-1.66E-02
5.298	-0.19	2.00E-04	-8.30E-03	2.80E-04	2.99E-04	3.76E-04	-7.33E-03
5.798	-0.156	6.66E-05		1.09E-04	9.51E-05	1.36E-04	-3.11E-03
6.298	-0.131	2.54E-05		4.15E-05	3.33E-05	4.88E-05	

Table B.17 – The complexation induced dipole moment change ($\|\mu^{comp}\| = \|\mu_{AB}\| - \|\mu_A^{iso}\| - \|\mu_B^{iso}\|$), labelled as "complexation", of the isolated fragments, from the total dipole of the Kohn-Sham treatment of the system. The errors of the dipole moment of two subsystem after Freeze and Thaw from the supermolecular reference are shown for the use of different nonadditive kinetic potentials in FDET. The empty entries mean that the Freeze and Thaw procedure is not converged in this separation distance with the corresponding potential. The system is $Na^+ - H_2O$.

		Decomposable			**Non-decomposable**		
Separation(Å)	complexation	GEA0	GEA2	LC94	NDCS	NDCS-LC94	NDCS-GEA2
2.423	-1.357	-6.03E-02		-1.66E-01	1.65E-02	-8.57E-02	
2.713	-1.371	-2.20E-02		-1.14E-01	4.01E-02	-4.83E-02	-3.64E-01
3.005	-1.307	1.58E-03		-7.30E-02	5.20E-02	-1.88E-02	
3.298	-1.197	1.45E-02		-4.22E-02	5.55E-02	2.34E-03	
3.593	-1.066	2.05E-02		-2.07E-02	5.39E-02	1.58E-02	
3.888	-0.931	2.21E-02		-6.25E-03	4.91E-02	2.32E-02	
4.184	-0.802	2.10E-02		3.32E-03	4.24E-02	2.67E-02	
4.481	-0.683	1.82E-02		8.81E-03	3.47E-02	2.65E-02	
4.777	-0.578	1.46E-02		1.05E-02	2.68E-02	2.33E-02	
5.174	-0.463	9.82E-03		9.20E-03	1.75E-02	1.69E-02	
5.67	-0.357	5.28E-03		6.02E-03	9.13E-03	9.73E-03	
6.167	-0.285	2.63E-03		3.31E-03	4.44E-03	4.98E-03	
6.764	-0.227	1.07E-03		1.43E-03	1.76E-03	2.04E-03	

Table B.18 – The complexation induced dipole moment change ($\|\mu^{comp}\| = \|\mu_{AB}\| - \|\mu_A^{iso}\| - \|\mu_B^{iso}\|$), labelled as "complexation", of the isolated fragments, from the total dipole of the Kohn-Sham treatment of the system. The errors of the dipole moment of two subsystem after Freeze and Thaw from the supermolecular reference are shown for the use of different nonadditive kinetic potentials in FDET. The empty entries mean that the Freeze and Thaw procedure is not converged in this separation distance with the corresponding potential. The system is $Na^+ - NH_3$.

In general, the results from the dipole moment follow a similar trend as the distance norm. NDCS functional does not improve the dipole moment in the long range for the Na^+ case.

Appendix C

Supporting information for [Fu M, Wesolowski TA, *J. Chem. Theory Comput.* 17, 3652-3665 (2021)]

Supporting Information for: The challenge of accurate computation of the two-photon absorption properties of organic chromophores in condensed phase

Mingxue Fu* and Tomasz A. Wesolowski

Department of Physical Chemistry, University of Geneva, 30, Quai Ernest-Ansermet, CH-1211 Genève 4, Switzerland

E-mail: Mingxue.Fu@unige.ch, Tomasz.Wesolowski@unige.ch

Table S1: The Cartesian coordinates of the complex $C_2H_4 - H_2O$ (in Å).

H	-0.03483	-0.24421	0.06365
C	-1.07660	-0.52427	-0.00236
H	-1.31326	-1.57676	-0.07573
C	-2.04363	0.39269	0.00613
H	-1.81376	1.44592	0.08045
H	-3.08598	0.11493	-0.05934
O	2.45322	0.21103	0.03922
H	2.72389	-0.57247	0.52337
H	2.57762	-0.03606	-0.88008

Table S2: The electrostatic potential derived net atomic charges from the Hartree-Fock density of the isolated water molecule derived using different basis sets.

basis set	q_H	q_O
6-31+G*	0.42	-0.84
aug-cc-pVDZ	0.37	-0.74
aug-cc-pVTZ	0.37	-0.74
aug-cc-pVQZ	0.37	-0.73
d-aug-cc-pVDZ	0.36	-0.73
d-aug-cc-pVTZ	0.36	-0.72
d-aug-cc-pVQZ	0.36	-0.72

Table S3: The vertical excitation energies ϵ^{isol} (in eV) and the two-photon cross-sections δ^{isol}_{TPA} (in atomic units) for the two lowest $\pi\pi^*$ transitions from the conventional ADC(2) calculations applied to the isolated C_2H_4 and the corresponding shifts in the C_2H_4-H_2O complex without counterpoise correction. The EOM-CCSD results (if available) are given in parentheses.

basis set	ϵ^{isol}	$\Delta\epsilon$	δ^{isol}_{TPA}	$\Delta\delta_{TPA}$
		first $\pi\pi^*$ state:		
cc-pVDZ	8.737(8.883)	-0.017(-0.019)	0(0)	0(0.1)
cc-pVTZ	8.363(8.469)	-0.026(-0.024)	0(0.7)	0.1(-0.6)
cc-pVQZ	8.215(8.305)	-0.035(-0.031)	0(0)	0.2(0.3)

For the cc-pVXZ(X=D,T,Q) basis sets the second $\pi\pi^*$ state is not found in ADC(2) and EOM-CCSD calculations.

Table S4: The ADC(2) complexation-induced shifts in the vertical excitation energy $\Delta\epsilon$ and the TPA cross-section $\Delta\delta_{TPA}$ with the counterpoise correction and the value of counterpoise correction in the vertical excitation energy $\delta^{CP}\epsilon$ and the TPA cross-section $\delta^{CP}\delta_{TPA}$ of the corresponding basis set for the first $\pi\pi^*$ state.

basis set	$\Delta\epsilon$	$\delta^{CP}\epsilon$	$\Delta\delta_{TPA}$	$\delta^{CP}\delta_{TPA}$
6-31+G*	-0.058	0.004	24.7	-0.5
cc-pVDZ	-0.006	0.011	-0.1	-0.1
cc-pVTZ	-0.012	0.014	-0.1	-0.2
cc-pVQZ	-0.019	0.016	-0.2	-0.4
aug-cc-pVDZ	-0.088	0.006	41.8	-1.4
aug-cc-pVTZ	-0.058	0.002	40.1	-0.3
aug-cc-pVQZ	-0.075	0.001	20.7	-0.1
d-aug-cc-pVDZ	-0.087	0.001	22.3	0
d-aug-cc-pVTZ	-0.069	0	23.7	0
d-aug-cc-pVQZ	-0.083	0	35.9	0

Table S5: The ADC(2) complexation-induced shifts in the vertical excitation energy $\Delta\epsilon$ and the TPA cross-section δ_{TPA} with the counterpoise correction and the value of counterpoise correction in the vertical excitation energy $\delta^{CP}\epsilon$ and the TPA cross-section $\delta^{CP}\delta_{TPA}$ of the corresponding basis set for the second $\pi\pi^*$ state.

basis set	$\Delta\epsilon$	$\delta^{CP}\epsilon$	$\Delta\delta_{TPA}$	$\delta^{CP}\delta_{TPA}$
6-31+G*	-0.101	0.024	0.2	-9.9
aug-cc-pVDZ	-0.187	0.166	-81.7	59.2
aug-cc-pVTZ	-0.180	0.107	-60.1	27.8
aug-cc-pVQZ	-0.177	0.070	-35.1	16.5
d-aug-cc-pVDZ	-0.179	0.002	-43.1	-10.2
d-aug-cc-pVTZ	-0.183	-0.001	-22.4	-1.4
d-aug-cc-pVQZ	-0.184	0	-20.2	0.5

Figure S1: The natural transition orbitals of the lowest excited states obtained by the exact Coulomb embedding using d-aug-cc-pVQZ basis sets.

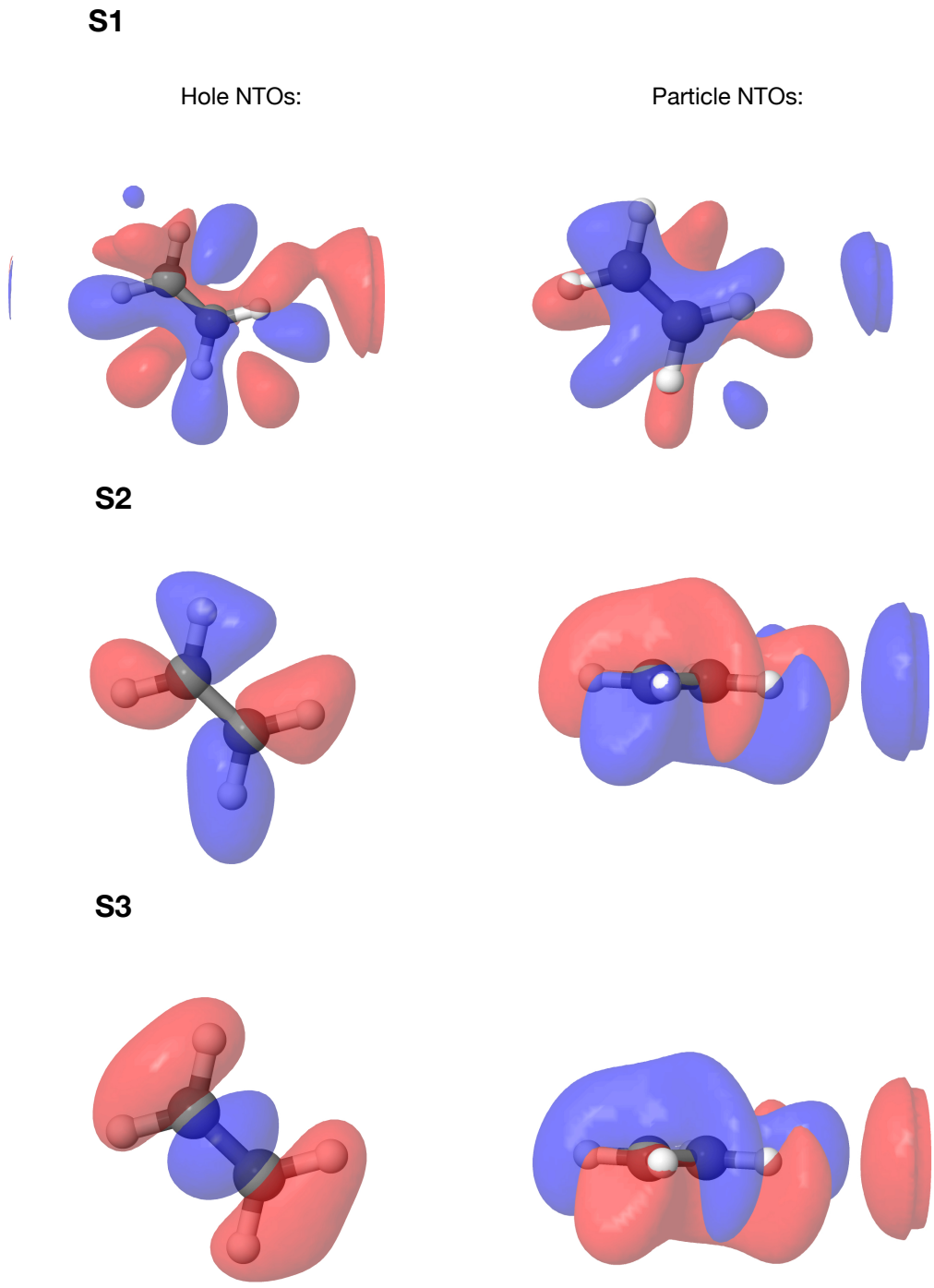

Appendix D

Additional supporting information for [Fu M, Wesolowski TA, *J. Chem. Theory Comput.* 17, 3652-3665 (2021)]

Additional analysis made after the publication is provided in this appendix.

D.1 Natural transition orbitals (NTOs) for the second $\pi\pi^*$ state

To better illustrate the genuine excitation character of the second $\pi\pi^*$ state, a smaller cutoff value was selected to highlight the delocalized nature of this state.

D.2 The exciton descriptor

In this section, a quantitative tool for the analysis of the excitation character of excited states was used. This approach utilizes the exciton wavefunction to analyze the excitation character of states that may be challenging to discern through visualization alone.[95]. The exciton wavefunction is introduced in which the hole and electron coordinate are written with the one-particle transition density matrix between the ground and excited state. The hole size d_h is defined as the variance of position operator at the hole coordinate $d_h = \sqrt{\langle \vec{r_h}^2 \rangle_{exc} - \langle \vec{r_h} \rangle^2_{exc}}$. The same applies to the electron size except that the position operator $\vec{r_h}$ is substituted by $\vec{r_e}$. The exciton size $d_{exc} = \sqrt{\langle |r_h - r_e|^2 \rangle_{exc}}$ measures both the spatial extension of particles and the distance between them.

In Table D.1, it is evident that the two states exhibit a similar hole size due to the similar ground state wavefunction. However, the significantly larger electron size and exciton size for the second $\pi\pi^*$ state suggests that the second $\pi\pi^*$ state is more delocalized in space than the first one.

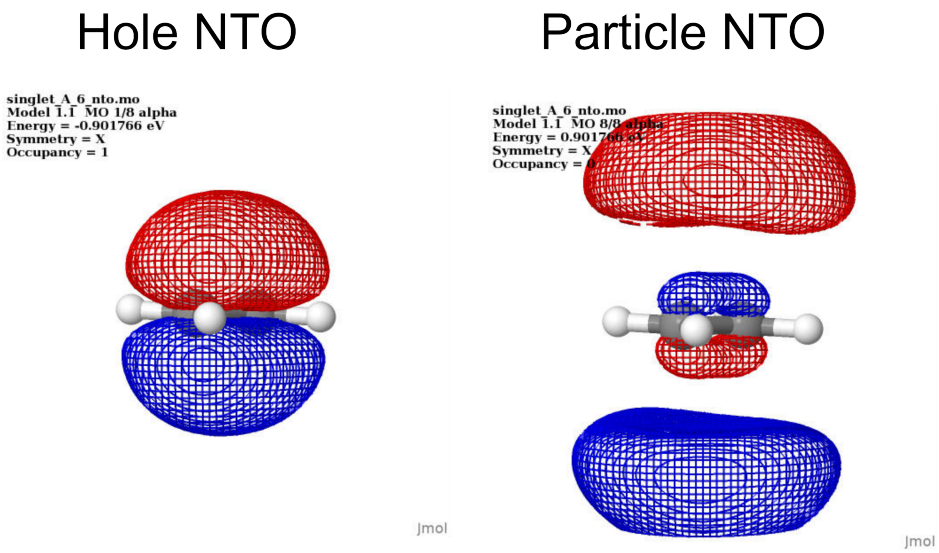

Figure D.1 – The natural transition orbitals of the isolated C_2H_4 for the second $\pi\pi^*$ state calculated by ADC(2) using aug-cc-pVDZ basis set.

Table D.1 – The exciton descriptors calculated by the reference ADC(2) method with the d-aug-cc-pVDZ basis sets for two $\pi\pi^*$ states.

	hole size σ_h	electron size σ_e	exciton size d_{exc}
first $\pi\pi^*$ state	1.278	3.191	3.455
second $\pi\pi^*$ state	1.270	4.926	5.083

Appendix E

Supporting document for [Fu M, Wesolowski TA, *J. Phys. Chem. A.* 127, 535-545 (2023)]

Supplemental material for: Explicit treatments of excitation-induced response of electron density of the environment within Frozen-Density Embedding Theory

M. Fu* and T. A. Wesolowski†
Department of Physical Chemistry,
University of Geneva, Geneva, Switzerland

* Mingxue.Fu@unige.ch
† Tomasz.Wesolowski@unige.ch

I. DERIVATION OF THE EXCITATION ENERGY IN A STATE-SPECIFIC CASE

The FDET energy functional $E_{v_{AB}}^{FDET}[\Psi_A, \rho_B]$ satisfies the basic equality which for embedded interacting wavefunction reads:

$$\begin{aligned} \min_{\Psi_A \to N_A} E_{v_{AB}}^{FDET}[\Psi_A, \rho_B] &= E_{v_{AB}}^{FDET}[\Psi_A^o, \rho_B] = E_{v_{AB}}^{HK}[\rho_A^o + \rho_B] \\ &= \min_{\substack{\forall \mathbf{r} \rho(\mathbf{r}) \geq \rho_B(\mathbf{r}) \\ \rho(\mathbf{r}) \to N_{AB}}} E_{v_{AB}}^{HK}[\rho] \end{aligned} \tag{1}$$

Perdew-Levy theorem states that the stationary solutions other than the ground-state in the ground-state Hohenberg-Kohn energy functional can be interpreted as excited state.

$$\epsilon_j = E_{v_{AB}}^{HK}[\rho_A^j + \rho_B^j] - E_{v_{AB}}^{HK}[\rho_A^o + \rho_B^o] \tag{2}$$

$$= E_{v_{AB}}^{FDET}[\Psi_A^j, \rho_B^j] - E_{v_{AB}}^{FDET}[\Psi_A^o, \rho_B^o] \tag{3}$$

$$= \underbrace{E_{v_{AB}}^{FDET}[\Psi_A^j, \rho_B^j] - E_{v_{AB}}^{FDET}[\Psi_A^o, \rho_B^j]}_{\mathbf{A}} + \underbrace{E_{v_{AB}}^{FDET}[\Psi_A^o, \rho_B^j] - E_{v_{AB}}^{FDET}[\Psi_A^o, \rho_B^o]}_{\mathbf{B}} \tag{4}$$

The first equality from Eq. 2 to Eq. 3 is exact if the density ρ_B does not violate the non-negativity conditions of the target density:

$$\forall_{\vec{r}}\, \rho_B \;\leq\; \rho_{v_{AB}}^j$$

and

$$\forall_{\vec{r}}\, \rho_B \;\leq\; \rho_{v_{AB}}^o,$$

where $\rho_{v_{AB}}^j$ and $\rho_{v_{AB}}^o$ are the exact densities for the whole system for the two considered states. If the above conditions are not satisfied, the energy evaluated for each state using the corresponding embedded wavefunction lies above the exact one.
Addition and subtraction $E_{v_{AB}}^{FDET}[\Psi_A^o, \rho_B^j]$ in Eq. 3 leads to Eq. 4.
We begin by evaluating **A** in Eq. 4. The linearization of the $E_{\mathrm{xc,T}}^{\mathrm{nad}}[\rho_A, \rho_B]$ is applied to avoid the ρ_A dependency in the embedding potential. Therefore **A** can simply be written as the eigenvalue difference between two states. For a same density ρ_B^j it can be shown:

$$
\begin{aligned}
A = &\left\langle \Psi_A^j \left| \hat{H}_A + \hat{v}_{emb}^{FDET}[\rho_A^{ref}, \rho_B^j; v_B] \right| \Psi_A^j \right\rangle + E_{v_B}^{HK}[\rho_B^j] && (5)\\
&+ V_A[\rho_B^j] + \underbrace{E_{\mathrm{xc,T}}^{\mathrm{nad}}[\rho_A^{ref}, \rho_B^j] + \int (\rho_A^j - \rho_A^{ref}) v_{xct}^{nad}[\rho_A^{ref}, \rho_B^j] d\mathbf{r}}_{\text{linearization of } E_{\mathrm{xc,T}}^{\mathrm{nad}}[\rho_A^j, \rho_B^j]} - \int \rho_A^j(\mathbf{r}) v_{xct}^{nad}[\rho_A^{ref}, \rho_B^j] d\mathbf{r}\\
&- \left\langle \Psi_A^o \left| \hat{H}_A + \hat{v}_{emb}^{FDET}[\rho_A^{ref}, \rho_B^j; v_B] \right| \Psi_A^o \right\rangle - E_{v_B}^{HK}[\rho_B^j] && (6)\\
&- V_A[\rho_B^j] - \underbrace{E_{\mathrm{xc,T}}^{\mathrm{nad}}[\rho_A^{ref}, \rho_B^j] - \int (\rho_A^o - \rho_A^{ref}) v_{xct}^{nad}[\rho_A^{ref}, \rho_B^j] d\mathbf{r}}_{\text{linearization of } E_{\mathrm{xc,T}}^{\mathrm{nad}}[\rho_A^o, \rho_B^j]} + \int \rho_A^o(\mathbf{r}) v_{xct}^{nad}[\rho_A^{ref}, \rho_B^j] d\mathbf{r}\\
= &\left\langle \Psi_A^j \left| \hat{H}_A + \hat{v}_{emb}^{FDET}[\rho_A^{ref}, \rho_B^j; v_B] \right| \Psi_A^j \right\rangle - \left\langle \Psi_A^o \left| \hat{H}_A + \hat{v}_{emb}^{FDET}[\rho_A^{ref}, \rho_B^j; v_B] \right| \Psi_A^o \right\rangle\\
= &\lambda_j[\rho_A^{ref}, \rho_B^j] - \lambda_o[\rho_A^{ref}, \rho_B^j] && (7)
\end{aligned}
$$

Note this result can be used in any correlated methods for excited states such as ADC(2), EOM-CCSD etc.

For the evaluation of $\mathbf{B}$, the embedded interacting wavefunction Ψ_A can be replaced by the single determinant wavefunction Φ_A self-consistenly obtained using the recent derived relation. In case of the correlation energy obtained by means of some non-variational method, this relation reads:

$$
\begin{aligned}
E_{v_{AB}}^{HK}[\rho_A + \rho_B] \;=\; & E_{v_{AB}}^{FDET}[\Phi_A^{'}, \rho_B] + E_{v'}^c && (8)\\
& - \int \rho_A^{'}(\mathbf{r}) \left(\int \Delta\rho_{v'}^c(\mathbf{r}') f_{xct}^{nad}[\rho_A^{'}, \rho_B](\mathbf{r}, \mathbf{r}') d\mathbf{r}' \right) d\mathbf{r} + O(\Delta^2\rho),
\end{aligned}
$$

where $\rho_A(\mathbf{r})$ is the density obtained from the exact solution of the FDET Schrodinger equation, $\rho_A^{'}(\mathbf{r}) = \langle \Phi_A^{'} | \sum_{i=1}^{N_A} \delta(\mathbf{r}_i - \mathbf{r}) | \Phi_A^{'} \rangle$, $v'(\mathbf{r}) = v_A(\mathbf{r}) + v_{emb}^{FDET}[\rho_A^{'}, \rho_B; v_B](\mathbf{r})$, $\Phi_A^{'}$ is the stationary single determinant obtained with the potential v', $E_{v'}^c$ is the correlation energy in the N_A-electron system defined by the potential v', $f_{xct}^{nad}[\rho_A^{'}, \rho_B](\mathbf{r}, \mathbf{r}') = \frac{\delta^2 E_{xct}^{nad}[\rho_A, \rho_B]}{\delta\rho_A(\mathbf{r})\delta\rho_A(\mathbf{r}')}$, and $\Delta\rho_{v'}^c$ is the correlation-induced change of the electron density, and $O(\Delta^2\rho)$ collects all contributions to energy due to the effect of correlation on density that are of higher order.

We again apply the linearization on $E_{\mathrm{xc,T}}^{\mathrm{nad}}[\rho_A, \rho_B]$ and ignore the higher order terms in $(\rho_A - \rho_A^{ref})$. The liner term in Eq. 8 disappears. Pluging in Eq. 8 and neglecting higher order terms $O(\Delta^2\rho)$ to Eq. 4 leads to:

$$
\begin{aligned}
B = &\left\langle \Phi_A^{\prime o(j)} \left| \hat{H}_A + \hat{v}_{emb}^{FDET}[\rho_A^{ref}, \rho_B^j; v_B] \right| \Phi_A^{\prime o(j)} \right\rangle + E_{v'j}^c + E_{v_B}^{HK}[\rho_B^j] \\
&+ V_A[\rho_B^j] + \underbrace{E_{\mathrm{xc,T}}^{\mathrm{nad}}[\rho_A^{ref}, \rho_B^j] + \int (\rho_A^{\prime o(j)} - \rho_A^{ref}) v_{xct}^{nad}[\rho_A^{ref}, \rho_B^j] d\mathbf{r}}_{\text{linearization of } E_{\mathrm{xc,T}}^{\mathrm{nad}}[\rho_A^{\prime o(j)}, \rho_B^j]} - \int \rho_A^{\prime o(j)}(\mathbf{r}) v_{xct}^{nad}[\rho_A^{ref}, \rho_B^j] d\mathbf{r} \\
&- \left\langle \Phi_A^{\prime o(o)} \left| \hat{H}_A + \hat{v}_{emb}^{FDET}[\rho_A^{ref}, \rho_B^o; v_B] \right| \Phi_A^{\prime o(o)} \right\rangle - E_{v'o}^c - E_{v_B}^{HK}[\rho_B^o] \\
&- V_A[\rho_B^o] - \underbrace{E_{\mathrm{xc,T}}^{\mathrm{nad}}[\rho_A^{ref}, \rho_B^o] - \int (\rho_A^{\prime o(o)} - \rho_A^{ref}) v_{xct}^{nad}[\rho_A^{ref}, \rho_B^o] d\mathbf{r}}_{\text{linearization of } E_{\mathrm{xc,T}}^{\mathrm{nad}}[\rho_A^{\prime o(o)}, \rho_B^o]} + \int \rho_A^{\prime o(o)}(\mathbf{r}) v_{xct}^{nad}[\rho_A^{ref}, \rho_B^o] d\mathbf{r} \\
= &\left\langle \Phi_A^{\prime o(j)} \left| \hat{H}_A + \hat{v}_{emb}^{FDET}[\rho_A^{ref}, \rho_B^j; v_B] \right| \Phi_A^{\prime o(j)} \right\rangle - \left\langle \Phi_A^{\prime o(o)} \left| \hat{H}_A + \hat{v}_{emb}^{FDET}[\rho_A^{ref}, \rho_B^o; v_B] \right| \Phi_A^{\prime o(o)} \right\rangle \\
&+ E_{v'j}^c - E_{v'o}^c + E_{v_B}^{HK}[\rho_B^j] - E_{v_B}^{HK}[\rho_B^o] \\
&+ V_A[\rho_B^j] - V_A[\rho_B^o] \\
&+ E_{\mathrm{xc,T}}^{\mathrm{nad}}[\rho_A^{ref}, \rho_B^j] - E_{\mathrm{xc,T}}^{\mathrm{nad}}[\rho_A^{ref}, \rho_B^o] \\
&- \left(\int \rho_A^{ref}(\mathbf{r}) v_{xct}^{nad}[\rho_A^{ref}, \rho_B^j] d\mathbf{r} - \int \rho_A^{ref}(\mathbf{r}) v_{xct}^{nad}[\rho_A^{ref}, \rho_B^o] d\mathbf{r} \right)
\end{aligned}
$$

The summation of the result from **A** and **B** gives the final result of ϵ_j in Eq. 14 in the manuscript.

II. COMPLEXATION INDUCED SHIFTS

The density matrix and properties were obtained with cc-pVDZ basis set unless specified.

III. CHELPG CHARGES USED FOR DIFFERENT PROTOCOLS

System	Excited state	ϵ_{shift}^{ref}	Excitation type	Protocol A	Protocol B	Protocol D	Protocol C	Protocol E
7-hydroxyquinoline(2NH3)	1	-0.2668	$\pi\pi^*$	0.0974	0.0728	0.0627	0.093	0.0583
	4	-0.261	$\pi\pi^*$	0.0967	0.0753	0.0643	0.0948	0.0621
	8	0.031	$\pi\pi^*$	0.0106	0.0147	0.0178	0.0275	0.0127
7-hydroxyquinoline(MeOH)(H-O)	1	-0.1017	$\pi\pi^*$	0.0406	0.0299	0.0261	0.029	0.0261
	5	-0.1157	$\pi\pi^*$	0.0504	0.0398	0.0358	0.0389	0.036
	9	0.0245	$n\pi^*$	0.0154	0.0221	0.0234	0.0221	0.0218
	10	-0.0391	$\pi\pi^*$	0.0325	0.0306	0.0314	0.0302	0.0296
xanthine(MeCN)	1	0.1424	$n\pi^*$	-0.0308	0.0015	0.0021	0.005	-0.0007
	2	-0.0483	$\pi\pi^*$	0.0423	0.0367	0.0358	0.0464	0.0332
	4	0.0208	$n\pi^*$	0.0052	0.0101	0.0111	0.0181	0.0095
	5	-0.0317	$n\pi^*$	0.0291	0.027	0.0271	0.0361	0.0248
	6	0.0847	$\pi\pi^*$	0.011	0.0309	0.0355	0.0344	0.0312
	7	-0.0954	$\pi\pi^*$	0.0442	0.0314	0.0291	0.045	0.028
	9	-0.0294	$\pi\pi^*$	0.0225	0.0231	0.0226	0.032	0.0222
7-hydroxyquinoline(2MeOH)	1	-0.2517	$\pi\pi^*$	0.0988	0.0745	0.0625	0.097	0.0485
	4	-0.269	$\pi\pi^*$	0.1212	0.0886	0.0726	0.1113	0.0633
	7	-0.1473	$\pi\pi^*$	0.0722	0.0594	0.0527	0.0798	0.041
xanthine(MeOH)	1	-0.1126	$\pi\pi^*$	0.0669	0.0559	0.048	0.0654	0.0295
	5	0.0617	$n\pi^*$	-0.0383	-0.0387	-0.037	-0.03	-0.0595
	6	0.0825	$\pi\pi^*$	0.0077	0.0219	0.0314	0.0273	0.026
	7	-0.0337	$n\pi^*$	0.0403	0.0422	0.0287	0.0471	0.0217
	8	-0.0876	$\pi\pi^*$	0.0444	0.036	0.0339	0.048	0.0146
	9	-0.0412	$\pi\pi^*$	0.0228	0.0218	0.0189	0.0307	0.0156
7-hydroxyquinoline(2H2O)	1	-0.2424	$\pi\pi^*$	0.0852	0.0657	0.0567	0.0858	0.0297
	2	-0.1609	$\pi\pi^*$	0.0533	0.0412	0.0361	0.0598	0.0088
	4	-0.2493	$\pi\pi^*$	0.0902	0.0725	0.0598	0.0923	0.0566
	5	-0.2144	$\pi\pi^*$	0.0946	0.0715	0.0659	0.0888	0.0591
	7	-0.1288	$\pi\pi^*$	0.0544	0.0445	0.0395	0.0626	0.0369
aminopurine(H2O)	1	-0.0148	$\pi\pi^*$	0.0131	0.0117	0.0105	0.0197	0.0061
	2	0.1171	$n\pi^*$	-0.0092	0.008	0.0161	0.0122	0.0096
	3	-0.1077	$\pi\pi^*$	0.0483	0.0383	0.0379	0.0485	0.031
	6	-0.0374	$\pi\pi^*$	0.0238	0.0215	0.0207	0.0297	0.0164
	7	0.0763	$\pi\pi^*$	-0.0078	0.0009	0.0038	0.0067	-0.0006
pyrimidine(H2O)	1	0.0725	$n\pi^*$	0.0054	0.0064	0.017	0.016	0.0113
	2	0.1436	$n\pi^*$	-0.0131	0.0108	0.005	0.0004	-0.0007
	3	-0.034	$\pi\pi^*$	0.0127	-0.0019	0.0072	0.0177	0.0045
	6	-0.0013	$\pi\pi^*$	0.0023	0.0	0.0013	0.0086	-0.0016
	9	-0.0261	$\pi\pi^*$	0.0352	0.0355	0.0384	0.0417	0.0337
uracil(5H2O)	2	-0.2237	$\pi\pi^*$	0.1109	0.0974	0.0941	0.1493	0.0632
	6	-0.3365	$\pi\pi^*$	0.1589	0.1406	0.1405	0.1943	0.1038
	8	-0.1185	$\pi\pi^*$	0.1006	0.1045	0.1673	0.1431	0.082
7-hydroxyquinoline(MeOH)(N-H)	1	-0.0884	$\pi\pi^*$	0.0419	0.033	0.0277	0.0524	0.0198
	3	-0.0999	$\pi\pi^*$	0.0455	0.0354	0.0304	0.0561	0.0248
	4	-0.1192	$\pi\pi^*$	0.0583	0.0475	0.0363	0.0675	0.0302
	7	-0.0786	$\pi\pi^*$	0.0508	0.0444	0.0421	0.0631	0.033
	8	-0.0454	$\pi\pi^*$	0.0246	0.0206	0.0161	0.0385	0.0104
	9	0.0148	$\pi\pi^*$	0.0156	0.02	0.0254	0.0352	0.0184

TABLE S1: The reference complexation induced shift [eV] and the error for different choices of ρ_B for all systems studied.

System	Excited state	ϵ_j^A	ϵ_j^B	ϵ_j^C	ϵ_j^D	ϵ_j^E
7-hydroxyquinoline(2NH3)	1	4.083	0.6720	0.0002	-0.7016	0.0253
	4	5.7354	0.5228	0.0005	-0.5586	0.0301
	8	6.8347	-0.0273	-0.0001	0.0382	-0.0071
7-hydroxyquinoline(MeOH)(H-O)	1	4.1885	0.9376	0.0002	-0.9531	0.0148
	5	5.7939	1.0746	0.0	-1.0911	0.0162
	9	6.7668	-0.8819	0.0	0.8946	-0.0083
	10	6.9821	-0.204	0.0	0.2076	-0.0029
xanthine(MeCN)	1	5.1777	1.0304	0.0011	-0.983	-0.0294
	2	5.2738	-0.8843	-0.0003	0.8869	-0.0011
	4	6.5491	-0.0529	0.0005	0.046	0.0058
	5	6.6377	-0.3438	0.0	0.3528	-0.0076
	6	6.7929	-1.042	0.0001	1.0464	-0.0026
	7	7.0035	0.3961	0.0	-0.4096	0.0125
	9	7.187	-0.18	0.0001	0.176	0.0036
7-hydroxyquinoline(2MeOH)	1	4.1005	0.7902	0.0004	-0.8172	0.0217
	4	5.7552	0.559	-0.0002	-0.5979	0.0309
	7	6.278	0.0409	0.0	-0.0579	0.0124
xanthine(MeOH)	1	5.2182	-1.1242	-0.0003	1.1149	0.0054
	5	6.5394	-0.2127	0.0	0.22	-0.0054
	6	6.7489	-0.3124	0.0003	0.3492	-0.0234
	7	6.9782	-3.0021	-0.0007	2.9942	0.0084
	8	6.9976	0.3351	0.0	-0.3443	0.0079
	9	7.1613	-0.3094	-0.0001	0.3031	0.0038
7-hydroxyquinoline(2H2O)	1	4.1035	0.2278	0.0001	-0.2497	0.017
	2	4.8162	0.3945	-0.0001	-0.4085	0.0112
	4	5.7598	-0.0029	-0.0001	-0.0287	0.0241
	5	6.1144	0.0714	0.0	-0.0859	0.0109
	7	6.2879	-0.0703	0.0	0.0571	0.0095
aminopurine(H2O)	1	4.5654	-0.2476	0.0	0.246	0.0009
	2	4.7202	1.1291	0.0001	-1.0983	-0.0158
	3	5.5826	0.3424	0.0	-0.3448	0.0029
	6	6.325	-0.0504	0.0	0.0481	0.0016
	7	7.0039	0.0627	0.0	-0.0502	-0.0082
pyrimidine(H2O)	1	4.4055	0.5273	0.0	-0.5151	-0.0044
	2	5.0542	0.8834	0.0	-0.8623	-0.0062
	3	5.3256	-0.2629	0.0	0.2566	0.0032
	6	7.1639	-0.0827	0.0	0.0808	0.0009
	9	8.3354	0.205	0.0	-0.1999	-0.0021
uracil(5H2O)	2	5.3063	0.4489	0.0003	-0.4517	0.0052
	6	6.872	-0.7644	-0.0005	0.7685	-0.0009
	8	7.5271	1.404	0.0013	-1.2844	-0.044
7-hydroxyquinoline(MeOH)(N-H)	1	4.2593	-0.1255	-0.0002	0.1153	0.0068
	3	4.9126	0.1541	-0.0003	-0.1635	0.0066
	4	5.8779	-0.5272	-0.0004	0.5054	0.0148
	7	6.2729	-0.1614	-0.0001	0.1568	0.003
	8	6.3441	-0.3142	-0.0002	0.304	0.0065
	9	6.8239	0.3777	0.0002	-0.3652	-0.0065

TABLE S2: The excitation energy [eV] contributions to ϵ_j in case of the state specific embedding (*Protocol D*).

System	Excited state	ϵ_{shift}^{ref}	Excitation type	Protocol D	Charge difference
7-hydroxyquinoline(2NH3)	1	-0.2668	$\pi\pi^*$	0.0627	-0.1023
	4	-0.261	$\pi\pi^*$	0.0643	-0.0928
	8	0.031	$\pi\pi^*$	0.0178	-0.084
7-hydroxyquinoline(MeOH)(H-O)	1	-0.1017	$\pi\pi^*$	0.0261	0.0808
	5	-0.1157	$\pi\pi^*$	0.0358	0.0821
	9	0.0245	$n\pi^*$	0.0234	0.0821
	10	-0.0391	$\pi\pi^*$	0.0314	0.1049
xanthine(MeCN)	1	0.1424	$n\pi^*$	0.0021	0.0566
	2	-0.0483	$\pi\pi^*$	0.0358	0.0577
	4	0.0208	$n\pi^*$	0.0111	0.0538
	5	-0.0317	$n\pi^*$	0.0271	0.0599
	6	0.0847	$\pi\pi^*$	0.0355	0.061
	7	-0.0954	$\pi\pi^*$	0.0291	0.08
	9	-0.0294	$\pi\pi^*$	0.0226	0.0564
7-hydroxyquinoline(2MeOH)	1	-0.2517	$\pi\pi^*$	0.0625	-0.1683
	4	-0.269	$\pi\pi^*$	0.0726	-0.1584
	7	-0.1473	$\pi\pi^*$	0.0527	-0.1473
xanthine(MeOH)	1	-0.1126	$\pi\pi^*$	0.048	-0.0896
	5	0.0617	$n\pi^*$	-0.037	-0.1225
	6	0.0825	$\pi\pi^*$	0.0314	-0.0699
	7	-0.0337	$n\pi^*$	0.0287	-0.0516
	8	-0.0876	$\pi\pi^*$	0.0339	-0.0676
	9	-0.0412	$\pi\pi^*$	0.0189	-0.0552
7-hydroxyquinoline(2H2O)	1	-0.2424	$\pi\pi^*$	0.0567	-0.1656
	2	-0.1609	$\pi\pi^*$	0.0361	-0.1574
	4	-0.2493	$\pi\pi^*$	0.0598	-0.1558
	5	-0.2144	$\pi\pi^*$	0.0659	-0.1371
	7	-0.1288	$\pi\pi^*$	0.0395	-0.1512
aminopurine(H2O)	1	-0.0148	$\pi\pi^*$	0.0105	-0.1092
	2	0.1171	$n\pi^*$	0.0161	-0.1457
	3	-0.1077	$\pi\pi^*$	0.0379	-0.1235
	6	-0.0374	$\pi\pi^*$	0.0207	-0.08
	7	0.0763	$\pi\pi^*$	0.0038	-0.1073
pyrimidine(H2O)	1	0.0725	$n\pi^*$	0.017	-0.1784
	2	0.1436	$n\pi^*$	0.005	-0.1716
	3	-0.034	$\pi\pi^*$	0.0072	-0.0833
	6	-0.0013	$\pi\pi^*$	0.0013	-0.0833
	9	-0.0261	$\pi\pi^*$	0.0384	-0.0833
uracil(5H2O)	2	-0.2237	$\pi\pi^*$	0.0941	-0.1899
	6	-0.3365	$\pi\pi^*$	0.1405	-0.182
	8	-0.1185	$\pi\pi^*$	0.1673	-0.226
7-hydroxyquinoline(MeOH)(N-H)	1	-0.0884	$\pi\pi^*$	0.0277	-0.1255
	3	-0.0999	$\pi\pi^*$	0.0304	-0.1113
	4	-0.1192	$\pi\pi^*$	0.0363	-0.1242
	7	-0.0786	$\pi\pi^*$	0.0421	-0.1463
	8	-0.0454	$\pi\pi^*$	0.0161	-0.1011
	9	0.0148	$\pi\pi^*$	0.0254	-0.1242

TABLE S3: The chelpg charge difference of the atom located on the chromophore which is affected most by the complexation effect using the *Protocol D* and its excitation error compared with the reference.

	Protocol D			Protocol E		
State	In	Out	Charge difference	In	Out	Charge difference
s2	-0.4548	-0.6447	0.1899	-0.6418	-0.6524	0.0106
s6	-0.447	-0.629	0.182	-0.6299	-0.6381	0.0082
s8	-0.315	-0.541	0.226	-0.6491	-0.5515	-0.0976

TABLE S4: The chelpg charge of the oxygen in the uracil used for pre-polarising and after pre-polarising the environment applying *Protocol D* and *Protocol E* in the uracil(5H2O) case.

System	Excited state	ϵ_{shift}^{ref}	Excitation type	Protocol A	Protocol B	Protocol D	Protocol C	Protocol E
aminopurine(H2O)	1	-0.0143	$\pi\pi^*$	0.0095	0.0080	0.0062	0.0297	-0.0006
	2	0.1104	$n\pi^*$	0.0076	0.0304	0.0413	0.0442	0.0313
	7	-0.0579	$\pi\pi^*$	0.0187	0.0174	0.0182	0.0399	0.0106
pyrimidine(H2O)	1	0.0685	$n\pi^*$	0.0186	0.0274	0.0357	0.0351	0.0267
	2	0.1306	$n\pi^*$	0.0078	0.0223	0.0317	0.0276	0.0237
	3	-0.0273	$\pi\pi^*$	0.0091	0.0070	0.0033	0.0193	-0.0012

TABLE S5: The reference complexation induced shift [eV] and the error for different choices of ρ_B using the augmented basis set aug-cc-pVDZ.

	N	N	C	C	C	C	H	H	H	H
s0	-0.3976	-0.403	0.1348	0.1528	0.1388	0.1492	0.0599	0.0526	0.0576	0.0548
s1	-0.1487	-0.1882	-0.0718	-0.0275	-0.0667	-0.0341	0.1392	0.1289	0.138	0.1309
s2	-0.0322	-0.0602	-0.1081	-0.0863	-0.1084	-0.0882	0.1238	0.1168	0.1235	0.1192
s3	-0.5061	-0.5121	0.2013	0.2214	0.2054	0.2164	0.0474	0.0394	0.0449	0.0419
s4	-0.0604	-0.0317	-0.0885	-0.0917	-0.0839	-0.0977	0.1148	0.112	0.1131	0.114
s5	0.0614	0.0922	-0.1313	-0.1465	-0.1317	-0.1481	0.1008	0.1004	0.1	0.1028
s6	-0.4436	-0.4456	0.1797	0.1899	0.1817	0.1875	0.0404	0.0344	0.0388	0.0368
s7	-0.2582	-0.2622	0.0869	0.1027	0.0963	0.0937	0.0378	0.0324	0.0361	0.0343
s8	-0.3347	-0.3483	0.1222	0.1419	0.1217	0.1428	0.0436	0.0338	0.0404	0.0366
s9	-0.0363	-0.0624	0.1622	0.1817	0.1714	0.1819	-0.1485	-0.1432	-0.1568	-0.1501
s10	-0.4602	-0.4692	0.0563	0.0799	0.0621	0.0737	0.1658	0.1634	0.1626	0.1656

TABLE S6: The chelpg charges used for the average in pyrimidine(H2O) complex.

	N	C	C	C	C	C	C	C	C	C	O	H	H	H	H	H	H	H
s0	-0.6222	0.3444	-0.4364	0.0626	-0.1172	-0.3459	0.5408	-0.7181	0.7568	-0.2414	-0.5396	0.402	0.2303	0.0549	0.173	0.1135	0.1473	0.1953
s1	-0.6253	0.2007	-0.2969	-0.0707	-0.1425	-0.4396	0.6075	-0.6475	0.7382	-0.1473	-0.4686	0.4148	0.2122	0.0545	0.1577	0.1059	0.1515	0.1956
s2	0.2439	-0.3141	-0.1133	-0.3934	-0.3026	-0.3374	0.4729	-0.6184	0.2206	0.1831	-0.5421	0.3977	0.2178	0.1968	0.1576	0.1669	0.1799	0.1841
s3	-0.6924	0.395	-0.5663	0.0484	-0.0032	-0.3075	0.4676	-0.5266	0.7937	-0.3433	-0.528	0.4092	0.2107	0.0438	0.1764	0.0925	0.134	0.1961
s4	0.2946	-0.2141	-0.2477	-0.2714	-0.2806	-0.2782	0.4254	-0.6206	0.1343	0.1201	-0.5432	0.3837	0.234	0.1897	0.1436	0.1888	0.174	0.1676
s5	-0.7022	0.3207	-0.4063	-0.0868	-0.0993	-0.3367	0.5415	-0.6032	0.7222	-0.176	-0.451	0.4079	0.221	0.0505	0.1565	0.1074	0.1509	0.1829
s6	-0.5955	0.263	-0.3168	-0.0113	-0.2013	-0.3625	0.573	-0.6268	0.6667	-0.2001	-0.435	0.3917	0.199	0.0454	0.1582	0.1182	0.1381	0.1958
s7	-0.6108	0.281	-0.466	0.1223	-0.1678	-0.266	0.4959	-0.7048	0.7212	-0.1982	-0.4815	0.4143	0.2233	0.0482	0.1661	0.0957	0.1531	0.1739
s8	0.2847	-0.1636	-0.0944	-0.2793	-0.4522	-0.2828	0.438	-0.66	0.131	0.1676	-0.5485	0.395	0.1969	0.1926	0.1534	0.1852	0.1637	0.1728
s9	-0.5671	0.3099	-0.4154	0.1366	-0.1992	-0.2271	0.4691	-0.7504	0.7975	-0.2755	-0.5516	0.4085	0.2188	0.0475	0.1701	0.1072	0.1427	0.1783
s10	-0.5751	0.3272	-0.3402	0.1126	-0.0813	-0.3619	0.4884	-0.3558	0.704	-0.2916	-0.2702	-0.0465	0.0566	0.0609	0.1599	0.096	0.1305	0.1864

TABLE S7: The chelpg charges used for the average in the 7-hydroxyquinoline(2H2O) complex.

	N	C	C	C	C	C	C	C	C	C	O	H	H	H	H	H	H	H
s0	-0.6247	0.3488	-0.4554	0.0829	-0.1177	-0.3536	0.5702	-0.7519	0.7846	-0.2621	-0.5524	0.4114	0.2319	0.0531	0.1786	0.1099	0.1494	0.197
s1	-0.629	0.2061	-0.3168	-0.0539	-0.149	-0.4446	0.6378	-0.6812	0.7675	-0.164	-0.4834	0.4263	0.2137	0.0522	0.1636	0.1027	0.1549	0.1969
s2	0.2414	-0.3114	-0.1332	-0.3743	-0.3044	-0.3476	0.51	-0.6607	0.2543	0.1632	-0.5576	0.4081	0.2211	0.1953	0.1633	0.1633	0.1828	0.1864
s3	-0.6977	0.4016	-0.5864	0.0665	-0.0079	-0.3149	0.4964	-0.552	0.8165	-0.3601	-0.5393	0.4187	0.2117	0.041	0.1823	0.0889	0.1373	0.1974
s4	0.2927	-0.2119	-0.2679	-0.2494	-0.2844	-0.2841	0.4555	-0.6608	0.1651	0.1017	-0.5549	0.3926	0.2372	0.1892	0.149	0.1846	0.1771	0.1688
s5	-0.7071	0.3294	-0.429	-0.0658	-0.1066	-0.3364	0.5644	-0.637	0.7543	-0.1966	-0.4612	0.4169	0.2232	0.048	0.1628	0.1039	0.1538	0.1828
s6	-0.6031	0.2654	-0.333	-0.0048	-0.2212	-0.3589	0.603	-0.6637	0.6989	-0.2123	-0.4652	0.4277	0.2022	0.0437	0.1637	0.1169	0.1432	0.1975
s7	-0.6112	0.2892	-0.4933	0.146	-0.172	-0.2613	0.5206	-0.7435	0.7469	-0.2157	-0.4958	0.4243	0.226	0.0456	0.172	0.0928	0.1562	0.1734
s8	0.2833	-0.1623	-0.1151	-0.2547	-0.4581	-0.2946	0.4748	-0.7013	0.1672	0.1434	-0.5658	0.4087	0.1995	0.1921	0.1591	0.1813	0.1668	0.1757
s9	-0.5649	0.3104	-0.4312	0.1676	-0.2046	-0.2462	0.4998	-0.7766	0.8227	-0.2993	-0.5708	0.4246	0.217	0.0467	0.1762	0.1018	0.145	0.1821
s10	-0.4967	0.3091	-0.3127	0.1164	0.0695	-0.4544	0.5029	0.0289	0.5164	-0.2947	0.0002	-0.5102	-0.0919	0.0567	0.1617	0.0857	0.1241	0.189

TABLE S8: The chelpg charges used for the average in the 7-hydroxyquinoline(2NH3) complex.

	N	C	C	C	C	C	C	C	C	C	O	H	H	H	H	H	H	H
s0	-0.6145	0.3295	-0.4396	0.076	-0.1083	-0.3517	0.5486	-0.734	0.7737	-0.2672	-0.5534	0.4123	0.2325	0.0597	0.1764	0.1117	0.1484	0.1999
s1	-0.6185	0.1911	-0.3035	-0.0592	-0.1425	-0.4368	0.6154	-0.6722	0.7591	-0.1669	-0.4872	0.4265	0.2162	0.0588	0.1614	0.1049	0.1539	0.1996
s2	0.2498	-0.3314	-0.113	-0.3844	-0.2938	-0.346	0.4905	-0.6458	0.2453	0.1592	-0.5593	0.4098	0.2214	0.2004	0.1603	0.1658	0.1818	0.1895
s3	-0.6873	0.3755	-0.5668	0.055	0.0029	-0.315	0.4777	-0.5279	0.7986	-0.3598	-0.5387	0.4194	0.2117	0.0482	0.1798	0.09	0.1364	0.2003
s4	0.298	-0.2235	-0.254	-0.2567	-0.2703	-0.2864	0.4378	-0.6447	0.1581	0.0918	-0.5567	0.3948	0.2366	0.1935	0.147	0.1871	0.1751	0.1726
s5	-0.6975	0.309	-0.4127	-0.0742	-0.0961	-0.3378	0.5457	-0.6172	0.7418	-0.2	-0.462	0.4172	0.2235	0.055	0.1607	0.1055	0.1527	0.1865
s6	-0.5902	0.2472	-0.3207	-0.004	-0.2134	-0.357	0.5821	-0.66	0.6918	-0.2176	-0.4619	0.4255	0.2052	0.0505	0.1615	0.1185	0.1423	0.2002
s7	-0.6068	0.2747	-0.4814	0.1272	-0.154	-0.2567	0.5009	-0.7202	0.735	-0.2224	-0.4972	0.4248	0.2275	0.0514	0.1699	0.0958	0.1549	0.1768
s8	0.2899	-0.1779	-0.0978	-0.2623	-0.4492	-0.2921	0.4534	-0.6899	0.1628	0.1378	-0.5683	0.4104	0.2007	0.1968	0.1565	0.1841	0.166	0.179
s9	-0.5533	0.2996	-0.419	0.1655	-0.1939	-0.2492	0.4805	-0.7563	0.8056	-0.3085	-0.5705	0.4247	0.2165	0.0528	0.1748	0.103	0.1423	0.1855
s10	-0.6691	0.3349	-0.3648	0.1128	-0.2025	-0.2683	0.4641	-0.6842	0.8603	-0.3115	-0.521	0.4008	0.2011	0.063	0.1644	0.0994	0.1392	0.1816

TABLE S9: The chelpg charges used for the average in the 7-hydroxyquinoline(MeOH) complex(H-O).

	N	C	C	C	C	C	C	C	C	C	O	H	H	H	H	H	H	H
s0	-0.627	0.3543	-0.4478	0.0771	-0.1061	-0.3617	0.5547	-0.7258	0.7629	-0.2551	-0.5378	0.3974	0.2334	0.052	0.1762	0.1085	0.1466	0.198
s1	-0.63	0.2134	-0.3103	-0.0538	-0.1316	-0.4527	0.6178	-0.6539	0.7427	-0.1613	-0.4656	0.4086	0.2155	0.0511	0.1614	0.1006	0.1505	0.1977
s2	0.2409	-0.3043	-0.1242	-0.3789	-0.2941	-0.3499	0.4824	-0.6205	0.2209	0.1728	-0.5393	0.3924	0.2194	0.1942	0.1607	0.1619	0.1792	0.1863
s3	-0.6956	0.4046	-0.5778	0.0648	0.0062	-0.3216	0.4797	-0.5337	0.798	-0.356	-0.5261	0.4038	0.2135	0.0411	0.18	0.0871	0.1335	0.1984
s4	0.2934	-0.2085	-0.2549	-0.2618	-0.2749	-0.2907	0.4367	-0.623	0.1337	0.1139	-0.5423	0.3802	0.2352	0.1879	0.1461	0.185	0.1741	0.17
s5	-0.7062	0.3301	-0.4181	-0.0719	-0.0893	-0.3512	0.5545	-0.6095	0.7263	-0.1883	-0.4499	0.404	0.2237	0.0478	0.16	0.1021	0.1505	0.1854
s6	-0.5996	0.276	-0.3305	0.0093	-0.1797	-0.3829	0.5873	-0.6334	0.6728	-0.2183	-0.4235	0.3694	0.2018	0.0424	0.1621	0.112	0.1364	0.1983
s7	-0.6161	0.2912	-0.4756	0.1347	-0.1571	-0.2833	0.5086	-0.7075	0.7248	-0.2111	-0.4784	0.4092	0.2258	0.0453	0.1697	0.0903	0.1525	0.1769
s8	0.2815	-0.1541	-0.1044	-0.2675	-0.4412	-0.2937	0.447	-0.662	0.1304	0.1581	-0.544	0.3866	0.1986	0.1901	0.1562	0.1804	0.1633	0.1747
s9	-0.5748	0.324	-0.4288	0.1457	-0.1868	-0.2373	0.4821	-0.7583	0.802	-0.2862	-0.5469	0.3994	0.2228	0.0439	0.1735	0.1029	0.1423	0.1803
s10	-0.6066	0.3499	-0.3681	0.1287	-0.1211	-0.3466	0.4989	-0.4942	0.7677	-0.3029	-0.3572	0.0977	0.116	0.0573	0.1649	0.0942	0.1333	0.1879

TABLE S10: The chelpg charges used for the average in the 7-hydroxyquinoline(2MeOH) complex.

	N	C	C	N	C	N	C	N	C	O	O	H	H	H	H
s0	-0.5448	0.5727	-0.1998	-0.3191	0.1869	-0.6327	0.6936	-0.6447	0.5732	-0.4569	-0.4986	0.3779	0.3922	0.3641	0.1361
s1	-0.4696	0.4092	-0.1784	-0.3069	0.0155	-0.5528	0.6354	-0.6424	0.3301	-0.0598	-0.4664	0.4175	0.3678	0.3618	0.1391
s2	-0.5719	0.5661	-0.059	-0.3391	0.0997	-0.4466	0.6556	-0.6279	0.378	-0.4962	-0.4065	0.3824	0.3818	0.357	0.1266
s3	-0.5239	0.5092	-0.0678	-0.313	0.176	-0.5708	0.644	-0.5861	0.4409	-0.4689	-0.4866	0.3765	0.3942	0.3651	0.1113
s4	-0.5036	0.4783	-0.0922	-0.3969	0.1818	-0.6975	0.4549	-0.7347	0.5133	-0.4196	-0.1674	0.435	0.4421	0.3768	0.1299
s5	0.3062	0.122	-0.164	-0.1937	-0.4453	-0.4843	0.614	-0.5457	0.4288	-0.4832	-0.457	0.353	0.3662	0.3496	0.2333
s6	-0.5073	0.4817	-0.3342	-0.2633	0.0075	-0.6722	0.698	-0.3158	0.4555	-0.3699	-0.3808	0.3422	0.3961	0.3327	0.1299
s7	-0.5187	0.4236	-0.2308	-0.2947	-0.0015	-0.6122	0.7101	-0.6358	0.3451	-0.5285	0.0289	0.4221	0.4145	0.3453	0.1324
s8	-0.5223	0.5063	-0.0293	-0.3374	0.2434	-0.4708	0.5132	-0.6564	0.4616	-0.4423	-0.5436	0.3951	0.3926	0.3686	0.1215
s9	-0.582	0.5095	0.031	-0.3606	0.1605	-0.4557	0.5938	-0.6226	0.4099	-0.4748	-0.4754	0.3944	0.3776	0.3656	0.1288
s10	-0.4848	0.3676	-0.0247	0.3963	0.2665	-0.3271	0.6541	-0.6752	0.6429	-0.4106	-0.4301	0.4001	0.339	-0.708	-0.0059

TABLE S11: The chelpg charges used for the average in the xanthine(MeCN) complex.

	N	C	C	N	C	N	C	N	C	O	O	H	H	H	H
s0	0.561	-0.2015	0.5796	-0.6329	0.6857	-0.628	-0.3214	0.1845	-0.545	-0.4955	-0.4607	0.3756	0.3917	0.368	0.139
s1	0.3201	-0.1803	0.4196	-0.5525	0.623	-0.6248	-0.3216	0.0207	-0.4741	-0.4665	-0.0561	0.4146	0.3673	0.3706	0.14
s2	0.3683	-0.0585	0.57	-0.4451	0.6448	-0.6121	-0.3403	0.0982	-0.5719	-0.4058	-0.4967	0.3798	0.3807	0.3587	0.1296
s3	0.4341	-0.0694	0.5174	-0.5701	0.6365	-0.5794	-0.315	0.1748	-0.5242	-0.4858	-0.4695	0.3749	0.3936	0.3678	0.1142
s4	0.5055	-0.1	0.487	-0.7034	0.4583	-0.7233	-0.395	0.1737	-0.4973	-0.1767	-0.4191	0.4342	0.4423	0.3802	0.1337
s5	0.4179	-0.1657	0.1293	-0.4831	0.6051	-0.531	-0.1917	-0.4434	0.2976	-0.4529	-0.4842	0.3514	0.3657	0.3507	0.2345
s6	0.4523	-0.3363	0.4899	-0.6719	0.6914	-0.3122	-0.2684	0.0016	-0.5055	-0.3802	-0.3676	0.3414	0.3954	0.3369	0.1331
s7	0.3358	-0.2323	0.4323	-0.614	0.7054	-0.6231	-0.3018	-0.0006	-0.5215	0.0327	-0.5335	0.4203	0.4153	0.3505	0.1345
s8	0.4536	-0.0313	0.5177	-0.4751	0.4995	-0.6454	-0.3385	0.2495	-0.5218	-0.5481	-0.4431	0.3949	0.3929	0.3703	0.125
s9	0.3994	0.0217	0.5088	-0.4544	0.5913	-0.5986	-0.3527	0.1472	-0.578	-0.4701	-0.4762	0.3899	0.3761	0.364	0.1316
s10	0.6362	-0.0104	0.376	-0.3358	0.6497	-0.6688	0.3989	0.2298	-0.4835	-0.4292	-0.4129	0.4014	0.344	-0.7208	0.0254

TABLE S12: The chelpg charges used for the average in the xanthine(MeOH) complex.

	C	N	C	C	N	C	N	C	N	N	H	H	H	H	H
s0	0.2296	-0.5244	0.1221	0.4607	-0.4587	0.1077	-0.587	0.7664	-0.6494	-0.7395	0.1352	0.3245	0.3315	0.1167	0.3646
s1	0.2565	-0.5264	0.2091	0.5388	-0.5489	-0.1245	-0.5482	0.7146	-0.7265	-0.487	0.122	0.303	0.3182	0.1134	0.3859
s2	0.0428	-0.4445	0.359	0.1743	-0.3724	-0.5561	0.0225	0.3304	-0.2675	-0.685	0.2385	0.3228	0.337	0.1388	0.3594
s3	0.1454	-0.4388	0.1539	0.4257	-0.3283	-0.0379	-0.5644	0.7094	-0.6201	-0.6814	0.1291	0.312	0.3205	0.1106	0.3642
s4	-0.1832	0.0154	-0.0312	0.4149	-0.3479	-0.209	-0.3234	0.6235	-0.5704	-0.7532	0.1581	0.3228	0.3404	0.1865	0.3567
s5	0.1417	-0.4318	0.2749	0.0614	-0.4012	-0.2512	-0.0871	0.2364	-0.1494	-0.7461	0.2228	0.3233	0.3288	0.1274	0.3503
s6	0.1945	-0.4724	0.2002	0.4327	-0.4177	-0.0236	-0.5814	0.6678	-0.6559	-0.5465	0.1295	0.2908	0.3085	0.108	0.3655
s7	0.1113	-0.6315	0.2134	0.5088	-0.5187	0.1292	-0.5669	0.735	-0.6685	-0.5176	0.1274	0.3002	0.2972	0.1119	0.3688
s8	-0.077	-0.2576	0.1223	0.2679	-0.3806	-0.1446	-0.3997	0.5714	-0.3466	-0.6843	0.1553	0.33	0.3367	0.1539	0.353
s9	0.1659	-0.4072	0.0851	0.5379	-0.491	-0.1291	-0.5518	0.6556	-0.6547	-0.4336	0.1376	0.2918	0.3041	0.1193	0.3701
s10	0.1697	-0.3008	-0.0462	0.444	0.0335	0.1975	-0.5271	0.704	-0.5113	-0.5892	0.1122	0.3187	0.313	0.0579	-0.3758

TABLE S13: The chelpg charges used for the average in the aminopurine(H2O) complex.

	C	C	C	H	O	N	C	H	N	H	H	O
s0	0.0736	-0.4988	0.6844	0.2131	-0.4922	-0.5349	0.634	0.3426	-0.4016	0.3298	0.1525	-0.5027
s1	-0.203	-0.5837	0.4817	0.2626	-0.0451	-0.4713	0.5623	0.3565	-0.3395	0.3097	0.157	-0.4871
s2	-0.1386	-0.3511	0.4506	0.2039	-0.4548	-0.442	0.5492	0.3227	-0.1703	0.3289	0.1315	-0.43
s3	-0.0479	-0.5765	0.6369	0.2046	-0.405	-0.6058	0.5132	0.3803	-0.4706	0.379	0.1517	-0.1598
s4	-0.217	-0.6885	0.5665	0.244	-0.3766	-0.1211	0.6469	0.283	-0.4764	0.3442	0.1509	-0.3559
s5	-0.1376	-0.6146	0.5617	0.2294	-0.2615	-0.5092	0.558	0.3762	-0.4044	0.3454	0.1628	-0.3061
s6	-0.0644	-0.4881	0.5664	0.2093	-0.4057	-0.5868	0.4937	0.4068	-0.4218	0.3443	0.1643	-0.218
s7	0.1845	-0.0593	0.521	0.1105	-0.3809	-0.6258	0.596	0.3722	0.1522	-0.2958	-0.1786	-0.396
s8	0.0615	-0.1439	0.5101	0.1606	-0.447	-0.6007	0.4437	0.381	-0.1542	0.2289	0.1037	-0.5435
s9	0.1247	-0.4601	0.6369	0.1542	-0.1617	-0.4303	0.5823	0.236	-0.2464	-0.0042	-0.0395	-0.3918
s10	0.0666	-0.5326	0.6449	0.1825	-0.3146	-0.3711	0.5389	0.3493	-0.3295	0.1216	0.0785	-0.4344

TABLE S14: The chelpg charges used for the average in the uracil(5H2O) complex.

	N	C	C	C	C	C	C	C	C	C	O	H	H	H	H	H	H	H
s0	-0.7388	0.7867	-0.2669	-0.1139	-0.3472	0.5516	-0.6279	0.34	-0.4407	0.0799	-0.5604	0.4151	0.2329	0.0572	0.1745	0.1093	0.1484	0.2001
s1	-0.6763	0.7724	-0.1709	-0.1465	-0.4389	0.62	-0.629	0.1983	-0.301	-0.0536	-0.4923	0.4296	0.216	0.0568	0.159	0.1023	0.1537	0.2004
s2	-0.6451	0.2434	0.1668	-0.3003	-0.3432	0.4919	0.2516	-0.3331	-0.1059	-0.3878	-0.5662	0.4123	0.221	0.201	0.1578	0.1648	0.1814	0.1897
s3	-0.5406	0.8146	-0.3606	-0.0079	-0.3052	0.4785	-0.6975	0.3872	-0.5678	0.0643	-0.548	0.4229	0.2124	0.0458	0.178	0.0877	0.1366	0.1998
s4	-0.6466	0.16	0.0981	-0.2738	-0.2832	0.4413	0.2949	-0.221	-0.2514	-0.2613	-0.563	0.3966	0.2376	0.1936	0.1448	0.186	0.1744	0.1729
s5	-0.6252	0.7561	-0.2029	-0.0991	-0.3377	0.5512	-0.7112	0.3204	-0.4151	-0.0677	-0.4659	0.4196	0.2245	0.0525	0.1581	0.103	0.1523	0.1869
s6	-0.6912	0.7092	-0.222	-0.2257	-0.3582	0.5811	-0.5882	0.2565	-0.3341	0.037	-0.4664	0.4324	0.2063	0.0489	0.1605	0.113	0.1415	0.1995
s7	-0.7011	0.7455	-0.2213	-0.1532	-0.2591	0.5113	-0.6309	0.2828	-0.4665	0.0987	-0.5053	0.4271	0.226	0.0491	0.1668	0.0956	0.1552	0.1794
s8	-0.6899	0.162	0.1472	-0.4574	-0.2856	0.4564	0.2902	-0.1799	-0.0921	-0.2695	-0.5761	0.414	0.2008	0.1972	0.1543	0.1831	0.1659	0.1794
s9	-0.7648	0.8213	-0.3025	-0.2025	-0.2384	0.4818	-0.5668	0.3055	-0.42	0.1643	-0.5788	0.4295	0.2183	0.0504	0.1726	0.1015	0.1437	0.1851
s10	-0.7047	0.8797	-0.3125	-0.2184	-0.2538	0.4658	-0.687	0.3519	-0.375	0.1193	-0.5417	0.4277	0.2072	0.0599	0.1634	0.0969	0.1398	0.1813

TABLE S15: The chelpg charges used for the average in the 7-hydroxyquinoline(MeOH) complex(N-H).

Appendix F

Supporting document for [Fu M, D. Tabakaev, R. T. Thew, and T. A. Wesolowski, *J. Phys. Chem. Lett.* 14, 2613-2619 (2023)]

Supplemental material for: Fine-tuning of entangled two-photon absorption by controlling the one-photon absorption properties of the chromophore

M. Fu* and T. A. Wesolowski†
Department of Physical Chemistry, University of Geneva, Geneva, Switzerland

D. Tabakaev and R. T. Thew
Department of Applied Physics, University of Geneva, Geneva, Switzerland

GEOMETRY

In Fig. 1, structure of (1),(3),(4),(7) were optimised at the second-order Møller-Plesset perturbation theory /cc-pVTZ level of theory, and the rest of structures were taken from our benchmarking paper[1].

UNIT CONVERSION

The macroscopic ETPA cross-section in the cgs unit of cm^2 using Lorentzian line shape functions for the resonant two photons can also be calculated as follows[2, 3]:

$$\sigma_e = \frac{4\pi^2 \alpha a_0^5 \omega^2 \langle \sigma \rangle}{c \Gamma A_e T_e} \tag{1}$$

where α is the fine constant, a_0 the Bohr radius, c the speed of light, Γ the half width, and A_e is the entanglement area. Averaged ETPA cross-sections $\langle \sigma \rangle$ and the photon frequency ω are in atomic units. A_e is typically $10^{-6} cm^2$[2]

MICROSCOPIC AVERAGED ETPA CROSS SECTION FOR ALL THE COMPLEXES

The intermediate state will be considered as dominant if by considering only this one intermediate state the ETPA cross section constitutes at least 5% of the final sum-over-state cross section. The natural transition orbitals are used to visualize the transition orbitals of different excited states in order to diagnose the excitation character or the symmetry if it presents. The results from the quantum calculations including excitation energies and transition properties for the selected number of excited states, were processed using our Python script to obtain the final averaged microscopic ETPA cross-section. Fig. 2 shows the microscopic ETPA cross section for the different complexes varied by the coherence time and the electronic structure of the corresponding dominant intermediate states.

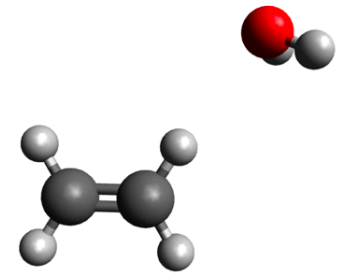

(1) ethylene-H_2O

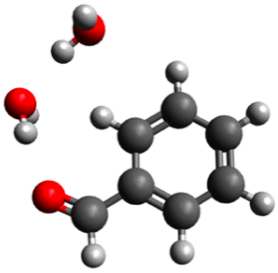

(2) benzaldehyde-$2H_2O$

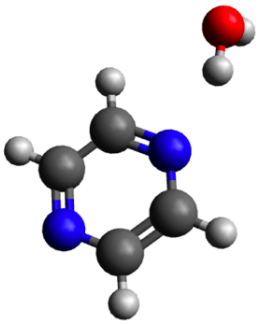

(3) pyrimidine (D_{2h})-H_2O

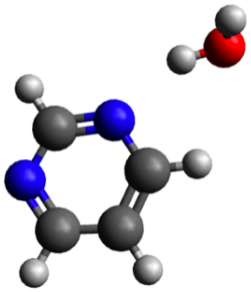

(4) pyrimidine (C_{2v})-H_2O

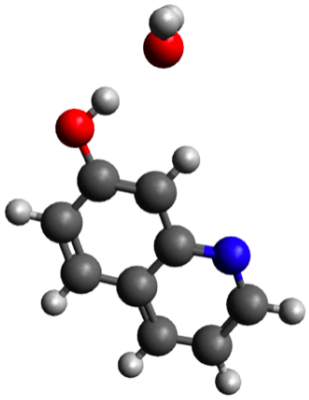

(5) 7-hydroxyquinoline-H_2O

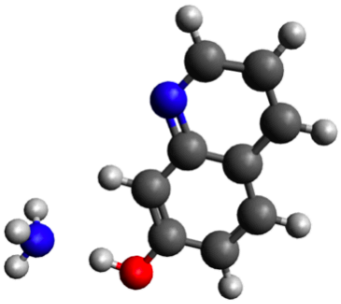

(6) 7-hydroxyquinoline-NH_3

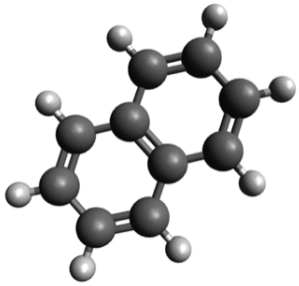

(7) naphthalene

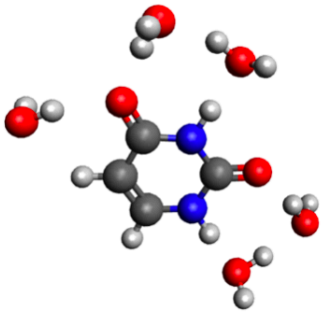

(8) dimethylaminopyridinium-$4H_2O$

FIG. 1: The optimised geometry for all structures.

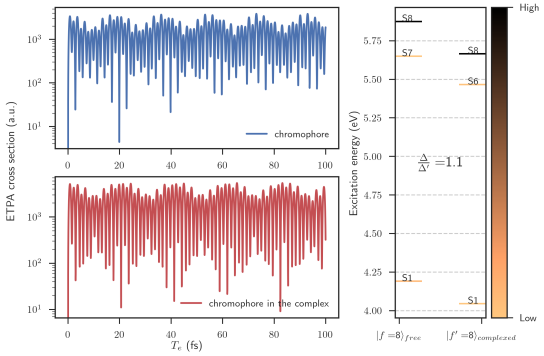

(a) 7-hydroxyquinoline -NH_3

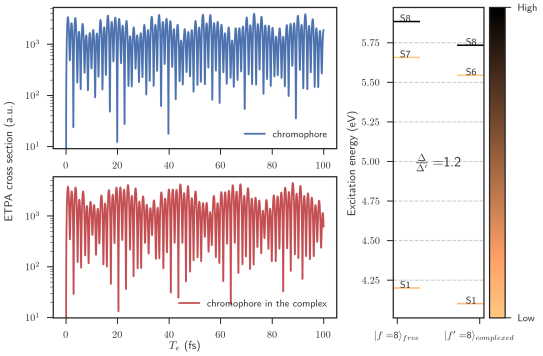

(b) 7-hydroxyquinoline -H_2O

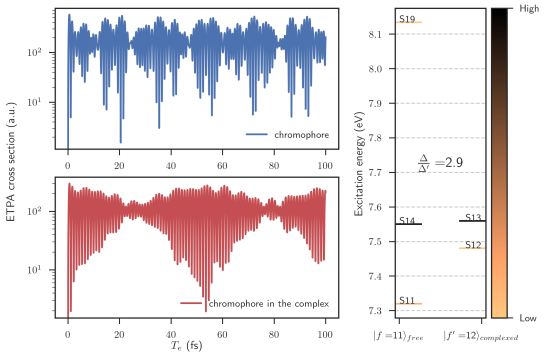

(c) pyrimidine(C_{2v})-H_2O

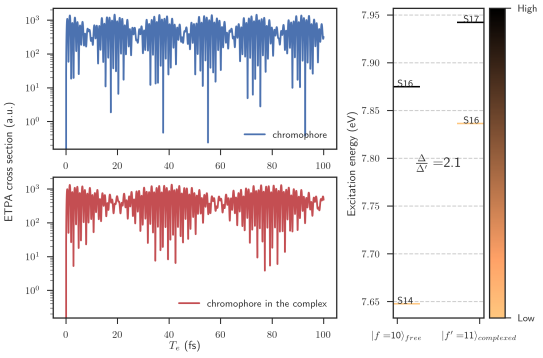

(d) pyrimidine(D_{2h}) -H_2O

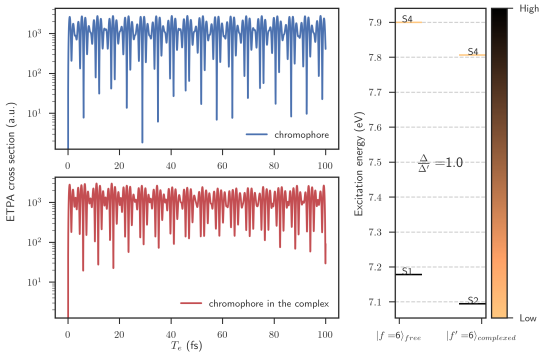

(e) ethylene-H_2O

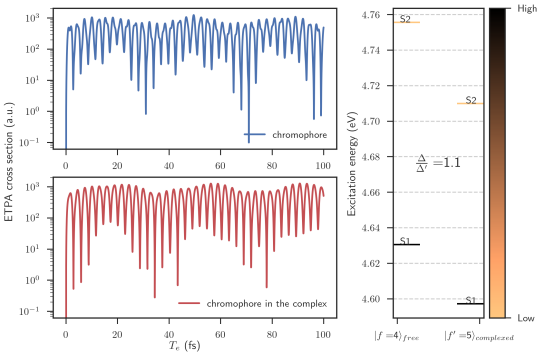

(f) dimethylaminopyridinium cation-4H_2O

FIG. 2: The microscopic ETPA cross section for the different complexes $a-f$ studied in this work. For each complex, on the right is the electronic structure of the corresponding dominant intermediate states. The horizontal axis labels the target state $|f\rangle$ for the free chromophore and the chromophore in the complex. Color bar on the right indicates the weight of each intermediate states contribution.

* Mungxue.Fu@unige.ch

† Tomasz.Wesolowski@unige.ch

[1] Alexander Zech, Niccolò Ricardi, Stefan Prager, Andreas Dreuw, and Tomasz A. Wesolowski. Benchmark of Excitation Energy Shifts from Frozen-Density Embedding Theory: Introduction of a Density-Overlap-Based Applicability Threshold. *J. Chem. Theory Comput.*, 14(8):4028–4040, August 2018.

[2] Hong-Bing Fei, Bradley M. Jost, Sandu Popescu, Bahaa E. A. Saleh, and Malvin C. Teich. Entanglement-Induced Two-Photon Transparency. *Phys. Rev. Lett.*, 78(9):1679–1682, March 1997.

[3] Maarten T. P. Beerepoot, Daniel H. Friese, Nanna H. List, Jacob Kongsted, and Kenneth Ruud. Benchmarking two-photon absorption cross sections: performance of CC2 and CAM-B3LYP. *Phys. Chem. Chem. Phys.*, 17(29):19306–19314, 2015.

Bibliography for the thesis

[1] Erwin Schrödinger. An undulatory theory of the mechanics of atoms and molecules. *Physical review*, 28(6):1049, 1926.

[2] Max Born and Robert Oppenheimer. Zur quantentheorie der molekeln. *Annalen der Physik*, 389(20):457–484, 1927.

[3] John C Slater. The theory of complex spectra. *Physical Review*, 34(10):1293, 1929.

[4] Douglas R Hartree. The wave mechanics of an atom with a non-coulomb central field. part i. theory and methods. In *Mathematical Proceedings of the Cambridge Philosophical Society*, volume 24, pages 89–110. Cambridge university press, 1928.

[5] Vladimir Fock. Näherungsmethode zur lösung des quantenmechanischen mehrkörperproblems. *Zeitschrift für Physik*, 61:126–148, 1930.

[6] Clemens Carel Johannes Roothaan. New developments in molecular orbital theory. *Reviews of modern physics*, 23(2):69, 1951.

[7] Attila Szabo and Neil S Ostlund. *Modern quantum chemistry: introduction to advanced electronic structure theory*. New York:McGraw-Hill, 1989.

[8] R. P. Feynman. Space-Time Approach to Quantum Electrodynamics. *Physical Review*, 76(6):769–789, September 1949.

[9] Chr Møller and Milton S Plesset. Note on an approximation treatment for many-electron systems. *Physical review*, 46(7):618, 1934.

[10] Pierre Hohenberg and Walter Kohn. Inhomogeneous electron gas. *Physical review*, 136(3B):B864, 1964.

[11] Tomasz A Wesolowski and Yan Alexander Wang. *Recent progress in orbital-free density functional theory*. World Scientific, 2013.

[12] R. G. Parr and W. Yang. *Density-Functional Theory of Atoms and Molecules*. Oxford University Press, 1989.

[13] T L Gilbert. Hohenberg-Kohn theorem for nonlocal external potentials. *Physical Review B*, 12(6):2111–2120, sep 1975.

[14] Mel Levy. Electron densities in search of Hamiltonians. *Physical Review A*, 26(3):1200–1208, September 1982.

[15] W. Kohn and L. J. Sham. Self-Consistent Equations Including Exchange and Correlation Effects. *Physical Review*, 140(4A):A1133–A1138, November 1965.

[16] Axel D. Becke. A new mixing of Hartree–Fock and local density-functional theories. *The Journal of Chemical Physics*, 98(2):1372–1377, January 1993.

[17] Christopher J Cramer. *Essentials of computational chemistry: theories and models*. John Wiley & Sons, 2013.

[18] Arieh Warshel and Michael Levitt. Theoretical studies of enzymic reactions: dielectric, electrostatic and steric stabilization of the carbonium ion in the reaction of lysozyme. *Journal of molecular biology*, 103(2):227–249, 1976.

[19] Christoph R. Jacob and Johannes Neugebauer. Subsystem density-functional theory. *WIREs Computational Molecular Science*, 4(4):325–362, 2014.

[20] Ronit Sarangi, Kaushik D Nanda, and Anna I Krylov. Charge-transfer-to-solvent states provide a sensitive spectroscopic probe of the local solvent structure around anions. *Molecular Physics*, 121(7-8):e2148582, 2023.

[21] Lars Onsager. Electric moments of molecules in liquids. *Journal of the American Chemical Society*, 58(8):1486–1493, 1936.

[22] John G Kirkwood. Theory of solutions of molecules containing widely separated charges with special application to zwitterions. *The Journal of Chemical Physics*, 2(7):351–361, 1934.

[23] E Cances, Benedetta Mennucci, and Jacopo Tomasi. A new integral equation formalism for the polarizable continuum model: Theoretical background and applications to isotropic and anisotropic dielectrics. *The Journal of chemical physics*, 107(8):3032–3041, 1997.

[24] Jacopo Tomasi, Benedetta Mennucci, and Roberto Cammi. Quantum Mechanical Continuum Solvation Models. *Chemical Reviews*, 105(8):2999–3094, August 2005.

[25] Jacopo Tomasi and Maurizio Persico. Molecular Interactions in Solution: An Overview of Methods Based on Continuous Distributions of the Solvent. *Chemical Reviews*, 94(7):2027–2094, November 1994.

[26] Tomasz Adam Wesolowski and Arieh Warshel. Frozen density functional approach for ab initio calculations of solvated molecules. *The Journal of Physical Chemistry*, 97(30):8050–8053, 1993.

[27] Tomasz A Wesołowski. Embedding a multideterminantal wave function in an orbital-free environment. *Physical Review A*, 77(1):012504, 2008.

[28] Katarzyna Pernal and Tomasz A Wesolowski. Orbital-free effective embedding potential: Density-matrix functional theory case. *International Journal of Quantum Chemistry*, 109(11):2520–2525, 2009.

[29] Tomasz A Wesolowski. On the correlation potential in frozen-density embedding theory. *Journal of Chemical Theory and Computation*, 16(11):6880–6885, 2020.

[30] Niccolò Ricardi, Michelle Ernst, Piero Macchi, and Tomasz Adam Wesolowski. Embedding-theory-based simulations using experimental electron densities for the environment. *Acta Crystallographica Section A: Foundations and Advances*, 76(5):571–579, 2020.

[31] Francesco Aquilante and Tomasz A. Wesołowski. Self-consistency in frozen-density embedding theory based calculations. *The Journal of Chemical Physics*, 135(8):084120, August 2011.

[32] Reena Sen, Cristina E González-Espinoza, Alexander Zech, Andreas Dreuw, and Tomasz A Wesolowski. Benchmark of the extension of frozen-density embedding theory to nonvariational correlated methods: The embedded-mp2 case. *Journal of Chemical Theory and Computation*, 17(7):4049–4062, 2021.

[33] Alexander Zech, Francesco Aquilante, and Tomasz A. Wesolowski. Homogeneity properties of the embedding potential in frozen-density embedding theory. *Molecular Physics*, 114(7-8):1199–1206, April 2016.

[34] Llewellyn Hilleth Thomas. The calculation of atomic fields. *Mathematical Proceedings of the Cambridge Philosophical Society*, 23(05):542, jan 1927.

[35] Enrico Fermi. Eine statistische Methode zur Bestimmung einiger Eigenschaften des Atoms und ihre Anwendung auf die Theorie des periodischen Systems der Elemente. *Zeitschrift für Physik*, 48(1-2):73–79, jan 1928.

[36] CF v Weizsäcker. Zur theorie der kernmassen. *Zeitschrift für Physik*, 96(7-8):431–458, 1935.

[37] Juan Maria Garcia Lastra, Jakub W Kaminski, and Tomasz A Wesolowski. Orbital-free effective embedding potential at nuclear cusps. *The Journal of Chemical Physics*, 129(7):074107, aug 2008.

[38] Elias Polak, Cristina E. González-Espinoza, Martin J. Gander, and Tomasz A. Wesolowski. A non-decomposable approximation on the complete density function space for the non-additive kinetic potential. *The Journal of Chemical Physics*, 156(4):044103, January 2022.

[39] James C Phillips and Leonard Kleinman. New method for calculating wave functions in crystals and molecules. *Physical Review*, 116(2):287, 1959.

[40] Tomasz A Wesolowski. Embedding potentials for excited states of embedded species. *The Journal of chemical physics*, 140(18), 2014.

[41] Alexander Zech, Francesco Aquilante, and Tomasz A. Wesolowski. Orthogonality of embedded wave functions for different states in frozen-density embedding theory. *The Journal of Chemical Physics*, 143(16):164106, oct 2015.

[42] Tomasz Adam Wesolowski and Jacques Weber. Kohn-Sham equations with constrained electron density: an iterative evaluation of the ground-state electron density of interacting molecules. *Chemical Physics Letters*, 248(1-2):71–76, jan 1996.

[43] Tomasz Adam Wesolowski, Henry Chermette, and Jacques Weber. Accuracy of approximate kinetic energy functionals in the model of Kohn-Sham equations with constrained electron density: The FH-NCH complex as a test case. *The Journal of Chemical Physics*, 105(20):9182–9190, nov 1996.

[44] Niccolò Ricardi, Alexander Zech, Yann Gimbal-Zofka, and Tomasz A. Wesolowski. Explicit *vs.* implicit electronic polarisation of environment of an embedded chromophore in frozen-density embedding theory. *Physical Chemistry Chemical Physics*, 20(41):26053–26062, 2018.

[45] John P. Perdew and Mel Levy. Extrema of the density functional for the energy: Excited states from the ground-state theory. *Physical Review B*, 31(10):6264–6272, may 1985.

[46] Yuriy G Khait and Mark R Hoffmann. Embedding theory for excited states. *The Journal of Chemical Physics*, 133(4):044107, jul 2010.

[47] Niccolò Ricardi, Cristina E. González-Espinoza, and Tomasz Adam Wesołowski. N-representability of the target density in Frozen-Density Embedding Theory based methods: Numerical significance and its relation to electronic polarization. *The Journal of Chemical Physics*, 157(6):064108, August 2022.

[48] Maarten T. P. Beerepoot, Arnfinn Hykkerud Steindal, Jacob Kongsted, Bjørn Olav Brandsdal, Luca Frediani, Kenneth Ruud, and Jógvan Magnus Haugaard Olsen. A polarizable embedding DFT study of one-photon absorption in fluorescent proteins. *Phys. Chem. Chem. Phys.*, 15(13):4735, 2013.

[49] I. Harczuk, N. Arul Murugan, O. Vahtras, and H. Ågren. Studies of pH-Sensitive Optical Properties of the deGFP1 Green Fluorescent Protein Using a Unique Polarizable Force Field. *J. Chem. Theory Comput.*, 10(8):3492–3502, August 2014.

[50] Riccardo Guareschi, Omar Valsson, Carles Curutchet, Benedetta Mennucci, and Claudia Filippi. Electrostatic versus Resonance Interactions in Photoreceptor Proteins: The Case of Rhodopsin. *J. Phys. Chem. Lett.*, 7(22):4547–4553, November 2016.

[51] Xuelan Wen, Daniel S. Graham, Dhabih V. Chulhai, and Jason D. Goodpaster. Absolutely Localized Projection-Based Embedding for Excited States. *J. Chem. Theory Comput.*, 16(1):385–398, January 2020.

[52] Linus Scholz and Johannes Neugebauer. Protein Response Effects on Cofactor Excitation Energies from First Principles: Augmenting Subsystem Time-Dependent Density-Functional Theory with Many-Body Expansion Techniques. *J. Chem. Theory Comput.*, 17(10):6105–6121, October 2021.

[53] Claudia Filippi, Francesco Buda, Leonardo Guidoni, and Adalgisa Sinicropi. Bathochromic Shift in Green Fluorescent Protein: A Puzzle for QM/MM Approaches. *J. Chem. Theory Comput.*, 8(1):112–124, January 2012.

[54] Mark S. Gordon, Quentin A. Smith, Peng Xu, and Lyudmila V. Slipchenko. Accurate First Principles Model Potentials for Intermolecular Interactions. *Annual Review of Physical Chemistry*, 64(1):553–578, 2013.

[55] Lyudmila V. Slipchenko. Solvation of the Excited States of Chromophores in Polarizable Environment: Orbital Relaxation versus Polarization †. *J. Phys. Chem. A*, 114(33):8824–8830, August 2010.

[56] Marco Caricato, Filippo Lipparini, Giovanni Scalmani, Chiara Cappelli, and Vincenzo Barone. Vertical Electronic Excitations in Solution with the EOM-CCSD Method Combined with a Polarizable Explicit/Implicit Solvent Model. *J. Chem. Theory Comput.*, 9(7):3035–3042, July 2013.

[57] Giovanni Macetti and Alessandro Genoni. Quantum Mechanics/Extremely Localized Molecular Orbital Embedding Strategy for Excited States: Coupling to Time-Dependent Density Functional Theory and Equation-of-Motion Coupled Cluster. *J. Chem. Theory Comput.*, 16(12):7490–7506, December 2020.

[58] Csaba Daday, Carolin König, Omar Valsson, Johannes Neugebauer, and Claudia Filippi. State-Specific Embedding Potentials for Excitation-Energy Calculations. *J. Chem. Theory Comput.*, 9(5):2355–2367, May 2013.

[59] Simon J. Bennie, Basile F. E. Curchod, Frederick R. Manby, and David R. Glowacki. Pushing the Limits of EOM-CCSD with Projector-Based Embedding for Excitation Energies. *J. Phys. Chem. Lett.*, 8(22):5559–5565, November 2017.

[60] Christoph R. Jacob and Johannes Neugebauer. Subsystem density-functional theory. *WIREs Computational Molecular Science*, 4(4):325–362, 2014.

[61] Georgios Fradelos and Tomasz A. Wesołowski. Importance of the Intermolecular Pauli Repulsion in Embedding Calculations for Molecular Properties: The Case of Excitation Energies for a Chromophore in Hydrogen-Bonded Environments. *J. Phys. Chem. A*, 115(35):10018–10026, September 2011.

[62] Dhabih V. Chulhai and Lasse Jensen. External orthogonality in subsystem time-dependent density functional theory. *Phys. Chem. Chem. Phys.*, 18(31):21032–21039, 2016.

[63] Jochen Schirmer. Beyond the random-phase approximation: A new approximation scheme for the polarization propagator. *Physical Review A*, 26(5):2395–2416, November 1982.

[64] F. J. Dyson. The Radiation Theories of Tomonaga, Schwinger, and Feynman. *Physical Review*, 75(3):486–502, February 1949.

[65] Alexander L. Fetter and John Dirk Walecka. *Quantum theory of many-particle systems*. International series in pure and applied physics. MacGraw-Hill, San Francisco, 1971.

[66] Aleksej A Abrikosov, Lev P Gorkov, IE Dzyaloshinski, Richard A Silverman, and George H Weiss. *Methods of quantum field theory in statistical physics*. American Institute of Physics, 1964.

[67] Arkadii Beinusovich Migdal and S Chomet. *Theory of finite Fermi systems and applications to atomic nuclei*. Interscience monographs and texts in physics and astronomy vol. 19. J. Wiley, New York [etc, 1967.

[68] J. Schirmer and A. B. Trofimov. Intermediate state representation approach to physical properties of electronically excited molecules. *The Journal of Chemical Physics*, 120(24):11449–11464, June 2004.

[69] Jane K Cullum and Ralph A Willoughby. *Lanczos algorithms for large symmetric eigenvalue computations: Vol. I: Theory*. SIAM, 2002.

[70] H.-D. Meyer and S. Pal. A band-Lanczos method for computing matrix elements of a resolvent. *The Journal of Chemical Physics*, 91(10):6195–6204, November 1989.

[71] S. Knippenberg, D. R. Rehn, M. Wormit, J. H. Starcke, I. L. Rusakova, A. B. Trofimov, and A. Dreuw. Calculations of nonlinear response properties using the intermediate state representation and the algebraic-diagrammatic construction polarization propagator approach: Two-photon absorption spectra. *The Journal of Chemical Physics*, 136(6):064107, February 2012.

[72] Jiří Čížek. On the Correlation Problem in Atomic and Molecular Systems. Calculation of Wavefunction Components in Ursell-Type Expansion Using Quantum-Field Theoretical Methods. *The Journal of Chemical Physics*, 45(11):4256–4266, December 1966.

[73] Henrik Koch and Poul Jørgensen. Coupled cluster response functions. *The Journal of Chemical Physics*, 93(5):3333–3344, September 1990.

[74] John F. Stanton and Rodney J. Bartlett. The equation of motion coupled-cluster method. A systematic biorthogonal approach to molecular excitation energies, transition probabilities, and excited state properties. *The Journal of Chemical Physics*, 98(9):7029–7039, May 1993.

[75] Rodney J. Bartlett and Monika Musiał. Coupled-cluster theory in quantum chemistry. *Reviews of Modern Physics*, 79(1):291–352, February 2007.

[76] Anna I Krylov. Equation-of-motion coupled-cluster methods for open-shell and electronically excited species: The hitchhiker's guide to fock space. *Annu. Rev. Phys. Chem.*, 59:433–462, 2008.

[77] Paul Ehrenfest. Bemerkung über die angenäherte gültigkeit der klassischen mechanik innerhalb der quantenmechanik. *Zeitschrift für physik*, 45(7-8):455–457, 1927.

[78] Patrick Norman, Kenneth Ruud, and Trond Saue. *Principles and practices of molecular properties: Theory, modeling, and simulations*. John Wiley & Sons, 2018.

[79] Ryogo Kubo. Statistical-Mechanical Theory of Irreversible Processes. I. General Theory and Simple Applications to Magnetic and Conduction Problems. *Journal of the Physical Society of Japan*, 12(6):570–586, June 1957.

[80] Jeppe Olsen and Poul Jørgensen. Linear and nonlinear response functions for an exact state and for an MCSCF state. *The Journal of Chemical Physics*, 82(7):3235–3264, April 1985.

[81] Kaushik D Nanda and Anna I Krylov. Two-photon absorption cross sections within equation-of-motion coupled-cluster formalism using resolution-of-the-identity and cholesky decomposition representations: Theory, implementation, and benchmarks. *The Journal of chemical physics*, 142(6), 2015.

[82] WARNER L Peticolas. Multiphoton spectroscopy. *Annual Review of Physical Chemistry*, 18(1):233–260, 1967.

[83] P. R. Monson and W. M. McClain. Polarization Dependence of the Two-Photon Absorption of Tumbling Molecules with Application to Liquid 1-Chloronaphthalene and Benzene. *The Journal of Chemical Physics*, 53(1):29–37, July 1970.

[84] Ronit Sarangi, Kaushik Nanda, and Anna I Krylov. Two-and one-photon absorption spectra of aqueous thiocyanate anion highlight the role of symmetry in condensed phase. 2023.

[85] Maria Göppert-Mayer. Über elementarakte mit zwei quantensprüngen. *Annalen der Physik*, 401(3):273–294, 1931.

[86] Mingxue Fu and Tomasz A. Wesolowski. The Challenge of Accurate Computation of Two-Photon Absorption Properties of Organic Chromophores in the Condensed Phase. *Journal of Chemical Theory and Computation*, 17(6):3652–3665, June 2021.

[87] Mingxue Fu and Tomasz A. Wesolowski. Excitation Energies of Embedded Chromophores from Frozen-Density Embedding Theory Using State-Specific Electron Densities of the Environment. *The Journal of Physical Chemistry A*, 127(2):535–545, January 2023.

[88] M. Fu, D. Tabakaev, R. T. Thew, and T. A. Wesolowski. Fine-Tuning of Entangled Two-Photon Absorption by Controlling the One-Photon Absorption Properties of the Chromophore. *The Journal of Physical Chemistry Letters*, 14(10):2613–2619, March 2023.

[89] Jan-Michael Mewes, Zhi-Qiang You, Michael Wormit, Thomas Kriesche, John M Herbert, and Andreas Dreuw. Experimental benchmark data and systematic evaluation of two a posteriori, polarizable-continuum corrections for vertical excitation energies in solution. *The Journal of Physical Chemistry A*, 119(21):5446–5464, 2015.

[90] Elias Polak, Cristina E González-Espinoza, Martin J Gander, and Tomasz A Wesolowski. A non-decomposable approximation on the complete density function space for the non-additive kinetic potential. *The Journal of Chemical Physics*, 156(4), 2022.

[91] AS Kompaneets and ES Pavlovskii. The self-consistent field equations in an atom. *Sov. Phys. JETP*, 4:328–336, 1957.

[92] A. Lembarki and H. Chermette. Obtaining a gradient-corrected kinetic-energy functional from the Perdew-Wang exchange functional. *Physical Review A*, 50(6):5328–5331, December 1994.

[93] John P Perdew, Kieron Burke, and Matthias Ernzerhof. Generalized gradient approximation made simple. *Physical review letters*, 77(18):3865, 1996.

[94] Michael J Frisch, John A Pople, and J Stephen Binkley. Self-consistent molecular orbital methods 25. supplementary functions for gaussian basis sets. *The Journal of chemical physics*, 80(7):3265–3269, 1984.

[95] Stefanie A Mewes and Andreas Dreuw. Density-based descriptors and exciton analyses for visualizing and understanding the electronic structure of excited states. *Physical Chemistry Chemical Physics*, 21(6):2843–2856, 2019.

Acknowledgements

I would like to thank Professor T. A. Wesołowski for the full support during my PhD studies. His enthusiasm and positive energy on the daily scientific research always impresses me. He would be happy, and ready to discuss science on any topics. For PhD in a computational science, gaining the ability to analyse computational data and understanding the physics behind it are more important than being able to submit some calculations. I would like also to thank Professor T. A. Wesołowski for providing the flexibility of conducting research in the group. Many opportunities I have received to extend my knowledge to different scientific topics. Thank you for the concern you have shown, which is always ahead of me, in also my life living in Geneva.

I would like to thank other reviewer members for agreeing to review my thesis: Professor Anna Krylov, Professor Rob Thew, as well as Professor Eric Vauthey. Thank you for spending your time to read my thesis. Thank you for the comments and valuable suggestions.

I would like to thank our big physical chemistry department with all the seminars and lectures. Thank you Professor Eric Vauthey, Professor Thomas Bürgi, Professor Alexndre Fürstenberg, and Professor Takuji Adachi for the excellent lectures on spectroscopic. Thank you, Sophie Jacquemet, for solving every time the administrative issues so efficiently. Thank the High Performance Computing team Yann Sagon, Luca Capello for your strong support on our clusters.

Thank Professor Andreas Savin for discussions on many conferences. Thank you, Dr. Cristina Elizabeth González-Espinoza, who has built the *Taco* code and taught me lots of programming knowledge. I will always remember the tea time, we had, together with Darya and Ana. Thank you, Dr. Niccolò Ricardi for your always energetic vibe and your help on, basically, everything. Thank you, Dr. Elias Polak, it was pleasant to share the apartment with you. The discussion on many topics is "thought-provoking". Dr. Alexander Zech even has already left our group for years. I still remember the farewell dinner at your home. The dinner you prepared was very tasty and we had such a nice time with the group members, also Chris and others in Vauthey's group. Thanks to Yann Gimbal-Zofka for his CHIPHY work we shared together and to Tanguy for your French assistance. Thanks to our launch table team. It was relaxing to have launch break with all of you.

Thanks to my friends Hancheng and Dongmei for preparing "home missing" food and many hikes in the Swiss mountains. I would like also to thank my flatmates in CUP2, Geoffroy, Paul and Abi for interesting culture exchanges. Thanks to my boyfriend Anil for comforting me and travelling with me to many places. You are precious for me. Finally, my deepest gratitude to my parents. Thanks to my father who has enlighten me for many interesting scientific questions since I was little. Thanks to my mother for your wholehearted support.